

**HIGH-RESOLUTION SPECTROSCOPIC STUDIES OF
ATMOSPHERIC GASES ($\text{C}_2\text{H}_2\text{-N}_2$, O_2 , and $^{15}\text{NH}_3$)**

HOIMONTI IMMACULATA ROZARIO

**Master of Science, University of Lethbridge, 2012
Master of Science, Jahangirnagar University, 2010
Bachelor of Science, Jahangirnagar University, 2009**

A Thesis
Submitted to the School of Graduate Studies
of the University of Lethbridge
in Partial Fulfillment of the
Requirements for the Degree

DOCTOR OF PHILOSOPHY

Department of Physics and Astronomy
University of Lethbridge
LETHBRIDGE, ALBERTA, CANADA

© Hoimonti Immaculata Rozario, 2019

HIGH-RESOLUTION SPECTROSCOPIC STUDIES OF ATMOSPHERIC GASES
(C₂H₂-N₂, O₂, and ¹⁵NH₃)

HOIMONTI IMMACULATA ROZARIO

Date of Defence: March 27, 2019

Dr. Brant Billinghamurst Co-supervisor Canadian Light Source Saskatoon, Saskatchewan	Senior Scientist	PhD
Dr. Karl Staenz Co-supervisor	Professor	PhD
Dr. Locke Spencer Thesis Examination Committee Member	Associate Professor	PhD
Dr. Arundhati Dasgupta Thesis Examination Committee Member	Associate Professor	PhD
Dr. Michael Gerken Internal External Examiner	Professor	PhD
Dr. Ann-Lise Norman External Examiner University of Calgary Calgary, Alberta	Professor	PhD
Dr. Craig Coburn Chair, Thesis Examination Committee	Associate Professor	PhD

Dedication Page

I would like to dedicate my PhD thesis work to my mother.

Abstract

With the modern technology and availability of spectrometer systems, it is possible to provide more accurate and new parameters to the spectroscopic databases. Accordingly, three spectroscopic studies were carried out in this thesis. The first study is intended to find the suitable line-shape models that can reproduce $\text{C}_2\text{H}_2\text{-N}_2$ spectra best as well as retrieve reliable parameters, which are very useful for spectroscopic studies. The second project of oxygen A-band spectra is dedicated to retrieving a new parameter, called the speed-dependent parameter. The main goal of the third study is to obtain a better ground state line list of $^{15}\text{NH}_3$, which has never been studied as extensively as in this thesis.

Performing the acetylene study will improve the use of line-shape profiles based on the spectral pressure regions. The new speed-dependent parameter and extended (439) lines of $^{15}\text{NH}_3$ spectroscopic results will progress the retrievals of atmospheric spectra and enrich spectroscopic databases.

Acknowledgements

My deepest gratefulness goes to the individuals who had always been supportive and encouraging me in any situation during my Ph.D. program. Drs. Brant Billingham and Karl Staenz were very kind with their suggestions and time frame. I truly appreciate their help and generosity. As my former supervisor, I am very thankful to Dr. Adriana Predoi-Cross for her support and guiding me through the various projects. My thankfulness goes to the Ph.D. committee members Drs. Arundhati Das Gupta and Locke Spencer for supporting my Ph.D. program and showing their interest in my research projects.

I would like to take the opportunity to show my gratitude to Drs. Gianfranco Di Lonardo of the University of Bologna, Italy and Georg Mellau of the Justus-Liebig University of Giessen, Germany who were my internship supervisors. I really appreciate the opportunity provided by the Canadian Light Source, Saskatoon, Canada to use their facility. I want to thank all my lab colleagues for being helpful and supportive. A special appreciation goes to Dr. Chad Povey for his help and being available for discussions regarding the various research topics.

My thanks go to my friends who have been understandable and supportive during the different stages of this program. I am very grateful to my family, because they have always encouraged me to explore and expand my skills and inspired me in continuing my dedication to work.

Final appreciation goes to the School of Graduate Studies, the Faculty of Arts and Science, and the Department of Physics and Astronomy for being very helpful and supportive. This will not be fulfilled without thanking the NSERC CREATE Advanced

Methods, Education and Training in Hyperspectral Science and Technology (AMETHYST) program and the Alberta Terrestrial Imaging Centre (ATIC) for all the funding and opportunities.

Contents

Dedication Page	iii
Abstract	iv
Acknowledgements	v
List of Figures	xiii
List of Tables	xviii
List of Abbreviations	xxi
List of Symbols	xxiii
Chapter 1 Introduction.....	1
1.1 Overview	1
1.2 History of Spectroscopy	2
1.3 Spectroscopy	2
1.4 Purpose and Literature Review of the Spectroscopic Studies.....	6
1.4.1 Line-Shape Models Testing on Acetylene Transitions	6
1.4.1.1 Literature Review.....	7
1.4.2 Line-shape Parameters of Oxygen A-band Transitions	10
1.4.2.1 Current State of Knowledge of the Oxygen A-band.....	12
1.4.3 Far-Infrared Assignment Study of Ammonia ($^{15}\text{NH}_3$)	17
1.4.3.1 Previous Studies.....	18

1.5	Contribution to Other Studies and Publications	19
1.6	Summary	22
Chapter 2	Theoretical background	24
2.1	Overview	24
2.2	Introduction	24
2.2.1	Fundamentals of Spectroscopy.....	25
2.2.2	Normal Modes of Molecules.....	28
2.2.3	Rotational Spectroscopy.....	29
2.2.4	Vibrational Spectroscopy	34
2.2.5	Rotational-vibrational Spectra and Band Structure.....	38
2.2.6	Types of Molecular Bands	41
2.3	Line-shape Theory.....	42
2.3.1	Beer-Lambert Law	42
2.3.2	Line-shape Function	43
2.4	Different Types of Line-shape Models/Profiles and Parameters	45
2.4.1	Line Position, Shift, and Intensity	45
2.4.2	Natural Line Width (Natural Broadening)	48
2.4.3	Doppler Width (Doppler Broadening), Gaussian Profile.....	49
2.4.4	Pressure-Induced Collisional Broadening.....	50
2.4.5	The Voigt Profile.....	51

2.4.6	Molecular Speed-dependency Effects	54
2.4.7	Speed-dependent Voigt Profile	55
2.4.8	Dicke Narrowing Effect and the Diffusion Coefficient	56
2.4.9	Galatry and Rautian-Sobel'man Profiles.....	57
2.4.10	Speed-Dependent Galatry (SDG) and Speed-Dependent Rautian-Sobel'man (SDR) Profiles	59
2.4.11	Line-mixing	61
2.4.12	Exponential Power Gap Scaling Law (EPG)	63
2.5	Summary	65
Chapter 3	Experimental Procedures	66
3.1	Overview	66
3.2	Tunable Diode-Laser Spectrometer System (C ₂ H ₂ -N ₂ study).....	66
3.2.1	Temperature and Pressure (T-P) Controlled Gas Cell (Channel-1) ...	70
3.2.2	Reference Gas Cell and the Background Signal	71
3.2.3	Pressure Measurements and Monitoring	72
3.2.4	Detectors.....	73
3.2.5	Instrumental Line-Shape Function	74
3.2.6	Fabry-Perot Cavity and Wavemeter	75
3.2.7	Data Processing	77
3.2.8	Wproffit2.exe	80

3.3	Fourier Transform Spectrometer (Ammonia and Oxygen Studies)	81
3.3.1	Spectral Resolution and Signal-to-noise Ratio (SNR)	83
3.4	Experimental Setup of the Far-infrared Study of Ammonia ($^{15}\text{NH}_3$).....	83
3.4.1	Raw Data Processing (OPUS).....	84
3.5	Experimental Setup (Pure O_2)	86
3.5.1	Labfit Program and Analysis.....	88
3.6	Conclusions	89
Chapter 4	Line-shape Study of $\text{C}_2\text{H}_2\text{-N}_2$	90
4.1	Overview	90
4.1.1	My Contribution to this Project.....	90
4.2	Introduction	92
4.2.1	Acetylene Molecule.....	92
4.2.2	Band Structure ($\nu_1+\nu_3$).....	93
4.3	Spectroscopic Analysis of the Acetylene Molecule	95
4.3.1	Line Fitting Using Different Line-Shape Models	96
4.4	Retrieved Line Parameters	100
4.4.1	Comparison of New Parameters of R(16) Lines	109
4.5	Molecular Interaction Potential: Influence on Line-shape	111
4.6	Conclusions	112
Chapter 5	Line-shape Study of Pure Oxygen (O_2).....	114

5.1	Overview	114
5.2	Introduction	114
5.3	Oxygen Molecule	115
5.4	Calibration of the Spectra.....	117
5.5	Retrieval of the Line Parameters	119
5.6	Results and Comparisons	122
5.6.1	Line Position	122
5.6.2	Line Intensities	126
5.6.3	Line Broadening.....	128
5.6.4	Line Shift.....	131
5.6.5	Line Narrowing	133
5.6.6	Line-mixing and Exponential Power Gap Law (EPG).....	136
5.6.7	Speed-Dependent Parameter	140
5.6.8	Molecular Constant for Upper Energy States	142
5.6.9	Einstein A Coefficient.....	144
5.7	Conclusions	146
Chapter 6	Assignment of $^{15}\text{NH}_3$ Far-Infrared Lines.....	148
6.1	Overview	148
6.2	Introduction	148
6.3	Ammonia Molecule.....	150

6.4	Present Study	151
6.5	Transitions in $^{15}\text{NH}_3$	152
6.6	Recorded Spectra.....	153
6.7	Calibration of Spectra.....	154
6.8	Ground-State Spectra	156
6.9	Details of Analysis and Results.....	157
6.9.1	Assignment of Absorption Transition	158
6.9.2	Intensity Analysis	159
6.9.3	Results of Molecular Constants.....	159
6.9.4	Ground-State Assignment	161
6.10	Conclusion	167
Chapter 7	Conclusions	168
7.1	Summary of the Work	168
7.2	Findings	170
	Bibliography	174
	Appendices.....	187
A.	Line-shape Tests on R(16) Line of $\text{C}_2\text{H}_2\text{-N}_2$	187
B.	Line-shape Parameters of O_2	192
C.	Calculation of Molecular Constants of $^{15}\text{NH}_3$	198

List of Figures

Figure 1.1: Source, medium, detector, and measured spectra from output signals...	3
Figure 1.2: Regions of the electromagnetic spectrum (ideas taken from [9, 10]).	4
Figure 2.1: Propagation of electromagnetic radiation (ideas taken from Figure 2.1 in [8]). E represents the strength of the electric field along the xy -plane and M is the strength of the magnetic field along the zx -plane.....	25
Figure 2.2: Absorption and emission processes in a two-level system when electromagnetic radiation interacts with matter. (1) induced absorption, (2) stimulated emission and (3) spontaneous emission (modification of Figure 2.2 in [8]).	27
Figure 2.3: Examples of transitions between rotational energy levels of linear molecules. The allowed selection rule for rotational transitions is $\Delta J = \pm 1$ (modification of Figure in 6.13 [101] and idea taken from Figure 5.2 in [8]).	30
Figure 2.4: Bending modes of vibrating molecule (A) and the circular path of the nuclei (B) (modification of Figure in 6.22 [101]).	36
Figure 2.5: P-, Q- and R-type transitions between two vibrational states are shown on the left of the Figure. The structure of the parallel band is shown in (a). Red curves are the absorption lines. The perpendicular band is a combination of (b) and (c) (modification of Figure 6.7 in [8]).	39
Figure 2.6: U_0 and U are the light intensity before and after passing through the sample (medium). L is the pathlength of the absorption medium.	43
Figure 2.7: Example of an absorption line presenting the line parameter (idea taken from Figure 1.1 in [102]). Symbol ν is the frequency of incident radiation, ν_0 is the transition frequency between two energy levels, γ is the half-width at half-maximum or HWHM of $2\Delta\nu$, and δ is the pressure induced line shift of the absorption line shown in dots.....	46
Figure 2.8: Differences between the following three line-shape profiles: Lorentz (dashes), Voigt (dots), and Doppler (solid line) (ideas taken from Ref. [114]).	53
Figure 2.9: Effects of speed-dependency in the spectroscopic analysis of broadening (left) and shift (right) parameters (modification of figures (2-6, III.14, 1) in [6, 114, 115], respectively). In these figures, the absorption lines are shown upwards in order to see the effects more clearly.....	54

Figure 2.10: Example of the line-mixing effect – Perturbed energy levels leading to line-mixing. Panel (a) shows two absorption lines of transition frequencies ν_1 and ν_2 . Panel (b) presents the two lines whose profiles overlap - an example of the evolution of typical doublet shape. Panel (c) shows the perturbed rotational states (energy levels) through collisions. The dashed horizontal lines represent the perturbed levels (modification of Figure 2.7 in [6] and ideas taken from Ref. [114]).62

Figure 3.1. Configuration of the 3-channel tunable diode-laser spectrometer. (A) Photo of the TDLS setup: 1. temperature and pressure controlled cell, 2. room-temperature reference cell, 3. Neslab Chiller ULT-80, 4. Wavemeter and 5. MKS Baratron pressure gauges. (B) Schematic diagram of the 3-channel tunable diode-laser spectrometer [36]: cell-1 is the temperature and pressure controlled gas cell; cell-2 is the room temperature gas cell. Nos. - 1. vacuum pump, 2. Neslab temperature controller, 3. gas cylinder (C_2H_2 and N_2), 4. Fabry-Perot interferometer 5. controller, 6. detector pre-amplifiers and power source, 7. Wavemeter, 8. laser head, 9. controller and 10. pressure gauges. L1, L2, and L3 are the lenses, while D1, D2 and D3 are the detectors. M1 and M2 are the beam guiding mirrors, C1, C2, C3, and C4 are the collimators, and S1, S2, S3, and S4 are the beam splitters (modified version of Figure 3-3 in [6]).68

Figure 3.2: Side view of the temperature-controlled cell: 1. coolant in pipe, 2. coolant return pipe, 3. vacuum port, 4a. gas inlet, 4b. vacuum feed-through for platinum resistors, 5. CaF_2 windows mounted at Brewster angle, 6. temperature sensors using platinum resistors, 7. vacuum valve, 8. fins for directing the coolant through the coolant jacket, 9. coolant jacket, 10. cell support, 11. outer cell body and 12. valve for de-pressuring the outer jacket (modified version of Figure 3-17 in [6]).70

Figure 3.3: Photodiode InGaAs detectors used for measuring the signal from the gas chambers and the laser (modified version of Photograph 3-9 in [6]).74

Figure 3.4: Panel (a): Example of a Channel-1 spectrum in the 6515.50 – 6516.50 cm^{-1} regions in blue and corresponding background in red. Panel (b): Edited spectrum after removal of the spectral features (blue) for the baseline correction using the background spectrum. Panel (c): Corrected baseline for Channel-1 spectrum. Panel (d): Channel-1 transmission spectrum of the absorption line P(16).78

Figure 3.5: Diagram of a Michelson interferometer [128]. L' is the distance between beam splitter and fixed mirror. L is the distance between beam splitter and moving mirror, which varies during the scanning.82

Figure 3.6: Example of $^{15}NH_3$ transmission spectra record at 0.002 Torr. The intensity is decreasing with increasing wavenumber. The transmission spectra were created in OPUS.85

Figure 4.1: A simulated vibrational spectrum for acetylene at 300-Torr room-temperature was generated using the data taken from the HITRAN website [134]. The selected six absorption lines are pointed with red dots (P-branch (6452 - 6555 cm^{-1}) and R-branch (6555 - 6630 cm^{-1}) regions).....	94
Figure 4.2: Broadening coefficients for six transitions in the $\nu_1+\nu_3$ band of $\text{C}_2\text{H}_2\text{-N}_2$ retrieved using the Voigt (VP), Rautian (RP), Galatry (GP), and Speed-Dependent Voigt (SDV) profiles.....	102
Figure 4.3: Broadening coefficients for transitions in the $\nu_1+\nu_3$ band of acetylene retrieved using the VP profiles and compared with previously published values from the literature (self-generated modified version of Figure 5 in [20]).	103
Figure 4.4: Broadening coefficients for transitions in the $\nu_1+\nu_3$ band of acetylene retrieved using the RP profile and compared with previous values from the literature...	103
Figure 4.5: Narrowing coefficients retrieved for six transitions in the $\nu_1+\nu_3$ band of $\text{C}_2\text{H}_2\text{-N}_2$ spectra and compared with previously published values from the literature. The black line represents the calculated narrowing (self-generated modified version of Figure 6 in [20]).	106
Figure 4.6: Shift coefficients retrieved for six transitions in the $\nu_1+\nu_3$ band of $\text{C}_2\text{H}_2\text{-N}_2$ spectra and compared with previously published values from the literature (self-generated modified version of Figure 7 in [20]).	108
Figure 5.1: Oxygen molecule vibrational mode. Two oxygen atoms are connected with a double intermolecular bond, which exhibits only the symmetric stretching vibrational mode.	115
Figure 5.2: Diagram showing possible transitions in the A-band. X is the lower energy level and b is the upper energy levels of the electronic energy state. J' and J'' represent the total angular momentum quantum numbers. N' and N'' represent the rotational quantum numbers. Green lines represent P-branch transitions (PP and PQ lines), while the blue lines indicate R-branch transitions (RR and RQ lines). Information gathered from the literature in [44].	116
Figure 5.3: Oxygen A-band spectra recorded at 337.1 Torr in the 13048 – 13160 cm^{-1} regions. The P3P3, P3Q2, R3R3, and R3Q4 lines are indicated with arrows.	117
Figure 5.4: Low-pressure spectrum (9.00 Torr) in red and high-pressure spectrum (878.45 Torr) in green in the 13048.00 – 1316.00 cm^{-1} region.	118

Figure 5.5: Oxygen A-band spectra in the P-branch range ($13048 - 13120 \text{ cm}^{-1}$). Top panel (a) presents a fitted spectrum recorded at 98.25 Torr using the RP and (b) indicates the residuals. Panel (c) presents all the spectra simultaneously fitted using SDV. Residuals after fitting all the spectra using VP, SDV, and SDR profiles are plotted in Panels (d), (e), and (f), respectively. 121

Figure 5.6: (A) Differences in line positions between the present values (VP) and previous studies, and (B) line positions retrieved in the present study using VP compared to RP, SDV, and SDR profiles. 125

Figure 5.7: (A) Comparison of intensities retrieved using VP in the present study and their corresponding error bars (100 times) with those in the literature. (B) Ratios of the line intensities between the values obtained in the present study and the previous studies. Here, $\mathbf{m} = -J'' = -N''$ is for the P-, and $\mathbf{m} = J''+1 = N''+1$ is for the R-branch. 127

Figure 5.8: Self-broadening coefficients obtained using the Voigt (VP) and Speed-dependent Voigt profiles (SDV) (A), and Rautian (RP) and Speed-dependent Rautian (SDR) profiles (B) (line-shape models that take into account the narrowing effects – from spectra below 100 Torr). Here, $\mathbf{m} = -J'' = -N$ is for the P- and $\mathbf{m} = J''+1 = N''+1$ is for R-branch. 130

Figure 5.9: Self-pressure shift coefficients for transitions in the oxygen A-band. Here, $\mathbf{m} = -J'' = -N$ is for the P- and $\mathbf{m} = J''+1 = N''+1$ is for R-branch. 132

Figure 5.10: Calculated and fitted narrowing coefficients compared with the experimental results from Long et al. [47]. Here, $\mathbf{m} = -J'' = -N$ is for the P- and $\mathbf{m} = J''+1 = N''+1$ is for the R-branch. 135

Figure 5.11: R-branch ($13124 - 13160 \text{ cm}^{-1}$) spectra of pressure 494.52 Torr. The pairs of two lines at the right corner indicated with arrows show an appearance of line coupling. Lines of the spectra recorded at pressures higher than presented in this graph show more overlap. 137

Figure 5.12: Line-mixing coefficients for transitions in the oxygen A-band. Comparison between experimental results and theoretically calculated values using the EPG-scaling law. Here, $\mathbf{m} = -J'' = -N$ is for the P- and $\mathbf{m} = J''+1 = N''+1$ is for the R-branch. 139

Figure 5.13: The speed-dependence parameters for transitions in the oxygen A-band. Here, $\mathbf{m} = -J'' = -N$ is for the P-, and $\mathbf{m} = J''+1 = N''+1$ is for R-branch. 141

Figure 5.14: P-branch fit plot to determine the molecular constants. 143

Figure 5.15: Comparison of the Einstein A_{ij} coefficient. Here, $m = -J'' = -N$ is for the P and $m = J''+1 = N''+1$ is for R-branch.	145
Figure 6.1: Stretching and bending vibrational modes of NH_3 (modification of Figure 4.17 in [8]).	150
Figure 6.2: Diagram of energy levels showing examples of few transitions. The blue arrows are rotation-inversion, the red ones are hot bands ($v_2 = 1 \rightarrow v_2 = 2$) and the black ones are vibration-rotation transitions (GS \rightarrow upper states, $v_2 = 1$ and 2).	152
Figure 6.3: Example of absorption lines in a portion of the far-infrared spectrum showing the rotation-inversion (GS, $J = 7\text{K} - 6\text{K}$, $a \leftarrow s$ and $s \leftarrow a$) transitions of the $^{15}\text{NH}_3$ molecule [79]. The red stars are the water (H_2O) lines and the green ones are the $^{14}\text{NH}_3$ lines.	155
Figure 6.4: Residuals of H_2O lines calculated using the results from the literature [151] and from 0.002 Torr spectra of the present study recorded in the $100 - 150 \text{ cm}^{-1}$ regions (red diamonds). The water lines were compared for calibration purposes.	155
Figure 6.5: Example of absorption lines in a portion of the FIR spectrum showing the rotation-inversion (GS, $J = 10\text{K} - 9\text{K}$, $a \leftarrow s$ and $s \leftarrow a$) transitions (black dotted lines) of the $^{15}\text{NH}_3$ molecule. The H_2O lines are marked with red stars. The presentation concept was taken from the literature [79].	157
Figure 6.6: Ground-state spectra of $^{15}\text{NH}_3$ in the $250 - 260 \text{ cm}^{-1}$ region. Water lines in this region are indicated with red stars.	164
Figure 6.7: Comparison of assigned experimental (present study [79]) and fitted experimental (present study) line position of $J = 13\text{K} \leftarrow 12\text{K}$ transitions in the ground states of ammonia. Error bars (1000 times) represent the errors in the fitted results from Column 8 of Table 6.3.	164
Figure 6.8: An example of the fit for the $^{15}\text{NH}_3$ -line ($J = 13\text{K} \leftarrow 12\text{K}$, $K'' = 6$) at 251.8973 cm^{-1} . The green and the red lines in the upper panel are the experimental and the fitted spectra, respectively.	165

List of Tables

Table 3.1: Example of pressure and temperature measurements as they were recorded after scans. The titles of the columns do not appear in the output files (CH1 = channel 1 and CH2 = channel 2).....	73
Table 3.2: Example of the “Peak” file where the first column represents the Fabry-Parot Voltage and the second one lists the wavenumber (free spectral range 0.05 cm^{-1})..	76
Table 4.1: Fundamental vibrational modes of the acetylene molecule (modification of Figure 6.20 in [8]).....	93
Table 4.2: Example of the gas concentration test, retrieved using the R(16) line. Pressures were recorded in Torr. The errors are given in the parenthesis (corresponding to one standard deviation referring to the last significant digits).....	96
Table 4.3: List of RMS (root mean square) values of residuals from the fits in Figure A.3 in Appendix A for the spectra of 5, 10, 20, 30, and 40 Torr.....	97
Table 4.4: List of RMS (root mean square) values of residuals from the fits in Figure 4.4 for the spectra of 5, 10, 20, 30, 40, 100, and 250 Torr.....	99
Table 4.5: Broadening coefficients ($\text{cm}^{-1}\text{atm}^{-1}$) for six transitions in the $\nu_1 + \nu_3$ band of acetylene retrieved from the room-temperature $\text{C}_2\text{H}_2\text{-N}_2$ spectra. The uncertainties in parenthesis are given as one standard deviation referring to the last significant digits. The Rautian Profile (RP), Galatry Profile (GP), Rautian-Galatry Profile (RGP), Correlated Rautian Profile (CRP), Speed-Dependent Voigt (SDV), Speed-Dependent Rautian (SDR), Correlated Speed-Dependent Rautian (CSDR) and Voigt Profile (VP) broadening are listed (modification of Table 2 in [20]).	101
Table 4.6: Narrowing coefficients ($\text{cm}^{-1}\text{atm}^{-1}$) for six transitions in the $\nu_1 + \nu_3$ band of acetylene retrieved from the room-temperature $\text{C}_2\text{H}_2\text{-N}_2$ spectra. The uncertainties in parenthesis are given as one standard deviation referring to the last significant digits. The Rautian Profile (RP), Galatry Profile (GP), Rautian-Galatry Profile (RGP), and Correlated Rautian Profile (CRP) narrowing are listed (modification of Table 3 in [20]).....	105
Table 4.7: Shift coefficients ($\text{cm}^{-1}\text{atm}^{-1}$) for six transitions in the $\nu_1 + \nu_3$ band of acetylene retrieved from the room-temperature $\text{C}_2\text{H}_2\text{-N}_2$ spectra. The uncertainties in parenthesis are given as one standard deviation referring to the last significant digits. The Rautian Profile (RP), Galatry Profile (GP), Rautian-Galatry Profile (RGP), Correlated Rautian Profile (CRP), Speed-dependent Voigt (SDV), Speed-dependent Rautian (SDR),	

correlated Speed-dependent Rautian (CSDR) and Voigt Profile (VP) shift coefficients are listed (modification of Table 4 in [20])..... 107

Table 4.8: The line-mixing coefficients ($\text{cm}^{-1}\text{atm}^{-1}$) for six transitions in the $\nu_1 + \nu_3$ band of acetylene retrieved from the room-temperature $\text{C}_2\text{H}_2\text{-N}_2$ spectra. The uncertainties in parenthesis are given as one standard deviation referring to the last significant digits. Speed-dependent Voigt (SDV), Speed-dependent Rautian (SDR), correlated Speed-dependent Rautian (CSDR) profiles line-mixing coefficients are listed (modification of Table 5 in) [20]. 109

Table 4.9: The RMS values from old [20] and new fits of R(16) lines using VP, RP, GP, and RGP..... 110

Table 4.10: The retrieved parameters from the old and new fits of R(16) lines.. 110

Table 5.1: Experimental conditions of oxygen A-band spectra used in the present analysis (13050 to 13159 cm^{-1} range)..... 119

Table 5.2: Average absolute error in the oxygen A-band line positions compared to the literature results..... 124

Table 5.3: The constants a, b and c were determined using the EPG scaling law for the sub-bands listed in the table. The error values are quoted in parentheses, which correspond to one standard deviation..... 138

Table 5.4: The fit values of molecular constants in the upper state of the oxygen A-band. All parameters are given in wavenumber unit (cm^{-1})..... 143

Table 6.1: Type of assigned transitions in the ground state of ammonia ($^{15}\text{NH}_3$) recorded in the FIR spectral region using a Bruker IFS 125 Fourier transform spectrometer system. 158

Table 6.2: Spectroscopic parameters presented in the wavenumber unit (cm^{-1}) for the ground state of $^{15}\text{NH}_3$. The uncertainties are given in the parenthesis as one standard deviation (1σ) referring to the last significant digits [79]. Here, (i) corresponds to the lower and upper state components (s) and (a) of the inversion doublet. This table is a modified version of Table 2 of the published paper (results are unchanged) [79]..... 160

Table 6.3: An example of assigned and fitted line positions, intensities and Einstein coefficients for the pure inversion and rotation-inversion transitions in the ground state ($J = 13\text{K} \leftarrow 12\text{K}$) of ammonia ($^{15}\text{NH}_3$). The uncertainties are given in the parenthesis corresponding to one standard deviation (1σ) referring to the last significant digits. J' and

K' are the upper, and J'' and K'' are the lower energy state rotational quantum numbers. S' and S'' are the inversion symmetry for the upper and lower energy states, respectively. 162

List of Abbreviations

CLS	Canadian Light Source
CR	Correlated Rautian
CSDR	Correlated Speed-dependent Rautian
ECDL	Extended Cavity Diode Laser
ECS	Energy Sudden Corrected
EPG	Exponential Power Gap
FIR	Far-infrared
FP	Fabry-Perot
FTS	Fourier Transform Spectrometer
Ge:Cu	Germanium-copper
GEISA	Gestion et Etude des Informations Spectroscopiques Atmosphériques (Management and Study of Spectroscopic Information)
GP	Galatry Profile
GS	Ground State
HITRAN	High-resolution Transmission Molecular Absorption Database
HWHM	Half-Width at Half-Maximum
ILS	Instrumental Line Shape
InGaAs	Indium Gallium Arsenide
LabVIEW	Laboratory Virtual Instrument Engineering Workbench
LM	Line-mixing
MD	Molecular Dynamics
MIR	Mid-infrared
MSD	Mean Square Displacement
NASA	National Aeronautics and Space Administration
NIR	Near-infrared
PRT	Platinum Resistance Thermometer
RB	Robert-Bonamy

RGP	Rautian-Galaty Profile
RP	Rautian Profile
SDV	Speed-dependent Voigt
SDR	Speed-dependent Rautian
SNR	Signal-to-Noise Ratio
TDLS	Tunable Diode-Laser Spectrometer
UV	Ultraviolet
VI	Virtual Instrument
VP	Voigt Profile

List of Symbols

P	Pressure
P_a	Partial pressure
T	Temperature
E	Energy
E'', E_m	Energy of lower energy state
E', E_n	Energy of upper energy state
m	Lower energy state
n	Upper energy state
E_v	Vibrational dependency of energy states
E_e	Electronic energy term
$E(J, l), E_r$	Rotational energy term
$G(v_i)$	Vibrational energy term
T'	Rotational-vibrational transition
h	Planck's constant
\hbar	Reduced Planck's constant
t	Time
λ	Wavelength
\hat{H}	Hamiltonian function
\hat{J}	Total angular momentum
\hat{l}	Vibrational angular momentum
\hat{R}	Rotational angular momentum
$ l $	Angular quantum number
q'	l -type doubling constant
Ψ, Ψ_m, Ψ_n	Quantum wavefunction
$\Psi_e(q, Q)$	Wavefunction of electron coordinates q and nuclear coordinates Q
Ψ_n	Wavefunction of nuclei
Ψ_r	Rotational part of the wavefunction
Ψ_v	Vibrational part of the wavefunction
Ψ_e	Electronic part of the wavefunction
$\{E_i\}$	Eigenvalues
$\bar{\mu}$	Dipole moment
R_{nm}	Transition dipole moment, transition probability
ν	Vibrational quantum number (also used for denoting molecular speed)
ν	Vibrational frequency (also used for denoting vibrational normal modes)
$\tilde{\nu}$	Radiation frequency in wavenumbers
$\tilde{\nu}_0$	Transition frequency
$\bar{x}, \bar{y}, \bar{z}$	Cartesian coordinates

B, A, C	Rotational constant
B_v	Representing the vibrational dependency of the rotational constants
$D, De, D_0, D_{JK}, D_J, H_0$	Centrifugal distortion constant
D_v	Representing the vibrational dependency of the centrifugal distortion constants
I, I_a, I_b, I_c	Moment of inertia
\bar{E}	Electric field
\bar{M}	Magnetic field
E_0	Magnitude of the sinusoidal periodic function of the electric field
M_0	Magnitude of the sinusoidal periodic function of the magnetic field
k	Wavevector
c	Speed of light
K_B	Boltzman constant
$f(\bar{v}), F_M$	Maxwell-equilibrium distribution
\bar{v}, \bar{v}_a	Velocity
ω_0	Angular frequency
$\Delta\omega_D$	Doppler width in rad.s^{-1}
Ω	Total collision frequency
Γ	Relaxation rate
V	Relaxation matrix
Γ_2	Speed-dependence of the relaxation rate
γ	Broadening coefficient
γ_D	Doppler HWHM
γ_C	Lorentz HWHM
$\gamma_{coll}(v)$	Collisional broadening
Δ	Pressure induced shift
δ	Shift coefficient
$\delta_{coll}(v)$	Collisional shift
β	Narrowing coefficient, narrowing rate
β_{diff}	Dynamical friction coefficient
D_s	Diffusion constant
z	New standardised narrowing parameter
δ'	Optical path difference
M	Mass of the molecule or particle
r	Distance
J	Rotational quantum number
N, K	Second quantum number
m	Index to represent P, Q, and R branch transitions
π	Constant value
q	Absorber-perturber interaction potential
q_i	Charge of particle
S	Electronic spin quantum number

$T'(v)$	Transmission of the absorption profile
τ	Lifetime of an excited energy state
U_0	Light intensity before passing the gas medium
U	Light intensity after passing the gas medium
L	Pathlength of the absorption medium
C'	Gas concentration
α	Absorption coefficient
$F(\tilde{\nu})$	Line-shape function
$F(\tilde{\nu} - \tilde{\nu}_0), F(\nu - \nu_i)$	Normalized line-shape function
$F_n(\tilde{\nu} - \tilde{\nu}_n)$	Line-shape of the n^{th} line
A_{Pn}	Intensity of the n^{th} line
$\tilde{\nu}_n$	Center the n^{th} line
$\Phi_G(t)$	Galatry function
A	Normalized factor
D_s	Self-diffusion constant
G_0	Band center
S_{ij}, S_{mn}	Line intensity
I_x	Isotopic abundance
ν_{ij}	Line position
g', g_k	Statistical weight
c_2	Second radiation constant
$Q(T)$	Total internal partition summation
A_{ij}, A_{mn}	Einstein-A coefficient
N'	Number of atoms
χ_{ik}, χ_e	Anharmonicity constant
d_i	Degeneracy factor of the i^{th} vibration
d_m, d_n	Dipole matrix elements corresponding to the ν_m and ν_n transition frequency
α_e, β_e	Constants
g_{uu}	Additional anharmonic term
E	Subscript e represents equilibrium
ϵ_0	Vacuum permittivity
e	The impact parameter
$\Pi \leftarrow \Pi, \Pi \leftarrow \Sigma, \Pi \leftarrow \Delta,$	Parallel and perpendicular type bands
$W(x, y), W(x', y+z)$	Complex probability function
$K^{EPGL}, K'_{mn}, K''_{mn}$	Collisional transfer rates between two rotational states
$R(\Delta E)$	Translational space factor
Y_n, Y_k	Line-mixing coefficient associated with the off-diagonal elements of the relaxation matrix
X_i	i^{th} data point
X_{avg}	Average signal

Chapter 1 Introduction

1.1 Overview

Spectroscopic methods have been used for decades [1] to understand the composition of Earth and other planetary atmospheres. Most of the molecules that play an important role in atmospheric studies are active in the infrared region of the electromagnetic spectrum. For this reason, performing spectroscopic studies on molecules using laboratory instrumentation and retrieving information from the associated molecular spectra are essential for contributing to spectroscopic databases [2]. Experimental studies using advanced technologies provide a more accurate and detailed knowledge of spectroscopic parameters of molecules that are present in the planetary atmosphere, also provide information on molecular structures and molecular constants.

This thesis presents three spectroscopic studies of three atmospheric gas molecules of interest. These studies will improve spectroscopic databases, atmospheric spectral measurements, and remote sensing applications. The first study is dedicated to testing different line-shape models using the spectra of acetylene perturbed by nitrogen ($\text{C}_2\text{H}_2\text{-N}_2$). The second one discusses the outcome of a line-shape analysis of spectral bands of oxygen molecules (O_2) and the resulting spectral parameters, while the third one covers the assignment of a symmetric top oblate molecule, ammonia ($^{15}\text{NH}_3$). Details of the data analysis and the results of the aforementioned three projects are presented in Chapters 4, 5, and 6, respectively. Chapter 2 discusses the theoretical background of spectroscopy, and Chapter 3 presents the experimental methods used in these three studies.

1.2 History of Spectroscopy

The concept of spectroscopy first arose after Sir Isaac Newton performed the dispersion experiment of light [3] in 1665. In this experiment, white light was sent through a round shaped hole onto a triangular prism, which splits the white light into seven colours known as the visible region of the electromagnetic spectrum [3]. Later on, more experiments revealed that this spectrum also contains non-visible regions. Accordingly, the particles (atoms or molecules) interact with light from different regions of the electromagnetic spectrum [4]. The wavelengths at which any particle is active is called its transition wavelength. In 1885, a mathematical formula based on classical mechanical theory was developed by Balmer to fit the atomic spectra of hydrogen to determine the transition wavelength [5]; however, his formula had limitations in dealing with other atoms [6, 7]. After a few years, Rydberg solved this problem and provided a mathematical method to determine transition wavelengths for other atomic spectra. However, this classical mechanics theory was unable to explain the transition mechanism. Finally, with the advent of the quantum mechanical theory and the development of reliable technologies in the early twentieth century, the current spectroscopic methods, experiments, and analyses are better understood. The contribution of Niels Bohr's atomic model (solar system model), Erwin Schrödinger's mathematical equation and Werner Heisenberg's uncertainty principle in quantum mechanics are notable and remarkable [8].

1.3 Spectroscopy

Spectroscopy deals with the interaction between electromagnetic radiation and matter. Spectroscopic measurements require some basic instrumentation that can record the

spectra of atoms or molecules. Figure 1.1. includes a source of radiation (for example, a tunable laser), a cell filled with sample molecules, and a suitable detector to measure output radiation. Radiation from the source interacts with the molecules in the cell and gets absorbed at specific wavelengths. The decrease in the radiation (output signal) can be detected using a detector and can be displayed as a spectrum (shown in Figure 1.1). It represents absorption features, and each of these features is called an absorption line. The electromagnetic spectrum is divided into several regions, such as starting from the longer wavelengths (lower frequency) to shorter wavelengths (higher frequency), namely the TV/radio, microwave (MW), infrared (far-infrared (FIR), mid-infrared (MIR), and near-infrared (NIR)), visible, ultraviolet, x-ray, and gamma-ray regions as shown in Figure 1.2. The relation between wavelength and frequency is as follows:

$$\nu = \frac{c}{\lambda}, \quad (1.1)$$

where ν (nu) is the frequency in Hz, c is the speed of light, and λ (lambda) is the wavelength. In these spectroscopic studies, the wavenumber (cm^{-1}), $\tilde{\nu} = \frac{1}{\lambda}$, is used as the unit of frequency. Spectra of different frequencies are also named based on their type of transition; for example, rotational, vibrational, rovibrational, electronic spectra as described in Sections 2.2.3 - 2.2.6. This thesis presents the experimental analysis of spectra in the infrared and visible regions.

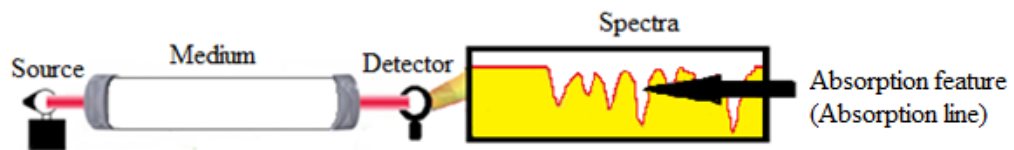


Figure 1.1: Source, medium, detector, and measured spectra from output signals.

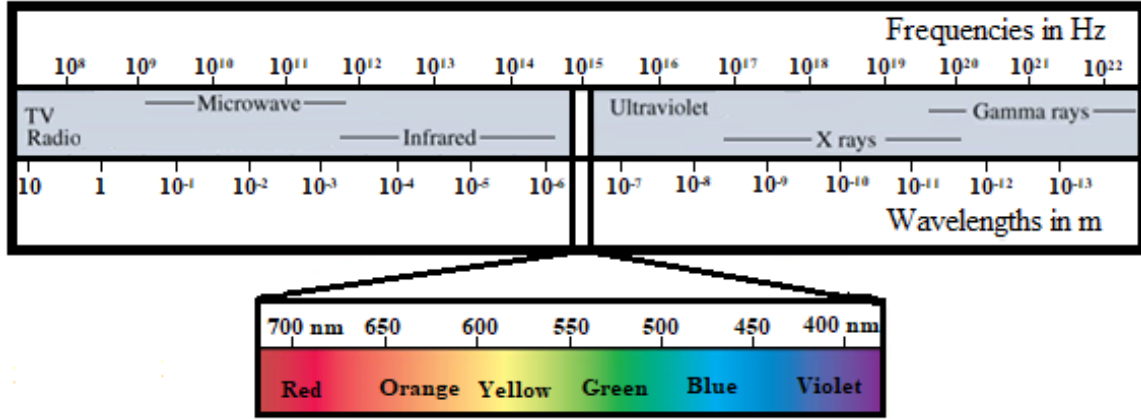


Figure 1.2: Regions of the electromagnetic spectrum (ideas taken from [9, 10]).

Lasers are useful radiation sources for spectroscopy. There are different types of laser systems available for spectroscopic studies. The first laser called the ammonia maser was invented by Charles Hard Townes in 1954, operating in the microwave (MW) region [8]. In the 1960's, Theodore H. Maiman developed the ruby and alexandrite solid-state lasers [8]. These two types of lasers had a drawback that the lasing (laser emission) occurs only at one or two wavelengths. Later on, new types of lasers were developed with the ability to be tuned over a range of wavelengths. For example, the dye laser (liquid or solid state) is tunable between 15748 and 17857 cm^{-1} (560 and 635) nm. The first of these was developed in 1966 by Sorokin and Schäfer [11, 12]. Over the last few decades, more sophisticated lasers have been developed, such as the tunable solid-state laser [13] tunable between 12500 and 13793 cm^{-1} (720 and 800 nm), the titanium sapphire laser covering $9090 - 14925 \text{ cm}^{-1}$ (670 - 1100 nm) [14], the semiconductor diode laser tunable between 500 and 25000 cm^{-1} (0.4 and 20 μm) [8], and the vertical cavity surface emitting laser covering the $6666 - 11764 \text{ cm}^{-1}$ (850 - 1500 nm) wavelength range [15].

One of the studies in this thesis was performed using a tunable-diode laser spectrometer (TDLS) suitable for the near infrared region. The other two studies were performed using a Fourier Transform Spectroscopy (FTS) system; one of them used a Globar source covering the FIR region, while the other one used a tungsten halogen lamp covering the NIR and visible regions.

Besides selecting a proper source, the cell and the detector must be chosen carefully. The sample cell must be long enough for absorption, and the window material of this cell must be suitable to transmit the radiation. For infrared regions, examples of some suitable cell-window materials are polypropylene (for FIR regions) and CaF_2 , NaCl or KBr (for MIR and NIR regions). The TDLS system used the CaF_2 windows, while the FTS systems used polypropylene.

Finally, the detectors must be selected keeping in mind whether the detector material is sensitive to the incident radiation falling on it [8]. Normally, a crystal diode is a suitable detector for the MW region; thermocouple devices for the millimeter wave; thermocouple and pyroelectric detectors for the far-infrared; thermocouple, photoconductive, and semiconductors for the mid- and near-infrared; and photomultiplier, photodiode, and photographic plate for the visible and ultraviolet regions [8]. Some examples of photoconductive semiconductor materials are Si, InGaAs, Ge, InSb, CdS, and PbS. InGaAs detectors were used in the TDLS system, a Si-bolometer in the FTS system for the ammonia study and an Si-diode for the oxygen study. Details of the experimental instrumentation used for the TDLS and FTS systems are given in Chapter 3. The literature reviews of these three studies are presented in the following sections.

1.4 Purpose and Literature Review of the Spectroscopic Studies

The purpose of this literature review is to introduce the related studies that the research community has previously reported over the past few decades. Its work techniques and achievements are briefly given as well.

1.4.1 Line-Shape Models Testing on Acetylene Transitions

Acetylene is a linear polyatomic molecule. It was first discovered more than 150 years ago by Sir Humphry Davy [16]. Since 1860, it has become one of the main subjects in the investigation of chemical reactions. It has been detected by the Earth-orbiting satellite, the Atmospheric Chemistry Experiment (ACE) [17]. Acetylene shows strong absorption features in the infrared region, which is useful for studying the atmospheric spectra of many planets, the interstellar medium and Titan [18]. Due to its simple linear structure, being infrared active and present in different planetary atmospheres have increased the importance of determining the line-shape parameters of acetylene.

Previous studies have noticed that narrowing and small asymmetries in the spectral lines that are not accounted for while fitting the Voigt profile (VP). The goal was to test other profiles if they can be used to fit spectra properly by taking narrowing and speed-dependent effects into account. It is expected that they would change the value of some important line-shape parameters. Therefore, this study is dedicated to testing line-shape profiles (line-shape models) of absorption lines of the $\nu_1+\nu_3$ combination band (described in Section 2.2.6) of acetylene, which appears between $6475 - 6625 \text{ cm}^{-1}$ (1500 - 1550 nm), and to report the retrieved line parameters. The line-shape parameters can be retrieved using several line-shape models; for example, the VP, the narrowing profiles, Rautian (RP) and

Galatry (GP), and speed-dependence profiles, such as Speed-Dependent Voigt (SDV) and Speed-Dependent Rautian (SDR) [19, 20], as described in Sections 2.4.5 - 2.4.10. The choice of the line-shape model depends on the conditions under which the spectra were collected, such as temperature and pressure. Thus, accurate line parameters need to be retrieved using appropriate line-shape profiles by accounting for all the physical conditions and the possible effects that occur during inter-molecular interactions.

1.4.1.1 Literature Review

This section covers the infrared spectra of acetylene used in different studies from the literature over the last few decades, perturber gases (broadeners) and the line-shape profiles that were used to analyze the acetylene spectra. Some theoretical studies will also be discussed in this section. Some of the previous studies have presented the results of acetylene spectra fitted using only one line-shape profile, the VP. It is a convolution of two other profiles, the Lorentz and the Gaussian models. For three decades, VP has been widely used in the spectroscopic field to retrieve line-shape parameters, namely line positions, intensities, broadening and shifting (theoretical aspects of these parameters are described in Chapter 2). Some of these studies have examined pure acetylene spectra and some have also used foreign broadeners. Lambot et al. [21] used room temperature C_2H_2 spectra perturbed by O_2 and N_2 molecules to retrieve line-shape parameters of the (the detail of vibrational normal modes is given in Section 2.2.2) fundamental band ν_5 , which is located in the 735 cm^{-1} (13600 nm) region. Later in 1992, Varanasi et al. [22] also studied the same fundamental band of acetylene and reported the line intensities and collision-broadened half-widths perturbed by He, Ar, H_2 , and N_2 . Artega et al. [23], Campbell et al. [24], and

Minutolo et al. [25] reported N₂-broadening and shift coefficients of acetylene gas for the $\nu_1+\nu_3$ spectral band in the 6493 cm⁻¹ (1540 nm) region.

The absorption line-shape of the $\nu_1+3\nu_3$ overtone-combination band of C₂H₂ in the 12787 cm⁻¹ (782 nm) region was studied by Biswas et al. [26] to measure the self- and N₂-broadening coefficients. N₂- and air- broadening line widths were measured by Malathy et al. [27] in 1985 for the $\nu_4+\nu_5$ combination band of acetylene, which is centered around 1329.99 cm⁻¹ (7518.80 nm). The study showed that the halfwidths of absorption lines show a decreasing trend with increasing lower energy state rotational quantum number J'' as described in Chapter 2.

Rautian and Sobel'man [28] and Louis Galatry [29] have introduced modified spectral line-shape models, known as the hard and soft collision, respectively. These models are non-VP type functions. They are also called the hard collision (RP) and the soft collision (GP) profiles and account for the presence of collisional narrowing in the absorption lines. The RP and GP profiles are used for fitting experimental spectra in order to account for the narrowing effects in the absorption lines and retrieve the narrowing coefficient.

Pine [30] reported the self-, N₂- and Ar-broadening coefficient of the $\nu_1+\nu_5$ band of acetylene retrieved with the RP. This band is located in the 4091 cm⁻¹ (2444.39 nm) region. In this study, the broadening coefficients were fitted with empirical rotationally inelastic collision rate laws (energy gap fitting and energy-corrected-sudden scaling fitting laws). These values were used in modeling the line-mixing in the Q-branch region where the line profiles overlap.

Rozario et al. [31] performed a line-shape study using the combination band $\nu_1+\nu_3$ of acetylene perturbed by nitrogen. This study was performed during my M.Sc. Program, which demonstrated the temperature dependencies of acetylene lines broadened by nitrogen. More specifically, the thesis reported the line-shape parameters of 47 absorption lines of *P*- and *R*-branches retrieved using VP and RP and the temperature dependencies of the broadening and shift coefficients. It also reported broadening and shift coefficients calculated using a semi-classical formalism calculation. Details of branching in band structures are given in Section 2.2.5.

Collisional broadening and pressure-induced shift coefficients were measured and analyzed by Dhyne et al. [32] for nine absorption lines of $C_2H_2-N_2$ spectra. McRaven et al. [18] tested only one *P*-branch line, P(11), to retrieve collisional parameters (self- and N_2 -broadening, narrowing, and shift) using the VP, RP, and GP. Zimmermann et al. [33] investigated the J'' dependency of the broadening, narrowing and shift coefficients for the $\nu_1+3\nu_3$ band of acetylene using RP and GP.

Speed-dependent profiles were developed by Berman [34] and Pickett [35] to take the asymmetry into account that is present in the absorption lines. This is due to the random velocity change of active molecules (speed dependency of line-shape parameters) [19, 20] [36] [37]. Popular speed-dependent profiles are the SDV and SDR. Povey et al. [36] used the VP and SDV profiles to retrieve the self-broadening line-shape parameters of the $\nu_1+\nu_2+\nu_4+\nu_5$ combination band of acetylene for 20 lines recorded at room temperature. Lance et al. [37] analyzed the ν_5 band of C_2H_2 perturbed by Xe using the SDR line-shape model to observe the speed-dependent and the Dicke narrowing effect [38, 39] on the collisional broadening and shifting coefficients. A total of 12 absorption lines of acetylene

in the $\nu_4+\nu_5$ band were used to retrieve N_2 -broadening coefficients by Fissiaux et al. [19] using the VP, RP, GP, and SDR profiles.

The study of acetylene presented in this thesis focuses on testing different line-shape profiles using spectra of acetylene perturbed by nitrogen. Spectra were recorded at pressures between 5 and 250 Torr. The results of fitted spectra of different pressures using eight different profiles (VP, RP, Correlated Rautian (CRP), GP, Rautian-Galatry (RGP), SDV, SDR, and Correlated Speed-Dependent Rautian (cSDR)) are demonstrated elaborately [20] in this study. It is presented in detail in Chapter 4.

Finally, some studies were also dedicated to theoretical calculations of acetylene line parameters, namely the ones included in the Robert-Bonamy formalism [40-42] and Energy Corrected Sudden law (ECS) [43]. These types of theoretical studies are important as they can be considered as a guide for experimental investigations or vice-versa.

1.4.2 Line-shape Parameters of Oxygen A-band Transitions

The distribution of oxygen in the different altitudes/layers of the atmosphere is very uniform. Oxygen is a diatomic molecule of two oxygen atoms. Being a homonuclear diatomic molecule, it possesses different characteristics than the other linear diatomic molecules that are heteronuclear. For example, oxygen does not have a permanent electric dipole moment and, therefore, it is MW and millimeter-wave inactive. However, it has a magnetic dipole transition moment. The magnetic dipole allows transitions of oxygen exhibiting absorption spectra. Transitions between the lower electronic state X and upper electronic state b give rise to the oxygen A-band, which is the strongest absorption band among the series of weak oxygen bands [44]. It is located in the visible region from 13020 to 13170 cm^{-1} (759-768 nm) of the electromagnetic spectrum.

Oxygen is one of the most abundant and most important elements of the Earth atmosphere. For over four decades, scientists have been gathering spectroscopic data of the oxygen A-band for atmospheric observations [1]. Ground-based remote sensing and satellite instruments, such as the NASA Stratospheric Aerosol Gas Experiment III (SAGE III), the Orbiting Carbon Observatory 2, ACE, Measurement of Aerosol Extinction in the Stratosphere and Troposphere Retrieved by Occultation (MAESTRO) [44-46], and Greenhouse Gases Observing Satellite (GOSAT) [47] are the known missions that have been using A-band spectra to determine temperature and pressure profiles. The presence of this gas in the atmospheric spectra of the Earth makes the researchers interested in studying the oxygen A-band for remote sensing purposes [47], namely measurements of cloud-top heights [48], airmass [49], aerosol and cloud optical properties such as surface pressure [50].

To improve the accuracy of the line parameters of this molecule listed in spectroscopic databases, such as HITRAN [51] and GEISA [52], these atmospheric spectra need to be fitted using several line profiles and not only with the traditional ones, such as the VP as described in Section 2.4. Modeling atmospheric or laboratory spectra requires that several effects to be taken into account; for example, the narrowing, speed-dependency and line-mixing effects. In spectroscopic studies, accurate information of key-line parameters, such as positions, intensities, broadening, shift, narrowing, line-mixing, speed-dependence, which are retrieved using appropriate line-shape models together with known concentration profiles can provide knowledge that is required to determine the temperature and pressure profiles at different altitudes of the atmosphere. These parameters in return enable the determination of concentration profiles of some of the other atmospheric species.

The improvement of oxygen A-band line parameters (line positions and pressure-induced shifts) will be very important in the future for the spectral calibration of the visible wavelength region [53]. Having a fairly stable distribution of the concentration with altitude and having well-structured non-saturated absorption bands even for long pathlengths make this molecule important for spectroscopic atmospheric studies.

This study includes the analysis of the oxygen A-band spectra using the line-shape profiles that take the speed-dependence, the collisional narrowing, and the line-mixing effects between two neighbouring lines into account. Besides analyzing the experimental spectra, an extended theoretical study has also been performed to calculate the broadening and line-mixing parameters using the Exponential Power Gap Scaling Law (EPG) to compare them with the experimental results. A further analysis was performed to retrieve the speed-dependent (SD) parameters, which have never been reported before for pure oxygen A-band spectra.

To fulfill the aforementioned goal of this study, it is important to retrieve the accurate line-shape parameters and compare them with the results from literature to confirm, where applicable, their accuracy. In addition, obtaining the SD parameters by fitting the spectra using the SDV and SDR profiles, the speed dependence of broadening should be implemented to give a more realistic/physical representation of the line-shapes.

1.4.2.1 Current State of Knowledge of the Oxygen A-band

Since 1927, scientists have been interested in examining the oxygen A-band absorption spectra to obtain information on the isotopic natural abundance using the band intensity and to determine the physical atomic mass of oxygen as $^{16}\text{O} = 15.999 \text{ u}$. They

used natural light to record weak (absorption feature) atmospheric oxygen spectra [54]. Later, scientists started to perform laboratory experiments to obtain oxygen A-band spectra using different types of spectrometer systems.

In 1987, the oxygen A-band was first modeled using a non-VP line-shape model called the GP by Ritter and Wilkerson [55]. The main goal was to measure line strength and width and test the VP and non-VP profiles using the A-band spectra recorded with an ultrahigh-resolution tunable dye-laser absorption spectrometer. They concluded that the line strength remains the same, but the line widths change linearly with pressure. In the 1990s, Kanamori et al. [56] recorded the oxygen A-band using a diode-laser spectrometer system to analyze 36 transitions in the oxygen A-band and determine the molecular constants (band center, rotational constant and centrifugal distortion constant) of the lower electronic state, b . O'Brien et al. [57] reported molecular constants of the oxygen A-band recorded using high-resolution intracavity laser-spectroscopic instrumentation. They applied an external calibration to the wavenumber scales of the oxygen A-band spectra.

An FTS system was first employed to observe the oxygen A-band by Phillips et al. [58] in 1995. They studied the pressure-induced line-shift parameters of the oxygen A- and B-bands. The shifts reported in their study are larger than usual, demonstrating the need to account for the pressure-induced shift when using the oxygen A-band line positions as a reference. In 1997, they continued this experimental study to determine the 'band center' of the oxygen A- and B-bands as well as the molecular constants, and to retrieve the line positions by performing a pressure shift correction [59].

High-resolution room-temperature and 198 K oxygen A-band spectra were used by Shermaul et al. [60] to retrieve line parameters. A least-square line-fitting procedure was implemented to obtain line intensities and self-broadening. After fitting with the standard VP profile, they noticed a deviation in the modeled spectra and concluded that it occurred due to the collisional narrowing effect.

Brown et al. [53] studied self- and N₂-broadened oxygen spectra obtained using a McMath FTS system. This study reports the line positions, intensities, self- and N₂-broadened halfwidths and their temperature dependencies, and pressure-induced self- and N₂-shifts. In the same year, two other research studies by Yang et al. [61] and Cheah et al. [62] reported the line intensities and self- and N₂-broadening coefficients of the oxygen A-band. Cheah and co-authors also reported the line shifts of oxygen, while Yang et al. performed a theoretical ECS calculation of the self-broadening coefficients. Both of these studies were compared to literature values to validate the results [61] and [62] to their references (4, 5 and 7) and (14 - 35), respectively.

An FTS system was used by Hill et al. [63] for recording oxygen A-band spectra. The average of the self- and N₂- induced shifts for the transitions in the oxygen A-band was determined as $-0.009 \pm 0.001 \text{ cm}^{-1}\text{atm}^{-1}$. Pope et al. [64] observed the influences of a variety of perturbers on the oxygen molecule by examining broadening coefficients of 42 A-band transitions obtained using an FTS system. A few years later, the same research group studied pressure-induced shift coefficients of oxygen gas perturbed by the Xe gas along with pressure-broadening coefficients perturbed by other noble gases (He, Ne, Ar, and Kr) [65].

In 1997, Ray and Ghosh [66] retrieved the collisional narrowing and pressure-broadening parameters of the oxygen A-band for pressures close to 100 Torr. In this pressure regime, they fitted the diode-laser spectra with the soft collision (GP) model to take the collisional narrowing into account. They also observed that the high-pressure absorption lines have a non-VP shape with constant Doppler broadening values. Tran et al. [67] performed an analysis of the oxygen A-band with and without accounting for the line-mixing effects in order to calculate the collision-induced absorption coefficients for both pure O_2 and O_2 - N_2 broadened spectra. The line-mixing effect and collision-induced absorption were also studied by Vangvichith et al. [68] for room temperature O_2 - CO_2 spectra.

Fally et al. [69] reinvestigated pure oxygen A-band spectra recorded using a high-resolution FTS. A couple of years later in 2008, Predoi-Cross et al. [44, 70] tested a number of line-shape profiles to retrieve oxygen-line parameters. Pure and nitrogen mixed oxygen spectra were recorded using a high-resolution FTS instrument. The VP, SDV, GP, and SDR profiles were used to retrieve the line positions, intensities, broadening, shifts, and line-mixing coefficients.

A total of 32 oxygen A-band lines were measured by Robichaud et al. [71] using a Cavity Ring-Down Spectrometer (CRDS) system. The line intensities, the line-shape parameters as well as the self-broadening and air-broadening widths, pressure-induced shifts, and collisional narrowing coefficients were determined. They also reported the molecular constants for the lower b state of the oxygen molecule in another study [72].

Long et al. [47] reported P- and R-branch lines of the oxygen A-band measured using a frequency stabilized CRDS (FS-CRDS) system. They tested VP and GP profiles on their data set and found that the spectral features exhibit narrowing. This study was focused on proving the line list, where they compared the calculated line intensities with the measured FS-CRDS intensities, which are within 0.1 % on average. They concluded that line parameters of the A-band would be very useful for remote sensing applications to determine temperature and pressure profiles. Miller and Wunch [73] used a high-resolution solar-viewing FTS system to record oxygen A-band spectra. For the first time, a very weak electric quadrupole transition in the A-band was detected in the solar-viewing spectra.

In a recent study, Drouin et al. [74] used multiple spectrometer systems to improve spectroscopic measurements of oxygen A-band lines by reducing the systematic errors and accounting for different instrumentation. An FTS system for both lab-based and atmospheric observations and a CRDS system were employed to acquire the data. Both FTS and CRDS spectra were fitted using a modified multispectral fitting program in order to combine the collision-induced absorption with the line parameters including narrowing, line-mixing and speed-dependent effects during the fits. All the above-mentioned studies are devoted to obtain and improve the parameters of oxygen A-band transitions to support spectral measurements.

The study of the pure oxygen A-band in this thesis presents the line-shape parameters, namely the line positions, line intensities, self-broadening coefficients, self-narrowing coefficients, pressure induced self-shift coefficients, the line-mixing coefficients, and the SD parameter, from spectra recorded between 8.90 – 3011 Torr. Spectra were recorded using an FTS system and analyzed using the VP, RP, SDV, and SDR

profiles. This is the first study that reports the SD parameter of pure oxygen A-band transitions. It is presented in detail in Chapter 5.

1.4.3 Far-Infrared Assignment Study of Ammonia ($^{15}\text{NH}_3$)

Ammonia is a pyramidal molecule made of one nitrogen and three hydrogen atoms (NH_3). This molecule is an important constituent in the Earth's atmosphere. It is also found in the atmosphere of other planets, interstellar space [75], comets, cold stars, and exoplanets [76]. The $^{14}\text{NH}_3$ [77] and $^{15}\text{NH}_3$ [78] isotopologues are considered to be very sensitive probes of the proton-to-electron mass ratio [79]. The natural abundance of ^{15}N varies due to natural [80] or anthropogenic enhancements [81]. Determining the isotopic abundance of ^{15}N will allow the determination of the $^{14}\text{N}/^{15}\text{N}$ ratio of the universe [82, 83].

A number of observatory missions are dedicated to recording spectra of the infrared region. The Stratospheric Observatory for Infrared Astronomy (SOFIA) [84, 85] features a telescope mounted on an aircraft. The space mission Herschel also features a telescope, which was the largest infrared telescope. The Atacama Large Millimeter/submillimeter Array (ALMA) [86] is a ground-based observatory, and the James Webb Space Telescope [87, 88] is designed for stars and exoplanet observations. Having a complete database, such as HITRAN [51, 89] for ammonia and its isotopologues, the infrared region will allow the interpretation and support of these ground-based and space-based spectroscopic observations.

There are few spectroscopic studies of the $^{15}\text{NH}_3$ molecule. Such studies also had some limitations, namely spectra of short range (only up to 250 cm^{-1}) and low resolution were used. The present study focused on a wide spectral range ($60 - 453\text{ cm}^{-1}$) of $^{15}\text{NH}_3$

infrared spectra to extend the absorption line list of the ground state (GS) rotation-inversion transitions. Spectra used in this study were recorded with a high-resolution (0.00096 cm^{-1}) FTS setup. Having a complete database of ammonia and its isotopologues, such as HITRAN [51, 89] for the infrared region, will allow the interpretation and support of these ground-based and space-based spectroscopic observations.

1.4.3.1 Previous Studies

One of the earliest studies of $^{15}\text{NH}_3$ was performed by Carlotti et al. [90] in 1980 to assign absorption lines of the GS rotation-inversion spectrum for transitions up to the rotational quantum number $J = 13$ (around 250 cm^{-1}). Spectra were recorded at a resolution of 0.03 cm^{-1} using an FTS system. Helminger et al. [91] reported the measurement of the millimeter-wave spectra of $^{15}\text{NH}_3$. Later in 1994, a study by Urban et al. [75] presented Fourier transform spectra of $^{15}\text{NH}_3$ recorded with a better resolution (0.0017 cm^{-1}) than Carlotti et al. for the $19\text{-}120\text{ cm}^{-1}$ spectral range. They stated that they were able to obtain the accurate molecular constants for the ground state, which includes the rotational and the distortion constants.

Some other research studies were also dedicated to the pure inversion transitions of the ground state [92], ground state and $v_2 = 1$ state [93], $v_4 = 1$ state and $v_2 = 2$ [92] state spectra [92], which appeared in the MW and sub-millimeter wave regions. Sasada [92] used a high-resolution laser Stark spectroscopic method to measure and assign absorption lines for the rotational transition up to $J = 18$. Urban et al. [93] used a microwave and FTS to record pure inversion and inversion-rotational spectra of the ground state transitions. Later in 1982, Sasada et al. [94] observed the $v_2 = 2$ and $2v_2$ bands of $^{14}\text{NH}_3$ and $^{15}\text{NH}_3$ using the

Stark and FTS technique. All these studies on 14- and 15-ammonia are important in building up a rich and accurate database of line-list parameters.

The study of ammonia ($^{15}\text{NH}_3$) in this thesis reports the molecular constant of GS rotation-inversion transitions determined from 439 assigned lines in the $60 - 453\text{ cm}^{-1}$ range [79]. This study demonstrates a comparison between the assigned and the fitted (VP) positions for the lines in the $250\text{-}260\text{ cm}^{-1}$ range and reports their corresponding intensity. This study is presented in detail in Chapter 6.

1.5 Contribution to Other Studies and Publications

A list of publications that I have authored and co-authored is given in the following paragraphs.

(1) R. Hashemi, H. Rozario, C. Povey, and A. Predoi-Cross, Line-shape models testing on six acetylene transitions in the $\nu_1 + \nu_3$ band broadened by N_2 , *Journal of Quantitative Spectroscopy and Radiative Transfer* 140 58-66 (2014). [20]. Details of my contribution are given in Chapter 4.

(2) L. Fusina, G. Di Lonardo, E. Canè, A. Predoi-Cross, H. Rozario, and M. Herman, The High-resolution spectrum of $^{15}\text{NH}_3$ in the far-infrared: line positions of rotation-inversion transitions in the ground, $\nu_2 = 1, 2$ and $\nu_4 = 1$ states, *Journal of Quantitative Spectroscopy and Radiative Transfer*, 203 417-424 (2017) [79]. Details of my contribution are given in Chapter 6.

(3) A. Predoi-Cross, H. Rozario, K. Esteki, H. Naseri, S. Latif, H. Naseri, F. Thibault, V. Malathy Devi, M.A.H.Smith, and A.W. Mantz, Theoretical and revisited experimentally retrieved He-broadened line parameters of carbon monoxide in the fundamental band,

Journal of Quantitative Spectroscopy and Radiative Transfer, 184 322-340 (2016). My contribution included preparing the manuscript along with the co-authors.

(4) A. Predoi-Cross, H. Rozario, G. Di Lonardo, L. Fusina, and F. Tamassia, Far-Infrared Spectra and Spectroscopic Parameters of $^{15}\text{NH}_2\text{D}$ in the Ground State, J. Mol. Spectrosc., 301 13-14 (2014) [95]. In this study, my contributions included data recording and raw data processing.

(5) A.A. Mashwood, A. Predoi-Cross, V. Malathy Devi, H. Rozario, and B. Billingham, Measurement and computations of line-shape parameters for the $12201\leftarrow 03301$, $11101\leftarrow 10002$ and $12201\leftarrow 11102$ self-broadened CO_2 Q-branches, J. Mol. Spectrosc., 348 2-12 (2017) [96]. I helped preparing the manuscript along with the co-authors.

(6) A. Predoi-Cross, E. Johnson, D. Hemsing, H. Rozario, and G. Ch. Mellau, Climbing up the vibrational ladder of HC^{15}N : High-temperature near-infrared emission measurements, J. Mol. Spectrosc., 293–294 27-32 (2013) [97]. I contributed towards the preparation of the manuscript.

(7) R. Hashemi, H. Rozario, A. Ibrahim, and A. Predoi-Cross, Line-shape study of the carbon dioxide laser band I, Canadian Journal of Physics 91(11), 924-936 (2013) [98]. In this publication, I supported the preparation of the manuscript along with R. Hashemi and A. Predoi-Cross.

(8) H. Rozario, J. Garber, C. Povey, D. Hurtmans, J. Buldyreva, and A. Predoi-Cross, Experimental and theoretical study of N_2 -broadened acetylene line parameters in the $\nu_1+\nu_3$ band over a range of temperatures, Molecular Physics. 110 (2012) 2645-2663. [31]. This work was performed and published during my M.Sc. program. During this study, I recorded and processed raw data and analysed the P- and R-branch lines. Dr. Povey helped me setting up the experiment while recording data. As a summer student, J. Garber

participated in some part of the initial analysis of the R-brunch lines using the Wproffitt2.exe written by D. Hurtmans. After completing all the analysis, J. Buldyreva performed a theoretical study to calculate the line parameters.

There were two other projects, which are not published in the primary literature yet, that I have contributed to. They are:

(9) The Ro-Vibrational Emission Spectra of $D^{12}C^{14}N$:

This study was focused on examining low-pressure, high-temperature (1370 K) and high-resolution (0.005 cm^{-1}) emission spectra of the $D^{12}C^{14}N$ molecule. Spectra were recorded in the 450 – 850 wavenumber regions using an FTS system. DCN spectra were analyzed using the SyMath software to assign weak emission lines and obtain improved spectroscopic constants (band center, rotational constants, and distortion constant) for the vibrational levels up to $v = 5$ of $v_1 v_2 l v_3 \leftarrow 0 v_2 l 0$ transition type. The presence of DCN allowed to performing a self-calibration, which helped to achieve better results compared to a previous study [99].

This project was performed in collaboration with K. Esteki, A. Mashwood (two former M.Sc. student of our research group) and myself, during the four months of my Ph.D. internship in 2015 with Dr. Georg Mellau of the University of Giessen in Germany. During the internship, my contribution to the data analysis of $v_1 v_2 l v_3 \leftarrow 0 v_2 l 0$ transitions was the same as for the other two collaborators. The work was equally distributed for analysis, which includes the assignment of emission lines and fitting the spectra to determine the molecular band using the SyMath software. After returning from the internship, this work was completed by Koorosh Esteki and included in his thesis [100].

(10) Line-shape study of the $\nu_1+\nu_3$ band of C_2H_2 broadened by CO_2 :

In this study, the combination $\nu_1+\nu_3$ band of C_2H_2 broadened by CO_2 was recorded using the TDLS system situated at the University of Lethbridge to perform line-shape studies. Line position, intensity, broadening, shift and their temperature dependencies of acetylene broadened by carbon dioxide were retrieved and reported for the P-branch [7] and R-branch [100]. This study is included in the M.Sc. thesis of A. Mashwood and K. Esteki where A. Mashwood analysed the P-branch lines and K. Esteki analysed the R-branch lines. My contribution involved the support of the raw-data processing procedure, such as guiding the generation of the channel, background, and transmission spectra (described in Section 3.2.7) and providing knowledge on the line-fitting method using different line-shape profiles in Wproffit2.exe (Section 2.4).

1.6 Summary

The three studies of this thesis are discussed in detail in the next chapters. The main objective of the first and second one is finding the best fitting profiles based on the experimental (atmospheric pressure) conditions of acetylene and retrieving the new SD parameters of pure oxygen spectra using SDV and SDR profiles, respectively. The primary goal of the third study is focused on enriching the spectroscopic database by extending the assignment of $^{15}NH_3$ spectral lines.

Theoretical background of spectroscopic methods and different line-shape profiles are discussed in Chapter 2. Detailed descriptions of instrumentation used for data recording, as well as the data monitoring software, analysis software and related programs are presented in Chapter 3. Results and the analysis procedures of the acetylene ($C_2H_2-N_2$),

oxygen (O_2), and ammonia ($^{15}\text{NH}_3$) studies are discussed in Chapters 4, 5 and 6, respectively. Chapter 7 presents the conclusions.

Chapter 2 Theoretical background

This chapter is based on the books Molecular spectroscopy by Hollas [8], Spectra of Atoms and Molecules by Bernath [101], and Collisional Line Broadening and Shifting of Atmospheric Gases by Buldyreva, et al. [102].

2.1 Overview

This chapter presents a discussion of the fundamentals of absorption spectroscopy, a brief description of spectral line profiles and associated line parameters. Effects that affect the spectral feature of an absorption line due to the molecular speed will be discussed. Finally, this chapter presents a semi-empirical method called the Exponential Power Gap scaling law (EPG), which has been implemented to calculate the theoretical line-mixing parameter.

2.2 Introduction

Spectroscopic methods are widely applied in atmospheric chemistry and remote sensing applications. Absorption spectroscopy is frequently used to examine regions of the electromagnetic spectrum. It quantifies changes in the electromagnetic radiation (light) as it travels through a medium. The output intensity of the light becomes smaller than the incident intensity. The frequency-selective loss of light intensity creates absorption features. An absorption curve in a spectrum is referred to as a line.

2.2.1 Fundamentals of Spectroscopy

Electromagnetic radiation travels at the speed of light in a vacuum, and it is characterized by its wavelength with the unit meters, or in frequency with the unit Hertz or wavenumber (cm^{-1}). Electromagnetic radiation contains electric and magnetic fields. In Figure 2.1, \vec{E} and \vec{M} represent the strength of the electric and magnetic fields, respectively. In this figure, the electric component propagates along the $\bar{x}\bar{y}$ -plane, while the magnetic component propagates along the $\bar{z}\bar{x}$ -plane. The following expressions represent the electric and magnetic field components of the electromagnetic radiation:

$$E_y = E_0 \sin(2\pi\nu t - kx) \quad (2.1)$$

$$\text{and } M_z = M_0 \sin(2\pi\nu t - kx), \quad (2.2)$$

where, E_0 and M_0 are the maximum amplitude of the sinusoidal periodic function for electric and magnetic components, respectively, and the photoconductive k is the wave vector. The electric and magnetic field oscillates with $2\pi\nu$ frequency.

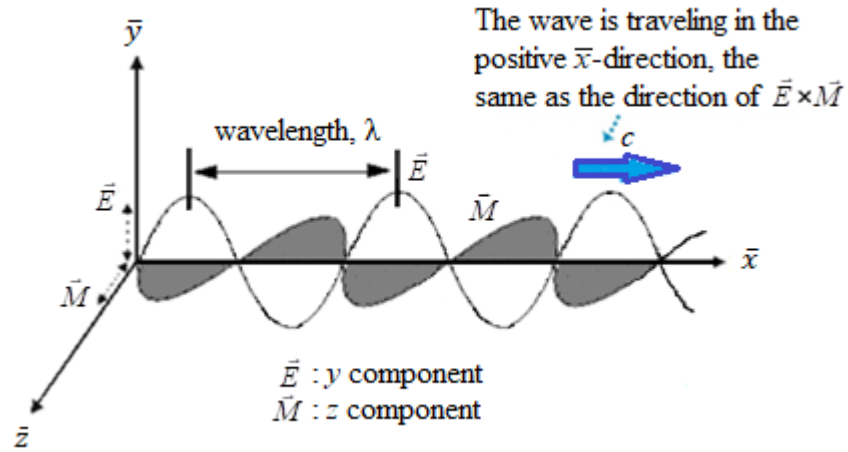


Figure 2.1: Propagation of electromagnetic radiation (ideas taken from Figure 2.1 in [8]). \vec{E} represents the strength of the electric field along the $\bar{x}\bar{y}$ -plane and \vec{M} is the strength of the magnetic field along the $\bar{z}\bar{x}$ -plane.

Absorption and emission of radiation: An example of a molecular system of two energy levels, where E_m represents the lower energy state and E_n the upper energy state is given in Figure 2.2 [101]. In order to induce a transition from one energy level to the other, the electromagnetic radiation and the two-level system must fulfill the following condition [8]:

$$\Delta E = E_n - E_m = h\nu_{nm} = hc\tilde{\nu}_{nm} = \frac{hc}{\lambda}, \quad (2.3)$$

where ΔE is the energy of a photon absorbed or emitted during the transition, c is the speed of light ($299792458 \text{ ms}^{-1}$), h is the Planck constant ($6.62607019 \times 10^{-34} \text{ Js}$), λ is the wavelength, ν_{nm} represents the radiation frequency in Hz, and $\tilde{\nu}_{nm}$ is the frequency in wavenumber which is inversely proportional to λ as $\tilde{\nu}_{nm} = \frac{1}{\lambda} (\text{cm}^{-1})$. Three possible types of transitions may occur when electromagnetic radiation interacts with matter: 1) induced absorption, 2) spontaneous emission, and 3) stimulated emission. An example of these absorption/emission transitions are shown in Figure 2.2.

- 1) **Induced absorption:** The molecular system of two energy levels induces an absorption transition from the lower energy state m to the upper energy state n when a photon of energy ΔE is absorbed.
- 2) **Spontaneous emission:** An emission occurs when the molecular system drops from the excited state E_n to the lower state E_m through the spontaneous emission of a photon of energy ΔE .
- 3) **Stimulated emission:** In this process, the interaction of a photon with an excited energy level stimulates an emission of another photon of the same energy. This

second photon is coherent to the first photon. The stimulated emission process contributes to the mechanism of the laser emission system.

In Figure 2.2, Ψ_m and Ψ_n are the wave functions corresponding to the lower, E_m , and upper, E_n , energy states. The energy values for the two energy levels involved in the transition can be obtained by solving the following time-independent Schrödinger equation, also called the wave equation as follows:

$$\hat{H}\Psi = E\Psi, \quad (2.4)$$

where \hat{H} is the Hamiltonian operator presenting the sum of kinetic and potential energies of the molecule. Solutions of this equation are a set of wave functions, $\{\Psi_i\}$, and associated eigenvalues (energy), $\{E_i\}$ [8].

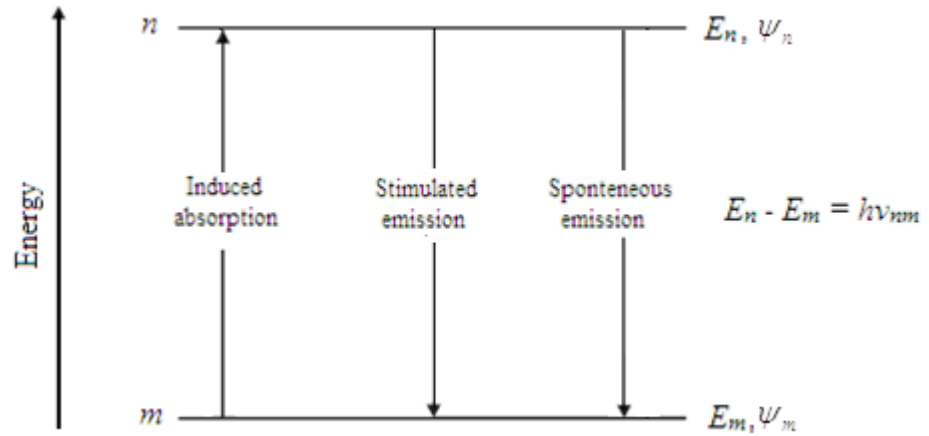


Figure 2.2: Absorption and emission processes in a two-level system when electromagnetic radiation interacts with matter. (1) induced absorption, (2) stimulated emission and (3) spontaneous emission (modification of Figure 2.2 in [8]).

The quantum mechanical theory of stationary nuclei and orbiting electron of molecules was given by Max Born and Robert Oppenheimer [8]. According to the Born-Oppenheimer approximation, the motion of nuclei and electrons in a molecular system can

be treated separately, as the electron moves very fast when orbiting around nearly stationary nuclei. Therefore, the wave function solution would have wavefunctions corresponding to each variable, which can be written as a product of the individual wave functions as follows:

$$\Psi = \Psi_e(q, Q)\Psi_n(Q) , \quad (2.5)$$

where Ψ_e is the function of electron coordinates q and nuclear coordinates Q . The wave function of nuclei Ψ_n can be factorized into

$$\Psi_n = \Psi_v \Psi_r , \quad (2.6)$$

where Ψ_v is the vibrational part and Ψ_r is the rotational part. Therefore, the total wave function can be factorized as

$$\Psi = \Psi_e \Psi_v \Psi_r \quad (2.7)$$

and the energy terms can be treated as follows:

$$E = E_e + E_v + E_r , \quad (2.8)$$

where E_e , E_v , and E_r represent the electronic, vibrational and rotational energy terms, respectively. Thus, the rotational, vibrational and electronic spectroscopy can be treated separately.

2.2.2 Normal Modes of Molecules

The number of rotational and vibrational degrees of freedom depends on the molecular structure, and the type of vibrational normal modes depends on the number of degrees of freedom. Molecules can be diatomic or polyatomic. Furthermore, they can be linear, non-linear, symmetric and asymmetric, and also stationary and moving. Gaseous

molecules can vibrate or rotate or both at a given temperature. Examples of vibrational motions are symmetric or asymmetric stretching and bending or rocking. These types of motions are categorized as normal modes of the molecules [8]. Linear molecules of N' atoms have $3N' - 5$ vibrational normal modes, while the non-linear molecules have $3N' - 6$ vibrational normal modes. The normal mode is also known as the fundamental mode of vibration. Normal modes are generally denoted by the Greek letter (ν_i), where the subscript i represents the numbering of the normal modes. For example, hydrogen cyanide (HCN) is a linear molecule of three atoms. Thus, it has $3 \times 3 - 5 = 4$ normal modes, where the H-C stretching mode, ν_1 , vibrates at the frequency of 3311 cm^{-1} , the $\text{C}\equiv\text{N}$ stretching mode, ν_3 , at 2097 cm^{-1} , and the doubly degenerate H-C \equiv N bending mode, ν_2 , vibrates at 713 cm^{-1} .

2.2.3 Rotational Spectroscopy

Molecular energy is a combination of four major components: rotational, vibrational, electronic, and translational energies. The first three lead to spectra in different regions of the electromagnetic spectrum through the absorption or emission processes as discussed in Section 2.2. Rotational spectra arise in the millimeter, microwave, and infrared regions, while the rotational-vibrational and electronic spectra are present in the infrared, visible, and the UV ranges.

A set of transitions that occur between energy levels, altogether can create a spectral band. Figure 2.3 shows an example of transitions between rotational energy levels, where J is the rotational quantum number ($J \geq 0$) associated with the rotational energy levels and B is the rotational constant of the molecule. The rotational constant determines the spacing between adjacent absorption lines of a spectral band. The value of the rotational constant

for a spectral band can be calculated from the physical property of the molecule using the following formula [8, 101]:

$$B = \frac{h}{8\pi^2 c I} \quad (\text{cm}^{-1}), \quad (2.9)$$

where I is the moment of inertia, which can be determined from the bond length, r , and the reduced mass of the molecule as shown in Equation 2.10. Here, the moment of inertia is the product of reduced mass and the squared value of the bond length between atom m_1 and m_2 as follows:

$$I = \frac{m_1 m_2}{m_1 + m_2} r^2. \quad (2.10)$$

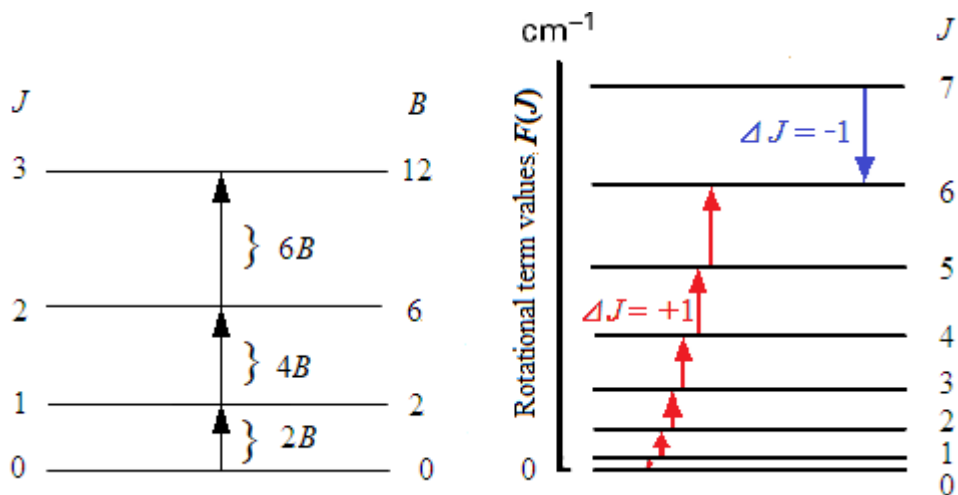


Figure 2.3: Examples of transitions between rotational energy levels of linear molecules. The allowed selection rule for rotational transitions is $\Delta J = \pm 1$ (modification of Figure in 6.13 [101] and idea taken from Figure 5.2 in [8]).

Rotational spectra are the result of transitions between two rotational energy levels within the same vibrational energy level. In order to induce a transition between a pair of quantized energy levels, the molecular system must obey the transition selection rules. To induce a pure rotational transition between two rotational energy states, a molecule must

have a permanent dipole ($\mu \neq 0$) and follow the transition selection rule $\Delta J = \pm 1$ [8] as shown in Figure 2.3.

Pure Rotation: Considering a rigid diatomic molecular system, the Schrödinger equation for a diatomic rigid rotor is given as follows [8, 101]:

$$\frac{\hat{J}^2 \Psi}{2I} = E\Psi, \quad (2.11)$$

where the total angular momentum \hat{J} is the sum of rotational, orbital, electronic and nuclear spins. The solutions of Equation 2.11 are wavefunctions, Ψ_i , and corresponding energy eigenvalues, E_i , associated with individual energy levels. The resulting eigenvalues are actually the energy term values of the energy levels. The energy term can then be expressed as follows [8, 101]:

$$E(J) = \frac{h^2}{8\pi^2 I} J(J+1). \quad (2.12)$$

In terms of wavenumber (cm^{-1}), the above expression can be given as follows [8, 101]:

$$E(J) = \frac{E(J)}{hc} = \frac{h}{8\pi^2 cI} J(J+1) = BJ(J+1). \quad (2.13)$$

To obey the $\Delta J = \pm 1$ selection rule, transitions must be of type $\Delta J = +1$ ($J' \leftarrow J''$) or $\Delta J = -1$ ($J'' \leftarrow J'$) as shown in Figure 2.3, where the rotational quantum number associated with the lower energy state is denoted by J'' and to the upper energy state by J' . Thus, an absorption line position (transition frequency) can be given in terms of wavenumber (cm^{-1}) as follows:

$$\begin{aligned} \tilde{\nu}_{J+1 \leftarrow J} &= E(J+1) - E(J) = E(J') - E(J'') = B(J+1)(J+2) - BJ(J+1) = \\ &2B(J+1). \end{aligned} \quad (2.14)$$

However, molecules are non-rigid, and their rotations are affected by the influence of an outward centrifugal type force. Due to this fact, molecules experience an increase in their rotational energy with increasing rotational speed. This phenomenon is known as the centrifugal distortion, which affects the spacing between absorption lines in a given spectral band. Therefore, the modified energy term obtained by taking the centrifugal distortion into account is given as follows:

$$E(J) = BJ(J + 1) - D[J(J + 1)]^2, \quad (2.15)$$

where D is the centrifugal distortion constant (cm^{-1}). The negative term in Equation 2.15 indicates that the spacing between lines in spectra decreases with increasing J number. The rotational transition wavenumbers (absorption line position) between two energy states can be given as follows:

$$\tilde{\nu}_{J+1 \leftarrow J} = 2B(J + 1) - 4D(J + 1)^3. \quad (2.16)$$

In a molecular energy level system, each vibrational state contains a set of rotational energy levels. B and D slightly vary for different vibrational states, which indicate that they are vibrationally dependent. Therefore, the expression of the energy term and the transition frequency can be modified as follows:

$$E_v(J) = B_v J(J + 1) - D_v [J(J + 1)]^2 \quad (2.17)$$

$$\text{and } \tilde{\nu} = 2B_v(J + 1) - 4D_v(J + 1)^3, \quad (2.18)$$

where B_v and D_v are the corrected form of B and D to specify vibrational dependence. B_v and D_v can be given as follows:

$$B_v = B_e - \alpha_e \left(v + \frac{1}{2}\right) + \gamma_e \left(v + \frac{1}{2}\right)^2 + \dots \quad (2.19)$$

$$\text{and } D_v = D_e - \beta_e \left(v + \frac{1}{2}\right) + \dots, \quad (2.20)$$

where α_e and β_e are constants, which have values much smaller than the rotational B_e and centrifugal distortion D_e constants, respectively.

Symmetric Top molecules: For symmetric top molecules, these expressions become more and more complicated. For symmetric rotors the term values are

$$E(J, K) = BJ(J + 1) + (A - B)K^2 \quad (2.21)$$

for prolate molecules and

$$E(J, K) = BJ(J + 1) + (C - B)K^2 \quad (2.22)$$

for oblate molecules.

In the aforementioned equations, A and C are the rotational constants, and K is a second quantum number [8] for the angular momentum (projection of angular momentum) along the symmetry axis, where $K = 0, 1, 2, \dots, J$ [8]. The allowed transition selection rules for symmetric top molecules are $\Delta J = \pm 1$ and $\Delta K = 0$. The rotational constants for the moment of inertia corresponding to their rotational axis can be given as follows:

$$A = \frac{h}{8\pi^2 c I_a} \text{ and } C = \frac{h}{8\pi^2 c I_c}, \quad (2.23)$$

where I_a and I_c are the moments of inertia associated with the rotational axis. The transition wavenumber for both prolate and oblate molecules is as follows:

$$\tilde{\nu} = E(J + 1, K) - E(J, K) = 2(B_v - D_{JK}K^2)(J + 1) - 4D_J(J + 1)^3, \quad (2.24)$$

where D_{JK} and D_J are the centrifugal distortion constants.

2.2.4 Vibrational Spectroscopy

For a diatomic simple harmonic oscillator that follows Hooke's law, the solution of the time-independent Schrödinger equation is given as follows [8, 101]:

$$E(v) = h\nu \left(v + \frac{1}{2} \right), \quad (2.25)$$

where $v (= 0, 1, 2, \dots)$ is the vibrational quantum number. Vibrational modes of molecules induce transitions in the infrared region due to changes in their dipole moments. For an anharmonic oscillator, the energy term values are determined from the solution of the Schrödinger equation. The energy term expression for vibrational energy levels can be written as follows [8, 101]:

$$E(v) = h\nu_e \left(v + \frac{1}{2} \right) - h\nu_e \chi_e \left(v + \frac{1}{2} \right)^2 + \dots, \quad (2.26)$$

where $\nu_e \chi_e$ represents the anharmonic constant where ν_e is the vibrational frequency and $\nu_e \gg \nu_e \chi_e$. The subscript e in both terms indicates that the molecular system is in an equilibrium state. The vibrational energy states in terms of wavenumber can be written as follows [8, 101]:

$$G(v) = \frac{E(v)}{hc} = \tilde{\nu}_e \left(v + \frac{1}{2} \right) - \tilde{\nu}_e \chi_e \left(v + \frac{1}{2} \right)^2 + \dots. \quad (2.27)$$

In the case of polyatomic harmonic linear molecules, the total wavefunction is a product of all the wavefunctions and can be written as follows:

$$\Psi = \Psi_1(Q_1)\Psi_2(Q_2) \dots \Psi_{3N-5}(Q_{3N-5}), \quad (2.28)$$

where the wavefunctions are associated with each normal vibrational mode (Q_N).

Therefore, the energy term value for a polyatomic harmonic linear oscillator is a summation and can be given as follows [8, 101]:

$$G(v_1, v_2, \dots, v_{3N-5}) = \tilde{\nu}_1 \left(v_1 + \frac{1}{2} \right) + \tilde{\nu}_2 \left(v_2 + \frac{1}{2} \right) + \dots \tilde{\nu}_{3N-5} \left(v_{3N-5} + \frac{1}{2} \right). \quad (2.29)$$

The energy term for a polyatomic anharmonic oscillator can then be expressed as follows:

$$\sum_i^{3N-5} G(v_i) = \sum_i^{3N-5} \tilde{\nu}_i \left(v_i + \frac{1}{2} \right) + \tilde{\nu}_i \sum_i \sum_{k \geq i} \chi_{ik} \left(v_i + \frac{1}{2} \right) \left(v_k + \frac{1}{2} \right) + \dots, \quad (2.30)$$

where the anharmonicity constant χ_{ik} in the above equation gives rise to combination bands, which are associated with i^{th} and k^{th} vibrational modes of the molecule.

2.2.4.1 Degeneracy and Vibrational Angular Momentum:

Each vibrational mode of molecules corresponds to a specific vibrating energy. Molecules that have two fundamental vibrational bending modes of identical frequency, but in two perpendicular planes, can show degeneracy of energy levels. Polyatomic molecules can bend in both sides of a plane. In Figure 2.4, the red and blue show two possible planes $\bar{x}\bar{y}$ and $\bar{z}\bar{x}$ that a molecule can bend in. Thus, the molecule in Figure 2.4 can bend along the $\bar{x}\bar{y}$ and the $\bar{z}\bar{x}$ plane. This four-directional type of bending makes the nuclei of the molecules (whose structure allows it) to rotate about the molecular axis. This type of motions gives rise to the angular momentum.

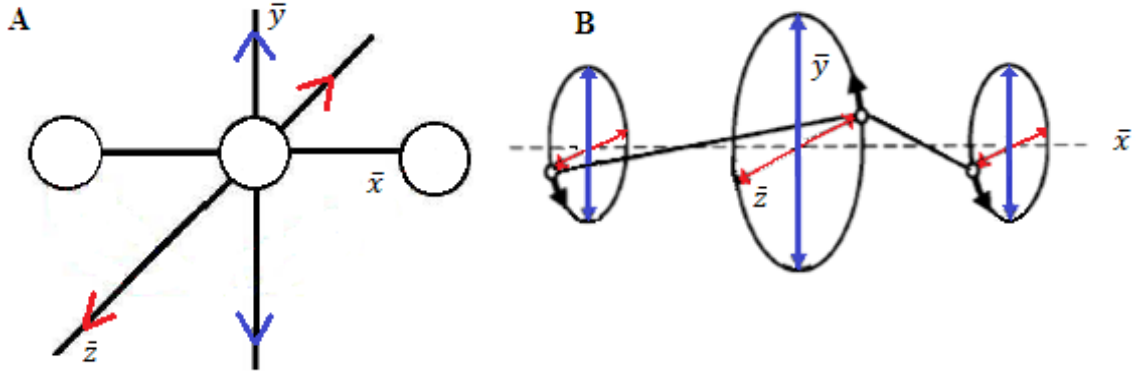


Figure 2.4: Bending modes of vibrating molecule (A) and the circular path of the nuclei (B) (modification of Figure in 6.22 [101]).

The angular momentum is quantized as $\pm |l|\hbar$. The possible values of the angular quantum number $|l|$ can be expressed in terms of the vibrational quantum numbers v_i as follows [101]:

$$|l| = v_i, v_i - 2, v_i - 4 \dots 0 \text{ or } 1. \quad (2.31)$$

Generally, the total angular momentum is known to be the sum of four angular momenta: rotational, electron, nuclear spin, and vibrational. But for most molecules, only the rotational and vibrational angular momenta are present; thus, $\hat{J} = \hat{R} + \hat{l}$. The coupling of \hat{R} (rotational angular momentum) and \hat{l} (vibrational angular momentum) contribute to a splitting of rotational energy levels. This phenomenon is known as the l -type doubling effect, which leads to a splitting of the energy levels of term values as follows:

$$\Delta E(J) = q'J(J + 1), \quad (2.32)$$

where $J = |l|, |l|+1, |l|+2 \dots$ is the rotational quantum number and q' is the l -type doubling constant. The split energy levels cause doublets in the spectrum with nearly identical line parameters. For a linear molecule, the double degeneracy for each l is associated with the

clockwise and the counter-clockwise motion of the nuclei. To account for the l -doubling, the rotational energy term given in Equation 2.17 can be modified as follows:

$$E(J, l) = B_v[J(J + 1) - l^2] - D_v[J(J + 1) - l^2]^2. \quad (2.33)$$

Similarly, the modified vibrational energy term in Equation 2.29 when including the degeneracy (for the case of harmonic oscillator) can be written as follows:

$$G(v_1, v_2, \dots, v_{3N-5}) = \sum_i^{3N-5} \tilde{v}_i \left(v_i + \frac{d_i}{2} \right), \quad (2.34)$$

where d_i is the degeneracy factor of the i^{th} vibration. For a polyatomic anharmonic oscillator, the energy term can be expressed as follows:

$$\sum_i^{3N-5} G(v_i) = \sum_i^{3N-5} \tilde{v}_i \left(v_i + \frac{d_i}{2} \right) + \tilde{v}_i \sum_i \sum_{k \geq i} \chi_{ik} \left(v_i + \frac{d_i}{2} \right) \left(v_k + \frac{d_k}{2} \right) + \dots \quad (2.35).$$

Including the l -type doubling, the transition energy term for the anharmonic oscillator can be written as follows:

$$\begin{aligned} \sum_i^{3N-5} G(v_i) = & \sum_i^{3N-5} \tilde{v}_i \left(v_i + \frac{d_i}{2} \right) + \tilde{v}_i \sum_i \sum_{k \geq i} \chi_{ik} \left(v_i + \frac{d_i}{2} \right) \left(v_k + \frac{d_k}{2} \right) + \dots + \\ & \sum_u g_{uu} l_u^2, \end{aligned} \quad (2.36)$$

where $g_{uu} l_u^2$ is an additional anharmonic l -doubling term where u represents the degeneracy mode with l (angular momentum).

2.2.5 Rotational-vibrational Spectra and Band Structure

Rotational-vibrational spectra are the results of simultaneous rotation and vibration of molecules. The formula for the total energy term of a rotational-vibrational transition T' is obtained by combining Equations 2.27 and 2.17 as follows:

$$T' = G(v) + E_v(J) = \tilde{\nu}_e \left(v + \frac{1}{2} \right) - \tilde{\nu}_e \chi_e \left(v + \frac{1}{2} \right)^2 + B_v J(J+1) - [J(J+1)]^2. \quad (2.37)$$

Including the anharmonicity and degeneracy, the total energy term of the rotational-vibrational system (in wavenumber) is given as follows:

$$T = G(v_1, v_2, \dots, v_{3N-5}) + E_v(J, l) = \sum_1^{3N-5} \tilde{\nu}_i \left(v_i + \frac{d_i}{2} \right) + \tilde{\nu}_i \sum_i \sum_{k \geq i} \chi_{ik} \left(v_i + \frac{d_i}{2} \right) \left(v_k + \frac{d_k}{2} \right) + \sum_u g_{uu} l_u^2 + B_v J(J+1) - D_v [J(J+1)]^2. \quad (2.38)$$

The angular momentum l_u and the constant g_{uu} is zero for non-degenerate levels. If $d_i = 0$ or 2 , Equation 2.38 corresponds to non-degeneracy or double degeneracy, respectively. As mentioned before, rotational-vibrational spectra appear mainly in the infrared region of the electromagnetic spectrum. To induce a transition between two vibrational energy levels of a molecular system, the molecule needs to have a change in its dipole moment. The selection rules that the rotational-vibrational spectra follow are $\Delta J = 0, \pm 1$ and $\Delta v = \pm 1$. Additionally, the selection rules $\Delta K = 0$ and ± 1 is required for symmetric rotors (oblate and prolate) [8].

Based on the direction of the change in the transition dipole moment, the rotational-vibrational (ro-vibrational) spectra of polyatomic molecules can be grouped in two main types of band structure: (1) parallel and (2) perpendicular bands. Figure 2.5 (a) shows a parallel band. The red curves are the absorption lines that occur due to transitions between

two energy levels as shown on the left of Figure 2.5. A set of ro-vibrational transitions between stacks of energy levels (as shown in Figure 2.5) gives a parallel band if the direction of the dipole moment change is parallel to the molecular axis. There is no change in the angular momentum during transitions. Accordingly, $\Delta l = 0$ and it follows the $\Delta J = \pm 1$ selection rule. This type of transitions give rise to two branches, namely *P* and *R*. The *P*-branch allows $\Delta J = -1$ type transitions and the *R*-branch allows $\Delta J = +1$ type transitions from the lower stack to the upper stack of energy levels as shown in Figure 2.5.

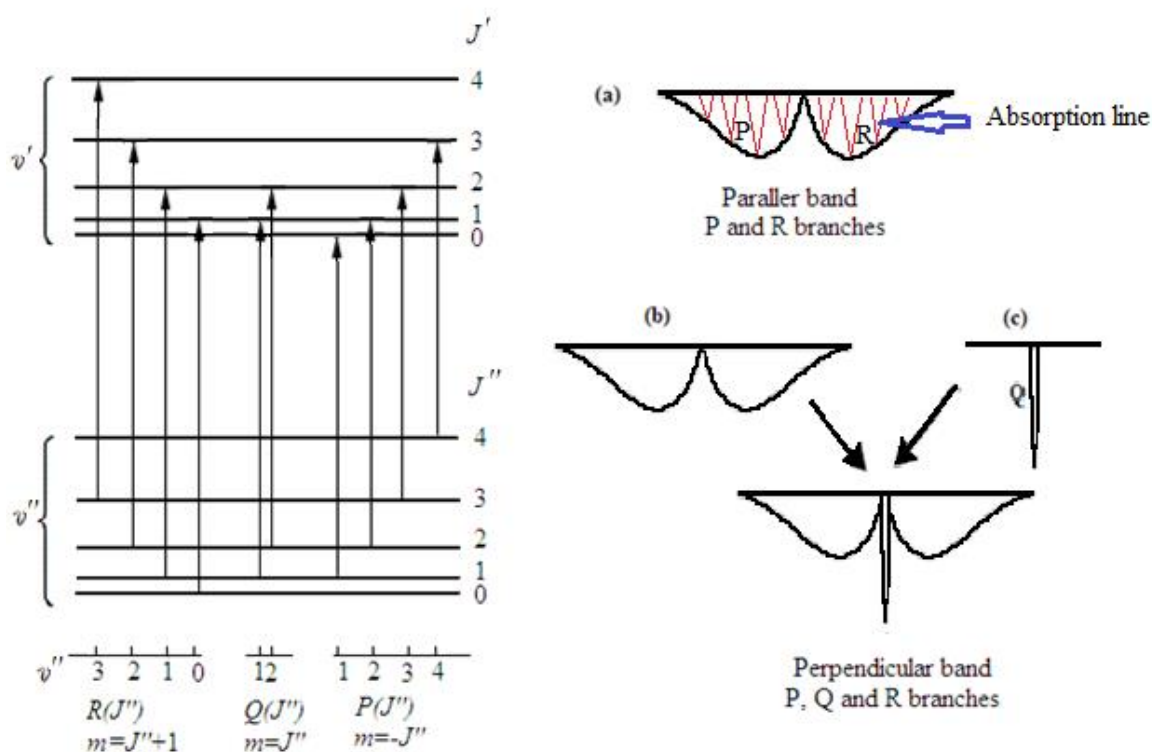


Figure 2.5: *P*-, *Q*- and *R*-type transitions between two vibrational states are shown on the left of the Figure. The structure of the parallel band is shown in (a). Red curves are the absorption lines. The perpendicular band is a combination of (b) and (c) (modification of Figure 6.7 in [8]).

A set of ro-vibrational transitions give a perpendicular band if the direction of the dipole moment change is perpendicular to the molecular axis. The vibrational angular

moment changes with the dipole moment change; thus, $\Delta l = \pm 1$ and $\Delta J = 0, \pm 1$. These types of transitions give rise to P -, Q - and R -branches, where $\Delta J = -1$ for the P -branch, $\Delta J = 0$ for the Q -branch, and $\Delta J = +1$ for the R -branch type transitions from the lower stack to the upper stack of energy levels. Figures 2.5 (b) and (c) show the P , Q , and R branches in a perpendicular band [103].

The parallel and the perpendicular bands are categorized based on the transition selection rules and are denoted using Greek capital letters. In the following are some examples of P , Q , and R branching structures [8, 101].

1. For $\Delta l = 0$ with $l = 0$ and $\Delta J = \pm 1$, the parallel bands are $\Sigma \leftarrow \Sigma$ type.
2. For $\Delta l = \pm 1$ and $\Delta J = 0, \pm 1$, the perpendicular bands are $\Pi \leftarrow \Sigma$ and $\Delta \leftarrow \Pi$ types with a strong Q - branch.
3. For $\Delta l = 0$ with $l \neq 0$ and $\Delta J = \pm 1$, the parallel bands are $\Pi \leftarrow \Pi$ and $\Delta \leftarrow \Delta$ types with a weak Q - branch ($\Delta J = 0$).

For parallel bands, the band is centered approximately at where the P - and R -branches join up, while the center of perpendicular bands is located inside the Q -branch as shown in Figure 2.5 [8, 101]. The notation of the P - and R - branch lines of the parallel and perpendicular bands can be represented using the m index as follows [8]:

$$m = (J' - J'') \frac{(J' + J'' + 1)}{2}, \quad (2.39)$$

which is a function of the rotational quantum numbers, upper (J') and lower (J''). Replacing $J' = J'' - 1$ for the P -branch transition gives an m index of $m = -J''$ (i.e., $m < 0$). For the R -branch transitions, replacing $J' = J'' + 1$ gives $m = J'' + 1$ (i.e., $m > 0$). The general

expression of the *P*- and *R*-branch transitions between lower v'' and upper v' vibrational state in terms of frequency (wavenumber) can be given as follows:

$$\tilde{\nu}_P(v', J - 1 \leftarrow v'', J) = \tilde{\nu}_0 - (B'_v + B''_v)J + (B'_v - B''_v)J^2 \quad (2.40)$$

$$\text{and } \tilde{\nu}_R(v', J + 1 \leftarrow v'', J) = \tilde{\nu}_0 + 2B'_v + (3B'_v - B''_v)J + (B'_v - B''_v)J^2 \quad (2.41).$$

Introducing the m index in the above two equations for the *P*- and *R*- branches in order to unify them into one equation as follows:

$$\tilde{\nu} = \tilde{\nu}_0 - (B'_v + B''_v)m + (B'_v - B''_v)m^2. \quad (2.42)$$

These equations can help to determine the transition frequency of absorption lines, if the rotational and distortion constants of a band are known.

2.2.6 Types of Molecular Bands

Four types of bands typically arise due to rotational and ro-vibrational transitions: fundamental, overtone, combination, and hot bands [8, 101]. Among them, the fundamental and overtone bands include transitions starting from the ground vibrational states. Fundamental bands are the result of transitions between the ground and the first vibrational energy states, i.e., $v = 0$ and $v = 1$, whereas the overtones consist of transitions between ground vibrational $v = 0$ state and $v = 2, 3, 4 \dots$ states. The notation for a band transition can be given as $1\nu_1-2\nu_1$, where 1 and 2 represent the vibrational quantum number and ν_1 represents the vibrational mode for a given molecule. For example, $0-1\nu_1$, $0-1\nu_2$ and $0-1\nu_3$ are the fundamental bands and $0-2\nu_1$, $0-3\nu_1$, $0-3\nu_2$, $0-3\nu_3$ are the overtone bands of molecules. On the other hand, the hot band transitions never contain the ground states, i.e., the hot bands are the result of transitions between $v = 1, 2, 3, \dots$ and $v = 2, 3, 4, \dots$ states

(i.e., $1\nu_1-2\nu_1, 2\nu_2-3\nu_2, \dots$ type of bands). The last type is called the combination bands. They are the combination of the fundamental and the overtone types of transitions; for example, $\nu_1+\nu_3, 2\nu_2+3\nu_3, 4\nu_1+5\nu_3\dots$ etc. type.

2.3 Line-shape Theory

Spectroscopic studies that are focused on the retrieval of molecular line parameters and on testing the line-shape profiles of absorption spectra are referred to as line-shape studies. The line-shape function plays a very important role in examining the absorption/emission features in spectra. Absorption lines are modeled using line-shape functions, also called line-shape profiles. One must select the appropriate line-shape function to analyze fine and detailed spectral features of these spectra and then retrieve the line parameters with sufficient accuracy. Different line-shape functions are tested and described in the literature [104, 105]. A brief discussion of some of the line profiles including their line-shape functions is provided in Section 2.4.

2.3.1 Beer-Lambert Law

According to the Beer-Lambert law [106-108], the intensity of incident light changes after traveling through an absorption medium as shown in Figure 2.6. Absorption lines in a spectrum are the result of the intensity loss of the incident light [6]. For a homogeneous medium this can be quantified using the Beer-Lambert law as follow:

$$U(\tilde{\nu}) = U_0(\tilde{\nu})e^{-\alpha c' L}, \quad (2.43)$$

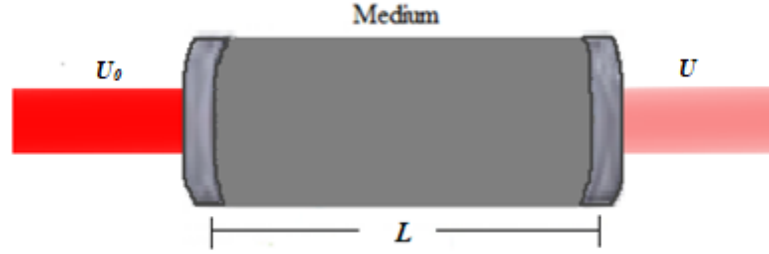


Figure 2.6: U_0 and U are the light intensity before and after passing through the sample (medium). L is the pathlength of the absorption medium.

where $\tilde{\nu}$ is the frequency of incident radiation (light), $U_0(\tilde{\nu})$ and $U(\tilde{\nu})$ are the intensity of monochromatic radiation before and after passing through the medium (sample molecules), respectively, L is the pathlength of the absorption medium, C' is the concentration and α is the absorption coefficient (in $1/(\text{molecule} \cdot \text{cm}^{-2})$) of the sample. This expression can also be written in terms of spectral absorbance $O(\tilde{\nu})L$ as follows [102]:

$$U(\tilde{\nu}) = U_0(\tilde{\nu})e^{-O(\tilde{\nu})L}. \quad (2.44)$$

The amount of light transmitted through the gas sample can be determined by the following expression:

$$\frac{U(\tilde{\nu})}{U_0(\tilde{\nu})} = e^{-O(\tilde{\nu})L}. \quad (2.45)$$

Therefore, the spectral absorption coefficient is as follows:

$$O(\tilde{\nu}) = \frac{1}{L} \ln \left[\frac{U_0(\tilde{\nu})}{U(\tilde{\nu})} \right]. \quad (2.46)$$

2.3.2 Line-shape Function

Line-shape functions account for several effects that appear in the absorption lines, which occur at the microscopic level. Defining $\tilde{\nu}_0$ is the frequency of absorption transition

(transition frequency between two energy levels) also called the line position. If $\tilde{\nu} \approx \tilde{\nu}_0$, ($\tilde{\nu}$ is the frequency of incident radiation) then the light is strongly absorbed when it is passed through the gas medium. At this frequency, the photon energy is absorbed to excite molecules from a lower energy state to a higher one. Due to this transition, a spectrum displays an absorption line. By varying the frequency of the incident light, one can observe all possible transitions that occur at a given temperature and gas pressure of a molecule and can create spectra of that frequency range. In a simplistic way, one can think of a spectrum as the fingerprint of a molecule, which provides information about its physical state. Spectral lines are defined by their inherent line parameters. Some line parameters are model specific, and others (line positions, intensities, and widths) are present in all line-shape models as discussed in section 2.4 and shown in Figure 2.7.

Based on the physical conditions of the spectra (for example, gas temperature, gas pressure, etc.), several line-shape functions can be considered to analyze the absorption lines and to retrieve accurate line-shape parameters. The expression that relates the line-shape function, $F(\tilde{\nu})$ centered at $\tilde{\nu}_0$ and the absorption coefficient, $O(\tilde{\nu})$ is given by Buldyreva et al. as follows [102]:

$$O(\tilde{\nu}) = AF(\tilde{\nu} - \tilde{\nu}_0), \quad (2.47)$$

where $F(\tilde{\nu} - \tilde{\nu}_0)$ represents a normalized line-shape function. Thus,

$$\int_{-\infty}^{+\infty} F(\tilde{\nu} - \tilde{\nu}_0) d\tilde{\nu} = 1. \quad (2.48)$$

Therefore,

$$A = \int_{-\infty}^{+\infty} O(\tilde{\nu}) d\tilde{\nu}, \quad (2.49)$$

where A is the normalized factor representing the integral of an absorption line (the number of molecules per unit pressure or volume).

2.4 Different Types of Line-shape Models/Profiles and Parameters

By fitting an absorption line using different line-shape profiles, it is possible to retrieve parameters. The position and the intensity are the most common parameters used in identifying an absorption line from an absorption spectrum. The line broadening effect is one of the line parameters, which appears even in the spectra of a stationary molecule. It determines the width of a given spectral line measured at half-maximum. Different types of broadening mechanisms that contribute to the width of an absorption line may include natural broadening, Doppler broadening, and pressure broadening (collisional broadening) [8, 101]. Other effects that occur at pressures above zero Torr are the pressure-induced line shifting (shifting in the peak position of a line), Dicke narrowing, the speed-dependent effect, and the line-mixing effect.

2.4.1 Line Position, Shift, and Intensity

The energy difference between two energy levels matches the energy of the photon that is absorbed or emitted to induce absorption transition between two energy levels. This amount of energy can be expressed in terms of frequency in Hz or in wavenumbers (cm^{-1}). This frequency corresponds to the position of the absorption line at its peak, as shown in Figure 2.7. Due to the motion and collision of the molecules, the line position is affected and gets shifted. Line positions in the low-pressure spectra are less shifted than in high-pressure spectra. The line position shifts more as the pressure increases. The figure shows

that the line position is shifted, which is called the pressure-induced shift and is denoted by the symbol δ .

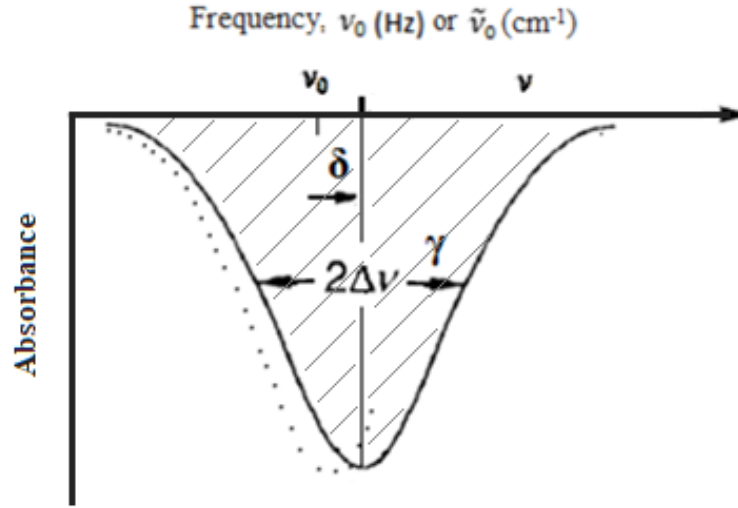


Figure 2.7: Example of an absorption line presenting the line parameter (idea taken from Figure 1.1 in [102]). Symbol ν is the frequency of incident radiation, ν_0 is the transition frequency between two energy levels, γ is the half-width at half-maximum or HWHM of $2\Delta\nu$, and δ is the pressure induced line shift of the absorption line shown in dots.

For all spectral lines, intensities are the rate of absorbed or emitted energy expressed in $\text{cm}^{-1}/(\text{molecule} \cdot \text{cm}^{-2})$. The intensity of an absorption line is the area under the curve (the shaded area shown in Figure 2.7). The probability of absorption or emission transitions depends on the population of the initial energy states. In addition, the population of the higher excited states depends on the temperature of the sample (population increases with increasing temperature). The transition probability and the intensity of a line are related to each other (shown through Equations 2.50 - 2.53). The transition probability is the square of the magnitude of the transition moment. The transition moment for absorption spectroscopy is also known as the transition dipole moment and is denoted by R_{nm} . It can be expressed in terms of the electric dipole moment for the transition (as it is related to the electric dipole selection rules) and the wavefunctions as follows [8, 101]:

$$R_{nm} = \int \Psi_n^* \mu \Psi_m d\tau, \quad (2.50)$$

where Ψ_m and Ψ_n^* are the wavefunctions corresponding to the lower and upper energy states, respectively. The electric dipole moment operator, $\vec{\mu}$, is given as follows:

$$\vec{\mu} = \sum_i q_i r_i, \quad (2.51)$$

where q_i is the charge and r_i is the position vector of the i^{th} particle. The square of magnitude R_{nm} is the transition probability for the initial m and the final n energy levels and is denoted as $|R_{nm}|^2$. The transition dipole moment is also a vector quantity, which often appears incorporated in the Einstein-A coefficient, in the expressions of line intensity. The intensity, S_{mn} , of the transition between these two energy levels is given as follows:

$$S_{mn} = I_a \frac{A_{mn}}{8\pi c \tilde{\nu}_0^2} \frac{g' e^{\frac{-c_2 E''}{T}} \left(1 - e^{\frac{-c_2 \tilde{\nu}_0}{T}} \right)}{Q(T)} \text{ (cm}^{-1}\text{/(molecule.cm}^{-2}\text{))}, \quad (2.52)$$

where A_{mn} is the Einstein-A coefficient (unit is s^{-1}), I_a represents the natural isotopologue abundance for the molecule, g' is the statistical weight of the upper level n , E'' is the energy of the lower level m (cm^{-1}), $\tilde{\nu}_0$ represents the line position (cm^{-1}) at the given pressure of the gas, c_2 is the second radiation constant ($c_2 = 1.4387770 \text{ cm.K}$), T is the temperature in Kelvin, and $Q(T)$ is the total internal partition function. An elaborated expression of the intensity equation is given in the literature [2, 109].

The Einstein coefficient, A_{mn} , stores the information of spontaneous transition probability between the initial energy level m (excited state) and the final energy level n , which can be expressed as follows:

$$A_{mn} = \frac{64\pi^4}{3h} \tilde{\nu}_0^3 \frac{g''}{g'} R_{mn} \times 10^{-36} \text{ (s}^{-1}\text{)}, \quad (2.53)$$

where R_{mn} can be calculated using the Equation 2.50. The partition function $Q(T)$ can be expressed in terms of the statistical weight g_k and total energy E_k that includes the rotational and vibrational energy as follows:

$$Q(T) = \sum_k g_k \exp\left(-\frac{c_2 E_k}{T}\right). \quad (2.54)$$

2.4.2 Natural Line Width (Natural Broadening)

Along with the line position (transition frequency), intensity, and shift, a typical absorption line is known also by its broadening parameter. Broadening is related to the line width of an absorption line. The symbol γ represents the half-width at half-maximum or HWHM of the value $\Delta\nu$ [8, 102, 110, 111].

Natural broadening is homogeneous in nature and is present in an absorption line, even in the spectrum produced from isolated stationary molecules. The reasons why an absorption line has a finite width can be explained using the Heisenberg uncertainty principle as follows [8]:

$$\Delta t \Delta E \geq \hbar, \quad (2.55).$$

where $\Delta t = \tau$ is the lifetime of an excited energy state (level), ΔE is the energy difference between the lower and higher states, and \hbar is related to the Plank's constant ($\hbar = h/2\pi$). According to Equation 2.55, the excited state will have the exact energy value only if the lifetime is infinite. But in reality, the excited energy states have a finite lifetime. This causes an energy spread of the excited states, resulting in a frequency distribution of the absorption line. This frequency distribution contributes to a very small line width ($\Delta\tilde{\nu}$). Subsequently, the absorption line experiences broadening due to the frequency distribution at which the

absorption occurs. This phenomenon is called natural line broadening. The Gaussian line-shape function is normally used for modeling the natural line broadening. The following equation

$$\Delta\tilde{\nu} \geq \frac{32\pi^3\tilde{\nu}^3}{(4\pi\epsilon_0)3h} |R^{nm}|^2 \quad (2.56)$$

illustrates the frequency spread that causes the natural line broadening for a transition between energy states m and n . In Equation 2.56, ϵ_0 represents the vacuum permittivity. The natural broadening is very small compared to other broadening mechanisms. The natural line width values are typically about 10^{-8} cm^{-1} .

2.4.3 Doppler Width (Doppler Broadening), Gaussian Profile

At low pressure (below 1 Torr), thermal and kinetic motions that affect the molecular speeds are not strongly affected by their collisions. Due to the kinetic motion, molecules move in all directions (towards, away, left, right, up, down, and in different angles) from the light source. This motion changes the position of molecules with time and modifies the frequency that is absorbed by these moving molecules (absorbing photon). That means, depending on the direction in which a molecule is moving in relation to the radiation beam, can change the frequency of the radiation observed by the molecule. This effect is called the Doppler effect and the frequency shift is called the Doppler shift (often used in astrophysics). The magnitude of the Doppler shift is defined by

$$\Delta\tilde{\nu} = \left(\frac{\tilde{\nu}\vec{v}_a}{c} \right), \quad (2.57)$$

where $\tilde{\nu}$ represents the transition frequency and \vec{v}_a is the molecular velocity. The velocity distribution of molecules depends on temperature and can be quantified by the Maxwell-

Boltzmann statistics; accordingly, the Maxwell-Boltzmann velocity distribution is defined as follows:

$$f(\vec{v}_a)d\vec{v}_a = \left(\frac{m_a}{2\pi K_B T}\right)^{\frac{3}{2}} \exp\left(-\frac{m_a v^2}{2K_B T}\right) d\vec{v}_a, \quad (2.58)$$

where $\left(\frac{2K_B T}{m_a}\right)^{\frac{1}{2}} = v$ is the most probable speed of the molecule, m_a is the mass of the moving molecule, and K_B is the Boltzmann constant. The line-shape function corresponding to the Doppler profile is given as follows [102]:

$$F_D(\tilde{\nu}) = \sqrt{\frac{\ln 2}{\pi}} \frac{1}{\gamma_D} \exp\left[-\ln 2 \left(\frac{\tilde{\nu}-\tilde{\nu}_0}{\gamma_D}\right)^2\right] (\text{cm}^{-1}), \quad (2.59)$$

where γ_D is the Doppler HWHM. In the thermal equilibrium, it is expressed by the following expression [102]:

$$\gamma_D = \sqrt{\frac{2\ln 2 K_B T}{m_a c^2}} \tilde{\nu}_0. \quad (2.60)$$

This profile is suitable at pressures below 1 Torr, and typically, the Doppler HWHM has a size of 10^{-3} cm^{-1} . The broadening coefficient is measured in $\text{cm}^{-1}\text{atm}^{-1}$.

2.4.4 Pressure-Induced Collisional Broadening

High-pressure lines cannot be accurately fitted with the Doppler or Gaussian profiles. At elevated pressures (>100 Torr for infrared), the effects of the thermal motion of molecules are small compared to the effects caused by the collisions between molecules. Collisional broadening is linearly proportional to the pressure of the sample in the high-pressure regime.

Molecular collisions are assumed to be elastic. According to the ‘impact approximation’ theory of collision, the time duration of each collision is much shorter than the time between consecutive collisions. During these collisions, the dipole moment of the vibrating and rotating absorbers undergoes a phase shift, which has a real part and an imaginary part. The real part represents the decay rate of the dipole moment, and the imaginary part represents the frequency shift. At high pressure, when a large volume of molecules experiences a phase shift, then the excited energy levels get perturbed and results in the frequency distribution that corresponds to the center of a spectral line. Therefore, the absorption lines become broadened. The corresponding line-shape function that considers the contribution of molecular collision in terms of a Poisson Distribution is given in the form of the Lorentzian profile as follows [102]:

$$F_c(\tilde{\nu}) = \frac{1}{\pi} \frac{\gamma_c}{(\tilde{\nu} - \tilde{\nu}_0 - \delta_c)^2 + \gamma_c^2} (1/\text{cm}^{-1}), \quad (2.61)$$

where γ_c represents the collisional half-width, which is linearly proportional to the decay rate of the dipole moment, and δ_c represents the collisional shift of a spectral line. The Lorentz profile takes the decreasing intensity along the wings of the absorption line into account while fitting spectra.

2.4.5 The Voigt Profile

The Voigt profile is the most commonly used line-shape function to model spectral lines [102]. It has been determined experimentally that spectra recorded at intermediate pressure regimes are better fitted with the Voigt profile than with the Doppler or Lorentz profiles [102]. The Voigt profile is a mathematical convolution of the Doppler and the Lorentz line-shape models. It takes both the thermal motion and the collisional effects into

account as an autocorrelation function. The mathematical expression of the Voigt function is as follows:

$$F_V(\tilde{\nu}) = \sqrt{\frac{\ln 2}{\pi}} \frac{1}{\gamma_D} \frac{y}{\pi} \int_{-\infty}^{\infty} \frac{\exp(-t^2)}{y^2 + (x-t)^2} dt, \quad (2.62)$$

where x and y are the dimensionless variables defined in terms of the Doppler and the Lorentz half-width as $x = \sqrt{\ln 2} \frac{\nu - \nu_0}{\gamma_D}$ and $y = \sqrt{\ln 2} \frac{\gamma_C}{\gamma_D}$. The integral part of the above equation is associated with a complex probability function, $W(x, y)$ [102]. A special numerical algorithm given by Humlicek and Kuntz can compute this probability function [102, 112, 113]. In Equation 2.62, the complex probability function is as follows:

$$W(x, y) = \frac{i}{\pi} \int_{-\infty}^{\infty} \frac{\exp(-t^2)}{x + iy - t} dt. \quad (2.63)$$

Taking the shift of the spectral line into account in the Voigt profile by changing the dimensionless variable x to x' , and normalizing it with the dx' element in the real (Re) part will give the Voigt profile in the following form:

$$F_V(x', y) = \frac{y}{\pi} \int_{-\infty}^{\infty} \frac{\exp(-t^2)}{y^2 + (x' - t)^2} dt = ReW(x', y), \quad (2.64)$$

where $x' \equiv x - s$ and $s = \sqrt{\ln 2} \frac{\delta_C}{\gamma_D}$. For spectroscopic studies like this one, the imaginary part is not accounted for, because it represents a dispersion term. Figure 2.8 shows the differences in the three different profiles: Doppler, Voigt, and Lorentz. It is clear from the line-shapes that the Lorentz shape is broader than the other two as it takes high-pressure collisional features into account, while the Doppler is narrower than the other two. The Voigt profile used for modeling the low-pressure spectra (where $\gamma_D \gg \gamma_C$) is dominated by

the Doppler shape, and for high-pressure spectra (where $\gamma_C \gg \gamma_D$), it is dominated by the Lorentz shape.

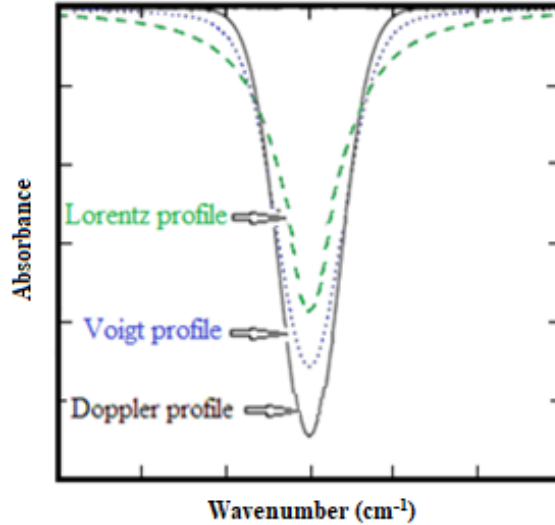


Figure 2.8: Differences between the following three line-shape profiles: Lorentz (dashes), Voigt (dots), and Doppler (solid line) (ideas taken from Ref. [114]).

The Voigt profile has been used for decades by the atmospheric physics and chemistry community to analyze laboratory and satellite spectral data. Despite the popularity, this model is no longer appropriate in some analyses due to its limitations, namely the lack of accounting for some of the important effects in the fits of high-resolution experimental spectra. There are models better than the Voigt profile as they take these effects into account. These effects are observable in the spectra recorded with high-tech spectroscopic instruments. For example, the effects of molecular speed and collisional narrowing are not accounted for in the Voigt model, but can be taken into account by other models. These effects and the associated models will be discussed in the next sections.

2.4.6 Molecular Speed-dependency Effects

The Voigt profile does not account for speed-dependency, which appears as an asymmetry in the absorption spectra. The velocities of molecules in a given sample are not the same, so it is difficult to assume their speed. Ideally, freely moving molecules follow the Maxwell-Boltzmann velocity distribution theory. To consider the random velocity of molecules, they are clustered into small groups of speeds called speed classes. The effect of molecular speed can influence the absorption line-shape. Therefore, researchers have developed new line-shape profiles to include this speed-dependency [34, 35].

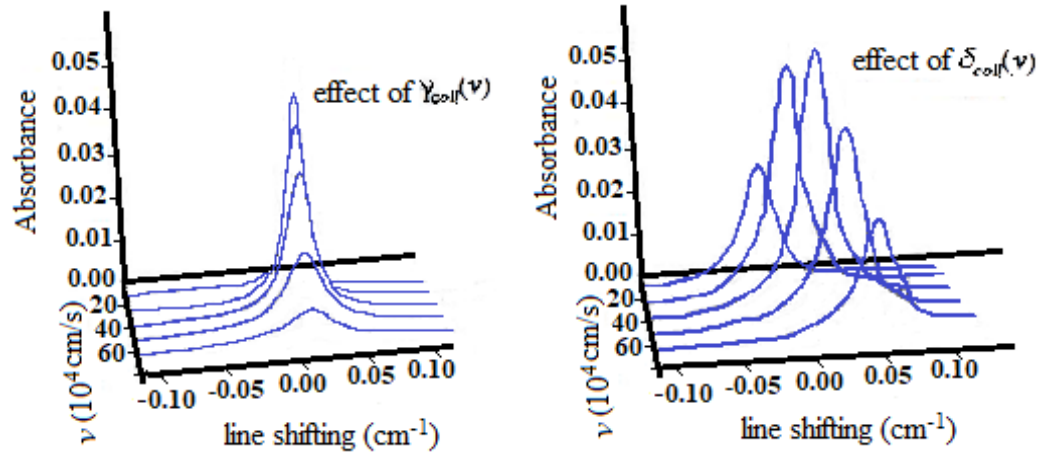


Figure 2.9: Effects of speed-dependency in the spectroscopic analysis of broadening (left) and shift (right) parameters (modification of figures (2-6, III.14, 1) in [6, 114, 115], respectively). In these figures, the absorption lines are shown upwards in order to see the effects more clearly.

Figure 2.9 is a 3-dimensional plot of the line position, intensity, and molecular speed. Here, v is the speed given in centimeter per second, $\gamma_{coll}(v)$ is the collisional broadening and $\delta_{coll}(v)$ is the collisional shift. The figure shows how both broadening- $\gamma_{coll}(v)$ and shift- $\delta_{coll}(v)$ change with the increasing/decreasing speed of the absorbers. These changes occur due to the speed-dependency effect, which results in asymmetries in

the line-shapes. High-resolution spectra can be modeled using profiles that account for these asymmetries in the spectra. A couple of speed-dependent profiles will be discussed in Sections 2.4.7 and 2.4.10.

2.4.7 Speed-dependent Voigt Profile

As discussed previously, the spectral line broadening and shift are affected by the molecular velocity (Figure 2.9). Berman [34] and Pickett [35] have introduced a modified Voigt function, which accounts for the molecular speed-dependency called the SDV profile. Their model describes the dependence of the relaxation rates on the molecular speeds and considers that the velocity changes and the speed-dependence of relaxation rates occur simultaneously. In the SDV line-shape function, the collisional broadening is determined by a weighted sum of the Lorentz function [102]. The theory by Berman implemented this Lorentz function for different absorber speeds to produce real line-shapes for collisional broadening, which was further developed by Pickett. This theory is known as the Berman-Pickett theory, and the mathematical function of the SDV profile is as follows:

$$F_{SDV} = \frac{1}{\pi} \text{Re} \left\{ \int \frac{F_M(\vec{v})}{[\Gamma(v) - i(\omega_0 - \Delta(v)) - \vec{k} \cdot \vec{v}]} d^3 \vec{v} \right\}, \quad (2.65)$$

where F_M is the Maxwell-equilibrium distribution, which can also be defined by $f(\vec{v})$ (given in Equation 2.58), $\Gamma(v)$ represents the speed-dependent broadening, $\Delta(v)$ represents the speed-dependent shift, and ω_0 is the angular frequency related to the transition frequency and is given by $\omega_0 = 2\pi c \tilde{\nu}_0$. Rohart et al. [116] introduced the dependence of the relaxation rate on the molecular speed as follows (semi-empirical quadratic form):

$$\Gamma(v_a) = \Gamma_0 + \Gamma_2 \left[\left(\frac{v_a}{v_{ao}} \right)^2 - \frac{3}{2} \right], \quad (2.66)$$

where Γ represents the relaxation rate, v_a is the molecular (absorber) speed, and v_{a0} is the most probable speed. Finally, all these expressions lead to the function of the SDV profile as follows:

$$\Phi_{SDV}(t) = \frac{\exp[-i\omega_0 t - (\Gamma_0 - \frac{3\Gamma_2}{2})t]}{(1 + \Gamma_2 t)^{3/2}} \exp\left[-\frac{(kv_{a0}t)^2}{4(1 + \Gamma_2 t)}\right], \quad (2.67)$$

where Γ_2 is the speed-dependency of the relaxation rate, t is the time, and $\Gamma_0 = \langle \Gamma(v_a) \rangle$ is the mean relaxation rate which is a linear function of pressure [102].

2.4.8 Dicke Narrowing Effect and the Diffusion Coefficient

Narrowing is observable in the spectra of the pressure regime when the mean free path of the active molecules of a sample gas becomes equal or shorter than the wavelength of the radiation. In this pressure regime, molecules experience a diffusion, which changes their path (trajectories). This effect reduces the mean thermal velocity of the molecules.

In this condition, the absorption lines become narrower and give a “w” shape in the residual when fitted using the Voigt profile, because it does not account for the narrowing effect. This “w” shape indicates the presence of the narrowing effect (an example is given in Figures A.1 and A.2 in Appendix A). As a consequence of this effect, the broadening coefficients become smaller than anticipated, i.e., the values obtained either in the Doppler or collisional regimes. This collisional narrowing is called the Dicke narrowing effect [38, 39].

Wittke and Dicke [117] introduced the first diffusional model in 1956, which was able to correctly reproduce only the high-pressure spectral line profiles but without considering the nature of the molecular collision. The line profiles, that can take the

narrowing effect into account are the Galatry and the Rautian profiles [102]. There are a few differences between these profiles. The Galatry profile is used for cases when the absorber (radiator) is heavier than the perturber. On the other hand, the Rautian profile is used for cases when the absorber (radiator) mass is less than the mass of the perturber. Both of these models will be discussed in the next section.

2.4.9 Galatry and Rautian-Sobel'man Profiles

Galatry Profile (Soft Collision): The Galatry profile is also known as the Soft collision model. This model also assumes that the number of collisions is large enough to cause significant changes in the velocity of the molecules [29]. Thus, the molecules experience soft collision due to small changes in their velocity. The diffusion formula given by Chandrasekhar [118] was applied to model this molecular displacement. The autocorrelation function that represents the soft collision model of the Galatry profile [29] is as follows:

$$\Phi_G(t) = \exp \left[-i\omega_0 t - \Gamma t + \frac{1}{2} \left(\frac{kv_{a0}}{\beta} \right)^2 (1 - \beta t - e^{-\beta t}) \right], \quad (2.68)$$

where β (rad s^{-1}) represents the narrowing rate. The narrowing rate is sometimes defined with the β_{diff} , known as the dynamical friction coefficient. The dynamical friction coefficient β_{diff} depends on the temperature T (K), molecular mass m_a , and the mass diffusion constant D ($\text{cm}^2 \text{s}^{-1}$) of the molecule and is given as follows:

$$\beta_{diff} \equiv \frac{k_B T}{m_a D}. \quad (2.69)$$

Equation 2.68 contains both the Doppler and Lorentz component of the Voigt profile; however, the Doppler component is modified to account for the velocity changes

that are caused due to molecular collisions [102]. Applying the numerical Fourier transformation on the $\Phi_G(t)$ function will give the corresponding Galatry profile (line-shape) as follows:

$$F_G(x', y, z) = \frac{1}{\pi} \text{Re} \left[\int_{-\infty}^{\infty} \exp \left(ix't - yt + \frac{1-zt-\exp(-zt)}{2z^2} \right) dt \right] = \frac{1}{\pi} \text{Re} \left[\frac{1}{\frac{1}{2z} + y - ix'} M \left(1; 1 + \frac{1}{2z^2} + \frac{y-ix'}{z}; \frac{1}{2z^2} \right) \right] (1/\text{cm}^{-1}), \quad (2.70)$$

where x' and y are the dimensionless variables [102], $M(\dots)$ is the confluent hypergeometric function and z is the new standardised narrowing parameter, which is related to the narrowing coefficient as follows:

$$z = \sqrt{\ln 2} \frac{\beta}{\gamma_D}. \quad (2.71)$$

Rautian-Sobel'man (Hard Collision) Profile: The hard collision model is applicable for the condition when the absorber mass \leq the buffer mass. This model also accounts for the effect of collisional narrowing. During hard collisions between the light absorber and heavy buffer, the absorber molecules completely lose the velocity information of pre-collision (initial velocity). As a result, the molecules experience randomized velocity changes during this intermolecular collision. The Rautian-Sobel'man profile [28] is the mathematical implementations of the hard collision models and can be expressed as follows:

$$F_R(x', y, z) = \frac{1}{\sqrt{\pi}} \text{Re} \left[\frac{W(x', y+z)}{1 - \sqrt{\pi} z W(x', y+z)} \right] (1/\text{cm}^{-1}), \quad (2.72)$$

where $W(x', y+z)$ is the complex probability function. Both the Rautian-Sobel'man and Galatry profiles lead to almost identical line-shapes. However, the Rautian-Sobel'man profile is used for heavy buffer and light absorber, while the Galatry profile is used for heavy absorber and light buffer. At high pressure when $z \rightarrow \infty$, both profiles (Equations 2.70 and 2.72) become the Lorentz line-shape function (Lorentz broadening). For no velocity changes ($\beta = 0$ and $z = 0$), Equation 2.72 tends to be the Voigt profile [102].

Two more profiles that take narrowing into account will be briefly discussed in the next section. They are called the Speed-dependent Rautian Profile and the Speed-dependent Galatry Profile. These two profiles take also the speed-dependence effects into account.

2.4.10 Speed-Dependent Galatry (SDG) and Speed-Dependent Rautian-Sobel'man (SDR) Profiles

Until now, only the line profiles that consider either the velocity changes (narrowing effect) or the speed-dependence have been discussed. However, there are other line-shape profiles that can take the speed-dependence of relaxation rates (speed-dependency of broadening) and the velocity changes (collisional narrowing) into account as both occur simultaneously during molecular collisions. Curylo and Szudy [119] have developed a formula for the correlation function by using the Anderson-Talman [120, 121] classical phase shift theory, which gives the Galatry model as follows:

$$\Phi_{SDG}(t) = \exp \left[-i\omega_0 t - \left(\frac{kv_a}{2\beta} \right)^2 (2\beta t - 3 + 4e^{-\beta t} - e^{-2\beta t}) \right] \times$$

$$\frac{4}{\sqrt{\pi}} \int_0^\infty dv^0 v^{0^2} \exp(-v^{0^2}) \text{Sinc} \left[\left(1 - e^{-\beta t} \right) \frac{kv_a^2}{\beta v_{a0}} \right] \times \exp[i\Delta(v^0 v_{a0})t - \Gamma(v^0 v_{a0})t].$$

(2.73)

In Equation 2.73, if $\beta = 0$ (i.e., neglecting the velocity changing collisions), then the expression reduces to the SDV model. On the other hand, neglecting the Doppler collision correlations and taking the velocity changing collision into account yields to the Galatry model. With the dimensionless variables, the Speed-dependent Galatry profile can be written as follows [102]:

$$F_{SDG}(x, y, z, \zeta, s) = F_G(x', y, Z) \text{ (1/cm}^{-1}\text{)}, \quad (2.74)$$

where $Z \equiv z \left(1 - y/\zeta\right) - isz/\zeta$. Here, the reduced variable ζ must follow the condition $y, s, z \leq \zeta$. $Z = \Omega/\Delta\omega'_D$, where $\Delta\omega'_D$ is the Doppler width in rad.s^{-1} and Ω is the total collision frequency.

Considering the case of heavy perturber and light absorber, the Speed-dependent Rautian and Sobel'man profile can be deduced by integrating the speed-dependence of relaxation rates. Thus, the SDR profile in dimensionless variables is [102] as follows:

$$F_{SDR}(x, y, \zeta, s) = \frac{1}{\sqrt{\pi}} \text{Re} \left[\frac{W(x, \zeta)}{1 - \sqrt{\pi}(\zeta - y - is)W(x, \zeta)} \right]. \quad (2.75)$$

This profile takes the molecular speed-dependency as well as the collisional narrowing effect into account. A Speed-dependent Rautian line-shape model is preferred in order for the resonant oxygen lines to retrieve their line-mixing coefficients as well as the speed-dependence values (Chapter 5).

2.4.11 Line-mixing

Ro-vibrational bands are normally very dense, and most of the absorption lines have neighbouring lines of the same band. In high-pressure spectra, pressure-broadened closely spaced lines cannot be treated as an isolated line, because their absorption features overlap as well as their intensities. This phenomenon is called line-mixing, also known as line interference or line coupling. An isolated absorption line can be fitted without considering the line-mixing effects. However, the line-mixing effect needs to be taken into account for two closely spaced adjacent lines, because they experience intensity transfer.

To describe this property, one can consider a pair of transitions at frequency $\tilde{\nu}_1$ and $\tilde{\nu}_2$ as shown in Figure 2.10. Figures 2.10 (a) and (b) demonstrate that when pressure increases, the absorption profiles of two closely spaced lines overlap. Thus, an intensity transfer takes place between them. Panel (c) shows that the rotational states of a molecular energy system become perturbed. These perturbations occur through the inelastic collision between molecules. Due to the perturbation, the transition from i_1 to f_1 transfers to i_1' to f_1' . Similarly, the transition from i_2 to f_2 transfers to i_2' to f_2' . These two coincidental paths result in one transition frequency, and as the pressure increases these two lines become one line with one peak position, which is ν . The width of the line increases at elevated pressure. Thus, the two lines $\tilde{\nu}_1$ and $\tilde{\nu}_2$ (Panel a) tend to overlap more (Panel b) and result in a doublet shape as the pressure of the sample molecules increases.

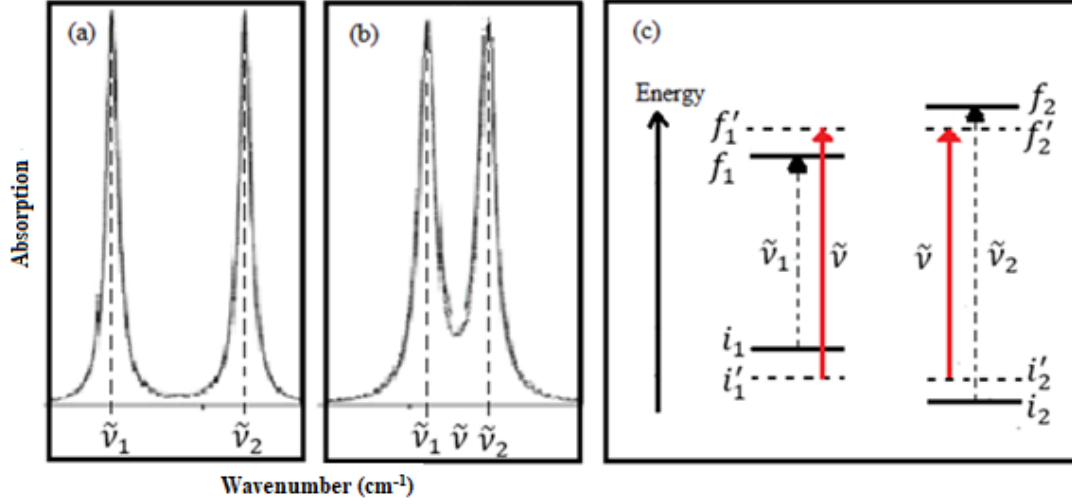


Figure 2.10: Example of the line-mixing effect – Perturbed energy levels leading to line-mixing. Panel (a) shows two absorption lines of transition frequencies $\tilde{\nu}_1$ and $\tilde{\nu}_2$. Panel (b) presents the two lines whose profiles overlap - an example of the evolution of typical doublet shape. Panel (c) shows the perturbed rotational states (energy levels) through collisions. The dashed horizontal lines represent the perturbed levels (modification of Figure 2.7 in [6] and ideas taken from Ref. [114]).

The formula that relates the line-shape function and the absorption coefficient is described in the Beer-Lambert Section (2.3.1) [102]. For a band of completely isolated lines, the absorption coefficient is given as the sum of the line as follows:

$$K(\tilde{\nu}) = P_a \sum_{n=1}^N A_{Pn} F_n(\tilde{\nu} - \tilde{\nu}_n), \quad (2.76)$$

where P_a is the partial pressure of the gas sample given in atmospheres, and $F_n(\tilde{\nu} - \tilde{\nu}_n)$ represents the line-shape of the n^{th} line of intensity A_{Pn} and line center $\tilde{\nu}_n$.

At elevated gas pressures, the collisional transfer between the energy levels of overlapped neighbouring lines also experiences intensity transfer. Therefore, the line interference is also influenced by the value of broadening and shifting coefficients. Line-mixing can also be accounted for and determined through the off-diagonal elements of the relaxation matrix that is related to the line-shape profiles. Rosenkranz [1] has studied and

has quantified the asymmetries due to line-mixing effects observed in slightly overlapped pairs of lines (weakly overlapped). The Lorentz function of the line-shape profiles can be modified to include the weak line-mixing effect as follows:

$$F_n(\tilde{\nu} - \tilde{\nu}_n) = \frac{1}{\pi} \frac{\gamma_c + (\tilde{\nu} - \tilde{\nu}_n) Y_n}{(\tilde{\nu} - \tilde{\nu}_n - \delta_n)^2 + \gamma_n^2} (1/\text{cm}^{-1}), \quad (2.77)$$

where the line widths γ_n and the line shift δ_n are the adjustable parameters in the following expression [102] of the line-mixing coefficient Y_n associated with the off-diagonal element Γ_{mn} of the relaxation matrix Γ ($m \neq n$):

$$Y_n = 2 \sum_{(m \neq n)} \frac{d_m}{d_n} \frac{\frac{\Gamma_{mn}}{2\pi c}}{\nu_n - \nu_m}, \quad (2.78)$$

where d_m and d_n represent the dipole matrix elements corresponding to the ν_m and ν_n transition frequencies.

2.4.12 Exponential Power Gap Scaling Law (EPG)

The Exponential Power Gap (EPG) scaling law is a theoretical semi-empirical method of calculating broadening and line-mixing coefficients. The broadening and line-mixing parameters can be calculated from the decay rates of rotational energy states by implementing a relaxation matrix V . The diagonal elements of the relaxation matrix have two parts: real and imaginary. The real part contains broadening coefficients, and the imaginary part contains pressure-induced shift coefficients. The off-diagonal elements of the relaxation matrix contribute to the collisional rates between energy levels (line-mixing information).

This thesis includes the results of EPG calculation for oxygen molecules in Chapter 5, and this section discusses the EPG method used for the diatomic molecules. The collisional transfer rates between two rotational states of oxygen molecules can be computed from the following expression [44]:

$$k_{n \leftarrow m}^{EPGL} = a \left| \frac{\Delta E_{mn}}{B_0} \right|^{-b} \exp \left(- \frac{c |\Delta E_{mn}|}{k_B T} \right) R(\Delta E) N_{n \leftarrow m} \quad (2.79)$$

where m and n represent the lower and the upper rotational states, respectively. ΔE_{mn} is the energy difference between these two energy states, B_0 is the rotational constant, $R(\Delta E)$ is the translational space factor, and $N_{n \leftarrow m}$ (where $N_{n \leftarrow m} = 2J+1$) represents the spin degeneracy of each rotational quantum number J .

For a diatomic molecule, the collisional transfer rates of N quantum numbers corresponding to transitions between lower energy E_m and upper energy E_n states can be calculated as follows:

$$k_{n \leftarrow m}^{EPGL} = a \left| \frac{\Delta E_{mn}}{B_0} \right|^{-b} \exp \left(- \frac{c |\Delta E_{mn}|}{k_B T} \right). \quad (2.80)$$

The goal is to optimize all three a , b and c fitting parameters in the above equations for a given molecular system. ΔE_{mn} is the energy gap between the lower rotational state energy E_m and the upper rotational state energy E_n . Assuming that the molecular system is in thermodynamic equilibrium; the detailed balance condition connects the off-diagonal elements from the lower half of the relaxation matrix to the off-diagonal elements from the upper half through the following expression:

$$k_{n \leftarrow m} = k_{n \leftarrow m} \left(\frac{2N_n + 1}{2N_m + 1} \right) \exp \left(- \frac{|\Delta E_{mn}|}{k_B T} \right). \quad (2.81)$$

The line-coupling effect between two transitions corresponding to two neighbouring lines is called the line-mixing effect and is computed from the off-diagonal matrix elements V_{mn} ($m \neq n$). The diagonal V_{mn} ($m = n$) and the off-diagonal V_{mn} ($m \neq n$) elements are given as follows:

$$V_{mn} (m = n) = \frac{1}{2} [\sum_m K'_{mn} + \sum_m K''_{mn}] \quad (2.82)$$

$$\text{and} \quad V_{mn} (m \neq n) = -\frac{\varepsilon}{2} [\sum_m K'_{mn} + \sum_m K''_{mn}], \quad (2.83)$$

where K'_{mn} and K''_{mn} are the collisional transfer rates. The impact parameter, ε , is determined experimentally. Finally, the off-diagonal elements V_{mn} ($m \neq n$) were used in the expression below to compute the theoretical line-mixing values as follows:

$$Y_k(T) = 2 \sum_{(m \neq n)} \frac{d_m}{d_n} \frac{W_{mn}}{v_n - v_m}. \quad (2.84)$$

The line-mixing effect is measured in per atmosphere (atm^{-1}). The EPG [44] code needs an input file that contains the retrieved broadening coefficients associated with each transition (rotational quantum numbers). This file also needs the lower state energy values corresponding to each transition and the electric or the magnetic dipole moment of the molecule. The output file gives the EPG calculated broadening and line-mixing coefficient.

2.5 Summary

This chapter provides the theoretical knowledge related to the spectroscopic studies of this thesis before presenting into the analyses and results. The explanations given in this chapter will help to gain basic knowledge, which is important to understand the three studies and their results that are presented in Chapters 4, 5, and 6.

Chapter 3 Experimental Procedures

3.1 Overview

Descriptions of the instrumentation used in the three experimental studies that make up this thesis are presented in this chapter. Two types of spectrometer systems were used for obtaining the experimental data: A Tunable diode-laser spectrometer (TDLS) and two Fourier-transform spectrometers (FTS). The experiment for the line-shape study of acetylene broaden by nitrogen was carried out using the TDLS system, located in the Department of Physics and Astronomy, University of Lethbridge, Canada. One of the FTS systems used in the ammonia study is located at the Canadian Light Source, Saskatoon, Canada, while the other FTS used in the oxygen study is located at the Justus-Liebig-University in Giessen, Germany. Section 3.2 will present a detailed description of the TDLS system used for the acetylene line-shape study. The two FTS setups will be presented in Sections 3.3 and 3.4. The software used for analyzing the TDLS and FTS spectra will be discussed in Sections 3.2.8 and 3.5, respectively.

3.2 Tunable Diode-Laser Spectrometer System (C₂H₂-N₂ study)

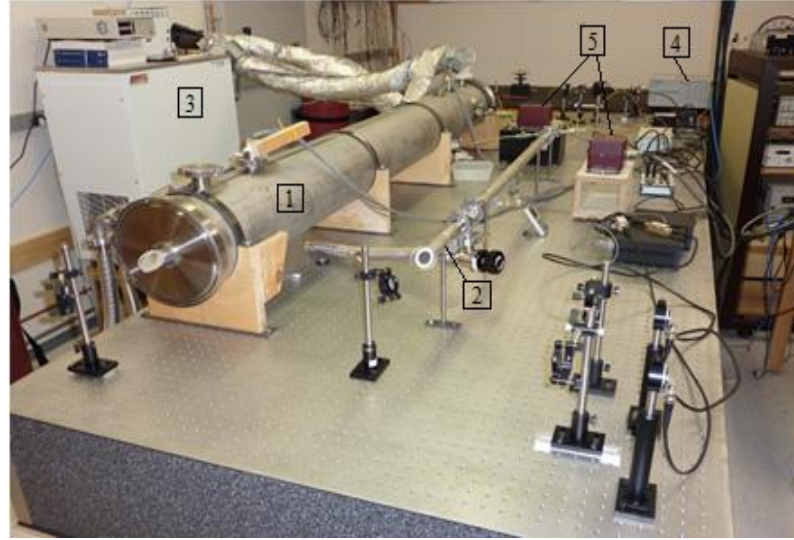
The three major components of a tunable diode-laser system are a laser-light source, gas chamber, and detectors. This type of system is commonly used for line-shape studies as the setup can be adjusted to obtain a very high-spectral resolution, as well as a high signal-to-noise ratio (SNR). This section presents a brief discussion of the TDL spectrometer.

Overview of the TDLS Schematic Diagram: For the acetylene study, a New Focus-Velocity laser has been used in the TDLS system as the radiation source. This laser is built based on the Littman-Metcalf cavity [122-124]. Scanning of the wavelength region using a diode-laser system was performed by a piezoelectric device (by the increment of voltage), which is a built-in component of the laser.

The TDLS system has two gas cells, a laser source, and three detectors. A picture and a schematic diagram of the 3-channel tunable diode-laser spectrometer system is given in Figure 3.1. Panel (A) of Figure 3.1 shows a photo of the laboratory spectrometer system [7] and (B) presents a diagram of the entire spectrometer setup. Panel (A) provides the photograph of the temperature and pressure controlled cell (1), room-temperature reference cell (2), Neslab Chiller ULT-80 that controls the temperature of the gas sample (3), wavemeter (4) and MKS Baratron pressure gauges (5). The laser radiation is sent through the two gas cells.

In panel (B), Cell 1 is a temperature and pressure-controlled cell used for recording spectra at different pressure and temperature conditions. Cell 2 is a room-temperature cell used for recording low-pressure and room-temperature spectra. The spectra recorded in cells 1 and 2 are also referred to as Channel-1 and Channel-2 spectra, respectively. The third channel of this laser setup is the laser output power [36]. For this spectrometer system, spectra are collected from all three channels simultaneously.

(A)



(B)

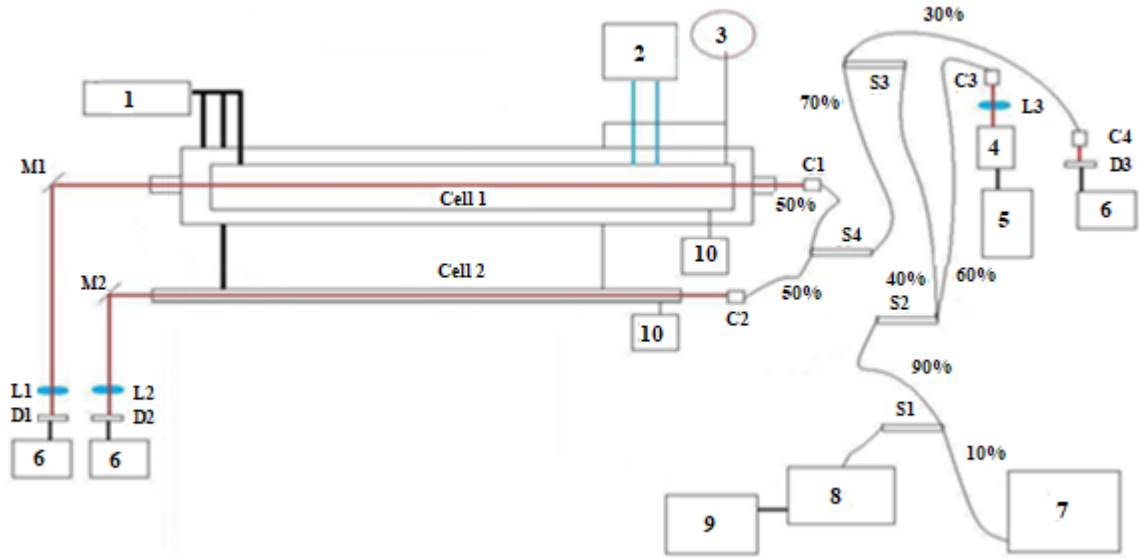


Figure 3.1. Configuration of the 3-channel tunable diode-laser spectrometer. (A) Photo of the TDLS setup: 1. temperature and pressure controlled cell, 2. room-temperature reference cell, 3. Neslab Chiller ULT-80, 4. Wavemeter and 5. MKS Baratron pressure gauges. (B) Schematic diagram of the 3-channel tunable diode-laser spectrometer [36]: cell-1 is the temperature and pressure controlled gas cell; cell-2 is the room temperature gas cell. Nos. - 1. vacuum pump, 2. Neslab temperature controller, 3. gas cylinder (C_2H_2 and N_2), 4. Fabry-Perot interferometer 5. controller, 6. detector pre-amplifiers and power source, 7. Wavemeter, 8. laser head, 9. controller and 10. pressure gauges. L1, L2, and L3 are the lenses, while D1, D2 and D3 are the detectors. M1 and M2 are the beam guiding mirrors, C1, C2, C3, and C4 are the collimators, and S1, S2, S3, and S4 are the beam splitters (modified version of Figure 3-3 in [6]).

No.1 represents the vacuum pump, no.2 the Neslab temperature controller, no.3 is the gas cylinder (C_2H_2 and N_2), and nos.4 & 5 are the Fabry-Perot interferometer and controller, respectively. No.6 represents the detector pre-amplifiers and power source, and no.7 is the wavemeter. Nos.8 and 9 are the laser head and controller, respectively. No.10 is the MKS Baratron pressure gauge. The lenses are shown using alphabetical symbols L_1 , L_2 and L_3 and the detectors labeled as D_1 , D_2 , and D_3 , respectively. M_1 and M_2 are the mirrors, C_1 , C_2 , C_3 , and C_4 are the collimators and S_1 , S_2 , S_3 , and S_4 represent the beam splitters [36]. The entire experimental setup is placed on an optical table (Kinetic System 5100H series) to reduce the effect of vibration from the vacuum pump and other laboratory mechanical instruments.

After shooting the laser beam, 100 % of the signal passes through the S_1 beam splitter. From there 10 % of the total signal it is sent to the wavemeter and 90 % to the S_2 beam splitter. S_2 splits the incoming signal into two parts of which 40 % goes to the third beam splitter S_3 and 60 % to the Fabry-Perot (FP) interferometer. The beam splitter S_3 divides the incoming 40 % light into two parts, of which 30 % is sent to the detector D_3 (records signal for the background spectra), while the remaining 70 % is sent to the two gas cells using the beam splitter S_4 . It splits this radiation into two 50 % portions before sending it to the gas cells 1 and 2. The output beams from cells 1 (temperature and pressure-controlled cell) and 2 (room temperature cell) are then recorded using detectors D_1 and D_2 , which provide the sample and reference spectra, respectively.

3.2.1 Temperature and Pressure (T-P) Controlled Gas Cell (Channel-1)

Cell 1 contains two stainless steel cylindrical chambers of different sizes. The small one is located concentrically inside the large one using adjustable support stands as shown in Figure 3.2. A vacuum is maintained in between them during the experiments. These two cylinders are known as the inner (smaller) chamber and the outer (larger) chamber [36]. The inner chamber is a single-pass, temperature and pressure-controlled gas cell with an optical pathlength of 1.54 m. The two ends of the inner chamber are covered with flanges, each containing four ports. One of the flanges contains a gas inlet, one port for the pressure gauge, and two temperature ports, while the second flange contains a gas outlet and three temperature ports. The flanges are made of stainless steel in which an anti-reflection coated CaF_2 window is sealed in the center of each flange using Fluoro-silicone O-rings.

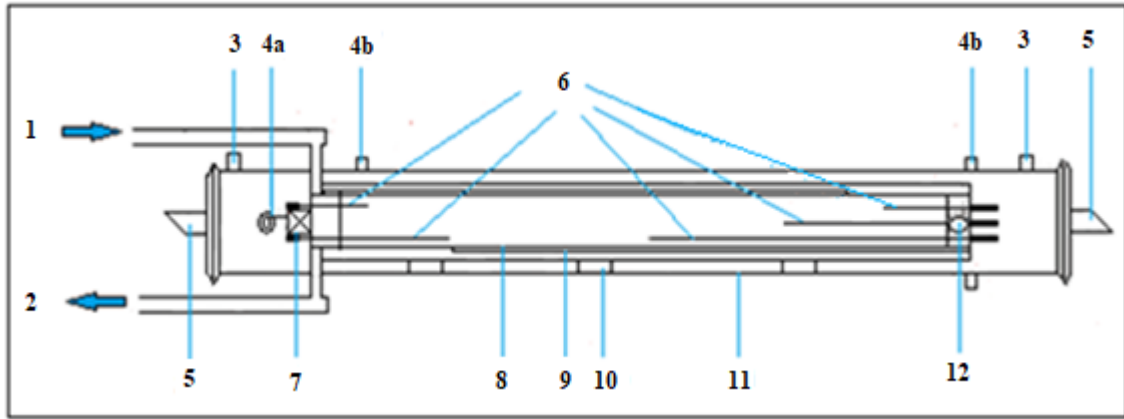


Figure 3.2: Side view of the temperature-controlled cell: 1. coolant in pipe, 2. coolant return pipe, 3. vacuum port, 4a. gas inlet, 4b. vacuum feed-through for platinum resistors, 5. CaF_2 windows mounted at Brewster angle, 6. temperature sensors using platinum resistors, 7. vacuum valve, 8. fins for directing the coolant through the coolant jacket, 9. coolant jacket, 10. cell support, 11. outer cell body and 12. valve for de-pressuring the outer jacket (modified version of Figure 3-17 in [6]).

Five temperature sensors called platinum resistor thermometers (PRT), are placed inside the cell 1. They are mounted on the flanges with 15.24, 45.72 and 76.20 cm long

rods to measure the temperatures at different positions in the cell (no. 6 in Figure 3.2). Ethanol is used as a heating/cooling fluid. Using ethanol one can obtain the sample gas temperature between 193 K and 353 K that is kept inside the temperature and pressure-controlled cell (Cell 1). The inner cell contains metal fins through which this fluid flows uniformly along the entire cell using a Neslab Chiller ULT-80 [6, 125].

The outer chamber is also made of stainless-steel (nominal 8" schedule 10 pipes). Both ends are covered with flanges and held in position using stainless steel compression rings. Both flanges contain a crystal window made of CaF_2 , which is mounted at the Brewster angle in the center of each flange (no. 5 in Figure 3.2) to avoid reflections of the laser beam. The outer chamber contains a gas inlet/outlet, heating/cooling fluid inlet/outlet, and pressure/temperature monitoring ports.

A vacuum pump is connected to maintain a vacuum in between the inner and outer chamber. This vacuum jacket isolates the inner chamber from the outer chamber to reduce thermal conductivity. This pump is also used for evacuating the gas cells. The outer chamber is always kept in a vacuum state during each experiment.

3.2.2 Reference Gas Cell and the Background Signal

Cell 2 is also known as the reference cell [36]. It is a room-temperature (~ 296 K) gas cell used for recording pure and unperturbed low-pressure spectra of gas. A very small amount of gas, a few hundred mTorr is loaded in this cell for recording the reference spectra. The cell needs to be pumped down to $\sim 10^{-4}$ Torr before loading the gas. These low-pressure spectra are needed to correct the peak positions of absorption lines as they are less shifted than the high-pressure spectra (discussed in the next sections).

The signals from the third channel, that is from the diode laser itself (New FocusTM Velocity model), is used to record background spectra for the baseline correction of the sample and reference spectra [36]. This laser system has a modified Littman-Metcalf design [122-124], which covers the 6666 - 6369 cm^{-1} (1500 - 1570 nm) range with a very narrow linewidth (few KHz or 10^{-6} cm^{-1}) and has an approximate output power of 9 mW.

3.2.3 Pressure Measurements and Monitoring

Pressure measurements and monitoring inside the gas cell was performed using two MKS Baratron pressure gauges and an MKS signal conditioner (model 670). Spectra below 100 Torr were recorded with a 0-100 Torr gauge and spectra of 100 Torr and above were recorded with a 0-1000 Torr gauge. At the beginning of each set of experiments, both cells were evacuated (to $\sim 10^{-4}$ Torr) for several hours using a turbo vacuum pump. After that, both cells were filled with the gases of interest. For this study, cells 1 and 2 were filled with a mixture of C_2H_2 (9.94%) and N_2 to record sample spectra, and with pure C_2H_2 to record reference spectra, respectively. The chiller was then set to the desired temperature point. Spectra were recorded once the temperature and the pressure of the gas sample in both channels showed stable readings [36] as shown in Table 3.1.

Example of a portion of the temperature-pressure file is given in Table 3.1. The first column shows the date and time recorded during scans. The second and the last columns represent the pressure readings of channels 1 and 2 in Torr, respectively. The temperatures recorded using the five platinum resistance temperature sensors (1, 2, 3, 4, and 5) are given in degree Celsius.

Table 3.1: Example of pressure and temperature measurements as they were recorded after scans. The titles of the columns do not appear in the output files (CH1 = channel 1 and CH2 = channel 2).

Time	Pressure in CH1 (Torr)	Reading in Temperatures Sensors (°C)					Pressure in CH2 (Torr)
		1	2	3	4	5	
7/25/2013 5:33:27 PM	249.36	22.37	22.75	22.90	22.57	22.60	0.25
7/25/2013 5:33:28 PM	249.36	22.36	22.74	22.89	22.57	22.62	0.25
7/25/2013 5:33:29 PM	249.36	22.36	22.75	22.89	22.58	22.60	0.25
7/25/2013 5:33:30 PM	249.36	22.37	22.74	22.89	22.58	22.61	0.25
7/25/2013 5:33:31 PM	249.36	22.37	22.76	22.89	22.58	22.61	0.25

3.2.4 Detectors

The output signals were obtained using indium gallium arsenide (InGaAs) detectors and preamplifiers. Three detectors were needed to record the intensity of the light transmitted through all three channels: Channel-1 (the temperature and pressure-controlled cell), Channel-2 (the room temperature reference cell) and the laser itself (background signal). These photodiode InGaAs detectors are connected to the computer. A detector was set in front of each of the focusing lenses corresponding to Channel-1 and Channel-2. They were attached to the optical table with holders as shown in Figure 3.3 [6].

After recording Channel-1 and Channel-2 spectra, the SNR needs to be measured to check the quality of the spectra. The SNR of the spectra can be measured from the acquired signals as follows:

$$SNR = \frac{X_{avg}}{\sqrt{\frac{1}{N} \sum_1^N (X_i - X_{avg})^2}}, \quad (3.1)$$

where X_i is the i^{th} data point, X_{avg} is the average signal, and N is the total number of data points. Accordingly, the SNR is the average signal divided by the root-mean-square (RMS). The spectra recorded using the aforementioned experimental setup have an SNR of approximately 2000:1

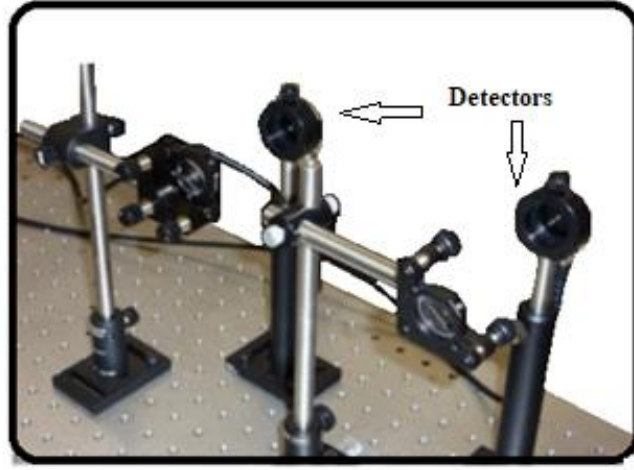


Figure 3.3: Photodiode InGaAs detectors used for measuring the signal from the gas chambers and the laser (modified version of Photograph 3-9 in [6]).

3.2.5 Instrumental Line-Shape Function

An essential element in the experimental setup is the instrumental line-shape function (ILS). The selection of a proper ILS is important, because the type of this function affects the quality of retrieved line parameters. For this experimental setup, the ILS has previously been determined and tested by Chad Povey, one of the spectroscopy group members of the Department of Physics and Astronomy, University of Lethbridge. The process of determining this function is outlined in his dissertation [6]. In that test, a number

of transitions of both P- and R- branch lines in the $\nu_1 + \nu_3$ band of acetylene were recorded at 30 mTorr and were fitted using the Gaussian and Lorentz profiles. According to the test, the Lorentz profile exhibited a better fit than the Gaussian profile. Therefore, the Lorentz function with a width of $8.167 \times 10^{-5} \text{ cm}^{-1}$ determined by Chad Povey has been used in the fitting program for modeling the instrumental line shape.

3.2.6 Fabry-Perot Cavity and Wavemeter

Assigning wavenumbers to the recorded raw sample and reference spectra were achieved using a wavemeter (WA-1500 EXFO) and a Fabry-Perot interferometer (Thor Labs SA200-14A) simultaneously. The free spectral range (fringe spacing) of the Fabry-Perot cavity as given by the manufacturer was 0.05 cm^{-1} (1.5 GHz). This free spectral range was used for determining the wavenumber scale, which is described below.

During the scans, the tuning of the laser output is achieved by voltage increment at the piezoelectric device (from -3.0 to 2.7 V with an increment of 0.001 V [6]). The wavemeter (associated error of 0.001 cm^{-1}) together with the Fabry-Perot cavity (associated error of 0.001328 cm^{-1}) produce the frequency scale (wavelength scale) in wavenumbers. After each scan, two files are generated: a “Peak” file and a “Spectra” file. The latter contains all the frequencies generated by the scanning laser and the corresponding spectral intensities recorded by the detectors. The ‘Peak’ file contains only those frequencies allowed to pass through the Fabry-Perot interferometer due to its free spectral range as shown in Table 3.2.

Table 3.2: Example of the “Peak” file where the first column represents the Fabry-Parot Voltage and the second one lists the wavenumber (free spectral range 0.05 cm^{-1}).

Fabry-Parot Voltage (V)	Wavenumber (cm^{-1})
0.588641	6517.209
0.751083	6517.159
0.549756	6517.109
0.523456	6517.059
0.756912	6517.009
0.664261	6516.959
0.659570	6516.909
0.457782	6516.859
0.730350	6516.809

The first peak position is measured with the wavemeter. The free spectral range ($0.0496 \pm 0.0007 \text{ cm}^{-1}$ [6]) of the Fabry-Perot interferometer was then used to assign the rest of the peaks in the ‘Peak’ file. These peak positions can be used in the ‘Spectra’ file to assign the wavenumbers of the whole spectra. The difference (0.05 cm^{-1}) between two peaks in the ‘Spectra’ file is divided by the number of points present between the peaks providing the spacing in wavenumbers for two adjacent sample points. This ratio is the resolution of each spectrum. Using the wavenumber of the first peak position and the resolution, it is then possible to assign wavenumbers to all the sample points of the entire region of the spectra.

3.2.7 Data Processing

The experimental setup was controlled using the software written in the LabView programming language (provided by National Instruments), which is used for the data acquisitions and monitoring the optical instruments [126]. Processing of the raw data to create spectra for analysis was also performed using LabVIEW. In a first step, spectra from the three channels: the sample spectra (temperature-pressure controlled cell – Channel-1), reference spectra (room temperature reference cell – Channel-2) and the background spectra (laser – Channel-3) were recorded simultaneously. A number of programs are implemented in this software for different purposes. Among them, “Velocity.vi”, “FabryParot.vi”, “PeakFileCorrection.vi”, and “WaveConverter.vi” have been used for the data recording and processing [36]. The “Velocity.vi” controls and monitors the data recording. The “FabryPerot.vi”, “PeakFileCorrection.vi” and “WaveConverter.vi” are used for assigning wavenumbers to the ‘Spectra’ file as discussed in Section (3.2.6).

The “FabryPerot.vi” generates the “Peak” and the “Spectra” files. The “PeakFileCorrection.vi” corrects each peak of the “Peak” file by using the free spectral range and starting wavenumber (first peak) recorded by the wavemeter. The “WaveConverter.vi” then uses the corrected “Peak” file to assign wavenumbers in the “Spectra” file, which creates a new file for each channel called “Converted_CH1” for Channel-1, “Converted_CH2” for Channel-2 and “Converted_BG” for the background.

Transmission spectra were created for channels 1 and 2. This process was performed using the “Correctionfit.vi” program. Spectra recorded with the sample gas have spectral features, whereas the background spectra are recorded directly from the laser source and have only a baseline. Figure 3.4 (a) shows an example of a Channel-1 spectrum

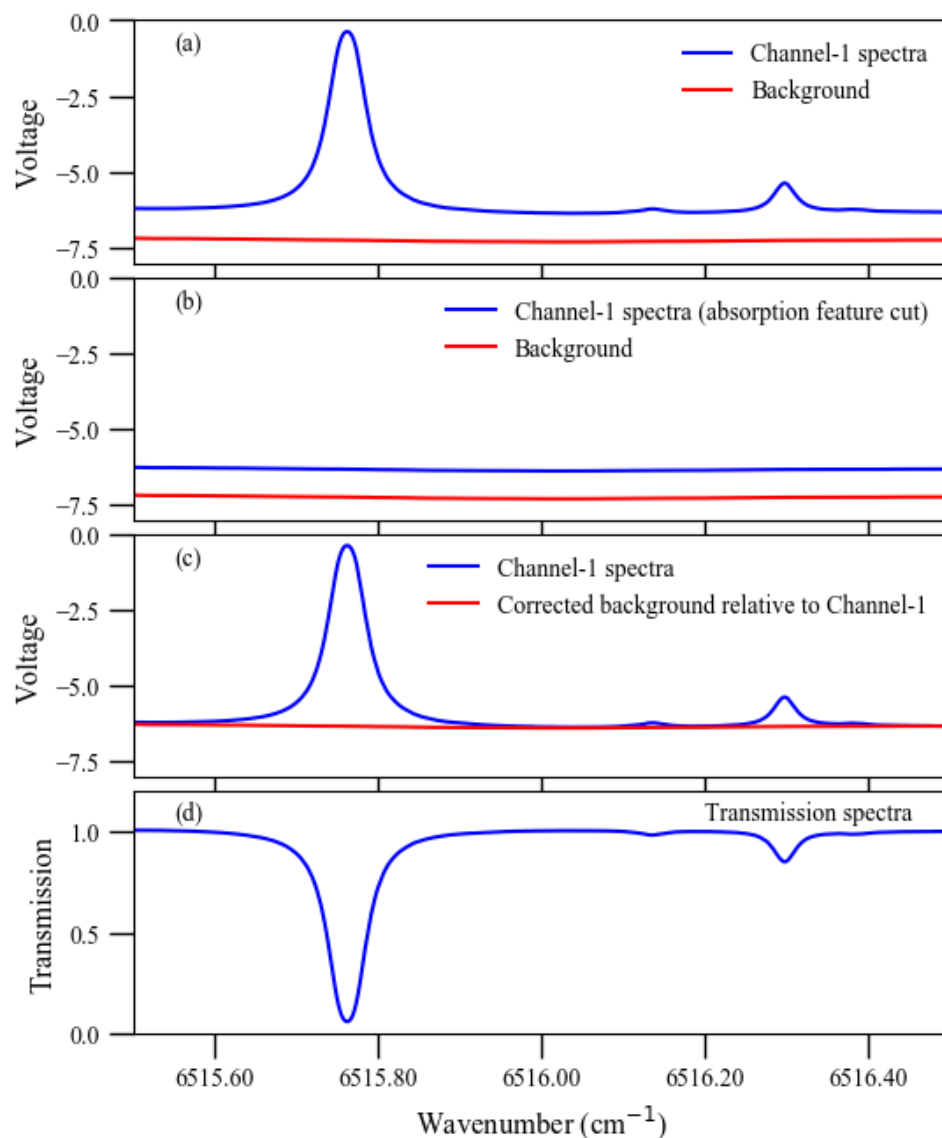


Figure 3.4: Panel (a): Example of a Channel-1 spectrum in the 6515.50 – 6516.50 cm^{-1} regions in blue and corresponding background in red. Panel (b): Edited spectrum after removal of the spectral features (blue) for the baseline correction using the background spectrum. Panel (c): Corrected baseline for Channel-1 spectrum. Panel (d): Channel-1 transmission spectrum of the absorption line P(16).

(blue) of an acetylene nitrogen mixture ($\text{C}_2\text{H}_2\text{-N}_2$) recorded in the 6515.50 – 6516.50 cm^{-1} range of the $\nu_1 + \nu_3$ band and corresponding background spectrum (red). The figure shows

that the blue line (Channel-1 spectrum) has some absorption features. The baseline signal of the Channel-1 spectrum (blue) is slightly off from the background spectra (red). The steps of the baseline correction and creating a Channel-1 transmission spectrum are as follows:

- In the first step, the spectral features are cut out from the Channel-1 spectrum (sample spectrum from “Converted_CH1” file). This is done by cutting absorption features starting from the left side of an absorption peak and stop to the right side of that peak where it seems to be baseline. Example of the Channel-1 spectrum after cutting the spectral feature is presented in Figure 3.4 (b). The residuals between the baseline of the Channel-1 spectrum and the background spectrum (spectrum from “Converted_BG” file) are then calculated as follows:

$$\text{Residual} = S' - B', \quad (3.2)$$

where S' is the Channel-1 spectrum after cutting the absorption feature (sample spectra baseline) and B' is the background.

- Secondly, the baseline is corrected by fitting the residual using Chebyshev Polynomials of different orders. Once the best polynomial order is found, one can correct the background signal as follows:

$$\text{Corrected baseline} = CP' + B', \quad (3.3)$$

where CP' is the Chebyshev Polynomial applied to the residual. Figure 3.4 (c) shows the corrected background spectrum relative to the Channel-1 spectrum.

- In the final step, the transmission spectrum is created by dividing the Channel-1 spectrum (spectrum from “Converted_CH1” file that includes the features) by the corrected baseline as shown in Figure 3.4 (d). The same steps need to be completed for Channel-2 transmission spectra.

Further calibration of peak positions in the Channel-1 spectrum is required for the line-shape analysis, which is completed using a program called “ShiftCall.vi”. Firstly, the difference between the HITRAN 2012 (the latest updated database used during this study) and Channel-2 spectrum was calculated. This difference was computed by fitting the Channel-2 (room temperature) spectrum using the “Wproffit2.exe”. The Channel-1 spectrum was then shifted by this difference using “ShiftCall.vi”. This is the reason why Channel-2 spectra are called reference spectra. The accuracy of this calibration depends on the accuracy of the HITRAN 2012 line positions [6].

3.2.8 Wproffit2.exe

Wproffit2.exe while performs a multispectrum fit technique was developed by Hurtmans et al. [126], and used for modeling the spectra to retrieve the line-shape parameters. This multi-fit program allows the fitting of several spectra simultaneously. Spectra can be modeled with different line-shape profiles. However, the choice of the line-shape profile will depend on the experimental conditions of the spectra. VP is the most commonly used profile for fitting low-pressure spectra. Spectra of different pressure ranges contain different types of effects, which need to be considered. For example, this program incorporates line profiles that can take the Dicke effect or confinement narrowing into account, while fitting spectra recorded at the intermediate/narrowing pressure regime (different line profiles are described in Section 2.4 of Chapter 2).

Wproffit2.exe needs an input file, which contains all the information of the spectra; for example, temperature and pressure conditions, gas concentration, spectral range, initial guesses of line position, intensity, broadening, narrowing, shift, speed dependency, and line-mixing parameter. The initial guess values are taken from the HITRAN database. The retrieved broadening and shifting parameters account for the mixing ratio and the total pressure of the sample [126]. Wproffit2.exe also takes the instrumental line shape of the laser spectrometer into account in the fitting procedure of the spectra.

3.3 Fourier Transform Spectrometer (Ammonia and Oxygen Studies)

A typical FTS system includes a light source, a sample cell, a beam splitter, one moving mirror, one fixed mirror, and a detector. Generally, an FTS-light source covers a wide spectral range of the electromagnetic spectrum. However, one can select the spectral range of interest before scanning using filters.

As shown in Figure 3.5, the beam splitter splits the light beam into two and directs one of the beams to the moving mirror and the other one to the fixed mirror. The reflected light strikes the stationary (fixed) mirror, reflects back and is then transmitted through the beam splitter to the sample. The light, which strikes the moving mirror, reflects back to the beam splitter and again to the sample. At the beam splitter, these two split beams recombine before entering the sample chamber. Finally, the recombined light beam strikes the detector after interacting with the sample [127].

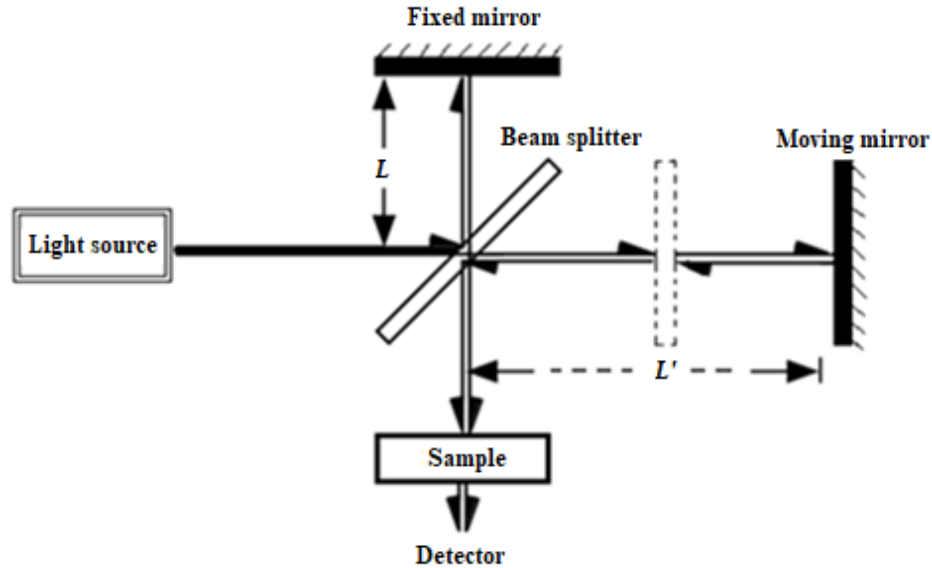


Figure 3.5: Diagram of a Michelson interferometer [128]. L is the distance between beam splitter and fixed mirror. L' is the distance between beam splitter and moving mirror, which varies during the scanning.

The distances traveled by the two split beams are different as one of them is changing due to the moving mirror. The difference in their traveled path length is called the optical path difference (OPD). The beams travel the same distance before recombining at the beam splitter when both mirrors are at the same distance from the beam splitter. Therefore, the beams have traveled the same pathlength. In this condition, the difference between pathlengths traveled by both beams is zero and is called the zero-path difference (ZPD). The moving mirror completes a two-way path: back and forth, i.e., moving away and then coming towards the ZPD position. The recombined beams form a constructive interference when they are totally in phase, i.e., OPD is zero. Recombined beams form a destructive interference [128] when they are out of phase. The moving mirror traveling back and forth once through the ZPD point is called a complete scan. After completing one full scan, the FTS generates a complete interferogram. The interferograms are presented in

the form of a spatial function, i.e., the X-axis is the optical path difference and the Y-axis is the light intensity. Interferograms are then Fourier transformed to obtain spectra.

3.3.1 Spectral Resolution and Signal-to-noise Ratio (SNR)

The spectral resolution depends on the maximum displacement of the traveling mirror. A low resolution is obtained with a short displacement (OPD), while a high resolution is achieved with a large OPD. The relation between resolution and the OPD is defined as follows:

$$resolution \propto \frac{1}{\delta'} \text{ in cm}^{-1}, \quad (3.4)$$

where the δ' represents OPD. The SNR ratio is a very important factor of a spectrum. It is the ratio between the absorption or emission peak height and the noise level at the baseline of the spectrum. Noise is a random fluctuation, which appears in the baseline mainly due to mechanical or pump vibrations. For an FTS system, the SNR can be improved by increasing the number of scans under given experimental conditions. The SNR is proportional to the square root of the number of scans (number of interferograms for a given resolution and spectral range) as follows:

$$SNR \propto \sqrt{N}. \quad (3.6)$$

3.4 Experimental Setup of the Far-infrared Study of Ammonia ($^{15}\text{NH}_3$)

An FTS (Bruker IFS 125) located at the Far-infrared Beamline of the Canadian Light Source (CLS) was used for recording $^{15}\text{NH}_3$ absorption spectra. This spectrometer system will be briefly presented in this section, while the data processing software, OPUS, is discussed in Section 3.4.1.

A number of unapodized spectra were collected to accomplish the assignment study of the $^{15}\text{NH}_3$ molecule [79]. Using a combination of the synchrotron light source, Si-bolometer, and 6- μm Mylar beamsplitter, it was possible to obtain ammonia spectra of the wavenumber range of interest, which is in the 60 – 500 cm^{-1} spectral region. All the spectra were recorded with a resolution of 0.00096 cm^{-1} and at pressures below 1 Torr. A Si bolometer and a Ge:Cu photoconductive-type infrared detector with nanosecond response and background-radiation limited noise were selected as they are suitable detectors for the 60 – 370 and 300 - 1850 wavenumber ranges, respectively. For best sensitivity, these types of detectors usually need to be cooled down only to a few kelvins. In this experiment, the detectors were cooled to 4 K with liquid helium. The aperture size was set to 2 mm, the scanner velocity to 80 kHz, and the electronic lowpass filter to 5 kHz.

A pressure and temperature controlled White type multi-pass gas cell of 2 m base length was used as the gas chamber. The cell windows were made of polypropylene. Pure $^{15}\text{NH}_3$ (98%), provided by Sigma Aldrich, was loaded into the cell. For this study, the cell pathlength was adjusted to 8 m to collect 0.002 Torr spectra and 72 m to acquire 0.005-, 0.051-, 0.767- and 1.000-Torr spectra. The pressures in the gas cell were measured using a Baratron pressure gauge.

3.4.1 Raw Data Processing (OPUS)

The data processing was carried out using the OPUS software [129]. Two sets of scans were needed. One of them was from the White-type multipass cell filled with the sample gas, $^{15}\text{NH}_3$, and the other one with the empty cell. The transmission spectra were created in three steps. At first, all the disturbed/noisy/bad interferograms were removed. Interferograms whose general shape/structure are qualitatively the same as all the others

were considered as a good interferogram. An average of the good interferograms was created for each set.

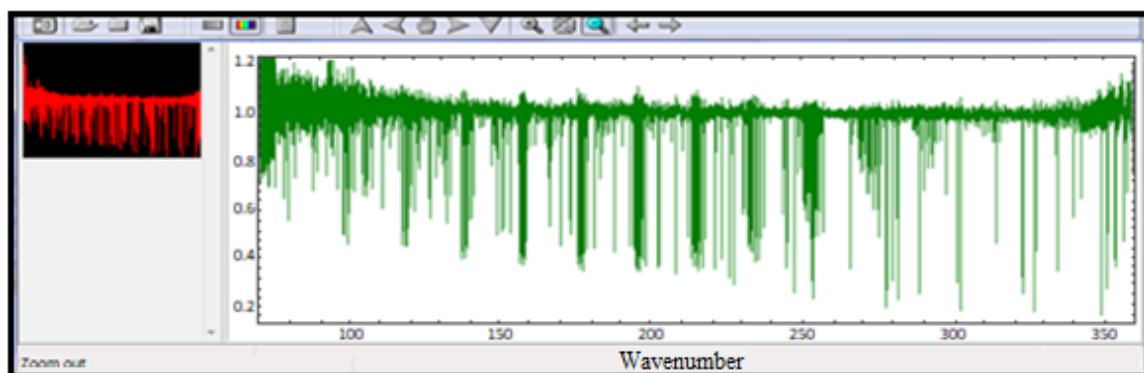


Figure 3.6: Example of $^{15}\text{NH}_3$ transmission spectra record at 0.002 Torr. The intensity is decreasing with increasing wavenumber. The transmission spectra were created in OPUS.

In a next step, a Fourier transform was performed on both the sample cell and empty cell-average interferograms using OPUS to obtain sample and background spectra, respectively. Empty cell spectra are called background spectra, which are recorded after pumping down the cell to the pressure less than 1 mTorr. During the Fourier transformations, a zero-filling factor of 2, Mertz-phase correction, phase resolution of 1.000 and Boxcar apodization (unapodized) were used. Similarly, four sample spectra were created for 0.0020, 0.0050, 0.051 and 1 Torr and for their corresponding backgrounds. Finally, the sample spectra were divided by their corresponding background spectra to create the transmission spectra. An example of sample ammonia spectra (green) is given in Figure 3.6. The transmission spectra show a region of 70 – 360 cm^{-1} . They are not saturated and can be used for the assignment study.

3.5 Experimental Setup (Pure O₂)

Gas Cell: A set of pure oxygen spectra were recorded using the FTS system located at the Justus-Liebig-University in Giessen, Germany. A detailed description of this experimental setup is reported in the literature by Predoi-Cross et al. [44, 70]. A brief description of this experimental setup are given in this section.

The main components of this setup include an IFS 120 HR FTS system, which accommodates a Halogen lamp as a source, a White-type multipass gas cell, and a Si-diode detector. The White-type multi-pass cell was made of quartz (Infrared Analysis Inc., model NO. 4-32). It contains a coated mirror to optimize the mirror-mirror reflection for the multi-pass purpose. The coating was made in two layers. Firstly, a silver coating and then a SiO₂-overcoat was applied to the mirror. An average value of the cell-base length was determined as 812.8 mm before and 812.6 mm after the measurements [44]. These optical pathlengths were measured from the mirror to mirror distance of the cell. The mirrors were adjusted to obtain two different optical-pathlengths of 3.370 m and 16.375 m for recording spectra. The accuracy of the pathlength measurement is reported as 0.2 % [44].

The gas cell was filled with 99.998 % pure oxygen gas to record oxygen A-band spectra in the 13010 - 13170 cm⁻¹ region. A 20-layered optical filter was selected to limit the incident light range to between 12280 and 14042 cm⁻¹. A total of 17 room-temperature spectra at 0.0222 cm⁻¹ resolution were selected for the analysis.

Temperature and Pressure: Pressure and temperature conditions for all 17 spectra are listed in Table 5.1 (Chapter 5). Room-temperature pure-oxygen spectra of pressure ranges between 8.90 and 30011.00 Torr (0.011 to 4.011 bar) were used for this study. The

temperature for each spectrum was determined by taking an average of the temperature measured before and after recording each spectrum. The room temperatures were measured using a mercury thermometer. For this purpose, it was assumed that the cell wall including the sample gas inside the cell was in thermal equilibrium with the laboratory environment. All spectra were recorded at temperatures between 293.65 and 297.95 K. Average temperatures of the spectra recorded before and after each experiment were corrected by 0.2 K, because of lower-night temperatures [44, 70]. The laboratory temperature fluctuated by 0.3 K maximum during the daytime.

Two pressure gauges were used in order to measure the gas cell pressure: 1) a Pfeiffer CMR 261 gauge and 2) an MKS Type 722A gauge. The former was used while spectra were recorded at pressures lower than 1275.1 Torr (1.7 bars) with an accuracy of 0.2 %. The MKS gauge was used for recording the other pressures, but with a lower accuracy of 0.5 %. A correction factor of 0.9993 [44] was used to multiply the average pressure due to the lower temperature at night time and corresponding lower pressures. The slight fluctuations in the pressure reading were also due to low temperatures during the night time.

Calibration: A self-calibration of the high-pressure spectra was performed using the low-pressure spectra. The low-pressure spectra are typically used for wavenumber calibration as their absorption-line positions do not shift as much as the high-pressure ones. Oxygen A-band line positions reported by Drouin et al. [74] (available latest study) were considered the standard for calibrating the spectra. Spectra were recorded in groups, where each group includes low-pressure spectra, which were used for calibration of the high-pressure spectra of that group. The calculation of the calibration factors was performed by

taking the ratio between fitted line positions from low-pressure spectra and positions published by Drouin et al. [74]. These calibration factors were then applied to each of the high-pressure spectra. Experimental conditions of the spectra and calibration factors are discussed in Section 5.1.

3.5.1 Labfit Program and Analysis

In the spectroscopic analysis, different methods are being used for the retrieval of line-shape parameters, and among them, the multispectrum fit technique is very popular. A multispectrum fitting routine based on the non-linear least square fitting algorithm, which is called the Levenberg-Marquardt algorithm [130, 131], has been gradually developed by Benner et al. [132]. An earlier version of this software is described in [133]. This software package is called Labfit. Later, it was updated to include line-mixing effects, speed dependence of broadening, and temperature-dependence effects for broadening and shift coefficients. The line-mixing implementation can be applied for any gas pressure conditions though it is important for the high-pressure spectra. The software developer, D. C. Benner, has described the implementation of the line-mixing effect in the literature [132].

One of the advantages of using Labfit is that more than one spectrum recorded at different conditions, such as various temperatures, pressures, and resolutions, can be fitted simultaneously. It also allows the simultaneous fitting of FTS and TDLS spectra. This multispectrum-fit technique reduces the random error by considering the simultaneous fit of a large number of spectra. The fitting method of this program minimizes the difference between the recorded spectra and the calculated (modeled) spectra through an iterative process (reduces summation of the square of their residuals). This software comes with the

flexibility of fitting or fixing parameters of interest. It can also take systematic errors of the line-shape into account. Labfit calculates the absolute errors of the retrieved parameters, which occur due to errors in the experimental conditions, such as pressure, temperature, pathlength, and fitting model deficiencies. In this thesis, the uncertainties of the retrieved parameters are presented in the parenthesis next to the value corresponding to one standard deviation (1σ) referring to the last significant digits.

Like Wproffit2.exe, Labfit also needs an input file, which contains the spectral range, temperatures and pressure conditions of the spectra, gas mixing ratio, initial guesses of line position, intensity, broadening, narrowing, shift, speed dependency, line-mixing parameter, the temperature dependency of broadening and shift, etc. Labfit fits a group of lines repeatedly by recalculating the spectra to the given number of iterations. It improves the fit after each iteration by taking small changes in the fitted parameters into account. If a spectrum contains a large number of sampling points, Labfit then performs a weighted multi-spectrum fit technique.

3.6 Conclusions

All the explanations presented in this chapter were an attempt to walk the readers through the experimental backgrounds and the type of spectra that were used for spectroscopic analysis. The TDLS system recorded each absorption lines of $\text{C}_2\text{H}_2\text{-N}_2$ separately, which is important for studying different line-shape functions. By using the FTS systems, it was possible to record the spectra of the O_2 A-band at 17 pressures and very high-resolution spectra of $^{15}\text{NH}_3$. The high-resolution (0.00096 cm^{-1}) spectra of $^{15}\text{NH}_3$ is needed to improve the assignment of the GS transitions.

Chapter 4 Line-shape Study of C₂H₂-N₂

4.1 Overview

Acetylene is, for example, present as a trace constituent in the atmosphere of Saturn and around it in Titan (moon of Saturn) [23]. It is currently being used to study the environment of these extraterrestrial bodies. It is important to consider the atmospheric pressure of different layers when modeling atmospheric spectra due to the variation of the pressure in planetary atmospheres. Therefore, understanding the pressure dependence of acetylene absorption line-shapes will help researchers in better interpretation of spectra from Saturn, Titan, and other extraterrestrial objects. None of the available line-shape profiles are suitable for all pressure regimes. It is important to understand and determine, which profile is suitable for the various regimes. This chapter focuses on the characterization of line-shape profiles using acetylene absorption lines. This study will deliver spectroscopic parameters of acetylene molecules retrieved using eight different line-shape profiles. For this work, six vibrational absorption lines of acetylene spectra recorded at various pressures were studied. Sections 4.2 and 4.3 discuss the vibrational modes of the acetylene molecule and present the analysis of the acetylene spectra recorded at various pressure, respectively. A summary of the results is then presented in Section 4.4.

4.1.1 My Contribution to this Project

This chapter presents my first project soon after having been admitted into the PhD program in January 2013, and it was carried out in collaboration with other group members (Robab Hashemi and Chad Povey) of the Spectroscopic Research Group in the Department of Physics and Astronomy at the University of Lethbridge led by Dr. Adriana Predoi-Cross.

The paper from this work was submitted for publication to the Journal of Quantitative Spectroscopy and Radiative Transfer in October 2013 and accepted in revised form in February 2014 [20].

This project was focused on analyzing six absorption lines of $C_2H_2-N_2$ room-temperature spectra recorded in the $\nu_1+\nu_3$ band region at seven different pressures (5, 10, 20, 30, 40, 100, and 250 Torr). Low-pressure (5, 10, 20, 30, and 40 Torr) spectra used in this study were recorded and processed by Chad Povey, a former PhD student of the University of Leathbridge spectroscopic research group. Spectra obtained at 100 Torr were initially recorded during my MSc. Program and also presented in the thesis published in 2012 [125]. The remaining spectra of pressure 250 Torr were recorded later in 2013 together with Robab Hashemi. After recording the 250 Torr spectra, they were sorted into two sets, the P and R branches. The P-branch lines (P(16), P(19) and P(21)) were processed and analyzed by myself, while Robab Hashemi processed and analyzed the R-branch lines (R(16), R(19) and R(21)). Data recording and processing were performed using LabVIEW. Detailed explanations of the data processing are provided in Section 3.2.7. The data analyses (line fitting and retrieval of line parameters) were completed using the profit2.exe software program described in Section 3.2.8. Transmission spectra were merged together to create final input files for the data analysis of each line. After creating the input files for the P-branch lines, retrieval of the parameters (broadening coefficients, shift coefficients, and narrowing coefficients) was performed by myself. The parameters for the R-branch lines were retrieved by Robab Hashemi. This project was dedicated to study the pressure dependency of the absorption line-shape and present the retrieved line parameters.

My M.Sc. project was focused on analyzing 47 absorption lines of $\text{C}_2\text{H}_2\text{-N}_2$ spectra recorded in the $\nu_1+\nu_3$ band region and at seven different temperatures between 213 K and 333 K. Spectra of different temperatures were used to study the temperature dependency of the broadening and shift coefficients. The line parameters (broadening and shift coefficients) were retrieved using the Voigt and Rautian profiles only. My thesis did not present any narrowing parameters, because the spectra were recorded above the Dicke narrowing pressure regime.

4.2 Introduction

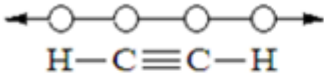
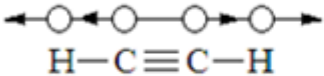
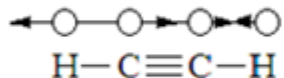
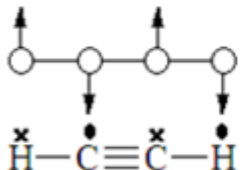
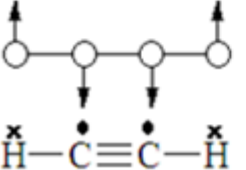
Pressure-dependent studies require spectra of various pressures. Spectra recorded below 100 Torr are needed to investigate the collisional narrowing, and above 100 Torr to investigate the speed-dependence effects [102]. Therefore, the nitrogen-broadened acetylene spectra (roughly 10 % C_2H_2 and 90 % N_2) of 5, 10, 20, 30, 40, 100, and 250 Torr were analyzed to perform this study using the eight profiles, VP, RP, GP, CR, RGP, SDV, SDR, and CSDR (correlated Speed-Dependent Rautian). No other studies have performed spectral analysis using so many profiles as carried out in this project [20].

4.2.1 Acetylene Molecule

Acetylene is a linear polyatomic molecule of four atoms. Accordingly, acetylene has $3N - 5 = 3(4) - 5 = 7$ vibrational modes. Table 4.1 shows three stretching (ν_1, ν_2, ν_3) and four bending (ν_4, ν_5) vibrational modes of acetylene [8]. The fundamental symmetric CH-stretching ν_1 occurs at 3374 cm^{-1} , the symmetric CC-stretching ν_2 occurs at 1974 cm^{-1} , and the anti-symmetric CH-stretching ν_3 occurs at 3287 cm^{-1} . Both the symmetric bending mode ν_4 that occurs at 612 cm^{-1} and the anti-symmetric bending mode ν_5 that occurs at 729 cm^{-1}

are doubly degenerate. The ν_3 and ν_5 modes are infrared active. The dots shown for the ν_4 and ν_5 modes represent the vibration of the atom out of the plane of the paper, and the crosses indicate vibration into the plane of the paper. The average bond length of C-H is 120 pm, and the average C-C bond length is 106 pm [8].

Table 4.1: Fundamental vibrational modes of the acetylene molecule (modification of Figure 6.20 in [8]).

Vibrational Modes	Comments
 $\text{H}-\text{C}\equiv\text{C}-\text{H}$	Symmetric C-H stretching mode, ν_1 (3374 cm^{-1}), infrared inactive
 $\text{H}-\text{C}\equiv\text{C}-\text{H}$	Symmetric $\text{C}\equiv\text{C}$ stretching mode, ν_2 (1974 cm^{-1}), infrared inactive
 $\text{H}-\text{C}\equiv\text{C}-\text{H}$	Anti-symmetric C-H stretching mode, ν_3 (3287 cm^{-1}), infrared active
 $\text{H}-\text{C}\equiv\text{C}-\text{H}$	Symmetric (<i>trans</i>) bending mode, ν_4 (612 cm^{-1}), infrared inactive
 $\text{H}-\text{C}\equiv\text{C}-\text{H}$	Anti-symmetric (<i>cis</i>) bending mode, ν_5 (729 cm^{-1}), infrared active

4.2.2 Band Structure ($\nu_1+\nu_3$)

For this study, the line-shape profiles were tested on six absorption lines of acetylene recorded in the $\nu_1 + \nu_3$ band region. Figure 4.1 shows a simulation of the acetylene spectrum in the $\nu_1 + \nu_3$ band, which appears between the 6475 and 6625 (cm^{-1}) wavenumbers. Strong absorption bands like $\nu_1 + \nu_3$ are suitable for line-shape studies. This

spectrum shows a total of 75 absorption lines of the acetylene molecule in the $\nu_1 + \nu_3$ band, where 37 lines are in the P-branch ($6452\text{-}6555\text{ cm}^{-1}$) region and 38 lines are in the R-branch ($6555\text{-}6630\text{ cm}^{-1}$) region.

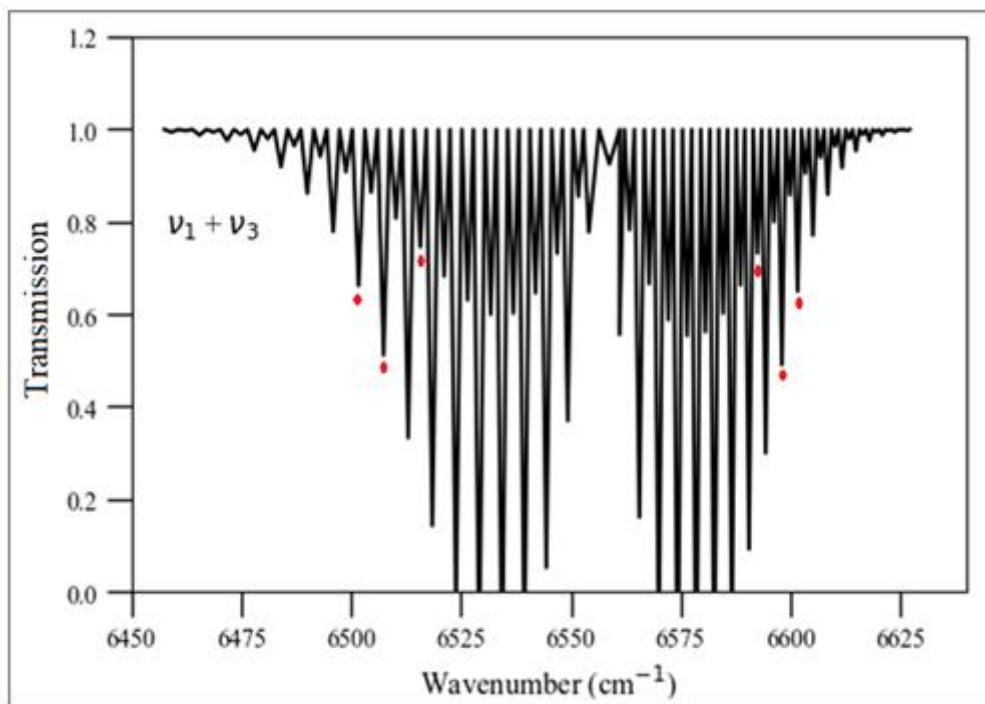


Figure 4.1: A simulated vibrational spectrum for acetylene at 300-Torr room-temperature was generated using the data taken from the HITRAN website [134]. The selected six absorption lines are pointed with red dots (P-branch ($6452\text{ - }6555\text{ cm}^{-1}$) and R-branch ($6555\text{ - }6630\text{ cm}^{-1}$) regions).

The six absorption lines selected P(21), P(19), P(16), R(16), R(19) and R(21) are located approximately at 6501.7046 , 6507.3981 , 6515.7514 , 6592.5029 , 6598.0774 and 6601.6617 cm^{-1} , respectively. These lines were recorded at different pressures as listed in Table 4.2 using the spectrometer system located in the spectroscopic research laboratory at the Department of Physics and Astronomy, University of Lethbridge (Section 3.2). This spectrometer system uses a Tunable-Diode Laser, which covers the $6369\text{ - }6666\text{ cm}^{-1}$ frequency range.

4.3 Spectroscopic Analysis of the Acetylene Molecule

A LabVIEW program was used for the data collection and processing as discussed in Section 3.2.7. The analysis was completed with the non-linear multispectrum fitting program, Wproffit2 [126]. The supplied gas mixture of $C_2H_2-N_2$ molecules was delivered from Praxair with a quoted concentration of 9.94 % of C_2H_2 . At first, the gas concentration was tested by fitting the ($C_2H_2-N_2$) spectra in Wproffit2. The isolated R(16) line is selected to report the results from the test of the gas concentration. The effect of gas pressures on the absorption line-shape will also be demonstrated using the R(16) line in this chapter. A list of pressures and temperatures that all the spectra were recorded are given in Table 4.2 for R(16) line as an example. The concentration values corresponding to each pressure of the R(16) line show that they are within 0.67 % on an average of the quoted value.

For analyzing the spectra listed in Table 4.2, the VP, RP, GP, CR, RGP, SDV, SDR, and CSDR profiles have been implemented in Wproffit2.exe. These profiles are described in Section 2.4. Spectra recorded at a given temperature but at different pressures can be fitted simultaneously using these profiles in Wproffit2.exe. The fitted spectra are displayed in Section 4.3.1, and the results are given in Section 4.4.

In a very low-pressure regime, broadening is dominated by the Doppler shape. Due to increasing molecular collisions at higher pressure, the active molecule experiences a change in their trajectories, which reduces their mean thermal velocity. This effect affects the broadening of the absorption line and leads to a narrower width. However, with the pressure increase, this influence gets smaller because the line width is dominated by collisional broadening [102]. Thus, the profiles including speed-dependent effects are suggested to be used to retrieve the broadening and shift parameters of high-pressure

spectra [114]. All the spectra listed in Table 4.2 are categorized into two sets, which will be referred to as the low and the high-pressure spectra. Spectra of 5 to 40 Torr will be considered as low-pressure and 100 to 250 Torr as high-pressure spectra.

Table 4.2: Example of the gas concentration test, retrieved using the R(16) line. Pressures were recorded in Torr. The errors are given in the parenthesis (corresponding to one standard deviation referring to the last significant digits).

Temperature (K)	Pressure (Torr)	Retrieved Concentration of C ₂ H ₂	Temperature (K)	Pressure (Torr)	Retrieved Concentration of C ₂ H ₂
295.767(6)	5.56	10.00(3)	295.886(9)	40.37	10.00(2)
	5.56	10.01(3)		40.37	9.96(2)
	5.56	9.95(3)		40.37	9.95(2)
	5.56	9.93(3)		40.37	9.95(2)
295.859(9)	10.53	9.95(2)	295.788(8)	102.58	10.01(1)
	10.53	9.85(2)		100.58	10.03(1)
	10.53	9.85(2)			
295.828(6)	19.86	10.02(2)	295.803(9)		
	19.86	9.94(2)			
	19.86	10.01(2)			
	19.87	10.05(2)			
295.795(6)	30.02	10.01(2)		249.40	9.81(1)
	30.02	9.95(2)		249.40	9.96(1)
	30.02	9.93(2)		249.41	9.97(1)
	30.02	9.94(2)		249.41	9.94(1)

4.3.1 Line Fitting Using Different Line-Shape Models

Each line profile is applicable to spectra obtained under certain conditions such as low or high-pressure environments as discussed in Section 2.4. For demonstration purposes, the R(16) line was selected [20]. Figures A.1, A.2, A.3 and A.4 in the Appendix A present the room-temperature spectrum of the R(16) line and different effects on its line-shape that occurred at various pressures. The VP, RP, GP, CR, RG, SDV, SDR, and CSDR profiles were used for fitting the lines. Firstly, a low-pressure spectrum recorded at 40 Torr

is used for demonstrating the differences in residuals after fitting the VP and non-VP profiles. The top panel of Figure (A) shows a room temperature spectrum of the R(16) line [20] obtained at a pressure of 40 Torr in blue and the best fit obtained using the VP in red. The bottom panel shows the residuals from the fit multiplied by 100. Fitting this spectrum with a VP results in a residual spectrum that shows a “w” shape, which is an indication that this spectrum was recorded in the Dicke narrowing regime.

In Figure (B), the top panel shows the same R(16) line recorded at 40 Torr (blue) and the best fit obtained using the Rautian profile (RP; red). The bottom panel presents the residuals from the fit multiplied by 100. Fitting this spectrum with the RP reduces the “w” shape by taking the narrowing effect into account and, therefore, minimizes the residuals.

The top panel in Figure (C) shows absorption spectra for the R(16) line obtained at 5 (red), 10 (black), 20 (blue), 30 (green) and 40 (purple) Torr. All the spectra were recorded at room temperature. The bottom seven panels in Figure (C) presents the residuals (observed – calculated) from fitting the spectra in the top panel using the VP, RP, GP, CR, RG, SDV, and SDR profiles. A list of RMS values from these fits are given in Table 4.3

Table 4.3: List of RMS (root mean square) values of residuals from the fits in Figure A.3 in Appendix A for the spectra of 5, 10, 20, 30, and 40 Torr.

Profiles	Voigt (VP)	Rautian (RP)	Galatry (GP)	Rautian- Galatry (RGP)	Correlated Rautian (CRP)	Speed- dependent Voigt (SDV)	Speed- dependent Rautian (SDR)
RMS	0.0016	0.0012	0.0013	0.0012	0.0022	0.0014	0.0013

Fitting all these spectra with the VP results in larger residuals with a well pronounced “w” shape. It is shown in Figure (A) that this is because the Voigt profile does

not take into account the Dicke narrowing effect. The residuals are smaller for the RP, GP, and RGP profiles, because all three profiles take into account the narrowing effect. The residuals from the CRP fit are higher for the 20, 30, and 40 Torr spectra. Therefore, this profile should be avoided to fit spectra of 20 Torr and above. Among the SDV and SDR residuals, the latter is smaller and also minimizes the “w” shape by taking the narrowing into account. However, both these two profiles take longer to fit which is 20 times more than the other profiles discussed.

From the RMS values of their residuals, it is visible that the RP, GP, and RGP result in an improved fit (20 – 22 % lower RMS) compared to the VP. The RMS errors from the fits of RP (0.0012), GP (0.0013), and RGP (0.0012) are very similar to each other (within 2 %), which are much better (41 – 43 %) residuals compared to the CRP (0.0022). For $\text{C}_2\text{H}_2\text{-N}_2$, the absorber and the perturber have a mass ratio of 0.93, which explains why the RP (absorber mass < perturber mass) works better than the GP in this case (discussed in Section 2.4.9). The RGP was also used if the absorber and the perturber were involved in either the “soft” or “hard” collisions as their mass ratio is 0.93. Molecules in this sample seem to be involved in hard collisions as the RGP results match better (Section 4.4) those retrieved using RP than with the GP results. The fitted residuals using SDV and SDR profiles results in RMS values of 0.0014 and 0.0013, respectively.

Spectra of pressure of ~100 Torr and above cannot be fitted adequately using the VP [102], because the broadening and shift-line parameters depend on the collisional speed of the molecules. VP does not account for the asymmetric effects that are present in the spectra and does not consider the speed-dependent effect in the retrieval of broadening and the shift coefficients (Section 2.4.6) [102]. Therefore, spectra of the entire pressure regime

(5 - 250 Torr) were fitted using the profiles that take the speed-dependent effect into account, such as the SDV, SDR, and CSDR profiles. This is due to the fact that the speed-dependent effect occurs in all pressure regimes; high-pressure spectra are more affected. A previous study has also shown that the broadening coefficients are larger when retrieved using the SDV than the VP [6]. The coefficient values differ slightly from profile to profile, because they take different effects on the line-shape into account when fitting the spectra to retrieve parameters, which depend on the speed of the molecules.

Table 4.4: List of RMS (root mean square) values of residuals from the fits in Figure 4.4 for the spectra of 5, 10, 20, 30, 40, 100, and 250 Torr.

Profiles	VP	SDV	SDR	CSDR
RMS	0.0032	0.0030	0.0029	0.0029

The top panel in Figure (D) shows absorption spectra for the R(16) line obtained at 5 (purple), 10 (blue), 20 (pink), 30 (green), 40 (yellow), 100 (orange), and 250 (red) Torr. The residuals of VP, SDV, SDR, and CSDR profiles are plotted in the lower panels, and the RMS values are given in Table 4.4. RMS values from the residuals are 0.0032 for the VP, 0.0030 for the SDV, 0.0029 for the SDR, and 0.0029 for the CSDR. In addition, the residuals at the absorption peak position of 20 and 30 Torr spectra are large so that they go out of the frame when fitting spectra of the wide pressure range (5-250 Torr) using the VP; however, they are minimized for the SDV, SDR, and CSDR fits. These fits are improved by 6 % for the SDV profile and 8 % for the SDR and the CSDR profiles. The broadening and the shift coefficients from these fits are presented in Section 4.4 along with the results of P(21), P(19), P(16), R(19), and R(21) lines.

4.4 Retrieved Line Parameters

Wproffit2.exe requires an input file containing information of the experimental conditions at which the spectra were recorded (spectral range, concentration of the active molecule, mass ratio of active and perturber, etc.), experimental conditions (temperatures, pressures, etc.), and initial guesses of the parameters (position, intensities, broadening, narrowing, and shift coefficients) taken from HITRAN [135]. It is already mentioned earlier that Wproffit2.exe uses a multi-spectrum non-linear least square fitting technique. It allows fitting spectra of different pressures altogether. The line-shape parameters were retrieved after running input files through this program using the profiles of interest (VP, RP, GP, CR, RGP, SDV, SDR, and CSDR) [136]. Unlike Labfit, Wproffit2.exe does not fit spectra of different temperature. In addition, it does not have the capacity of fitting the temperature-dependence coefficients.

Broadening: Broadening values for the six absorption lines, P(21), P(19), P(16), R(16), R(19) and R(21) in the $\nu_1 + \nu_3$ band of $C_2H_2-N_2$ spectra are listed in Table 4.5. The first four rows present the broadening coefficients retrieved using the RP, GP, CR, and RGP profiles from spectra of the low-pressure regime (up to 40 Torr). The next four rows present the broadening coefficients from spectra of the entire pressure regime (5 - 250 Torr) using the VP, SDV, SDR, and CSDR profiles. The uncertainties given in parenthesis are one standard deviation referring to the last significant digits. The VP fit spectra of all pressures without considering any narrowing or speed-dependent effects. In general, the broadening is expected to be smaller for RP than VP as the former takes the narrowing of the absorption lines into account [102]. In the present study, the retrieved RP broadenings are smaller than the VP except for the P(21) line. The broadening coefficients retrieved

from low-pressure spectra using the RP and GP are within 2.5 %, while the RP and RGP are within 1.2 % with each other. For heavier perturbers, the broadening is expected to be much smaller for the VP than SDV profile. In the present study, the broadening coefficients show no considerable differences with discrepancies between 0.4 % and 2.1 % as the absorber (C_2H_2) and perturber (N_2) have similar mass. The effect of perturber of different masses on the broadening parameter are different.

Table 4.5: Broadening coefficients ($cm^{-1}atm^{-1}$) for six transitions in the $\nu_1 + \nu_3$ band of acetylene retrieved from the room-temperature $C_2H_2-N_2$ spectra. The uncertainties in parenthesis are given as one standard deviation referring to the last significant digits. The Rautian Profile (RP), Galatry Profile (GP), Rautian-Galatry Profile (RGP), Correlated Rautian Profile (CRP), Speed-Dependent Voigt (SDV), Speed-Dependent Rautian (SDR), Correlated Speed-Dependent Rautian (CSDR) and Voigt Profile (VP) broadening are listed (modification of Table 2 in [20]).

Line profiles	Pressure	Line names					
		P(21)	P(19)	P(16)	R(16)	R(19)	R(21)
RP	Up to 40 Torr	0.0704(2)	0.0755(4)	0.0781(1)	0.0742(2)	0.0744(2)	0.0673(2)
GP		0.0707(2)	0.0764(3)	0.0793(1)	0.0754(2)	0.0751(2)	0.0690(2)
RGP		0.0710(2)	0.0764(3)	0.0789(1)	0.0748(2)	0.0749(2)	0.0678(2)
CR		0.0705(2)	-	0.0782(2)	0.0747(2)	0.0744(2)	0.0693(1)
SDV	Up to 250 Torr	0.0709(4)	0.0765(3)	0.0798(3)	0.0748(4)	0.0750(2)	0.0721(5)
SDR		0.0701(4)	0.0757(3)	0.0795(2)	0.0744(5)	0.0742(2)	0.0714(5)
CSDR		0.0702(4)	0.0756(3)	0.0795(2)	0.0748(4)	0.0738(2)	0.0715(5)
VP		0.0694(4)	0.0768(4)	0.0783(3)	0.0751(5)	0.0754(2)	0.0724(4)

Also, a previous study on the $\nu_1 + \nu_2 + \nu_4 + \nu_5$ band on self-broadened C_2H_2 by Povey et al. [36] have observed that the VP and SDV broadening coefficients are within 2.3 %, which is almost the same as the in the present study. The broadening values retrieved using the speed-dependent profiles (SDV, SDR, and cSDR) are in pretty good agreement with each other, with discrepancies between 0.3 % and 1.2 %. A comparison of these broadening

coefficients from the present study using VP, RP, SDV, and SDR profiles are presented in Figure 4.2. According to Table 4.5, the broadening coefficients retrieved using RP, GP, RGP, CRP, SDV, SDR, and CSDR profiles are within 2.3 % compared to the VP (except for R(21) with up to 7 %).

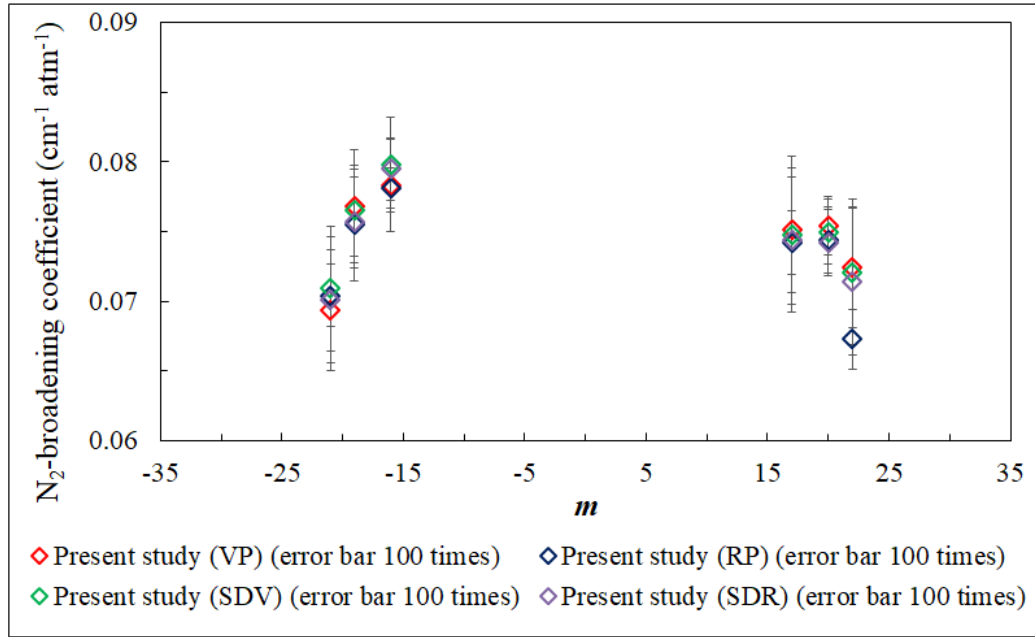


Figure 4.2: Broadening coefficients for six transitions in the $\nu_1+\nu_3$ band of $C_2H_2-N_2$ retrieved using the Voigt (VP), Rautian (RP), Galatry (GP), and Speed-Dependent Voigt (SDV) profiles.

Figure 4.3 shows a comparison of the broadening coefficients between the present study and studies available from the literature. The plot presents broadening results against the m index. For the P -branch transitions, $m = -J''$ (i.e., $m < 0$) and for the R -branch transitions, $m = J'' + 1$ (i.e., $m > 0$), where J'' is the rotational quantum number of the lower

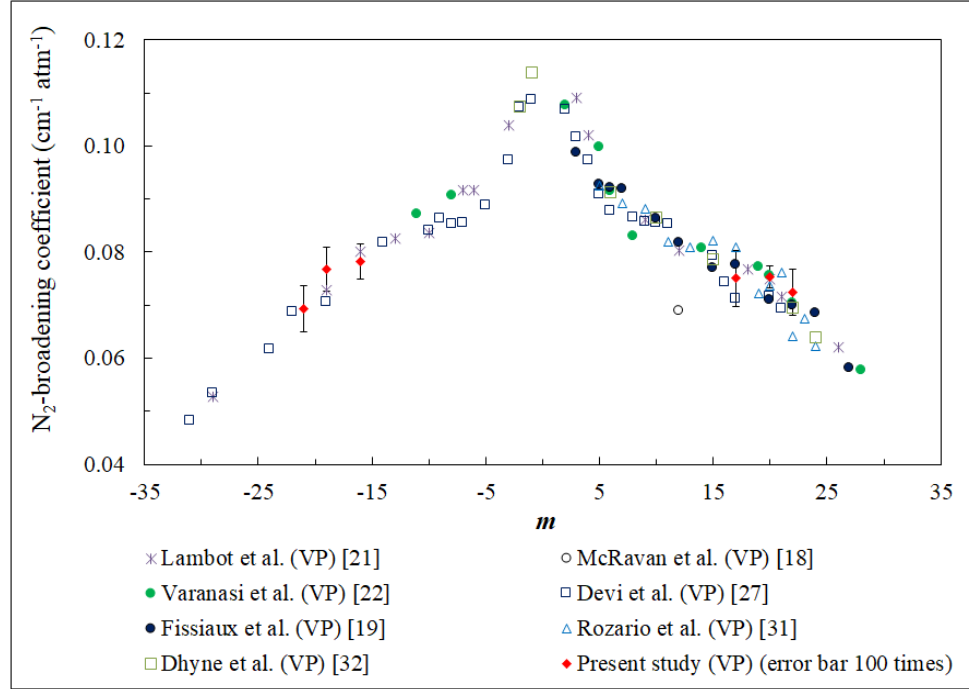


Figure 4.3: Broadening coefficients for transitions in the $\nu_1+\nu_3$ band of acetylene retrieved using the VP profile and compared with previously published values from the literature (self-generated modified version of Figure 5 in [20]).

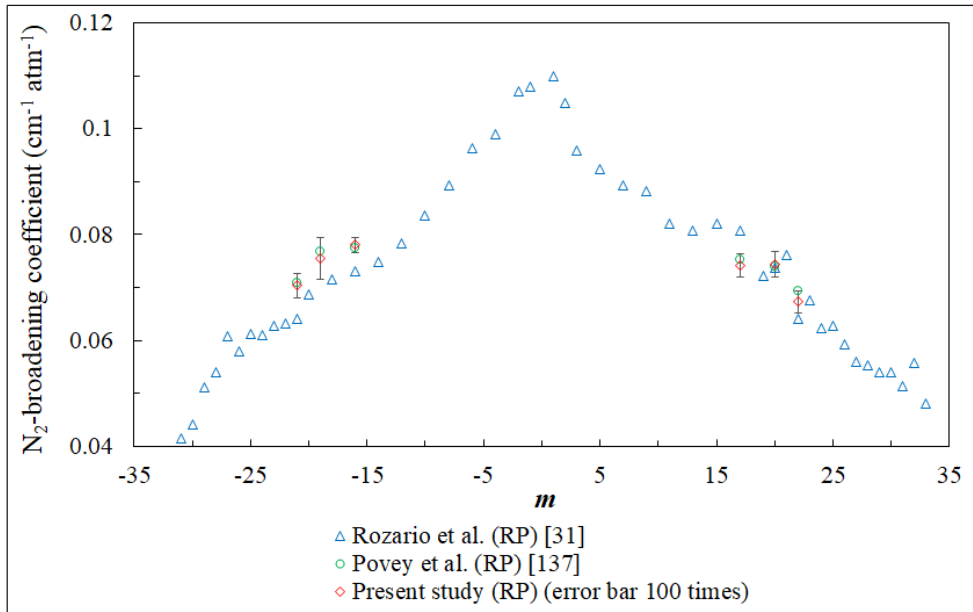


Figure 4.4: Broadening coefficients for transitions in the $\nu_1+\nu_3$ band of acetylene retrieved using the RP profile and compared with previous values from the literature.

energy state of corresponding transitions. As expected, the plot exhibits that broadening coefficients are J'' dependent. The broadening values are high at lower J'' and tend to decrease as the J'' increases in both P - and R -branches (i.e., broadening decreases with the absolute value of the increasing m index) as expected, because broadening of absorption lines in a spectral band is not independent. A theoretical calculation of the N_2 -broadening parameter of the acetylene molecule has been performed in a previous study [31], which shows the same trend of broadening with J dependency.

Broadening coefficients were compared with the coefficients from studies by Lambot et al [21], Dhyne et al. [32], Fissiaux et al. [19], Rozario et al. [31], Varanasi et al. [22], Devi et al. [27], and Povey et al. [137]. As most of the studies from the literature have results obtained using VP (Figure 4.3) and RP (Figure 4.4), the comparison is concentrated on these profiles. There are differences as well as agreements in the results from the present study and those from the literature. For example, in Figure 4.4 the present RP results agree better with those achieved by Povey et al. (within 2.8 %) than those presented by Rozario et al. (within 10.0 %), because the former study used low-pressure spectra, which fall in the Dicke narrowing regime. The latter one used high-pressure spectra (above 100 Torr), which cannot be fitted properly with the RP profile. Therefore, by performing this study, according to the RMS values from the R(16) fit results, it is established that the spectra of 5 - 40 Torr fit better (1 – 75 % lower RMS) using the Rautian profile than other profiles (VP, GP, and CRP). Despite no other studies were available to compare the SDV and SDR broadening at that moment when this study was performed, it is also worthwhile to report the parameters retrieved using these profiles.

Narrowing: Narrowing coefficients retrieved from low-pressure (5 - 40 Torr) spectra are listed in Table 4.6. Results are compared with the results from the literature (Povey et al. [6, 137] and McRaven et al [18]) and shown in Figure 4.5. The results are plotted against the lower J'' number (1m1). The calculated narrowing parameter $\beta_{diff} = 0.0191 \text{ cm}^{-1}\text{atm}^{-1}$ [20] is also plotted in Figure 4.5. In this narrowing pressure regime, the RP and RGP fit spectra slightly better than the GP as the RMS values for the RP (1.6 %) and RGP (0.8 %) profiles are smaller than the GP (Table (A) in Appndix A). Theoretically, to retrieve the $\text{C}_2\text{H}_2\text{-N}_2$ narrowing using GP is not the proper way due to the absorber and perturber mass ratio. However, fitting of spectra using the RGP turned out as good as the RP, because C_2H_2 is slightly lighter than N_2 . The narrowing coefficients from the present study are also pretty similar to the values published by Povey et al. [137] for P(21), P(16), R(16), and R(19) for those that were retrieved using RP; they show similar patterns (Figure 4.5). The narrowing retrieved using the RP are smaller than the GP, which is shown in the study by McRaven et al [18] as well.

Table 4.6: Narrowing coefficients ($\text{cm}^{-1}\text{atm}^{-1}$) for six transitions in the $\nu_1 + \nu_3$ band of acetylene retrieved from the room-temperature $\text{C}_2\text{H}_2\text{-N}_2$ spectra. The uncertainties in parenthesis are given as one standard deviation referring to the last significant digits. The Rautian Profile (RP), Galatry Profile (GP), Rautian-Galatry Profile (RGP), and Correlated Rautian Profile (CRP) narrowing are listed (modification of Table 3 in [20]).

Line profiles	Pressure	Line names					
		P(21)	P(19)	P(16)	R(16)	R(19)	R(21)
RP	Up to 40 Torr	0.0182(6)	0.0205(14)	0.0214(6)	0.0142(7)	0.0171(9)	0.0163(7)
GP		0.0236(8)	0.0253(16)	0.0294(7)	0.0246(10)	0.0209(11)	0.0222(9)
RGP		0.0226(7)	0.0284(16)	0.0216(6)	0.0181(9)	0.0199(10)	0.0200(9)
CRP		0.0187(8)		0.0274(7)	0.0148(8)	0.0173(9)	0.0187(0)

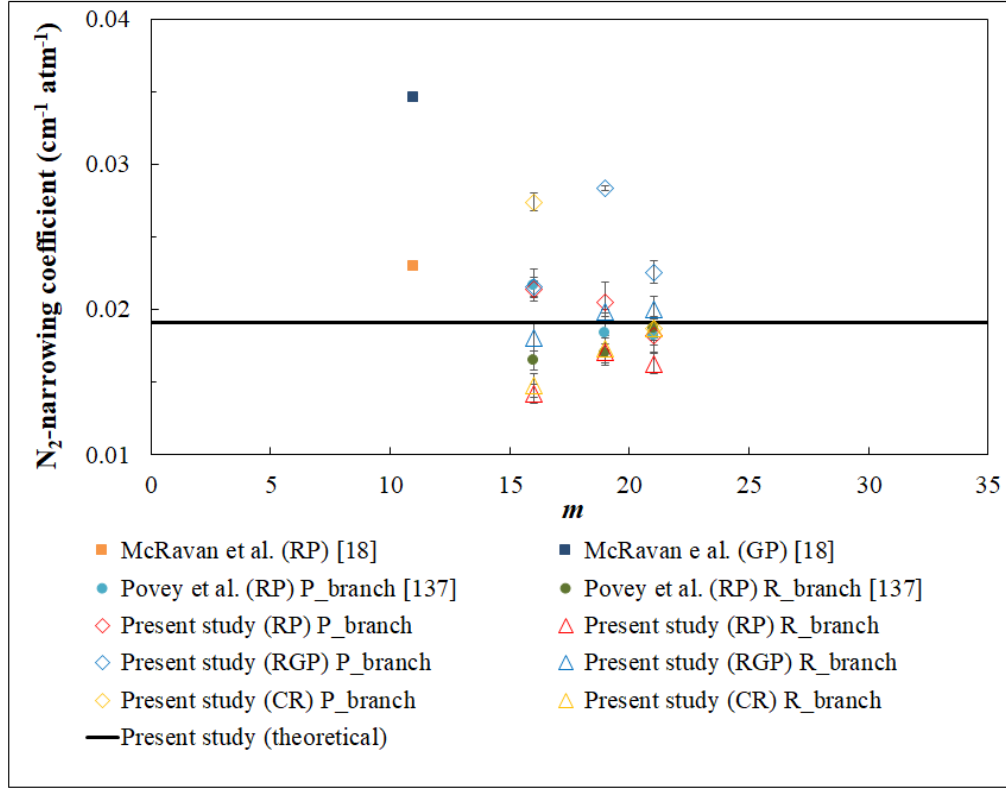


Figure 4.5: Narrowing coefficients retrieved for six transitions in the $\nu_1+\nu_3$ band of C_2H_2 - N_2 spectra and compared with previously published values from the literature. The black line represents the calculated narrowing (self-generated modified version of Figure 6 in [20]).

Shift: This study also presents the results of pressure-induced shift coefficients for the six transitions in the $\nu_1+\nu_3$ band of acetylene. Table 4.7 lists the shift coefficients retrieved from the RP, GP, RGP, CRP, SDV, SDR, CSDR, and VP. Figure 4.6 shows a comparison of the shift coefficients. Results retrieved with the RP, GP, RGP, and CRP are from spectra of low pressures (5 - 40 Torr) while the VP, SDV, SDR, and CSDR from the spectra of the entire pressure regime (5 - 250 Torr). All the results are in negative values to the order of $10^{-3} \text{ cm}^{-1}\text{atm}^{-1}$ as expected.

The shift coefficients are plotted in Figure 4.6 against the m index to represent both P- ($m = -J''$) and R- ($m = J''+1$) branches. The comparison of the coefficients in Figure 4.6 with results from the literature, Artega et al. [23] and Rozario et al. [31], show the same

trend. Like a previous study on the $\nu_1 + \nu_2 + \nu_4 + \nu_5$ band of C_2H_2 by Povey et al. [138], this present study also shows that the absolute value of the shift coefficients retrieved using RP and RGP are smaller (up to 24 %) than those retrieved using the VP and SDV profiles (except for P21 and P19). This is due to the fact that this parameter is a linear function of the buffer gas pressure, and RP and RGP used only the low-pressure spectra. The absolute values of the VP results are smaller (12 % - 15 %) than those retrieved with the SDV profile for the P-branch lines, which was also demonstrated in the literature [36] for acetylene lines. This study is the first one to report the shift coefficients of C_2H_2 - N_2 spectra using eight different profiles.

Table 4.7: Shift coefficients ($cm^{-1}atm^{-1}$) for six transitions in the $\nu_1 + \nu_3$ band of acetylene retrieved from the room-temperature C_2H_2 - N_2 spectra. The uncertainties in parenthesis are given as one standard deviation referring to the last significant digits. The Rautian Profile (RP), Galatry Profile (GP), Rautian-Galatry Profile (RGP), Correlated Rautian Profile (CRP), Speed-dependent Voigt (SDV), Speed-dependent Rautian (SDR), correlated Speed-dependent Rautian (CSDR) and Voigt Profile (VP) shift coefficients are listed (modification of Table 4 in [20]).

Line profiles	Pressure	Line names					
		P(21)	P(19)	P(16)	R(16)	R(19)	R(21)
RP	Up to 40 Torr	-0.0089(1)	-0.0071(2)	-0.0083(1)	-0.0084(1)	-0.0088(1)	-0.0097(1)
GP		-0.0089(1)	-0.0070(2)	-0.0086(1)	-0.0091(1)	-0.0091(1)	-0.0101(1)
RGP		-0.0089(1)	-0.0069(2)	-0.0083(1)	-0.0085(1)	-0.0089(1)	-0.0098(1)
CR		-0.0084(1)	-	-0.0077(1)	-0.0078(1)	-0.0092(2)	-0.0122(1)
SDV	UP to 250 Torr	-0.0083(2)	-0.0064(3)	-0.0097(2)	-0.0099(3)	-0.0094(2)	-0.0127(3)
SDR		-0.0072(2)	-0.0055(3)	-0.0089(2)	-0.0100(3)	-0.0093(2)	-0.0130(3)
CSDR		-0.0071(2)	-0.0053(3)	-0.0085(2)	-0.0098(3)	-0.0092(2)	-0.0129(3)
VP		-0.0072(3)	-0.0056(4)	-0.0086(2)	-0.0102(3)	-0.0093(2)	-0.0128(3)

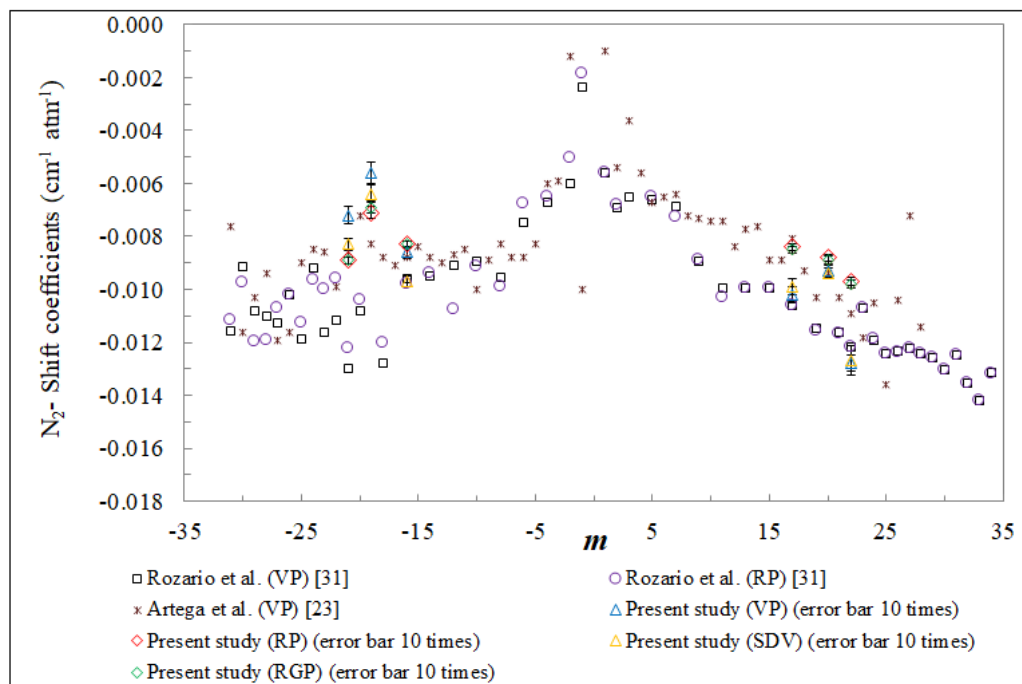


Figure 4.6: Shift coefficients retrieved for six transitions in the $\nu_1+\nu_3$ band of $C_2H_2-N_2$ spectra and compared with previously published values from the literature (self-generated modified version of Figure 7 in [20]).

Line-mixing: The line-mixing effect can be considered in the fitting of an absorption line when there is a presence of any other strong or weak neighboring line. For demonstrating the line-mixing effect, the R(16) lines were selected. This effect was considered for the spectra recorded at pressures above 100 Torr. The top panel of Figure A.5 in Appendix A represents spectra of the R(16) line fitted using SDV profiles where the presence of a weak neighboring line on the left is visible for the 100 and 250 Torr spectra. This might have a small influence on the line-shape of R(16) (shown with an arrow). It was tested by taking the line-mixing into account for the fitting using the SDV and SDR profiles. Bottom panels of Figure A.5 in the Appendix A represent residuals from the SDV and SDR fits without and with taking the line-mixing effect into account, respectively. Based on the RMS values, the fitting of the spectra improved by 4 % for the SDV and by 3.3 % for SDR after taking the line-mixing into account. However, the values of the line parameters, the

positions, intensities, and broadening coefficients deviated less than 0.1 %, while the shift coefficients changed by 12 %. The retrieved line-mixing coefficients are listed in Table 4.8. No comparison was performed, because there are no other studies, which had reported the line-mixing coefficients for the $\nu_1+\nu_3$ band of the C_2H_2 molecule before this study was performed.

Table 4.8: The line-mixing coefficients ($cm^{-1}atm^{-1}$) for six transitions in the $\nu_1+\nu_3$ band of acetylene retrieved from the room-temperature $C_2H_2-N_2$ spectra. The uncertainties in parenthesis are given as one standard deviation referring to the last significant digits. Speed-dependent Voigt (SDV), Speed-dependent Rautian (SDR), correlated Speed-dependent Rautian (CSDR) profiles line-mixing coefficients are listed (modification of Table 5 in) [20].

Line profiles	Pressure	Line names				
		P(21)	P(19)	P(16)	R(19)	R(21)
SDV	Up to 250 Torr	-0.0192(21)	-0.0687(85)	0.0138(19)	0.0018(18)	0.0354(23)
SDR		-0.0198(21)	-0.0757(85)	0.0120(19)	0.0006(18)	0.0337(23)
CSDR		-0.0214(21)	-0.0926(83)	0.0090(19)	0.0036(19)	0.0347(23)

4.4.1 Comparison of New Parameters of R(16) Lines

The R(16) lines were fitted again to make new plots for a better demonstration. These new fits have resulted in almost the same RMS values and slight differences in the retrieved parameters. The old and new RMS values are given in Table 4.9. An example of comparisons to show the differences was made using the parameters of VP, RP, GP and the RGP in Table 4.10. The broadening coefficients from the previous fits are within 1.5 % [20]. The shift coefficients are within 5 % when fitted using VP and GP, and within 9 % when fitted using RP and RGP. The narrowing coefficients retrieved using the RP and RGP are within 1 %, while GP is within 18.5 %. These new values are listed in the third column of Table 4.10.

Table 4.9: The RMS values from old [20] and new fits of R(16) lines using VP, RP, GP, and RGP.

Profiles	RMS (Old)	RMS (New)
Voigt (VP)	0.0015	0.0016
Rautian (RP)	0.0011	0.0012
Galatry (GP)	0.0012	0.0013
Rautian-Galatry (RGP)	0.0013	0.0012

Table 4.10: The retrieved parameters from the old and new fits of R(16) lines.

Profiles	Old	New	Percentage (%)
Broadening ($\text{cm}^{-1} \text{ atm}^{-1}$)			
Voigt (VP)	0.0751(5)	0.0751(2)	0.02
Rautian (RP)	0.0742(2)	0.0749(2)	1.03
Galatry (GP)	0.0754(2)	0.0758(3)	0.57
Rautian-Galatry (RGP)	0.0748(2)	0.0755(1)	0.90
Narrowing ($\text{cm}^{-1} \text{ atm}^{-1}$)			
Rautian (RP)	0.0142(7)	0.0141(1)	0.87
Galatry (GP)	0.0246(10)	0.0201(1)	18.21
Rautian-Galatry (RGP)	0.0181(9)	0.0180(1)	0.72
Shift ($\text{cm}^{-1} \text{ atm}^{-1}$)			
Voigt (VP)	-0.0102(3)	-0.0101(4)	1.09
Rautian (RP)	-0.0084(1)	-0.0092(2)	8.70
Galatry (GP)	-0.0091(1)	-0.0095(1)	4.20
Rautian-Galatry (RGP)	-0.0085(1)	-0.0092(1)	7.60

One reason for these differences is that in the old analysis the range of the baseline around the wings was different. The second reason is that the number of spectra used in the old fittings was different than the number of spectra used in the present fittings. Comparing the old and new results, it can be concluded that both sets of broadening coefficients are

correct, because they are within only 1.03 % and do not change up to the 3rd decimal number. Table 4.6 and a previous study by Povey et al. [6] showed that the narrowing coefficient retrieved using the GP is 1.2 to 1.4 times larger than the RP. This means for R(16) that the new narrowing values are better than the previous ones. The study by Povey et al. [6] also demonstrated that the shift values retrieved using the RP and GP profiles are very close to each other which is also the case for the new R(16) results.

4.5 Molecular Interaction Potential: Influence on Line-shape

The introducers of the speed-dependent profile, Berman [34] and Pickett [35] found that the broadening and shift show dependency also on the inter-molecular interaction potential energy [139]. For the isotropic component, the interaction potential can be expressed as follows [35]:

$$V_{iso}(r) \cong r^{-q}, \quad (4.1)$$

where q is the exponent representing the expansion for absorber-perturber interaction potential and r represents the intermolecular distance. Different values of $q = 1 - 12$ have been tested using the SDV profile. Wproffit2.exe only allowed taking fixed values of q (fit of q is not possible). The Figure A.6 in the Appendix A represents the influence of interaction potential on the line-shape.

The top panel of Figure A.6 in the Appendix A represents the R(16) line fitted using the SDV profile. Different values of q show slight differences in the fitted residuals. The residuals of fitted lines in Figure A.6 and their RMS errors show that there is a potential influence on the line-shape, which varies based on the absorber and perturber mass ratio [139]. The influence increases with increasing ratio. For this case, the mass ratio is

approximately one. After fitting with the SDV, the RMS errors indicated that the fit for values of $q = 5$ (RMS = 0.002771) slightly improved by 0.3 % to 1.5 % than compared to $q = 4$ (RMS = 0.002817) and $q = 6$ (RMS = 0.002778). The RMS increases as q decreases from 4 and as q increases from 6, at least by 2 % to 5 %.

4.6 Conclusions

This study investigated the differences in the line parameters retrieved using different line-shape profiles. For the low-pressure regime (5 - 40 Torr), better fits (smaller RMS values - see Table 4.9 and Figure A.3 in Appendix A) were obtained using RP, GP, and RGP than using VP. This means that the narrowing profiles improved the fit of the low-pressure spectra. Among them, the RP profile works slightly better than the GP profile. Figure A.3 in the Appendix A also shows that fitting the low-pressure spectra (up to 40 Torr) using CRP, SDV, and SDR profiles resulted in larger RMS values of 0.0021, 0.0014, and 0.0014, respectively, which means larger residuals than resulting with RP. Therefore, it can be concluded that RP fits spectra that are lower than 100 Torr better than other profiles.

Comparisons of line parameters retrieved from the spectra of entire pressure regime (5 - 250 Torr) were also carried out. Line parameters from the overall spectra were determined using VP, SDV, SDR, and CSDR profiles. The SDV broadening coefficients are around 0.5 % - 1.0 % higher than those found with the SDR and CSDR profiles. The SDV shift coefficients were 12 % - 15 % higher than the VP shift coefficients, which is expected for cases of heavier perturbers. To choose a profile between VP and SDV can be a bit difficult, because both have advantages and disadvantages. The SDV profile improves

the RMS value of a fit by considering the speed-dependence effect (Tables 4.3 and 4.4) while the VP performs any fit much faster than the SDV profile. However, sometimes it is more important to improve the results than considering the time frame.

This study clearly shows that taking the contribution of the collisional narrowing (for the case of low-pressure spectra – below 100 Torr) and the speed-dependent effects (for the case when high-pressure spectra are included) into account allowed better fits and more accurate line-shape information. In addition, this study provides the idea of selecting suitable line-shape fitting profiles for different pressure regimes with examples; therefore, it verified the important observations about the use of eight profiles and the retrieved line parameters. Furthermore, no other study has reported the line-shape parameters retrieved using eight profiles as this study has done. The knowledge of using proper line-fitting models will ease the work of spectroscopic research groups around the world and will improve the analysis of atmospheric spectra.

Chapter 5 Line-shape Study of Pure Oxygen (O₂)

5.1 Overview

This chapter presents the line-shape parameters of pure oxygen A-band spectra. A description of oxygen A-band transitions and structure is given in Section 5.3. The calibration procedure is briefly described in Section 5.4. The retrieved line-shape parameters are reported in Section 5.6. Results from the theoretical calculations of the narrowing and line-mixing parameters are presented in Sections 5.6.5 and 5.6.6, respectively. The speed-dependent parameter of the pure oxygen molecule is also presented for the first time in Section 5.6.7. All these parameters are listed in Tables B.1 – B.4 of the Appendix B.

5.2 Introduction

Oxygen has a uniform mixing ratio in the atmosphere, which makes this molecule very useful in the retrieval of several environmental parameters from atmospheric spectra, such as temperature, cloud-top pressure, optical properties, and airmass. In addition, the oxygen A-band has the strongest absorption features among the series of weak absorption bands in the visible region, which makes the line-shape parameters of this band very important for studying atmospheric spectra [44]. This study is intended to obtain line-shape parameters of the oxygen A-band spectra, because having a list of accurate line-shape parameters plays an important role in the above-mentioned applications. In this study, four fitting profiles have been used, namely, VP, SDV, RP, and SDR to analyze the pure oxygen A-band spectra.

For this work, the pure oxygen spectra were collected by Dr. Georg Mellau at the Justus Liebig University, Giessen, Germany using a Fourier Transform spectrometer. A description of the experimental setup is given in Section 3.4. My contribution in this study was performing the calibration of 17 pure oxygen spectra and analyzing them to retrieve line-shape parameters, and to perform a theoretical calculation for the narrowing coefficients and the line-mixing coefficients. The quality of the spectra was tested by comparing the retrieved parameters for further analysis to determine the speed-dependent parameter, which has never been reported before for pure oxygen.

5.3 Oxygen Molecule

Oxygen is a homonuclear diatomic linear molecule as shown in Figure 5.1, which has $3 \times 2 - 5 = 1$ normal mode. The symmetry property of this molecule restricts it from having a permanent electric dipole moment. This means that only the vibrational mode is infrared inactive. However, this molecule fulfills the selection rule for the magnetic dipole-allowed transition. The oxygen A-band appears due to the photon transitions from the ground vibrational levels of the ground electronic state X to an excited electronic state b .



Figure 5.1: Oxygen molecule vibrational mode. Two oxygen atoms are connected with a double intermolecular bond, which exhibits only the symmetric stretching vibrational mode.

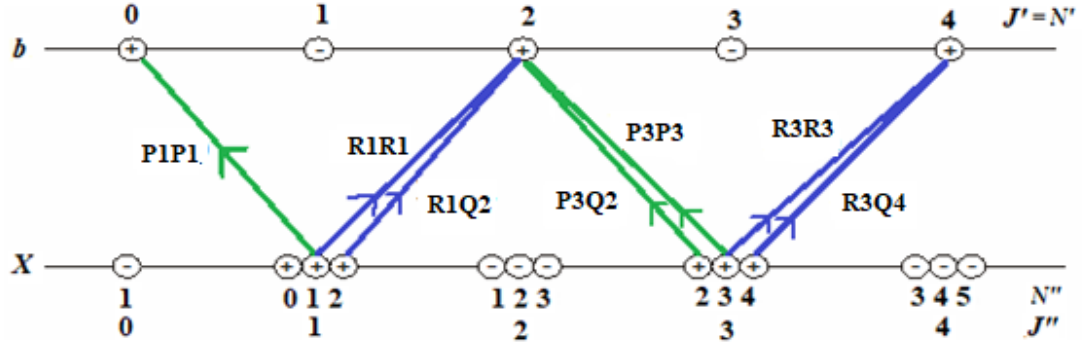


Figure 5.2: Diagram showing possible transitions in the A-band. X is the lower energy level and b is the upper energy levels of the electronic energy state. J' and J'' represent the total angular momentum quantum numbers. N' and N'' represent the rotational quantum numbers. Green lines represent P -branch transitions (PP and PQ lines), while the blue lines indicate R -branch transitions (RR and RQ lines). Information gathered from the literature in [44].

The diagram in Figure 5.2 shows examples of possible transitions types that create the A-band. The electronic spin quantum number of the X state is $S = 1$ and b state is $S = 0$. Therefore, the ground state has a triplet state ($2S+1 = 3$ degenerate spin states), while b is a singlet state [8, 44]. For the oxygen electronic and rotational states, the energy levels are denoted by both the rotational quantum number N and total angular momentum quantum number J [60]. Therefore, the magnetic-dipole allowed selection rule for the oxygen A-band transitions involves the change in the quantum numbers J and N . In Figure 5.2, J'' and N'' represent the lower state and J' and N' indicate the upper state quantum numbers, respectively. The oxygen A-band is formed as ${}^{\Delta N}\Delta J(N'', J'')$, which creates two sub-bands in the P -branch and two sub-bands in the R -branch. The lines are organized as the pairs of PP and PQ sub-bands in the P -branch region [${}^pP(N'', J'' = N'')$ and ${}^pQ(N'', J'' = N'' - 1)$] and as RR and RQ sub-bands in the R -branch region [${}^rR(N'', J'' = N'')$ and ${}^rQ(N'', J'' = N'' + 1)$]. Typical P , Q , and R branching structures are discussed in Section 2.2.5. In Figure 5.2, P1P1, P3Q2, and P3P3 are the P -branch, and R1R1, R1Q2, R3R3, and R3Q4 are the R -branch

transitions. According to the P, Q, and R branch transition rule, PP lines follow $\Delta J = -1$ and $\Delta N = -1$, PQ lines $\Delta J = -1$ and $\Delta N = 0$, RR lines $\Delta J = +1$ and $\Delta N = +1$, and RQ lines $\Delta J = +1$ and $\Delta N = 0$.

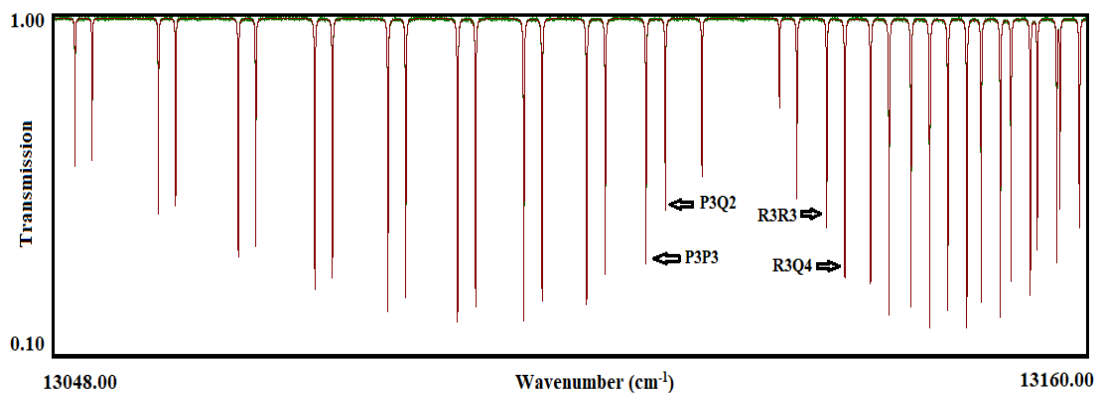


Figure 5.3: Oxygen A-band spectra recorded at 337.1 Torr in the 13048 – 13160 cm^{-1} regions. The P3P3, P3Q2, R3R3, and R3Q4 lines are indicated with arrows.

The oxygen A-band is a very well-structured band situated in the 13048–13160 cm^{-1} region of the electromagnetic spectrum as shown in Figure 5.3. Among the four sub-bands, PP and PQ are in 13048 to 13119 cm^{-1} , and RR and RQ are within 13126 to 13160 cm^{-1} .

5.4 Calibration of the Spectra

A list of 17 pure oxygen A-band spectra including their physical conditions is given in Table 5.1. All these spectra were recorded in the 13050 to 13159 cm^{-1} spectral range with a resolution of 0.0222 cm^{-1} . These spectra were recorded at room temperature and various pressures. The first column is the run number of each spectrum followed by the corresponding temperature in Kelvin, the pressure in Torr and the pathlength in meters. An example of a low-pressure and a high-pressure spectrum is given in Figure 5.4. The spectrum recorded at 9.00 Torr is plotted in red, while the spectrum recorded at 878.45 Torr is plotted in green. Spectra of two very different pressures are plotted to show the difference

of line strength as well. Absorption lines in the low-pressure spectrum (red) are less intense than the high-pressure one (green).

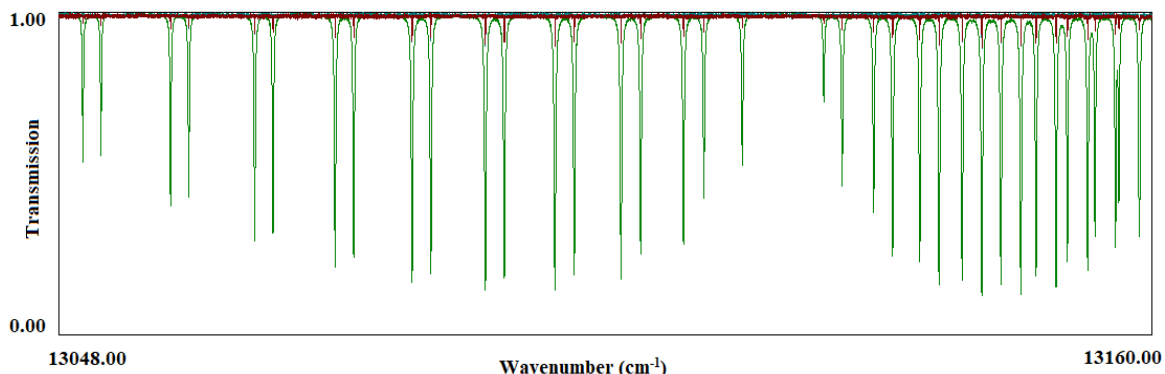


Figure 5.4: Low-pressure spectrum (9.00 Torr) in red and high-pressure spectrum (878.45 Torr) in green in the 13048.00 – 1316.00 cm^{-1} region.

Like any other instrumental calibration, the calibration of the wavenumber scale is important for accuracy in the retrieval of line parameters. The calibration factors were found by taking the ratio between the line positions from low-pressure (8.90 – 9.50 Torr) spectra and the line positions from the paper published by Drouin et al. [74]. Line positions from the low-pressure spectra can be found by running the spectra file using the Labfit program to find the position of each peak one-by-one. The calibration factors were then calculated using the following formula:

$$\text{Calibration factor} = ((1 - \text{Average of the line position ratios}) * 10^{10}). \quad (5.1)$$

The Labfit, program does not store these average ratios as they are. This is why they need to be multiplied by 10^{10} before inserting. The average calibration factor was then multiplied to the uncalibrated wavenumbers of the high-pressure spectra (98.25 Torr and above) using the Labfit program [133] to adjust their wavenumber scale. The accuracy of calibration was $\sim 0.0002 \text{ cm}^{-1}$.

Table 5.1: Experimental conditions of oxygen A-band spectra used in the present analysis (13050 to 13159 cm^{-1} range).

Spectrum run number	Temperature (K)	Pressure (Torr)	Pathlength (m)
	Uncertainty (0.5 K)	Uncertainty 0.2 % (below 1254.5 Torr) and 0.5 % (above 1254.5 Torr)	
4549	294.55	98.25	3.370
4550	294.80	98.75	3.370
4551	294.75	494.52	3.370
4552	294.85	592.95	3.370
4553	294.50	690.5	3.370
4554	295.10	787.95	3.370
4556	297.95	337.1	16.375
4558	297.80	878.45	16.375
4560	297.70	9.00	16.375
4657	294.65	999.50	16.375
4658	294.75	1254.5	16.375
4659	294.40	1595.5	16.375
4660	293.75	1971.5	16.375
4661	294.35	2463.5	16.375
4662	294.40	3011.00	16.375
4564	293.65	9.00	16.375
4666	296.95	8.90	16.375

5.5 Retrieval of the Line Parameters

Four different line-shape models, the VP, SDV, RP, and SDR profiles were used to fit the experimental spectra and retrieve the parameters. The SDV model takes the effect of molecular speed into account. The Rautian model considers the collisional narrowing effect, whereas the SDR accounts for both speed and narrowing effects. Details of these profiles are given in Chapter 2. The line-mixing coefficients were retrieved using these four models, while the speed-dependent parameters were retrieved using the SDV and SDR models. Spectra were fitted simultaneously to obtain the following line-shape parameters;

line positions, intensities, self-broadening, self-narrowing, self-shift and line-mixing coefficients, and speed-dependent parameters. Derivation of the line-mixing coefficients using the exponential power gap (EPG) law is presented in this chapter. All the experimental and theoretical spectroscopic results were compared with available published results, where appropriate.

This section contains the spectroscopic results of oxygen A-band spectra. Figure 5.5 (Panel a) shows the A-band spectra after fitting with the RP and Panel (b) the corresponding residual (Global Standard Deviation: 0.246 %). Panel (c) presents all the spectra fitted simultaneously using the SDV profile. Panels (d), (e), and (f) show the residuals of the spectra after fitting with the VP (Global Standard Deviation: 0.249 %), SDV (Global Standard Deviation: 0.244 %) and SDR (Global Standard Deviation: 0.249 %) profiles, respectively. These fits were performed using the Labfit software. Tables B.1, B.2, B.3 and B.4 in the Appendix B contain line positions, line intensities, self-broadening, self-shift, and the line-mixing coefficients fitted with the VP, RP, SDV, and SDR profiles, respectively. Tables (C) and (D) also contain the speed-dependent parameters retrieved with the SDV and the SDR profiles, respectively. The uncertainty given in parentheses corresponds to one standard deviation referring to the last significant digits. Simultaneously analyzing a large number of spectra minimizes the random errors [140].

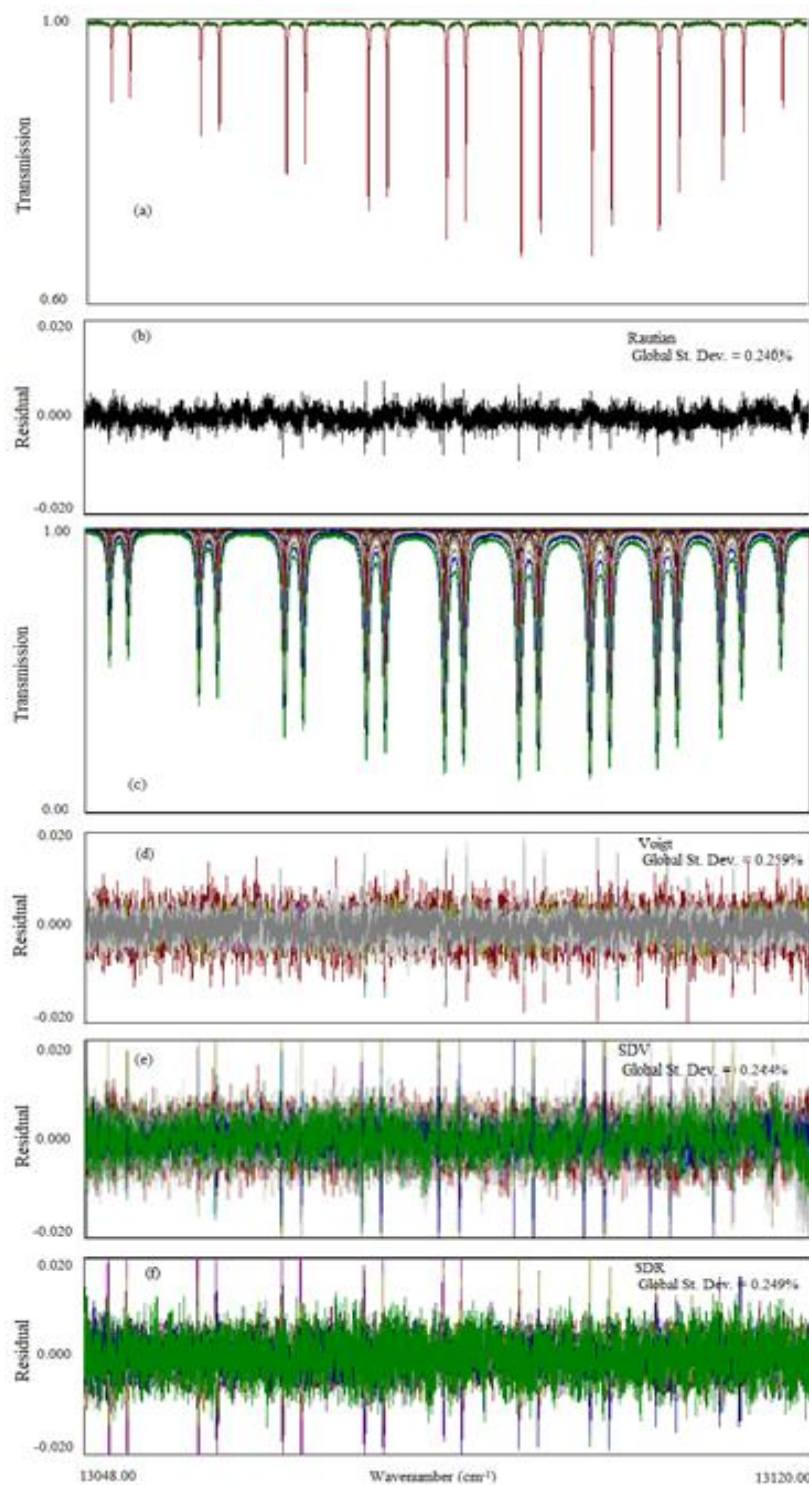


Figure 5.5: Oxygen A-band spectra in the P-branch range (13048 – 13120 cm^{-1}). Top panel (a) presents a fitted spectrum recorded at 98.25 Torr using the RP and (b) indicates the residuals. Panel (c) presents all the spectra simultaneously fitted using SDV. Residuals after fitting all the spectra using VP, SDV, and SDR profiles are plotted in Panels (d), (e), and (f), respectively.

The transmission profiles of absorption lines are a convolution of instrumental line shape (ILS) and the molecular absorption line-shape functions. Predoi-Cross et al. [44] reports the expression of the oxygen transmission profiles as follows:

$$T'(v) = \int_{-\infty}^{\infty} ILS(v - \tilde{\nu}) [exp(LP\alpha(\tilde{\nu}))] d\tilde{\nu}, \quad (5.2)$$

where $T'(v)$ represents the transmission of the absorption profile, L is the absorption pathlength, α is the absorption coefficient, P is the partial pressure of the gas sample, v is the radiation frequency, $\tilde{\nu}$ is the transition frequency, and ILS is a sinc function for the FTS spectra. The absorption coefficient can be written as the product of the integrated absorption coefficient of the transmission (α_i^{int}) and the normalized line-shape function $F(v - v_i)$ as follows:

$$\alpha(v) = \alpha_i^{int} \times F(v - v_i). \quad (5.3)$$

5.6 Results and Comparisons

The following section will report the line-shape parameters of pure oxygen spectra. Some comparisons will also be presented to test the accuracy of the results.

5.6.1 Line Position

In this study, the line-shape parameters were retrieved by simultaneously fitting 17 pure oxygen spectra in the Labfit software. It uses a multispectrum nonlinear least-square fitting technique as described in Section 3.6. The line positions of 38 oxygen A-band transitions were retrieved and then compared with previous results from the literature to check the accuracy. Further analysis was performed to retrieve the speed-dependent

parameters, which have never been reported before for pure oxygen A-band transitions. All the line positions are listed in Tables B.1 – B.4 in the Appendix B.

The line positions in the present study were retrieved using VP, RP, SDV, and SDR profiles. However, comparisons in Figure 5.6 (A) were only made with the present VP results, because the results available in most of the published literature were retrieved using this profile. Residuals were calculated to determine the accuracy of the line positions. They are plotted along the y-axis versus the index m on the x-axis, where $m = -J'' = -N''$ (defined in Section 5.3) is for the P-, and $m = J'' + 1 = N'' + 1$ [44] is for the R-branch transitions.

The residuals closest to the zero axis imply less difference with the corresponding literature results. The line positions retrieved from the VP fit were compared with the line positions from the literature and are reported in Table 5.2 (the calculated mean value of the residuals \pm standard deviation of the mean). The first and second columns list the literature and the average of the absolute error for the 38 lines, respectively.

Figure 5.6 (A) shows that the results are in excellent agreement (<0.000001 % on average) with HITRAN 2016 [141] and Long et al. [47]. The line positions in the present study agree within 0.000002 % with the ones in Drouin et al. [74]. The results are also in good agreement (0.000004 %) with the line positions reported by Predoi-Cross et al.'s [44] and Brown et al. [53], who have used spectra of CO-calibrated O₂-line positions. The FTS line positions given by Fally et al. [69] show similar patterns with little deviation. A consistent difference in Cheah et al.'s [62] line positions in the R-branch values except for $m = 8$ to 16, is noticeable. On the other hand, the results given by Kanamori et al. [56]

retrieved from diode-laser spectra and by O’Brien et al. [57] retrieved from intracavity-laser spectra (I_2 calibration) show random differences with the results from the present study. A comparison with the former study gives a difference of 0.000027 %, while increasing to 0.000037 % consistency compared to the latter one. These two studies have used a different experimental technique than the present study. Calibration using CO and I_2 lines have caused a systematic difference in the results, which was also evident in a study by Predoi-Cross et al. [44]. Their study [44] showed that the line positions retrieved using spectra from I_2 calibrated O_2 -lines are on an average $0.0473 \pm 0.0421 \text{ cm}^{-1}$ (0.000038 %) different than the positions retrieved using spectra from CO calibrated O_2 -line spectra.

Table 5.2: Average absolute error in the oxygen A-band line positions compared to the literature results.

Studies from literature	Mean residuals (Standard deviation of mean) in cm^{-1}	Error (%)
Long et al.	0.00017(3)	0.000001
HITRAN 2016 database	0.00017(3)	0.000001
Drouin et al.	0.00022(3)	0.000002
Robichaud et al.	0.00046(4)	0.000003
Predoi-Cross et al.	0.00059(5)	0.000004
Brown et al.	0.00057(6)	0.000004
Shermaul et al.	0.00074(6)	0.000005
Fally et al.	0.00199(7)	0.000015
Cheah et al.	0.00193(14)	0.000013
O’Brien et al.	0.00468(69)	0.000037
Kanamori et al.	0.00597(88)	0.000027
Rautian (Present study)	0.00008(1)	0.0000007
SDV (Present study)	0.000003(1)	0.00000003
SDR (Present study)	0.00009(1)	0.0000007

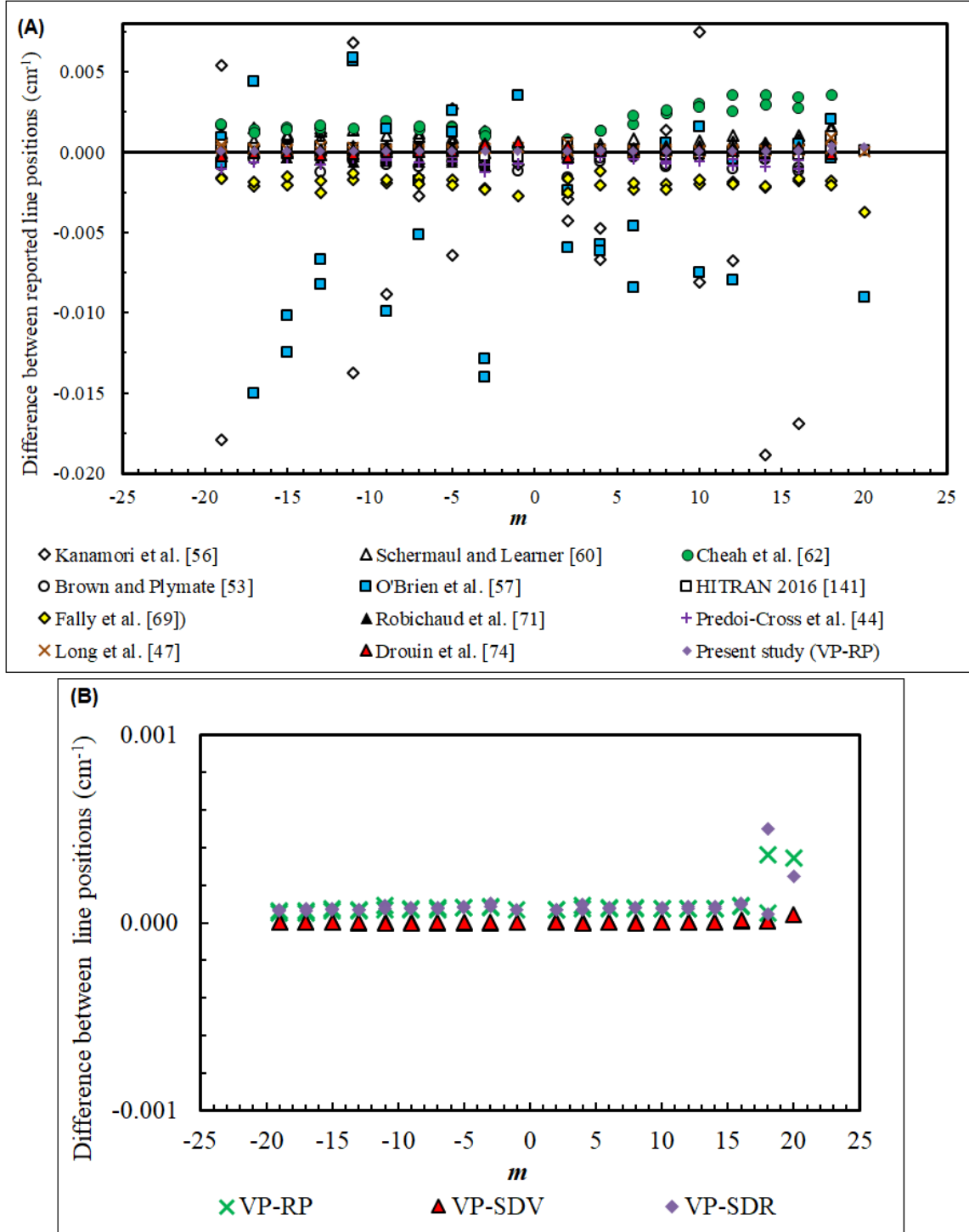


Figure 5.6: (A) Differences in line positions between the present values (VP) and previous studies, and (B) line positions retrieved in the present study using VP compared to RP, SDV, and SDR profiles.

Comparisons of the line positions between the VP and SDV, Rautian, and SDR from the present study were also made to check the accuracy (Figure 5.6 (B)). The mean residuals for the RP, SDV, and SDR are 0.0001 cm^{-1} , 0.000003 cm^{-1} , and 0.0001 cm^{-1} (also given in Table 5.2), respectively. This means that the retrieved line positions using VP are closest to SDV, while the ones fitted with RP are closest to SDR, implying that the line positions are not model dependent.

5.6.2 Line Intensities

The oxygen A-band is the strongest among the weak absorption bands of oxygen found, which are not saturated even for very long absorption pathlengths. In this study, the maximum pathlength used is 1633.6 cm for up to 3011 Torr. Therefore, the intensity parameters can be retrieved for this band. In this study, the intensities of 38 P-branch and R-branch lines were retrieved using the multispectrum fitting method of the Labfit software.

Comparisons of the line intensities between the present study and available studies from the literature are shown in Figure 5.7 (A). This figure shows the intensities retrieved using the VP in the present study with their corresponding error bars (100 times). It shows that the results from the present study are in very good agreement with the HITRAN 2016 database [141], Predoi-Cross et al. [44], Drouin et al. [74], and Long et al. [47].

The second set of comparisons were made by taking ratios of intensities between the VP profile retrieved results and the ones from the literature. The intensity ratios are only 0.2 %, 0.5 %, and 0.9 % off with respect to the RP, SDV, and SDR intensities, respectively.

Therefore, VP results instead of the RP, SDV, and SDR results from the present study were selected to compare with other studies as they are not model dependent.

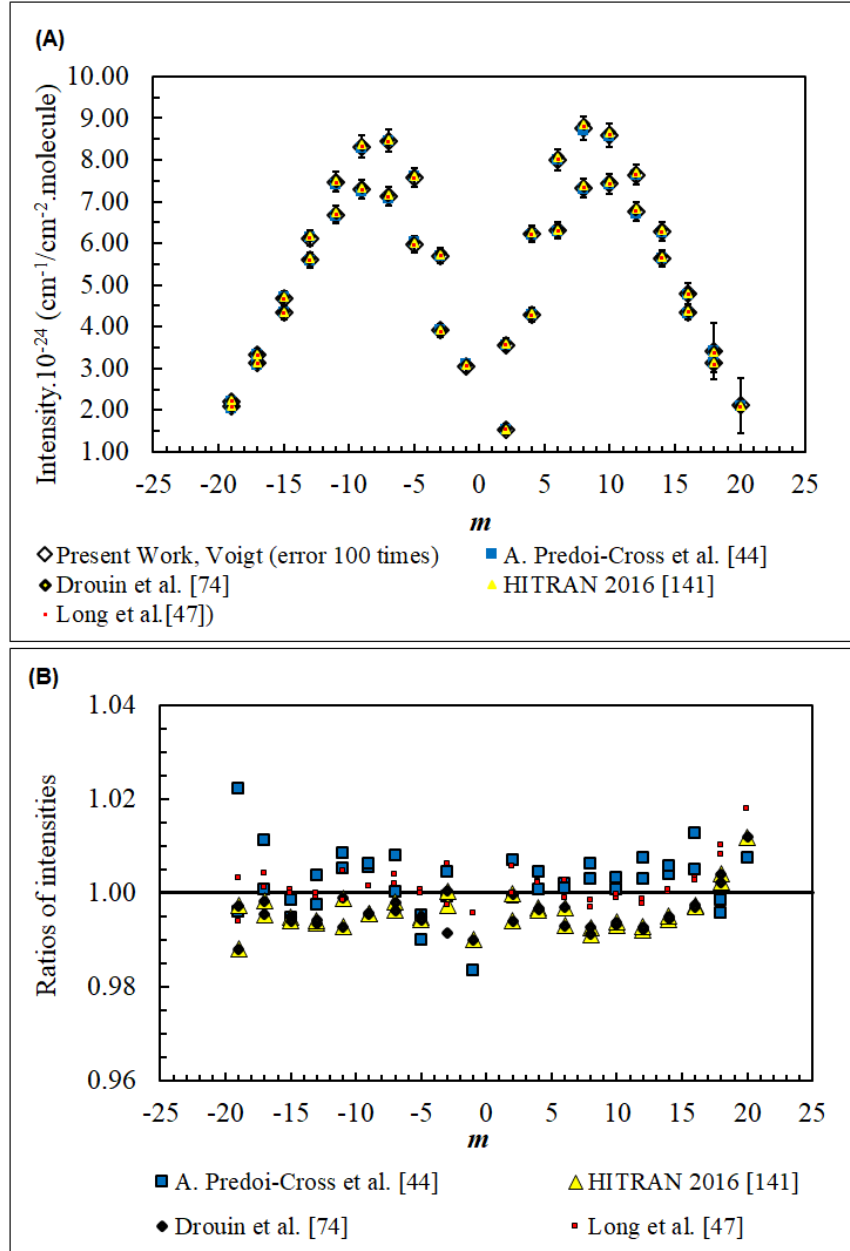


Figure 5.7: (A) Comparison of intensities retrieved using VP in the present study and their corresponding error bars (100 times) with those in the literature. (B) Ratios of the line intensities between the values obtained in the present study and the previous studies.

Here, $m = -J'' = -N''$ is for the P-, and $m = J'' + 1 = N'' + 1$ is for the R-branch.

Figure 5.7 (B) shows plots of intensity ratios versus the m index. The values close to the axis at 1 are in good agreement. It is visible from the plot that the intensities retrieved in the present study agree very well with the intensities in the HITRAN 2016 [141] database, which are within 1.20 %. Other than that, they also agree with the intensities given by Predoi-Cross et al. (2.22 %) [44] and Long et al. (1.77 %) [47]. The comparison with Drouin et al.'s [74] data shows the same trend as with HITRAN 2016 and Long et al. [47] for the entire band, but most points are in between 0.99 and 1.01, which is also within 1.20 %. In general, the reason behind differences in the intensity values is mainly due to the gas impurity (gas concentration). This problem can be fixed if the changes in the concentration that occur during the experiments are known or can be determined.

5.6.3 Line Broadening

As discussed in Chapter 2, there are different types of line broadenings: natural broadening, Doppler broadening, and pressure broadening. Line broadening is measured using HWHM of the absorption lines. The broadening coefficients were retrieved by the multispectrum and simultaneous fitting method using the Labfit program which was also used to retrieve the line positions and intensities. The broadening coefficients obtained from the fitted spectra are presented in the unit of $\text{cm}^{-1}\text{atm}^{-1}$.

The retrieved self-broadening coefficients are plotted in Figure 5.8, where panel (A) contains results obtained using the VP and SDV profiles. This figure shows comparisons between fitted data from the present work and the values from the literature. Like the position residuals and the intensity ratios, the broadening coefficients are also plotted against the m index. The broadening coefficients from the present study are plotted with the error bars to show uncertainty of the results. The errors are quoted in parentheses in

Tables B.1 – B.4 of the Appendix B as one standard deviation referring to the last significant digits, and the error bars in Figure 5.8 are a magnification (50 times) of those values. The present broadening coefficients match very closely with the coefficients reported by Predoi-Cross et al. [44] and Brown and Plymate [53]. The agreement with the former study is on average of 0.51 %, and the latter one is 0.75 %. The broadening results given by Schermaul et al. [60] is consistently larger (12.45 % on average) than the present results; however, both the P- and R-branches follow the same trend. Schermaul et al. [60] have used the line-by-line analysis method and a modified Doppler-narrowed VP, which implies that the retrieval method could be a reason why their values are a bit different.

Panel (B) of Figure 5.8 displays a comparison of the present experimental results retrieved using the RP and the SDR profiles with results from previous studies. The error bars were magnified by 50 times of their values. The figure shows that the self-broadening coefficients given by Ritter et al. [55], Predoi-Cross et al., Long et al. [47], and Drouin et al. [74] agree very well between $m = -17$ and -5 in the P-branch, and $m = 6$ and 18 in the R-branch with the retrieved self-broadening results. Broadening retrieved using the RP is within 2.19 % and 1.45 % (average) for the Ritter et al. [55] and Long et al. [47] results, respectively. The accuracies published by Predoi-Cross et al. [44] and Drouin et al. [74] are on average within 2.94 % and 2.03 % , respectively, for the SDR profile.

Generally, the coefficients retrieved from lines corresponding to a very low J (below 5 ($m = -5$ in P- branches and 6 in R- branches)) and to a very high J (above 18) do not fit well, because the transitions corresponding to these rotational quantum numbers are weaker than the other lines. The results from all four fitting profiles (VP, SDV, RP, and SDR) of the present study as well as the literature results, show a jump for the lower J'' broadening

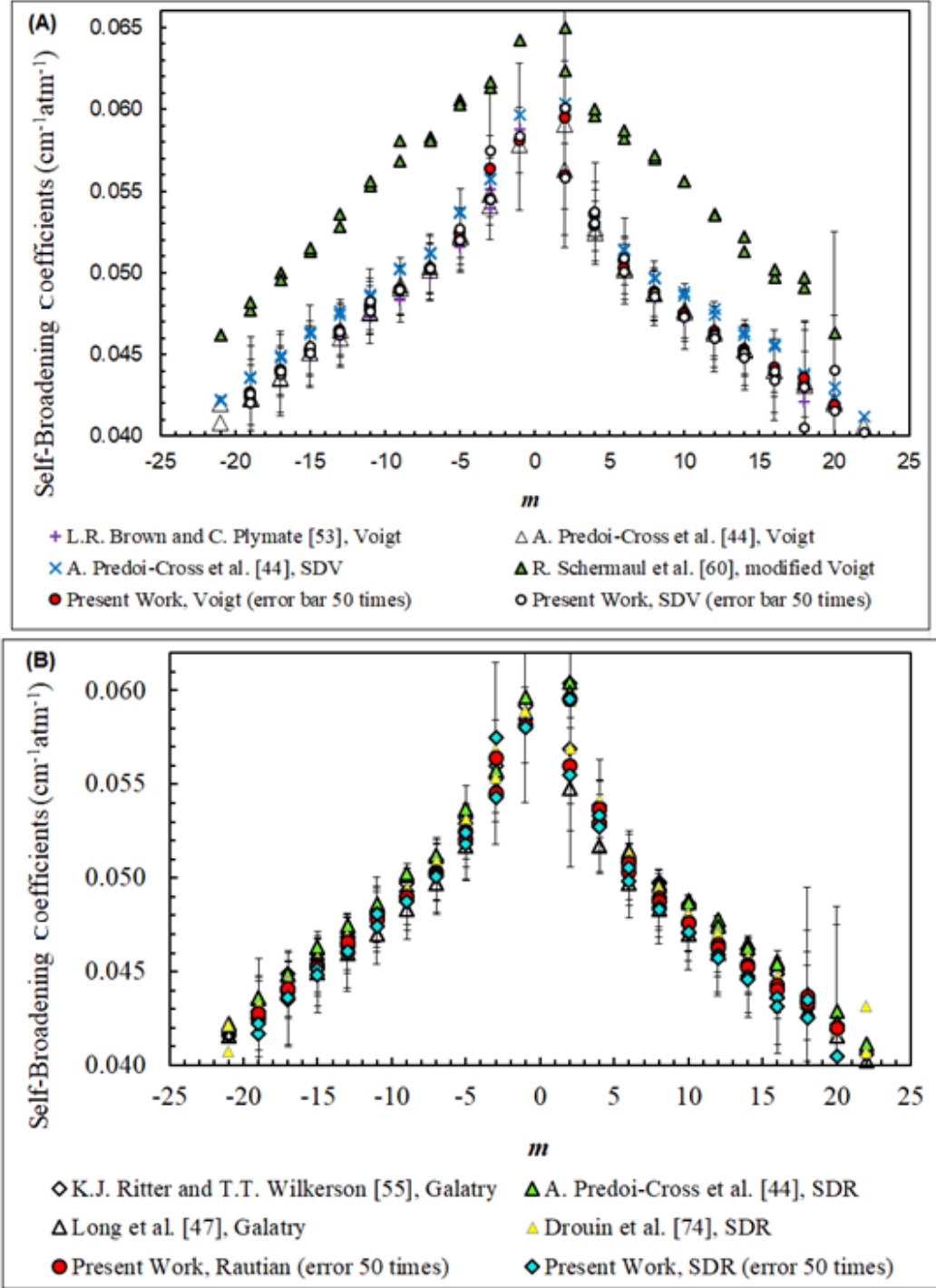


Figure 5.8: Self-broadening coefficients obtained using the Voigt (VP) and Speed-dependent Voigt profiles (SDV) (A), and Rautian (RP) and Speed-dependent Rautian (SDR) profiles (B) (line-shape models that take into account the narrowing effects – from spectra below 100 Torr). Here, $m = -J'' = -N$ is for the P- and $m = J'' + 1 = N'' + 1$ is for R-branch.

values. The gradual increase between successive coefficients is 1.1 times, but for $m = -3$ to 2, and for $m = 18$ and 20, the increment is higher in VP and SDV profiles fits, because they are weak ($m = -3$ to 2) and dense ($m = 18$ and 20) lines and do not fit as good as the others.

5.6.4 Line Shift

The line shift refers to the slight change in the line position (transition wavenumber). It is present in the spectra recorded at any pressures. It is observable more in the absorption lines of spectra recorded at high pressures, because they cause a larger shift. In the present experimental study, the shifting coefficients of the oxygen A-band were retrieved from 17 pure oxygen spectra using the Labfit software. The shift coefficients are listed in Tables B.1 – B.4 in Appendix B. They were retrieved using the following four line-shape profiles: VP, SDV, RP and, SDR profiles.

Plotted graphs of the shifting coefficients are shown in Figure 5.9 to demonstrate the P- and R- branch patterns and to verify the results by comparing with literature values to check the accuracy for further analysis to retrieve the speed-dependent parameters. Shift coefficients in some of the studies provide similar trends in both the P- and R-branches, which show an increase with the decreasing rotational quantum numbers; therefore, J and N dependency. It shows that the shift coefficients between $J = 3$ and 17 are only differ by $0.0025 \text{ cm}^{-1}\text{atm}^{-1}$ for all the profiles used in the present study and most studies from the literature. They are larger (absolute value) for the P-branch than for the R-branch lines. The shift coefficients of stronger lines agree better than the weaker lines (for a higher $|m|$ index) when compared to literature values. The shift coefficients reported by Drouin et al. [74] are in good agreement with the present experimental results. Almost a consistent difference is observable with the results from Predoi-Cross et al. [44] and Brown and Plymate [53] data.

Similarly, the same is true for the line positions. However, absolute values of the shift coefficients reported by Predoi-Cross et al. [44], Brown et al. [53], and Long et al. [47] are higher (most are 3 to 6 times) than the present experimental values.

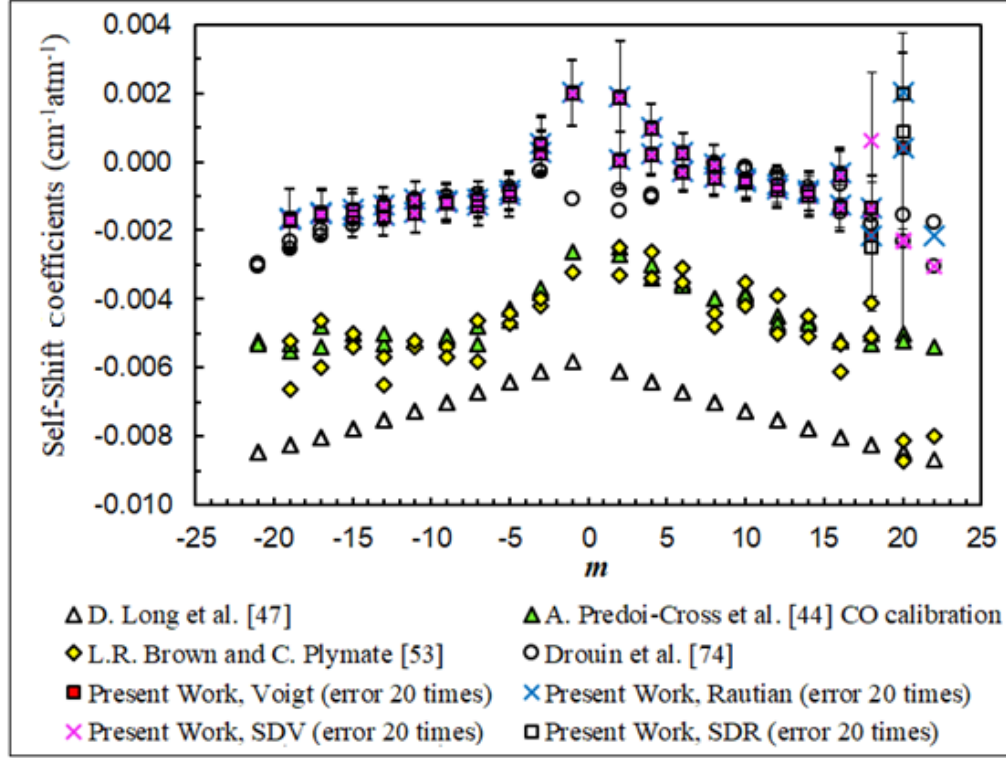


Figure 5.9: Self-pressure shift coefficients for transitions in the oxygen A-band. Here, $m = -J'' = -N$ is for the P- and $m = J'' + 1 = N'' + 1$ is for R-branch.

Different calibrations used in the literature may be the cause of the discrepancy in shift coefficients from the present study. For example, Predoi-Cross et al. [44] used the same set of oxygen spectra twice to retrieve shift coefficients. They have established that indirect internal calibration using CO- and I₂-lines give slightly different scales. The values of the shift coefficients retrieved from the I₂-calibrated spectra are between -0.012 and -0.007 cm⁻¹atm⁻¹, which are higher than the values of the shift coefficients (between -0.006 and -0.003 cm⁻¹atm⁻¹) when extracted from the CO-calibrated spectra. This suggests that

using different calibration procedures caused the disagreement between the present experimental results and the ones retrieved by Predoi-Cross et al. (calibration to CO-lines) [44]] and Brown and Plymate (calibration using CO-lines) [53].

The shift coefficients retrieved using the VP and RP are within 1%, except for $m = 2, 6, \text{ and } 18$. The shift coefficients retrieved using the SDV and SDR profile are within 3%, except for $m = 2, 6, 18, \text{ and } 20$. These types of comparisons of line-shape parameters with the literature help to examine the relative accuracy and quality of the present experimental measurements. The outcome from the comparison suggests that the wavenumber calibration and the calibration procedure have effects on the shift coefficient values as well as on the line positions. In addition, using different analysis methods might also be a reason for the discrepancy in the values of the parameters in question.

5.6.5 Line Narrowing

The line-narrowing effect is accounted for while fitting the spectra using the RP and SDR profiles. Narrowing coefficients retrieved using the RP are presented in Figure 5.10. The narrowing parameters were also theoretically obtained in this study using the expression given by Brault et al. [142] and were then compared with Long et al.'s [47] experimental values.

The calculations of the Mean Square Displacement (MDS) and the diffusion constant for this study were performed by Dr. Aziz Goufi, University of Rennes 1, France. To carry out this calculation, the van der Waals interaction potential model given by Lennard-Jones (L-Js potential) was used [143]. This method was established for the intermolecular interaction of an oxygen molecule, which was modeled using a single united

atom force field [143]. A sample of 200 molecules with a 12-Å cutoff, and a box of the $L_z=L_y=L_x=202$ Å dimensions were selected for this calculation.

Molecular dynamics (MD) simulations were performed using the molecular simulation software called DLPOLY [144]. The time step was set to 1fs during this simulation. The data acquisition was set to 10 ns. The MD simulations were performed for N particles kept in the above-mentioned volume at a temperature of $T = 300$ K (NVT-constant volume-temperature statistical ensemble). The relaxation time of the thermostat was 0.5 fs, considering the constant temperature of the canonical ensemble statistics, by means of the Nose-Hoover algorithm [145]. The velocity Verlet algorithm [146] was then used for integrating the motion equation of the particles.

After all these assumptions and calculation of the self-diffusion coefficient for the oxygen molecule, the narrowing parameter was calculated by the author of the thesis. The mathematical expression was given by Brault et al. [142], which is as follows:

$$\beta_d = \frac{K_b T}{2\pi c M D_s} . \quad (5.4)$$

The narrowing parameter obtained using the above formula for the pure oxygen sample was $1.557 \times 10^{-2} \text{ cm}^{-1}$. For the pure oxygen sample, the self-diffusion constant D_s was computed by Dr. Aziz Goufi using the MSD of the particles at time t , as follows:

$$D_s = \frac{1}{6} \lim_{t \rightarrow \infty} \frac{MSD}{t} . \quad (5.5)$$

The calculated diffusion value was found to be, $D_s = 1.945 \times 10^{-1} \text{ cm}^2 \text{ s}^{-1}$. In addition, the MSD of this molecular system was computed using the correlation expression for every i^{th} particle at position $r_i(t)$ and time t as follows:

$$MSD(t) = \left\langle \frac{1}{N} \sum_{i=1}^N (r_i(t) - r_i(0))^2 \right\rangle. \quad (5.6).$$

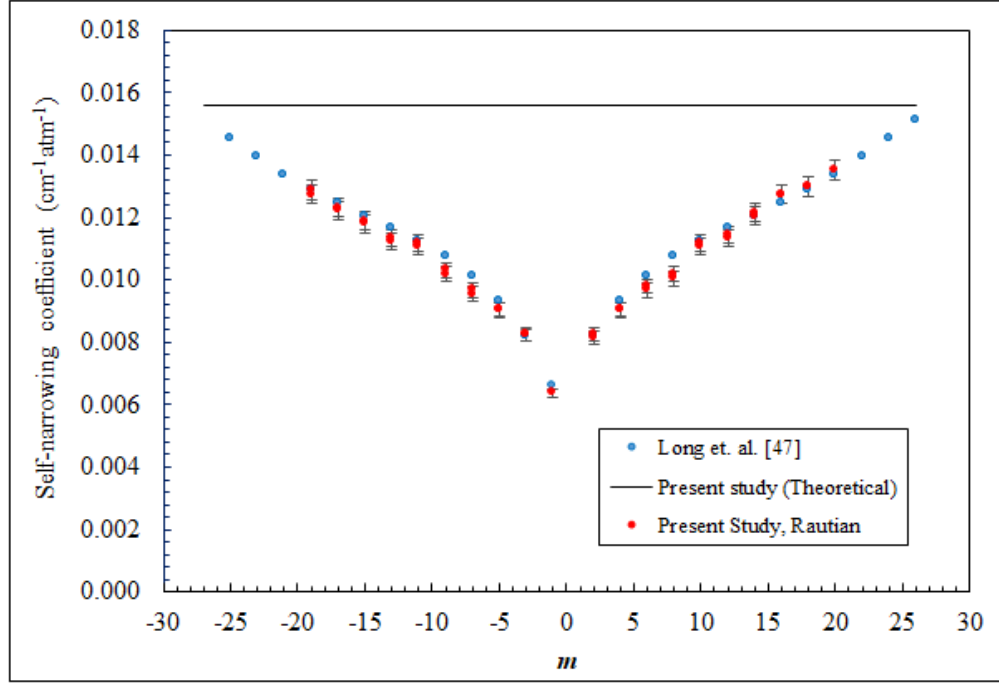


Figure 5.10: Calculated and fitted narrowing coefficients compared with the experimental results from Long et al. [47]. Here, $m = -J'' = -N$ is for the P- and $m = J'' + 1 = N'' + 1$ is for the R-branch.

Figure 5.10 shows the narrowing parameters obtained using the aforementioned theoretical calculation. The relation between the m index with the rotational quantum number of lower energy level J'' corresponding to the P- and R- branch is $m = -J''$ and $m = J'' + 1$, respectively. The calculated narrowing value of $1.557 \times 10^{-2} \text{ cm}^{-1}\text{atm}^{-1}$ as a straight line from $m = -24$ through 24 are plotted in the figure. The narrowing coefficients, retrieved from the spectra of pressure 337.10 Torr and below using the RP fit, are also plotted and compared to the experimental narrowing coefficients reported by Long et al. [47]. The percentage difference between the present experimental narrowing and Long et al.'s narrowing was computed, which is on an average of 2.34 % (plotted error bars). The

narrowing retrieved from experimental spectra increases with the increasing rotational quantum number J'' (absolute value of the m index), which gives the opposite pattern of the broadening coefficient, which decreases with the increasing rotational quantum number J'' . The broadening coefficients retrieved in this fit are smaller, but very close (within 4%) to the broadening coefficients retrieved from the 17 spectra using the RP profile.

5.6.6 Line-mixing and Exponential Power Gap Law (EPG)

The line-mixing effect is observed in the spectra recorded at an elevated pressure. Figure 5.11 shows spectra of the R-branch ($13124 - 13160 \text{ cm}^{-1}$) recorded at 494.52 Torr, where the absorption lines indicate the presence of line-mixing. The high-pressure spectra experience overlapping profiles between neighboring absorption lines (indicated with arrows in the Figure). These lines can be fitted [44] properly by taking this line interference effect into account [102]. This is also known as the line coupling effect. Line-mixing can be retrieved for lines if their spectral features overlap, and if the difference between their consecutive rotational energy levels (both lower and upper case) is small enough to change the rotational states through inelastic collisions [44]. A detailed description of the line-mixing effect is given in Section 2.4.11. If two neighboring lines overlap, they then should not be considered as isolated lines while fitting to reproduce the experimental spectra.

Spectra of higher pressures than 494.52 Torr show more overlapping of the lines. Having high-pressure spectra (up to 3011 Torr) for this oxygen study suggests that the line-mixing effect should be considered while fitting the spectra. Therefore, the line-mixing coefficients were retrieved using all four models: VP, RP, SDV, and SDR to fit experimental spectra. The retrieved line-mixing coefficients (atm^{-1}) are listed in Tables B.1 – B.4 of Appendix B.

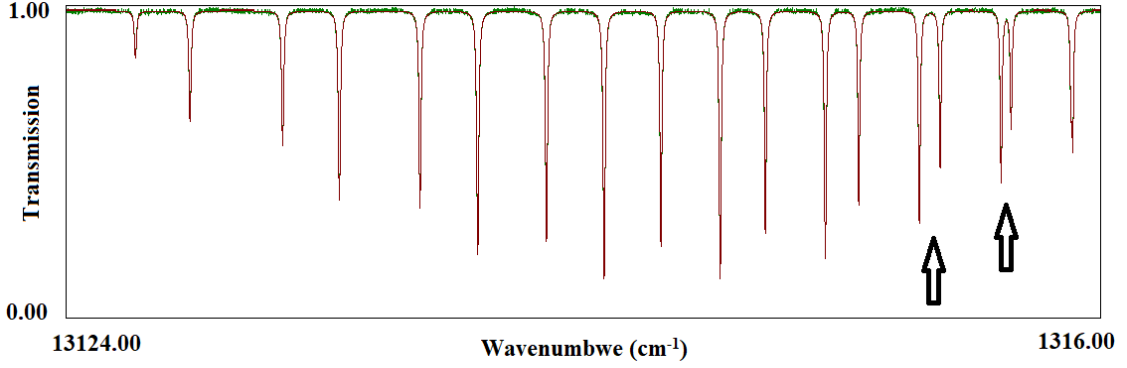


Figure 5.11: R-branch (13124 – 13160 cm^{-1}) spectra of pressure 494.52 Torr. The pairs of two lines at the right corner indicated with arrows show an appearance of line coupling. Lines of the spectra recorded at pressures higher than presented in this graph show more overlap.

For comparison, the line-mixing coefficients were also calculated by the author of the thesis using the Exponential Power Gap (EPG) scaling law. The MATLAB programming language [44] was used to implement the EPG calculation. In this calculation, the broadening and the line-mixing coefficients can be computed by solving a relaxation matrix W , where the real part of diagonal elements corresponds to the broadening coefficients, and the off-diagonal elements correspond to the mixing effect. A detailed explanation of the EPG law is given in Section 2.4.12. A Matlab code was used to determine the constants a , b , and c using Equation 2.79. These parameters are defined in Equation 2.79 in Chapter 2, which were optimized in order to improve the EPG line-mixing results. The off-diagonal elements W_{jk} of the relaxation matrix were used in Equation 2.84 using the Matlab code to compute the theoretical line-mixing values. EPG line-mixing coefficients are plotted in Figure 5.12 along with the experimental Voigt, Rautian, SDV, and SDR data. Table 5.3 contains the a , b , and c parameters for the four sub-bands (PP, PQ, RR, and RQ). The errors quoted in the parentheses are one standard deviation referring to the last significant digits. Their optimized values were determined when the diagonal

elements of the relaxation matrix matched up to the fourth decimal of the experimental broadening values.

Table 5.3: The constants a , b and c were determined using the EPG scaling law for the sub-bands listed in the table. The error values are quoted in parentheses, which correspond to one standard deviation.

Sub-bands	a	b	c
P(N)P(J)	0.05708(3)	0.34093(11)	1.19277(31)
P(N)Q(J)	0.07386(1)	0.40539(3)	1.15345(10)
R(N)R(J)	0.06531(11)	0.38563(35)	1.1632(99)
R(N)Q(J)	0.05203(3)	0.32417(11)	1.20436(32)

Figure 5.12 shows a comparison of retrieved and calculated-EPG line-mixing coefficients from the present study, Predoi-Cross et al. [44], and Drouin et al. [74]. They are plotted against the m index ($m = -J''$ and $m = J'' + 1$). The absolute value of the line-mixing coefficient increases with decreasing J'' (m index) numbers in both P - (negative values) and R -branches. This follows the trend of the broadening coefficient, which is expected because line-mixing is related to the line width. An interesting pattern to notice is that the far-right absorption lines in both branches of the A-band give negative line-mixing values, which means negative values for a lower J'' in the P -branch and for a higher J'' in the R -branch. Uncertainties in the EPG results are presented in the graph using error bars with 100 times magnification.

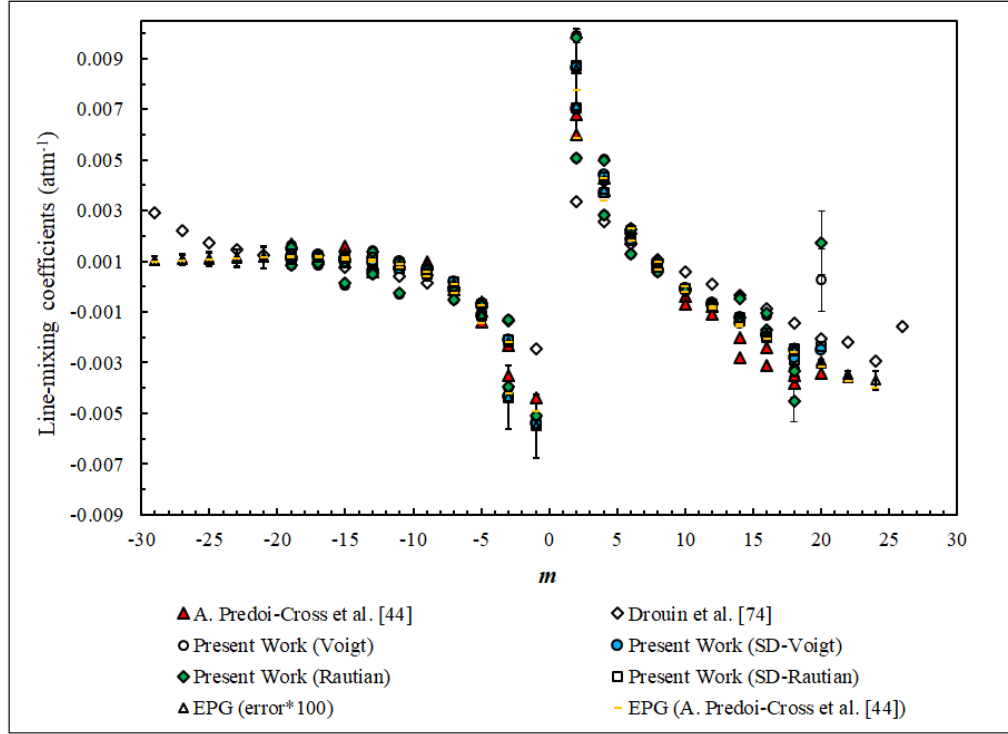


Figure 5.12: Line-mixing coefficients for transitions in the oxygen A-band. Comparison between experimental results and theoretically calculated values using the EPG-scaling law. Here, $m = -J'' = -N$ is for the P- and $m = J'' + 1 = N'' + 1$ is for the R-branch.

The coefficients reported by Drouin et al. [74] show a noticeable deviation between $m = -25$ and -30 , and between $m = 20$ and 24 . Experimentally retrieved VP and RP line-mixing coefficients are on average within 3 %, and the SDV and SDR are within 5 % on average due to differences in the experimentally retrieved broadening values. However, they deviated from the experimental results reported by Predoi-Cross et al. [44] for $m = 14$ to 22 . Nevertheless, the best agreement can be found between the present EPG and the Predoi-Cross et al. EPG values in both branches.

In general, the line-mixing coefficients are very small (10^{-3} atm^{-1}) and determining their values according to the trends along the m axis can be very complicated. For this reason, there are only a few studies including this one (shown in the comparison), which

have presented the experimentally or theoretically determined line-mixing coefficients. Comparisons with the literature as well as with the theoretical results where possible (like EPG in this study) are important to provide reliable spectroscopic results to the database.

5.6.7 Speed-Dependent Parameter

The broadening and the shifting of lines are dependent on the absorber speed. For this reason, it is important to consider the speed-dependent line-shape profiles while fitting spectra. Drouin et al. [74] have modified the Voigt line-shape model to introduce the narrowing and the SD parameters.

In the present study, the SD parameters were retrieved using the SDV (with the line-mixing fix “SDV_lmfix” and line-mixing fit “SDV_lmfit”) and SDR (with line-mixing fit “SDR_lmfit”) profiles. The SD parameters retrieved from the SDV and the SDR profiles are listed in Tables B.3 and B.4 of the Appendix B, respectively, and plotted in Figure 5.13 along with the results reported by Drouin et al. [74]. The SD parameters are plotted with the corresponding error values (error bars). Here, the errors are given in one standard deviation (in Tables B.1 and B.4) uncertainty of the last digit.

All values are positive but are very small (less than 0.035) compared to the Drouin et al. values (above 0.072) [74]. The latter are different than the ones retrieved in the present study, because their results were obtained from nitrogen-broadened oxygen spectra, while the magnitude of the effect depends on the mass of the absorber and the perturber. For pure oxygen, the absorber and the perturber have the same molecular mass of 32 g/mol, but for O₂ broaden by N₂ is 32 g/mol and 28 g/mol, which explains why they are different. Theoretically, it is known that those parameters, which represent asymmetry in the modeled

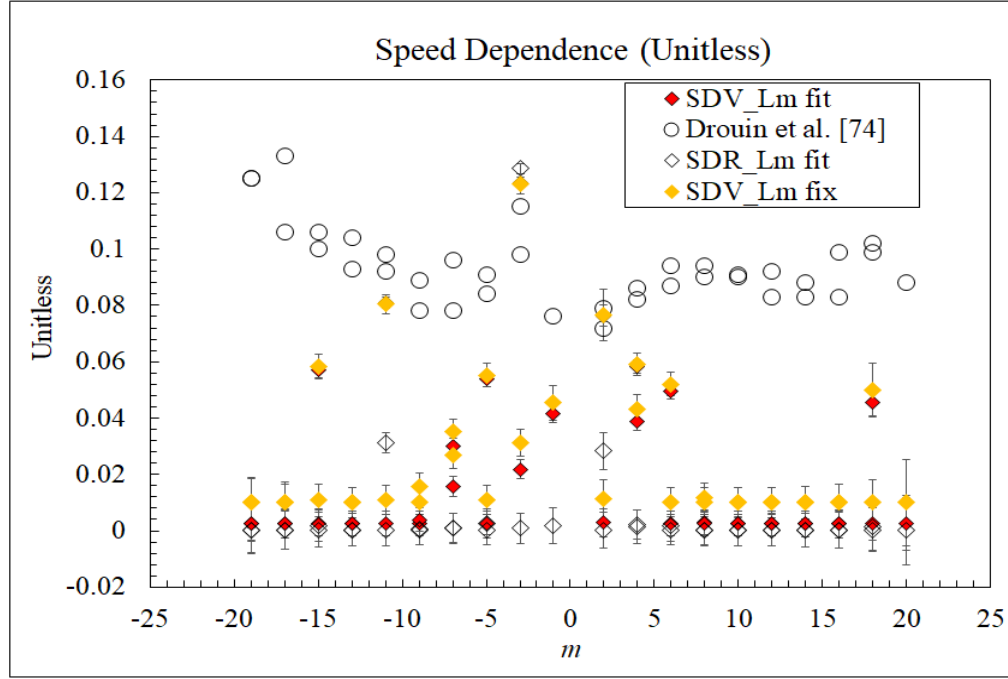


Figure 5.13: The speed-dependence parameters for transitions in the oxygen A-band. Here, $m = -J'' = -N$ is for the P-, and $m = J'' + 1 = N'' + 1$ is for R-branch.

spectra are supposed to be $|m|$ independent. According to the theoretical assumption, the SD parameters are supposed to be constant for a given band [74]. Most of the SD parameters retrieved in the present study using the SDR profile follow that trend when plotted against the m index (which is constant across the band) in Figure 5.13. The (SDR)_Lm fit parameters also give the lowest standard deviation (0.007) compared to the Drouin et al.'s standard deviation (0.014). Mainly for the SDV fits, some of the results deviated from the usual trend, because this profile does not consider the correlation of collisional narrowing and speed-dependence simultaneously. It is noticeable from the plot and the calculated standard deviation of SDV_Lm fit (0.024) and SDV_Lm fix (0.021) that both give a quite similar pattern beside $m = -11$, -3 , and 2 .

5.6.8 Molecular Constant for Upper Energy States

The molecular constants were derived for the upper energy state (*b*) of the oxygen A-band. Lower state (*X*) energy values were added with their corresponding line positions (transition wavenumbers) of the A-band to determine energy values of the upper state. The lower state energy values are listed in the HITRAN 2016 database [141]. The upper state energy values were then fitted using the following expression to determine the band center (transition term value, G_0), the rotational constant, B_0 , and the centrifugal distortion constants, D_0 and H_0 :

$$E' = G_0 + B_0 J'(J' + 1) - D_0 J'^2 (J' + 1)^2 + H_0 J'^3 (J' + 1)^3 \text{ (cm}^{-1}\text{)}. \quad (5.7)$$

The molecular constants were determined for both *P*- and *R*-branch lines. Energy data were fitted using the 3rd order polynomial of the upper rotational quantum number, $J'(J'+1)$, as shown in the Equation 5.7. Figure 5.14 shows an example of the *P*-branch fit. The upper level energy terms are plotted against $J'(J'+1)$, where J' represents the rotational quantum numbers associated with the upper energy levels. The results for *P*-branch and the *R*-branch constants are listed in Table 5.4.

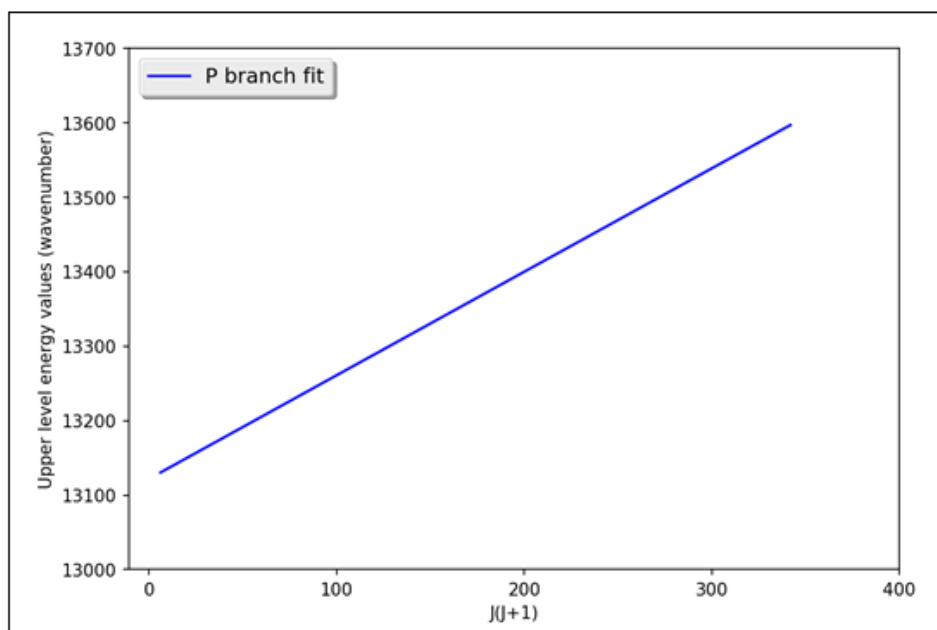


Figure 5.14: *P*-branch fit plot to determine the molecular constants.

Table 5.4: The fit values of molecular constants in the upper state of the oxygen A-band. All parameters are given in wavenumber unit (cm^{-1}).

Parameter cm^{-1}	Present study (<i>P</i> -branch)	Present study (<i>R</i> - branch)	Drouin et al. [74]	Predoi-Cross et al. [44] (CO calibration)
G_0	13122.00567(7)	13122.00084(564)	13122.006033(8)	13122.2521(1)
B_0	1.391252(1)	1.391461(135)	1.39124765(8)	1.391251(6)
$D_0 \times 10^6$	5.382(9)	-	5.3631(2)	5.373(8)
$H_0 \times 10^{11}$	2.15(18)	-	-0.87(2)	-0.095(5)

The molecular constants retrieved in this study are compared with two other studies, Predoi-Cross et al. [44] and Drouin et al. [74] (Table 5.4). The constants determined using the *P*-branch lines agree more closely than those computed using the *R*-branch lines. However, the band constants determined using the *P*- and *R*- branches are in very good

agreement with each other, where the retrieved band centers and rotational constants are within 0.00003 % and 0.0150 %, respectively. For the P-branch, they are within 0.0018 %, 0.0005 %, and 0.7868 % with the literature values for the band center, rotational constant, and distortion constant, respectively. For the R-branch, the results are within 0.0019 % and 0.0336 % of the literature values for the band center and rotational constant, respectively. This comparison shows that the results are in very good agreement.

Drouin et al. [74] have used air mixed oxygen spectra of very long pathlengths, which is a reason for the slight difference in the values. Predoi-Cross et al. [44] have utilized spectra calibration to the CO-line, which explains why the constants are slightly different than the present results. Calibration for the correction of the wavenumber scale and having different perturbers may have caused the difference in values of the molecular constants. Another reason behind the small divergence could be due to the fact that not all the research groups have used the same formula to compute the energy levels.

5.6.9 Einstein A Coefficient

Oxygen A-band line positions and intensities were tested by also comparing the Einstein A_{ij} coefficient with the HITRAN 2016 database [141] and the Long et al. [47] values. Einstein A_{ij} coefficients for each transition were calculated using the experimental positions and intensity values using the following formula from HITRAN 2016 [141]:

$$S_{ij} = I_x \frac{A_{ij}}{8\pi c v_{ij}^2} \frac{g' e^{-c_2 \frac{E''}{T}} \left(1 - e^{-c_2 \frac{v_{ij}}{T}} \right)}{Q(T)}, \text{ (cm}^{-1}\text{/(molecule.cm}^{-2}\text{))} \quad (5.8)$$

where S_{ij} is the line intensity, I_x is the isotopic abundance, v_{ij} is the line position (in wavenumber cm^{-1}), g' represents the statistical weight of the upper state, c_2 is the second

radiation constant ($c_2 = hc/k$ (cm.K)), E'' represents the lower energy state (cm^{-1}), and the partition function $Q(T)$ represents the total internal partition summation.

The unit of the Einstein coefficients A_{ij} is s^{-1} . The comparisons of the Einstein A_{ij} coefficients between the present study, HITRAN 2016 database [141], and Long et al. [47] are shown in Figure 5.15 for 20 P -branch and 20 R -branch transitions as a function of the rotational constant (J'') of the lower energy level. In equation 5.8, line intensity and position are variables, and the others are constant terms for the same molecule.

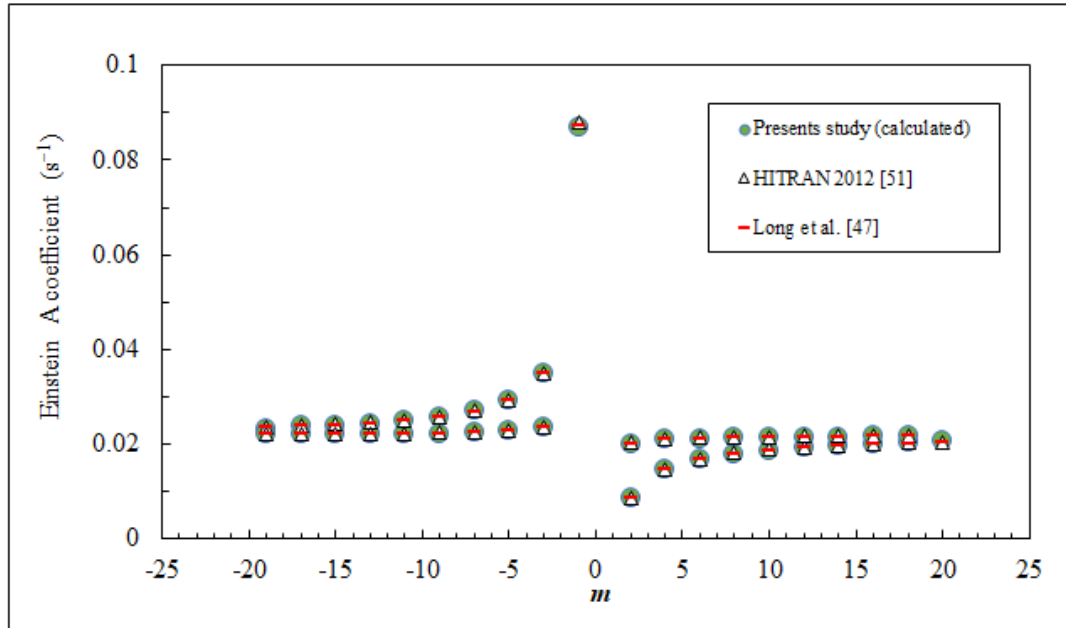


Figure 5.15: Comparison of the Einstein A_{ij} coefficient. Here, $m = -J'' = -N$ is for the P and $m = J'' + 1 = N'' + 1$ is for R-branch.

The Einstein coefficients of the lower energy levels (rotational constants (J'')) are plotted in Figure 5.1, where $m = -J''$ is for the P -branch (PP and PQ), and $J'' + 1$ is for the R -branch (RR and RQ) transitions. The Einstein coefficients calculated for the present study agree with the HITRAN 2016 (0.51 %) and Long et al. (0.27 %) results.

5.7 Conclusions

This study was intended to confirm and to extend the line-shape parameters of room-temperature pure oxygen spectra recorded at different pressures to enrich the spectroscopic database by publishing these accurate results. Spectral line positions, intensities, broadening and shift coefficients, line-mixing coefficients, and the speed-dependent parameters have been reported and compared to other studies in the literature. An FTS system was used for recording all the spectra, and an internal calibration procedure has been applied, which gives assurance of good quality spectra for analysis purposes.

All four models (VP, RP, SDV, and SDR) agree with each other in terms of their trends with varying rotational quantum numbers. In the comparisons, the line positions and line intensities were verified by comparing studies from the literature. Determining the band constants validated the line-position values and calculating the Einstein A_{ij} coefficients validated the line intensities values. The broadening coefficients were also in good agreement. They varied on average only by 0.17 %, while the shift coefficients retrieved using VP and RP indicate a 0.59 % difference on average when the narrowing parameter is fixed. Therefore, it is not necessary to use RP when fitting low and high-pressure spectra altogether. The broadening values varied on average only by 0.93 % when fitted with the SDV and SDR (similar as shown in Chapter 4). The simultaneous fitting procedure of a group of spectra using the Labfit software allows minimizing the random errors associated with the parameters. All these comparisons were made to validate the spectra before determining the SD parameters, because the broadening and the SD parameters retrieved in this study using the SDV and SDR profiles are important to give a more realistic representation of the modeled line shapes. Beside the present study, there

was only one other study by Drouin et al. [74], which has reported the SD parameters. The line-mixing and the speed-dependent effects are important to take the asymmetry into account. Furthermore, the calculated line-mixing coefficients using the EPG-scaling law were validated with the retrieved values from the experimental spectra. Comparisons of the line-shift coefficients showed that different calibration procedures have significant effects on the shift results (comparison with Predoi-Cross et al. [44] and Brown et al. [53]). Line-shape parameters retrieved in this study will be very useful for accurate measurements of oxygen abundance, climate change and cloud-top pressure from the atmospheric spectra, which are important for weather prediction.

Chapter 6 Assignment of $^{15}\text{NH}_3$ Far-Infrared Lines

6.1 Overview

In molecular spectroscopic studies, the goals at the initial stage of any spectral analysis are assigning line positions and determining molecular constants. Finding accurate line positions and identifying associated quantum numbers in a spectral band provides information on the molecular structure. The molecular constants, namely the rotational constants and centrifugal distortion constants can be used to calculate the moment of inertia of the corresponding rotational axis and bond lengths as discussed in Section 2.2.3.

This chapter presents an assignment study on far-infrared ground-state $^{15}\text{NH}_3$ spectra and the calculated molecular constants. A detailed description of ground-state transitions with examples will be discussed. The line positions from the assignment and the fitted results will be presented and compared to each other in this chapter.

6.2 Introduction

Studying nitrogen has been important to the scientific world for decades, because it is one of the major components of the Earth's atmosphere and also the fourth major component of the human body. Ammonia ($^{15}\text{NH}_3$) is one of the compounds, which contains nitrogen. There are a number of chemical products, which contain ammonia, and people use them in their everyday life for various purposes. Anthropogenic activities [81], such as the utilization of cleaning products, fertilizer, and fermentation, can directly or indirectly cause changes to environments, ecosystems, and natural resources. These activities increase or decrease the amount of nitrogen (including its isotopic species) in the Earth's

atmosphere. Natural causes such as rainwater and volcanic eruption can also alter the amount of atmospheric nitrogen [80]. The terrestrial abundance of ^{15}N in the atmosphere is 0.36 % [51], and it is inconstant in the lower terrestrial regions. Studying ammonia and its isotopes will allow the determination of the ratio between ^{14}N and ^{15}N , which is not constant [78, 82, 83]. Ammonia and its isotopes are also found in planetary atmospheres, comets and interstellar media [79]. They are also present in exoplanets and in the atmosphere of cold stars.

There are theoretical as well as experimental studies available on $^{14}\text{NH}_3$ and $^{15}\text{NH}_3$ [90, 147]. Spectral databases and archives, such as HITRAN, report a list of ammonia transitions; however, the information about $^{15}\text{NH}_3$ is limited, because there were only a few studies, which have been performed on ammonia and its isotopes over the last four decades. The present study provides an extended line list of $^{15}\text{NH}_3$ ground-state transitions from high-resolution infrared spectra. This line list and the calculated molecular constants will have use in the worldwide known HITRAN and GEISA databases. The HITRAN database has already been used in the atmospheric retrievals and for tropospheric observations of IASI (Infrared Atmospheric Sounding Interferometer) [148], and MIPAS (Michelson Interferometer for Passive Atmospheric Sounding) [149] for ammonia. In the future, this will be useful for the spectroscopic observations of SOFIA (Stratospheric Observatory for Infrared Astronomy) [84, 85] and ground-based ALMA (Atacama Large Millimeter Array) [86] [79]. For example, SOFIA is a joint project between the U.S. and German governments for stratospheric observations using infrared radiation. SOFIA observations include spectral imagery to study the composition of the planetary atmosphere, comets, and

interstellar medium. Therefore, it is important to perform studies like the one that is presented in this chapter to augment the aforementioned databases.

6.3 Ammonia Molecule

Ammonia is a symmetric top oblate molecule of one nitrogen and three hydrogen atoms. The angle between two adjacent hydrogen atoms is 107 degrees. Ammonia can undergo an inversion bending motion. The non-linear four-atom ammonia has $3 \times 4 - 6 = 6$ fundamental modes of vibration. The normal vibrational modes of NH_3 are shown in Figure 6.1 [8]. In this figure, the ν_1 and ν_2 are symmetric stretching and bending modes, respectively. The a_1 represents the symmetry of these two modes. The other four ν_{3a} , ν_{3b} , ν_{4a} , and ν_{4b} are degenerate modes.

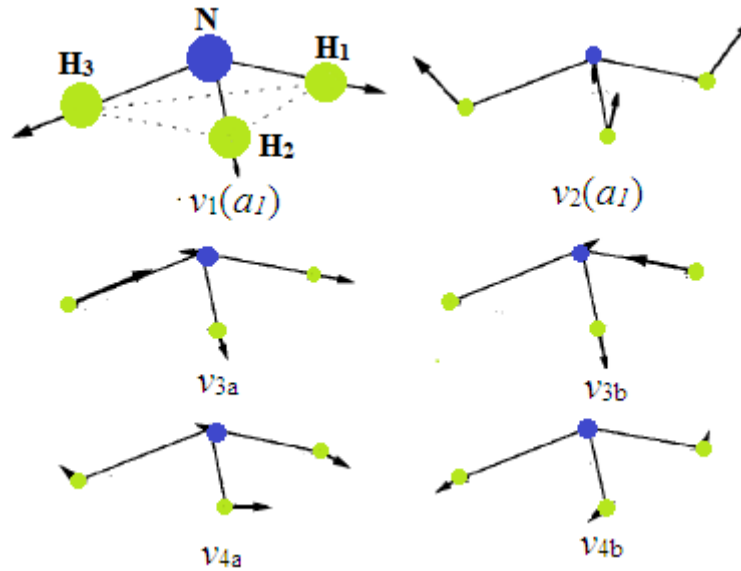


Figure 6.1: Stretching and bending vibrational modes of NH_3 (modification of Figure 4.17 in [8]).

6.4 Present Study

This study is dedicated to the assignment of $^{15}\text{NH}_3$ (ammonia) absorption lines of the GS transitions that occur in the far-infrared region. This work is published in the Journal of Quantitative Spectroscopy and Radiative Transfer (2017) by Fusina et al. [79]. The title is “The high-resolution spectrum of $^{15}\text{NH}_3$ in the far-infrared: Rotation-inversion transitions in the ground, $v_2 = 1, 2$ and $v_4 = 1$ states”. The types of studies reported in this chapter include the assignment of $^{15}\text{NH}_3$ absorption lines and the calculation of the molecular constants for the GS transitions in the $60 - 453 \text{ cm}^{-1}$ regions. The GS rotation-inversion transitions are the result of the bending mode, v_2 . This chapter will also present the line positions and intensities of the transitions retrieved from the spectra recorded within the $250 - 260 \text{ cm}^{-1}$ spectral range using the fitting method.

Only a few research groups have studied the ammonia ($^{15}\text{NH}_3$) molecules, but not very extensively. Some of them reported lists of lines up to 120 cm^{-1} [75], 250 cm^{-1} [90], and millimeter-wave regions [91]. Chapter 1 includes a brief description of previously published studies of ammonia ($^{15}\text{NH}_3$) [62-79]. The spectra used in these studies were recorded with lower resolution in than the present study (0.00096 cm^{-1}). Therefore, the goal of this study is to extend and advance the knowledge of the ammonia isotopologue ($^{15}\text{NH}_3$) using high-resolution FTS spectra of the IR region, which is very important for building a reliable and good-quality database [79].

Spectra of $^{15}\text{NH}_3$ were recorded and processed by the author of the thesis. The author of this thesis also performed the calibration procedure and the assignment of GS transitions in the $^{15}\text{NH}_3$ spectra, while L. Fusina, G. Di Lonardo, and E. Cane, spectroscopic

research group, Dipartimento di Chimica Industriale "Toso Montanari", University of Bologna, Italy completed the calculation of molecular constants. After that, the author of this thesis performed a fitting analysis to retrieve line positions from the experimental spectra. Dr. Adriana Preoi-Cross, the former PhD supervisor who had guided her during this project, also provided the funding. All the figures presented in this chapter were created by the author of this thesis.

6.5 Transitions in $^{15}\text{NH}_3$

Spectra of the ammonia molecule in the FIR region are the result of pure inversion and rotation-inversion transitions in the ground, $v_2 = 1$, 2 and $v_4 = 1$ states. Figure 6.2 shows an energy level diagram of $^{15}\text{NH}_3$ and examples of rotation-inversion, hot band, and vibration-rotation transitions.

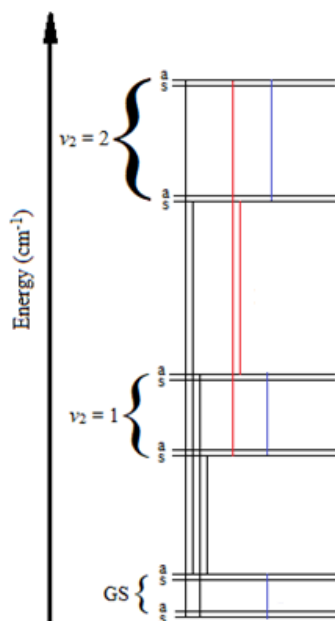


Figure 6.2: Diagram of energy levels showing examples of few transitions. The blue arrows are rotation-inversion, the red ones are hot bands ($v_2 = 1 \rightarrow v_2 = 2$) and the black ones are vibration-rotation transitions (GS \rightarrow upper states, $v_2 = 1$ and 2).

Three different types of transitions between lower and upper energy levels are indicated with coloured arrows. Lines that follow the black arrows correspond to the vibration-rotation transitions. They start from GS and go to $v_2 = 1$ and $v_2 = 2$ states. The red ones are the hot band transitions, from $v_2 = 1$ to $v_2 = 2$. The last type in the figure represents the inversion-rotation transitions shown with the blue arrows. Energy levels are presented in terms of wavenumber. Each energy state has two stacks of the sub-state called (*s*) and (*a*) symmetry. This chapter will focus only on the analysis and results of the GS transitions.

6.6 Recorded Spectra

A Bruker IFS 125 FTS system situated at the Canadian Light Source, Saskatoon, Canada was employed to record room temperature, low-pressure and unapodized spectra of $^{15}\text{NH}_3$ with a resolution of 0.00096 cm^{-1} . Details of the experimental setup are given in Section 3.3. Ammonia ($^{15}\text{NH}_3$) spectra (in the $60 - 360\text{ cm}^{-1}$ range) of very low-pressure (0.002 Torr) were recorded to avoid the saturation of the absorption lines. Spectra at pressures of 0.005, 0.051, and 1.000 Torr in the $60 - 360\text{ cm}^{-1}$ range and 0.767 Torr in the $350 - 500\text{ cm}^{-1}$ range were also collected and used for the analysis of the rotation-inversion bending mode. These spectra were analyzed to report the rotation-inversion GS transitions up to $J = 23$.

Raw data (interferograms) were processed using the OPUS software [129]. Details of the data processing are given in Section 3.4.1. The transmission spectra of all the pressures (0.002, 0.005, 0.051, and 1.000 Torr) were created from the sample spectra

divided by their corresponding background spectra. These transmission spectra were then used for calibration purpose. A portion of the 0.002 Torr spectra is presented in Figure 6.3.

6.7 Calibration of Spectra

The 15-ammonia ($^{15}\text{NH}_3$) gas sample (98 % purity) was supplied from Sigma-Aldrich. Even though it was a pure sample, some other species identified in the transmission spectra were 14-ammonia and water. The rotational water lines present in the 15-ammonia spectra were used for the calibration of spectra. Figure 6.3 shows a small spectral region ($137 - 140 \text{ cm}^{-1}$) of $^{15}\text{NH}_3$ recorded at 0.002 Torr pressure. This region displays the rotation-inversion GS ($J = 7_K - 6_K$, $a \leftarrow s$ and $s \leftarrow a$) transitions of the room-temperature $^{15}\text{NH}_3$ molecule. The water lines present in this region are shown with red stars and the ones of the $^{14}\text{NH}_3$ with green stars.

Water-line positions reported in two well-known H_2O studies by Johns [150] and Matsushima et al. [151] were considered as the standard values for the calibration. An example of the residuals (literature – present study) of H_2O line position is given in Figure 6.4 for the $100 - 150 \text{ cm}^{-1}$ spectral range. The average of the difference of H_2O lines was around $0.4 \times 10^{-4} \text{ cm}^{-1}$, which is smaller than the accuracy of the measurements (minimum $0.9 \times 10^{-3} \text{ cm}^{-1}$). Therefore, no correction was applied to the wavenumber scale of the spectra.

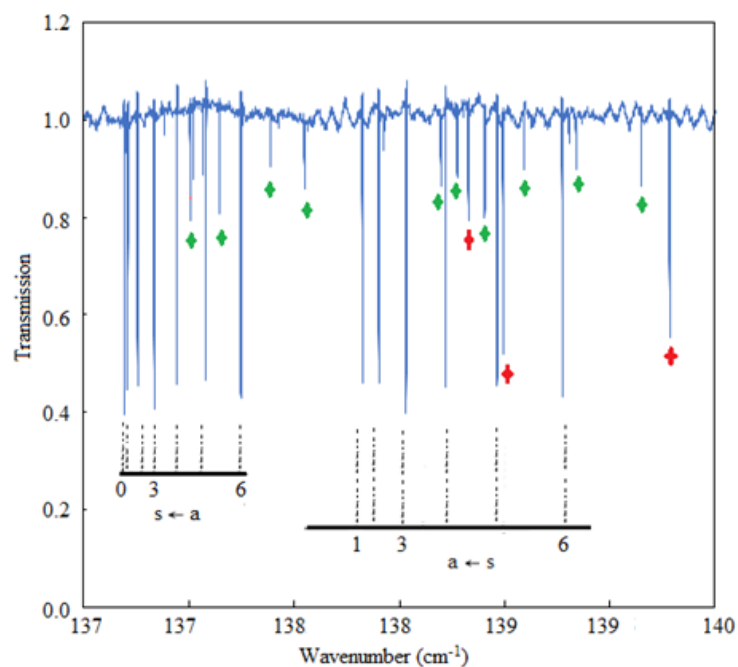


Figure 6.3: Example of absorption lines in a portion of the far-infrared spectrum showing the rotation-inversion (GS, $J = 7_K - 6_K$, $a \leftarrow s$ and $s \leftarrow a$) transitions of the $^{15}\text{NH}_3$ molecule [79]. The red stars are the water (H_2O) lines and the green ones are the $^{14}\text{NH}_3$ lines.

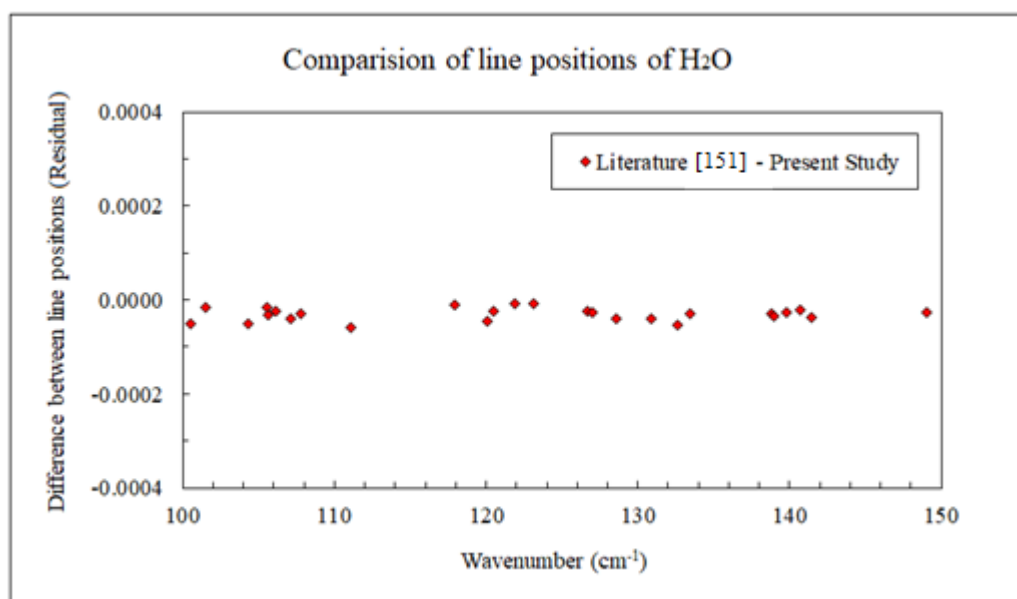


Figure 6.4: Residuals of H_2O lines calculated using the results from the literature [151] and from 0.002 Torr spectra of the present study recorded in the $100 - 150 \text{ cm}^{-1}$ regions (red diamonds). The water lines were compared for calibration purposes.

6.8 Ground-State Spectra

The rotation-inversion GS transitions of the pure $^{15}\text{NH}_3$ spectra appear due to the inversion tunneling of ^{15}N through three hydrogen nuclei. These types of transitions contain the two rotational quantum numbers, J and K , and associated symmetric (s) and (a) components. For $J = \text{odd numbers}$, $K = 0$ gives (s)-type energy levels; and for $J = \text{even numbers}$ and $K = 0$ provides (a)-type energy levels. Transitions are usually defined as $(J'K'S') \leftarrow (J''K''S'')$, where J' and K' are the rotational quantum numbers of the upper state and S' is the corresponding inversion symmetry, while J'' and K'' are the rotational quantum numbers of the lower energy state and S'' is the corresponding inversion symmetry. A clear pattern is noticeable in the GS ammonia spectra. The absorption lines corresponding to $K = 3n$ (where, $n = 1, 2, \dots$) are strong, but $K = 3n+1$ and $3n+2$ (where, $n = 1, 2, \dots$) are weak. For each $(J'K'S') \leftarrow (J''K''S'')$, two sub-branches, $a \leftarrow s$ and $s \leftarrow a$, are present. From $J'' = 1$ to 7, the sub-branches in the rotation-inversion spectra are completely separated by twice the rotational constant B values. From $J'' = 18$, the lines for the same K rotational quantum numbers start to overlap.

Figure 6.5 shows a portion of the FIR spectrum of the $^{15}\text{NH}_3$ GS transitions. It displays absorption lines of $J = 10_K \leftarrow 9_K$ located between 194 and 199 cm^{-1} . The $J'K'S' \leftarrow J''K''S''$ type transitions occupy this region, where $J' = 10, J'' = 9, K'' = 1$ to J'' and $s \leftarrow a$; and $a \leftarrow s$. Here, $s \leftarrow a$ and $a \leftarrow s$ create the sub-branches; these sub-branches overlap. The lines corresponding to $3, 6$, and $9K''$ are the stronger ones and for $s \leftarrow a$ the $K = 0$ line is missing. The water lines are marked with red stars.

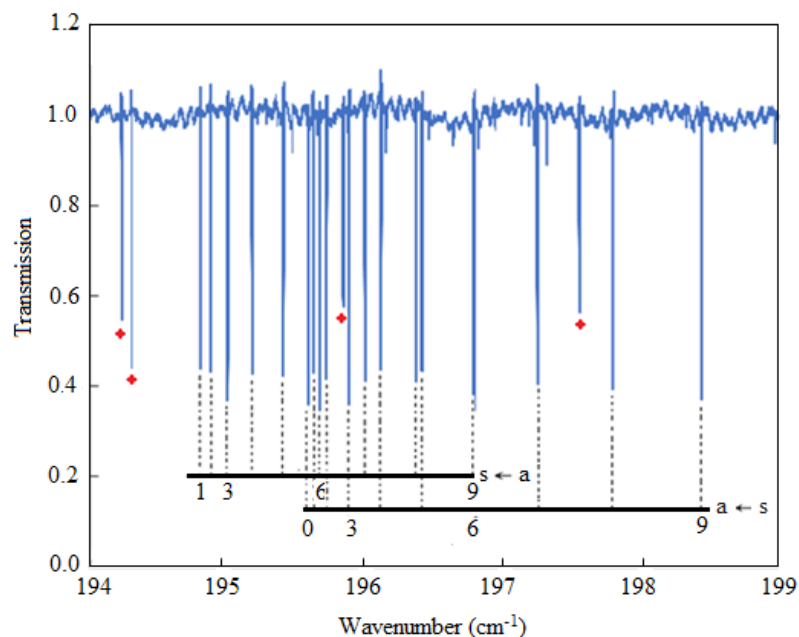


Figure 6.5: Example of absorption lines in a portion of the FIR spectrum showing the rotation-inversion (GS, $J = 10_K - 9_K$, $a \leftarrow s$ and $s \leftarrow a$) transitions (black dotted lines) of the $^{15}\text{NH}_3$ molecule. The H_2O lines are marked with red stars. The presentation concept was taken from the literature [79].

The structural configuration of the $^{14}\text{NH}_3$ (14-ammonia) and $^{15}\text{NH}_3$ (15-ammonia) GS spectra are very similar. The observation of the full spectral range used in this study shows that the $^{15}\text{NH}_3$ GS spectrum is shifted by 0.20 wavenumbers (cm^{-1}) around 80 cm^{-1} , 0.44 wavenumbers (cm^{-1}) around 180 cm^{-1} , 0.68 wavenumbers (cm^{-1}) around 270 cm^{-1} and by 1.15 wavenumbers (cm^{-1}) around 450 cm^{-1} .

6.9 Details of Analysis and Results

The following sections present the results from the assignment of the $^{15}\text{NH}_3$ GS transitions – the molecular constants. The fitted results of line positions and intensities are also given in the next sections.

6.9.1 Assignment of Absorption Transition

For the assignment of spectra, one has to predict the transition frequencies from the estimated molecular constants, namely, the rotational constants in the lower and upper state and centrifugal distortion constants, which are identical. One can also explore the literature for available theoretical values to start. The typical patterns of absorption bands need then to be sought. The structures of the branch system (P, Q, and R) are described in Section 2.2.5. The theoretical knowledge of band patterns of molecules can be found in the literature [8, 90, 101, 147]. These typical patterns are periodically recurring spectral features. The description of the GS spectra is given in Section 6.8. An example of transitions of type $J = 10_K - 9_K$, $a \leftarrow s$ and $s \leftarrow a$ is shown in Figure 6.5. This is the typical branch structure of $^{15}\text{NH}_3$ -GS spectra around the 200 cm^{-1} regions. The distance between two adjacent absorption lines can be calculated from the rotational constants. Accordingly, it is then possible to find the successive line positions, if one knows the rotational constant of a band. This assignment was performed by the author of the thesis [79].

Table 6.1: Type of assigned transitions in the ground state of ammonia ($^{15}\text{NH}_3$) recorded in the FIR spectral region using a Bruker IFS 125 Fourier transform spectrometer system.

Vibrational state	Type of transitions	No. of Assigned lines	Observed higher J
Ground State	FIR $\Delta K = 0$	439	23

Spectra of the $60 - 453\text{ cm}^{-1}$ range were used in this assignment study. Table 6.1 lists the total number of assigned lines for the GS transitions. In this study, 439 transitions of the selection rules $\Delta J = +1$ and $\Delta K = 0$ (i.e., up to $J = 23_K \leftarrow 22_K$) have been assigned.

6.9.2 Intensity Analysis

The line intensity is one of the parameters essential for spectroscopic databases. Accurate measurements of the intensity along with the line position of a transition is a unique piece of spectroscopic information for a given molecular spectrum. Once the line positions (assignment) and the molecular constants of the GS rotational spectra are determined, the spectra can be used for the retrieval of line-shape parameters [79]. Thus, the author of this thesis analyzed a portion of the $^{15}\text{NH}_3$ spectra to retrieve experimental line intensities.

The line positions and corresponding intensities were retrieved by fitting the $^{15}\text{NH}_3$ spectra in the Labfit software. The intensity of an absorption line depends on the concentration of the gas. Input files of the absorption lines in 250 - 260 cm^{-1} range were created using the Labfit software. At the end of each fit, Labfit gives an output file of results (line positions and intensities) and a plot file to display the fitted spectra. The spectrum of the 250 – 260 cm^{-1} region, the retrieved line positions, and intensities, and an example of a fitted line using the VP and its residual are given in Section 6.9.4.

6.9.3 Results of Molecular Constants

Molecular constants of the GS of $^{15}\text{NH}_3$ were calculated after the assignment procedure was completed. Before calculating the spectroscopic parameters, the assigned transitions were compared with their theoretically predicted values given by Yurchenko [147] as stated in his paper [79]. The calculated spectroscopic parameters for the GS transitions are given in Table 6.2 and details of the calculation are given in Appendix C. These are the final results obtained after performing several fits.

Table 6.2: Spectroscopic parameters presented in the wavenumber unit (cm^{-1}) for the ground state of $^{15}\text{NH}_3$. The uncertainties are given in the parenthesis as one standard deviation (1σ) referring to the last significant digits [79]. Here, (i) corresponds to the lower and upper state components (s) and (a) of the inversion doublet. This table is a modified version of Table 2 of the published paper (results are unchanged) [79].

Parameter		(s)	Uncertainty	(a)	Uncertainty
$^{(i)}E^0$ ^b		0.0 ^c		0.7576866676	(50169)
$^{(i)}B$		9.92235895860	(89904)	9.9174300244	(10041)
$^{(i)}C$		6.2278859346	(12710)	6.2298007878	(122722)
$^{(i)}D_J$	$\times 10^3$	0.8519558694	(59434)	0.8352214549	(64304)
$^{(i)}D_{JK}$	$\times 10^3$	-1.5846673531	(24513)	-1.538665275	(25094)
$^{(i)}D_K$	$\times 10^3$	0.917908105	(47085)	0.886499394	(47137)
$^{(i)}H_J$	$\times 10^6$	0.24433924	(46205)	0.20485761	(15894)
$^{(i)}H_{JJ}$	$\times 10^6$	-0.7751107	(13745)	-0.6139901	(13547)
$^{(i)}H_{JK}$	$\times 10^6$	0.8674744	(22557)	0.64907860	(22314)
$^{(i)}H_K$	$\times 10^6$	-0.3132425	(12800)	-0.2154453	(27363)
$^{(i)}L_J$	$\times 10^9$	-0.12421585	(17692)	-0.05371813	(27363)
$^{(i)}L_{JJ}$	$\times 10^9$	0.6847699	(25240)	0.3001968	(26352)
$^{(i)}L_{JK}$	$\times 10^9$	-1.596196	(12618)	-0.816811	(12568)
$^{(i)}L_{KK}$	$\times 10^9$	1.635519	(17884)	0.939147	(17766)
$^{(i)}L_K$	$\times 10^9$	-0.657195	(10540)	-0.425787	(10496)
$^{(i)}M_J$	$\times 10^{12}$	0.04987155	(20363)	-0.038497688	(58660)
$^{(i)}M_{JJ}$	$\times 10^{12}$	-0.5401160	(27486)	-0.038497688	(58660)
$^{(i)}M_{JK}$	$\times 10^{12}$	2.269098	(16085)	0.592208	(17049)
$^{(i)}M_{KK}$	$\times 10^{12}$	-3.894898	(34479)	-1.617351	(35289)
$^{(i)}M_{KKK}$	$\times 10^{12}$	2.896958	(35722)	1.365902	(36375)
$^{(i)}M_K$	$\times 10^{12}$	-0.650454	(22162)	-0.242944	(22307)
$^{(i)}N_J$	$\times 10^{15}$	0.0 ^c		0.05584039	(52686)
$^{(i)}N_{JJ}$	$\times 10^{15}$	0.0 ^c		-0.4761334	(31807)
$^{(i)}N_{JK}$	$\times 10^{15}$	0.0 ^c		1.6749657	(90100)
$^{(i)}N_{KK}$	$\times 10^{15}$	0.0 ^c		-3.101659	(15390)
$^{(i)}N_{KKK}$	$\times 10^{15}$	0.0 ^c		3.176832	(16846)
$^{(i)}N_{KKKK}$	$\times 10^{15}$	0.0 ^c		-1.702744	(11070)
$^{(i)}N_K$	$\times 10^{15}$	0.0 ^c		0.3725286	(33143)
Interaction parameters					
A	$\times 10^3$	0.19390236		(70529)	
α_J	$\times 10^6$	-0.08861480		(12253)	
α_K	$\times 10^6$	-0.0696449		(47304)	
α_{JJ}	$\times 10^9$	0.03728633		(24887)	
α_{JK}	$\times 10^9$	0.3387465		(50384)	
α_{KK}	$\times 10^9$	-0.2305381		(50383)	
$^{(a)}\eta_3 = ^{(s)}\eta_3$	$\times 10^9$	-4.082670		(74343)	

^b Inversion splitting in the GS for $J = K = 0.0$

^c Constrained.

The rotational energy values were obtained for inversion states (*a*) and (*s*). The correlations were also taken into account, while fitting the parameters. The *k*-dependent parameters (distortion constants) were obtained to the 12th power for *J* up to 23 rotational quantum numbers. During the fitting procedure, the distortion constants *C*, *D_K*, *H_{JKK}*, *H_K*, *L_{JKKK}*, *L_K*, and *M_K* were fully correlated to the corresponding (*a*) components [79]. The uncertainties corresponding to each parameter are given in the column next to them. The molecular constants and interaction parameter, η_3 , in Table 6.2 were compared with the values given in references [75, 93, 152, 153] and found to be in very good agreement (stated in the paper [79]).

6.9.4 Ground-State Assignment

In Table 6.3, the capital letters, *J'* and *K'*, represent the rotational quantum numbers for the upper and *J''* and *K''* for the lower energy states. *S'* and *S''* are symmetry notation for the upper and lower energy states. Columns 7 and 8 list the assigned line positions and the fitted line positions, respectively. The corresponding intensities are listed in column 9, while the Einstein coefficients [79] are given in the last column. The uncertainties of the line positions and the intensities are given in the parenthesis corresponding to one standard deviation (1σ) referring to the last significant digits [79]. Line positions and intensities were retrieved using the Labfit software. The multispectral fitting routine used here is a least-square fitting, which follows an iterative process minimizing the random errors through its iteration steps. They are calculated as the sum of the squares of the difference between the calculated spectra and observed spectra. The initial values of the spectroscopic parameters get updated at the end of each iteration. Details of the Labfit output are given in Section 3.6.

Table 6.3: An example of assigned and fitted line positions, intensities and Einstein coefficients for the pure inversion and rotation-inversion transitions in the ground state ($J = 13_K \leftarrow 12_K$) of ammonia ($^{15}\text{NH}_3$). The uncertainties are given in the parenthesis corresponding to one standard deviation (1σ) referring to the last significant digits. J' and K' are the upper, and J'' and K'' are the lower energy state rotational quantum numbers. S' and S'' are the inversion symmetry for the upper and lower energy states, respectively.

J'	K'	S'	J''	K''	S''	Assigned lines (cm^{-1})	Fitted (Experimental) (cm^{-1})	Intensity $\text{cm}^{-1}/(\text{molecule} \cdot \text{cm}^{-2})$	Einstein coefficient [79]
1	2	3	4	5	6	7	8	9	10
13	0	s	12	0	a	250.74285	250.743574(1)	1.18E-21(4)	0.535E+01
13	1	s	12	1	a	250.77461	250.775308(2)	6.63E-22(4)	0.532E+01
13	2	s	12	2	a	250.86989	250.870618(2)	6.74E-22(4)	0.523E+01
13	3	s	12	3	a	251.03930	251.04004(2)	1.474E-21(10)	0.507E+01
13	4	s	12	4	a	251.25279	251.253515(3)	7.62E-22(5)	0.484E+01
13	5	s	12	5	a	251.54170	251.542413(4)	8.11E-22(9)	0.456E+01
13	6	s	12	6	a	251.89662	251.897347(2)	1.547E-21(10)	0.421E+01
13	7	s	12	7	a	252.31849	252.319204(2)	9.89E-22(6)	0.379E+01
13	8	s	12	8	a	252.80799	252.808719(3)	1.133E-21(11)	0.332E+01
13	9	s	12	9	a	253.36563	253.366364(4)	2.043E-21(30)	0.278E+01
13	10	s	12	10	a	253.99109	253.99182(3)	1.302E-21(14)	0.218E+01
13	11	s	12	11	a	254.68285	254.68358(2)	1.325E-21(7)	0.151E+01
13	12	s	12	12	a	255.43710	255.437851(3)	1.858E-21(20)	0.785E+00
13	1	a	12	1	s	251.29535	251.296072(5)	6.58E-22(8)	0.535E+01
13	2	a	12	2	s	251.40471	251.403437(6)	5.8E-23(71)	0.526E+01
13	3	a	12	3	s	251.57642	251.577128(2)	1.265E-21(8)	0.510E+01
13	4	a	12	4	s	251.84755	251.848291(3)	7.61E-22(6)	0.488E+01
13	5	a	12	5	s	252.18582	252.186525(4)	8.27E-22(9)	0.459E+01
13	6	a	12	6	s	252.60662	252.607335(2)	1.549E-21(10)	0.424E+01
13	7	a	12	7	s	253.11502	253.115743(2)	1.006E-21(7)	0.383E+01
13	8	a	12	8	s	253.71762	253.718332(2)	1.134E-21(6)	0.335E+01
13	9	a	12	9	s	254.42288	254.423625(3)	2.066E-21(22)	0.281E+01
13	10	a	12	10	s	255.24201	255.24277(2)	1.342E-21(7)	0.221E+01
13	11	a	12	11	s	256.18967	256.190438(2)	1.333E-21(8)	0.154E+01
13	12	a	12	12	s	257.28544	257.28621(3)	1.877E-21(22)	0.802E+00

Figure 6.6 shows the spectral range that was used for retrieving the line positions and corresponding intensities. A comparison of the retrieved $^{15}\text{NH}_3$ -line positions is presented in Figure 6.7. These are the positions for the transitions $J = 13_K \leftarrow 12_K$ in GS. Comparisons of line positions were made between assigned and fitted values, the HITRAN 2016 database, and literature values [90]. For the present study, the fitted line positions show better agreement (within of 0.0005 %) with the assigned line positions [79] (maximum difference 0.0012 cm^{-1}) than with those reported in the HITRAN 2016 database (0.0011 %) and literature by Carlotti et al. (0.0051 %) [90]. Both assigned and fitted lines were obtained from the same FTS spectra, which means that these are good fits. Accordingly, they are reliable results, which are within an average of 0.0003 % and an average difference of 0.0007 cm^{-1} . This is smaller than the resolution.

According to Figure 6.7, the comparison of fitted line positions in the present study with the assigned line positions by Carlotti et al. [90] shows overall a similar trend as the comparison with HITRAN 2016. However, the results of Carlotti et al. indicate more deviations. The maximum shift of 0.01 cm^{-1} between the present fitting results and the Carlotti et al. lines were found at 253.99 cm^{-1} . Their spectra were recorded with a resolution of 0.03 cm^{-1} , which is lower than the one used in the present study. They have reported it as a blended line, and the accuracy was only 0.01 cm^{-1} . The present experimental lines show a maximum shift of 0.003 cm^{-1} with the HITRAN 2016 lines at 251.404 cm^{-1} . The fitted $^{15}\text{NH}_3$ -lines start to shift around 252.319 cm^{-1} toward the right when compared to the HITRAN 2016 lines. There were no other experimental studies for additional comparisons.

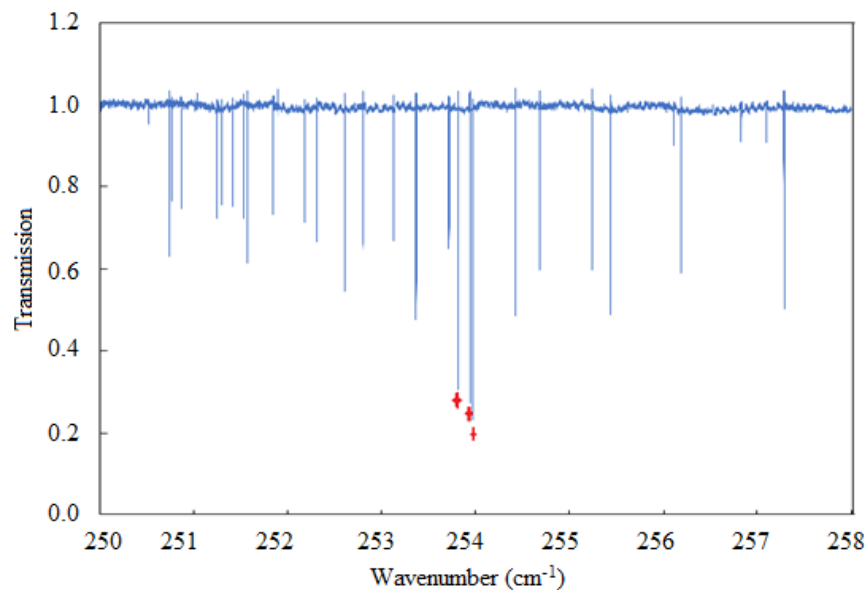


Figure 6.6: Ground-state spectra of $^{15}\text{NH}_3$ in the 250 – 260 cm^{-1} region. Water lines in this region are indicated with red stars.

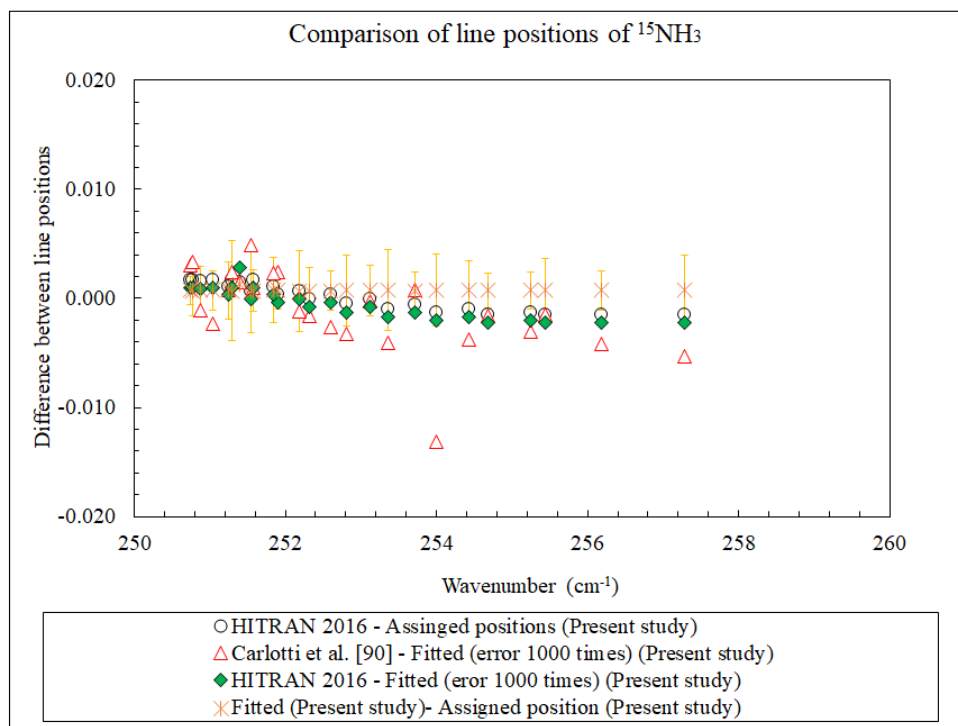


Figure 6.7: Comparison of assigned experimental (present study [79]) and fitted experimental (present study) line position of $J = 13_K \leftarrow 12_K$ transitions in the ground states of ammonia. Error bars (1000 times) represent the errors in the fitted results from Column 8 of Table 6.3.

Figure 6.8 shows a $^{15}\text{NH}_3$ line after fitting for the line position and the intensity (upper panel). This line was chosen for display, because it is nicely isolated and no other absorption lines are overlapped near the wings. The green line is experimental, and the red line is the fitted spectrum (VP). The residual in the bottom panel with 0.565 % global standard deviation implies that it is a good fit.

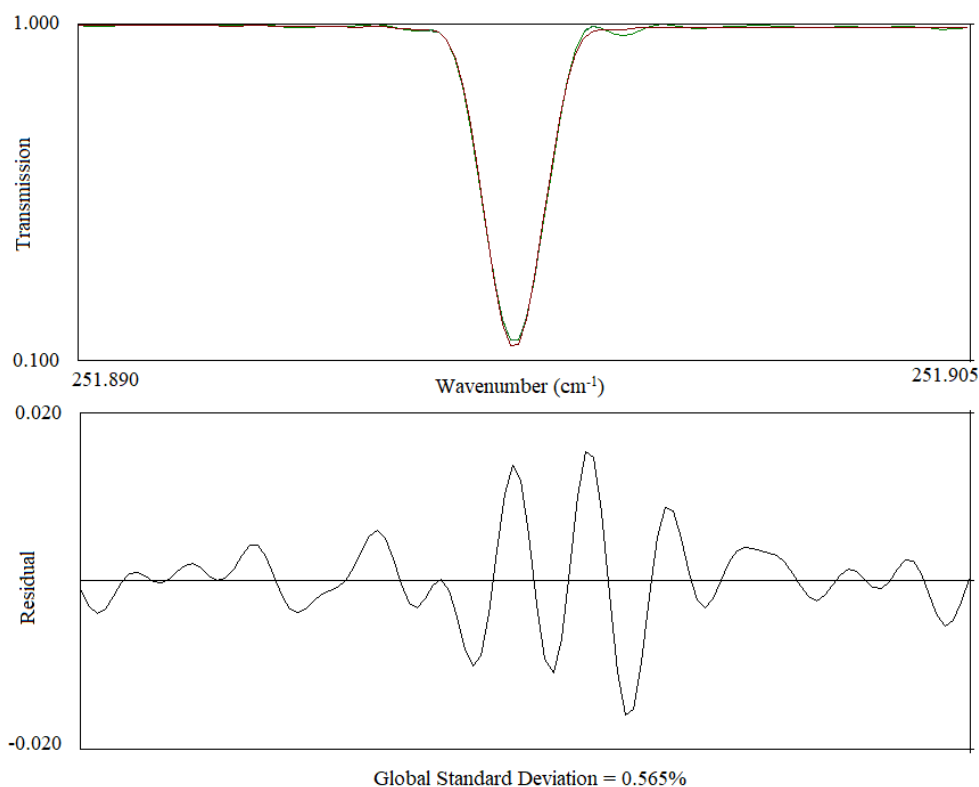


Figure 6.8: An example of the fit for the $^{15}\text{NH}_3$ -line ($J = 13_K \leftarrow 12_K$, $K'' = 6$) at 251.8973 cm^{-1} . The green and the red lines in the upper panel are the experimental and the fitted spectra, respectively.

The fitted intensities were on average 7.59 times smaller than the HITRAN 2016 database values. However, the positions of the assigned lines and the fitted lines have an average difference of 0.00075 cm^{-1} , which implies a good agreement. The 25 fitted line positions that agree very well with the assigned lines gave a low global standard deviation between 0.43 % and 0.95 %. The lines that were fitted nicely with the low global standard

deviation were fitted to retrieve the intensity values as well. However, an attempt was made to find the reason behind this difference between experimental and HITRAN intensity values, which was assumed due to a change in the $^{15}\text{NH}_3$ gas concentration. The $^{15}\text{NH}_3$ -sample used in this study is isotopically enriched with a purity of about 98 %. This gas has a bad characteristic of adhering to the walls of the gas cell, leading the concentration of $^{15}\text{NH}_3$ to decrease down to 40 % of the initial concentration. Also, over the long scanning hours, the pressure went down 30 % below the initial pressure. This is the likely reason for the discrepancies occurred in the intensity values between the experimental and the HITRAN results. It was determined using the calculations as described in the following paragraphs.

HITRAN reports intensities of the $^{15}\text{NH}_3$ for 0.36 % abundance whereas the $^{15}\text{NH}_3$ -sample of the present study had a purity of 98 %. Therefore, the following formula was considered to compare the intensity values of the HITRAN database and present retrievals:

$$\text{HITRAN intensity} / 0.0036 = \text{Intensity in the present study} / 0.98. \quad (6.1)$$

The above formula resulted in an intensity of the present study, which was 7.59 smaller than the HITRAN values as mentioned above. A test was then performed while fitting the spectra of $^{15}\text{NH}_3$. The gas concentration of 40 % was selected instead of 98 %. The pressure was set to 30 % less than the actual pressure, because the pressure went down over the scanning period. Therefore, the above formula was corrected using 40 % purity of $^{15}\text{NH}_3$ in the sample after retrieving the new intensity value as follows:

$$\text{HITRAN intensity} / 0.0036 = \text{Intensity in the present study} / 0.40. \quad (6.2)$$

The newly calculated intensities were then a factor of ~ 1 off compared to the HITRAN intensity. It indicates that the pressure and the concentration correction is needed when fitting $^{15}\text{NH}_3$ spectra for the intensity retrieval as the line strength depends on them and the gas has a bad characteristic of adhering to the walls. The $^{15}\text{NH}_3$ spectra showed presence of $^{14}\text{NH}_3$ and H_2O lines, among them, the water lines were used for calibrating the spectra. In addition to them, many unknown extra lines were observed. These lines were the results of transitions by HOD and $^{15}\text{NH}_2\text{D}$ [95], causing more impurity. There are no other experimental studies available to compare the intensity results.

6.10 Conclusion

High-resolution 0.00096 cm^{-1} $^{15}\text{NH}_3$ -spectra were recorded using the FTS facility located at the far-infrared beamline of the Canadian Light Source. Using these spectra, the assignment of rotation-inversion transitions up to $J = 23_K \leftarrow 22_K$ in the GS ($60 - 453\text{ cm}^{-1}$) was performed. This study also reports the line intensities for the $J = 13_K \leftarrow 12_K$ transitions in the $250 - 260\text{ cm}^{-1}$ range.

This study concluded with a better line list than the previous studies for the $^{15}\text{NH}_3$ transitions in the GS from high-resolution FTS spectra (as shown in Section 6.10.2). No other experimental studies have used $^{15}\text{NH}_3$ -spectra of a resolution of 0.00096 cm^{-1} like this one. Such an extended line list of ammonia ($^{15}\text{NH}_3$) will improve the HITRAN database and observation of the terrestrial atmosphere. This spectroscopic research group, Department of Physics and Astronomy, University of Lethbridge, intends to send these results to the HITRAN database with permission from the collaborators after the completion of my PhD work.

Chapter 7 Conclusions

7.1 Summary of the Work

The work presented in this thesis is devoted to testing the performance of different line-shape profiles, checking the accuracy of retrieved parameters through comparisons with literature values and retrieving new parameters, which were not experimentally studied before, and determining the molecular constants and extend the assignment analysis of molecular spectra. Two spectrometer systems, a diode-laser spectrometer and Fourier Transform Spectrometers (FTS), were employed for these purposes. Firstly, the focus was to test different line-shape profiles in the first study. The goal of the second study was to obtain new line-shape parameters and validate them so that the values can be used for future studies. The goal of the third one was to assign absorption lines of molecular spectra from FTS spectra, which were not experimentally performed before as extensively as in this one. This information will improve the spectral databases, such as HITRAN and GEISA. Last but not least, these experimental results were also used for validating some of the theoretical calculations where appropriate and vice versa. A summary of the result chapters and the findings of each experimental study are discussed in the following paragraphs.

Spectra of the three spectroscopic studies were recorded using different types of instrumental setups located at different locations and are as follows:

- 1) Acetylene spectra were recorded using the 3-channel diode-laser spectrometer system at the University of Lethbridge, Lethbridge, Canada. This system was developed by the spectroscopic group of the Department of Physics and

Astronomy, University of Lethbridge and was tested by Chad Povey [6], one of the former PhD students.

- 2) The oxygen spectra were collected using the FTS system at the Justus Liebig University in Giessen, Germany.
- 3) The ammonia spectra were acquired at the facility of the Canadian Light Source, Saskatoon, Saskatchewan, Canada using an FTS system.

Chapter 4 presents a study of testing line-shape models on six acetylene transitions in the $\nu_1+\nu_3$ band broadened by nitrogen. The six isolated lines, P(21), P(19), P(16), R(16), R(19) and R(21), were selected for this study. Eight line-shape models were tested using room temperature spectra recorded at different pressure ranges. Low-pressure spectra (5 – 40 Torr) were fitted with the Voigt (VP), Galatry (GP), Rautian (RP), fully-correlated Rautian (CRP), and Rautian-Galatry (RGP) models by taking the narrowing effect into account. The spectra of the entire pressure range (5 – 250 Torr) were fitted using the Speed-dependent Voigt (SDV), Speed-dependent Rautian (SDR), and Correlated Speed-dependent Rautian (CSDR) profiles to take the speed dependency into account. Influence of molecular interaction potential on the line-shapes was also examined for the SDV profile.

Chapter 5 reports the line-shape study of the oxygen A-band spectra recorded from a pure gas sample. Results for line positions, intensities, self-broadening, self-shifting, self-narrowing, line-mixing and speed-dependent (SD) parameters were reported. Line-position values were validated by determining the band constants and line intensities by calculating the Einstein A_{ij} coefficients. All these parameters were obtained, and their accuracy was tested to retrieve the speed-dependent parameters. Furthermore, the experimental self-

broadening and self-line-mixing values were implemented in the Exponential Power Gap scaling law to derive the theoretical line-mixing coefficients.

Chapter 6 presents an extended assignment study of the ammonia ($^{15}\text{NH}_3$) molecule for the rotation-inversion up to $J = 23_K$, (60 - 453 cm^{-1} region) transitions in the ground state. The 15-ammonia lines were never assigned to this extent before from experimental spectra. A high-resolution instrument (FTS) was used for recording spectra of 0.00096 cm^{-1} resolution. Rotational and centrifugal distortion constants were determined up to the 12th power in the angular momentum defined in the Hamiltonian (Equation C.3 of Appendix C) with the collaboration of the Spectroscopic research group of the Dipartimento di Chimica Industriale "Toso Montanari", University of Bologna, Italy. Intensities of absorption lines for the $J = 13_K - 12_K$ transitions were also retrieved and reported.

7.2 Findings

This section presents an overview of the achieved goals from the results of the three researches reported in the previous section.

Acetylene: This line-shape study was intended to find the best-fit models. The most commonly used VP results were within 10 % with the VP results from the literature. The residuals of the fitted spectra were also examined based on their RMS values. This observation determines that the VP can fit experimental spectra, however the residuals of 5 – 40 Torr spectra show the presence of a narrowing effect, which were fitted better with 20 % smaller residuals using the Rautian profile. In addition, the spectra of acetylene absorption lines of the entire pressure range (2 - 250 Torr) fit better using SDV (6 %), SDR and CSDR (8 %) than the VP, because SD profiles take the asymmetric effect (speed

dependency) into account. The smaller the residuals the better the fits are, which resulted in the retrieval of parameters with less errors.

Furthermore, tests were also performed to check the influence of the molecular (absorber-perturber) interaction potential on line-shape models. After fitting the interaction potential for different values of $q = 1$ to 12 using the Speed-dependent Voigt profile, the $q = 5$ gives a slightly better residual because of the absorber-perturber mass ratio which is ~ 1 . The RMS increases at least by 2 % - 5 % with decreasing q (from 4) and increasing q (from 6).

Oxygen: This study provides detailed knowledge of the oxygen A-band spectra and accurate values of individual absorption-line parameters. The accuracy was tested against literature values. The line positions and the line intensities are in very good agreement with most previous studies (0.000037 % for the positions and 2.22 % for the intensities). A comparison of calculated band constants and Einstein A_{ij} coefficients also support the result of the line position and line intensity investigations, respectively. The broadening coefficients of all four-tested models agree well (within 1 % for the VP and SDV and within 3 % for the RP and SDR) when compared to the corresponding values reported in most literature. In addition, both experimental and theoretical line-mixing coefficients are in very good agreement when compared to Predoi-Cross et al. [44] and Drouin et al. [74].

All these steps were accomplished to proceed with the analysis to retrieve the SD parameters. The experimental values of these parameters was not reported until 2017 [74]. All these above-mentioned parameters validated the present spectra to determine reliable

values of SD parameters. The fitted lines using the SDV and SDR profiles are a more realistic representation of the experimental spectra. Therefore, it is important to have reliable SD parameters in the spectroscopic database. The retrieved SDV parameters show expected patterns of asymmetric parameters when plotted against the m -index. The speed-dependent values will improve the quality of the database.

The comparison of the shift coefficient also indicates that the results can vary even due to using different calibration as well as different experimental procedures. This study also suggests that the SDV profile models the spectra better with the lowest standard deviation of 0.244 and, therefore, can retrieve the SD parameters with a reasonable accuracy.

Ammonia: A comparison of all the assigned transitions to the corresponding theoretically estimated values show a very good agreement. This is the first time that a study made the assignment of ground-state transition from the experimental FTS spectra to this extent ($J = 22_K \rightarrow 23_K$). Further analysis provided information on the line intensities from the fit result of $J = 12_K \rightarrow 13_K$ transitions, which was never performed before.

The comparison of the assigned and the fitted lines show excellent agreement (within 0.0003 %) as expected, which mean that they were fitted very well. Finally, a comparison between the retrieved intensities and the intensities given in HITRAN 2016 revealed a discrepancy factor of value 7.59. Later it was found that the discrepancy was probably due to a change in the gas concentration, because the pressure dropped by 30 % and the purity dropped by 40 % as $^{15}\text{NH}_3$ has a bad characteristic of getting absorbed by the cell wall. These new assignments of the ground state $^{15}\text{NH}_3$ -spectra will noticeably

improve the HITRAN line list. The high-resolution (0.00096 cm^{-1}) ammonia spectra allowed obtaining more accurate data than in previous studies. The intensity values will be very helpful in the observations of atmospheric spectra recorded by ground-based and satellite spectroscopic instruments.

The knowledge of the data analysis using different line-shape profiles as shown in the acetylene study will help researchers to better analyze spectra of various pressure regions. The gradual improvements of the spectroscopic results, for example, the parameters of the oxygen study, will progress the retrieval of atmospheric spectra and the use of spectroscopic databases, which are increasing day-by-day for the interpretation of satellite observation. The extended assignment data from the ammonia study will also improve the databases, such as HITRAN and GEISA.

Bibliography

- [1] P. Rosenkranz, Shape of the 5 mm oxygen band in the atmosphere, IEEE Transactions on Antennas and Propagation, 23 (1975) 498-506.
- [2] L.S. Rothman, R.R. Gamache, A. Goldman, L.R. Brown, R.A. Toth, H.M. Pickett, R.L. Poynter, J.M. Flaud, C. Camy-Peyret, A. Barbe, N. Husson, C.P. Rinsland, M.A.H. Smith, The HITRAN database: 1986 edition, Appl. Opt., 26 (1987) 4058-4097.
- [3] I. Newton, A Letter of Mr. Isaac Newton, Professor of the Mathematicks in the University of Cambridge; Containing His New Theory about Light and Colors: Sent by the Author to the Publisher from Cambridge, In Order to be Communicated to the R. Society, Philosophical Transactions, 6 (1671) 3075-3087.
- [4] G. Kirchhoff, R. Bunsen, XLII. Chemical analysis by spectrum-observations.—Second memoir, Philosophical Magazine, 22 (1861) 329-349.
- [5] J.J. Balmer, Note on the Spectral Lines of Hydrogen, Annalen der Physik und Chemie, 25 (1885) 80-85.
- [6] C.A. Povey, High Resolution Spectroscopy and Application, Department of Physics and Astronomy, University of Lethbridge, 2013.
- [7] A.A. Mashwood, Laboratory Spectroscopic Study of Acetylene and Carbon Dioxide for Atmospheric Remote Sensing Purpose, Department of Physics and Astronomy, University of Lethbridge, Lethbridge, Alberta, Canada, 2016.
- [8] J.M. Hollas, Modern Spectroscopy, 4th Edition, John Wiley & Sons, Southern Gate, England 2004.
- [9] https://www.engineeringtoolbox.com/electromagnetic-spectrum-d_1929.html.
- [10] A. Mehta, Introduction to the Electromagnetic Spectrum and Spectroscopy, Pharmaxchange.info. , Retrieved 2011-11-08.
- [11] F.P. Schäfer, Dye Lasers, Springer-Verlag, Berlin, 1990.
- [12] F.J. Duarte, L.W. Hillman, Dye Laser Principles, Academic, New York, 1990.
- [13] W. Koechner, Solid-State Laser Engineering, 3rd ed. ed., Springer-Verlag 1992.
- [14] P.F. Moulton, Spectroscopic and laser characteristics of Ti:Al₂O₃, J. Opt. Soc. Am. B, 3 (1986) 125-133.

- [15] F. Koyama, K. Susumu, I. Kenichi, Room temperature cw operation of GaAs vertical cavity surface emitting laser, *Trans. IEICE.*, E71 (1988) 1089–1090.
- [16] E.R.H. Jones, D.Sc., F.R.I.C., Acetylene and acetylenic compounds in organic synthesis, *Journal of the Chemical Society (Resumed)*, DOI (1949).
- [17] M. Herman, The acetylene ground state saga, *Molecular Physics*, 105 (2007).
- [18] C.P. McRaven, M.J. Cich, G.V. Lopez, T.J. Sears, D. Hurtmans, A.W. Mantz, Frequency comb-referenced measurements of self- and nitrogen-broadening in the $\nu_1+\nu_3$ band of acetylene, *J. Mol. Spectrosc.*, 266 (2011) 43-51.
- [19] L. Fissiaux, M. Dhyne, M. Lepère, Diode-laser spectroscopy: Pressure dependence of N_2 -broadening coefficients of lines in the $\nu_4+\nu_5$ band of C_2H_2 , *J. Mol. Spectrosc.*, 254 (2009) 10-15.
- [20] R. Hashemi, H. Rozario, C. Povey, A. Predoi-Cross, Line-shape models testing on six acetylene transitions in the $\nu_1+\nu_3$ band broadened by N_2 , *Journal of Quantitative Spectroscopy and Radiative Transfer*, 140 (2014) 58-66.
- [21] D. Lambot, G. Blanquet, J.-P. Bouanich, Diode laser measurements of collisional broadening in the ν_5 band of C_2H_2 perturbed by O_2 and N_2 , *J. Mol. Spectrosc.*, 136 (1989) 86-92.
- [22] P. Varanasi, Intensity and linewidth measurements in the 13.7 μm fundamental bands of $^{12}C_2H_2$ and $^{12}C_{13}CH_2$ at planetary atmospheric temperatures, *Journal of Quantitative Spectroscopy and Radiative Transfer*, 47 (1992) 263-274.
- [23] S.W. Arteaga, C. M. Bejger, J. L. Gerecke, J. L. Hardwick, Z. T. Martin, J. Mayo, E. A. McIlhattan, J. M. F. Moreau, M. J. Pilkenton, M. J. Polston, B. T. Robertson, E.N. Wolf, Line broadening and shift coefficients of acetylene at 1550nm, *J. Mol. Spectrosc.*, 243 (2007) 253-266.
- [24] N.T. Campbell, J.D. Cook, B.A. Coombs, E.P. Fuller, J.L. Hardwick, S.M. Hurley, L.K. Ho, P.A. Kovac, E.J. Robertson, E.N. Senning, J.K. Utterback, R.S. Wiser, Temperature dependence of pressure broadening and shifts of acetylene at 1550 nm by N_2 , *Molecular Physics*, 109 (2011) 2199-2208.
- [25] P. Minutolo, C. Corsi, F. D'Amato, M.D. Rosa, Self- and foreign-broadening and shift coefficients for C_2H_2 lines at 1.54 μm , *The European Physical Journal D*, 17 (2001) 175.
- [26] B.R. Biswas D., S. Dutta, P.N. Ghosh, Diode laser spectroscopic measurement of line shape of $(\nu_1+3\nu_3)$ band transitions of acetylene, *Applied Physics B*, 68 (1999) 1125-1130.
- [27] V. Malathy Devi, D. Chris Benner, C.P. Rinsland, M.A.H. Smith, B.D. Sidney, Tunable diode laser measurements of N_2 - and air-broadened halfwidths: Lines in the $(\nu_4 + \nu_5)$ band of $^{12}C_2H_2$ near 7.4 μm , *J. Mol. Spectrosc.*, 114 (1985) 49-53.

- [28] S.G. Rautian, I.I. Sobelman, Influence on collisions on Doppler's width of spectral lines, Soviet Physics Uspekhi-Uss, 90 (1966) 209-236.
- [29] L. Galatry, Simultaneous Effect of Doppler and Foreign Gas Broadening on Spectral Lines, Physical Review, 122 (1961) 1218-1223.
- [30] A.S. Pine, Self-, N₂- and Ar-broadening and line mixing in HCN and C₂H₂, Journal of Quantitative Spectroscopy and Radiative Transfer, 50 (1993) 149-166.
- [31] H. Rozario, J. Garber, C. Povey, D. Hurtmans, J. Buldyreva, A. Predoi-Cross, Experimental and theoretical study of N₂-broadened acetylene line parameters in the $\nu(1) + \nu(3)$ band over a range of temperatures, Molecular Physics, 110 (2012) 2645-2663.
- [32] M. Dhyne, P. Joubert, J.-C. Populaire, M. Lepère, Collisional broadening and shift coefficients of lines in the $\nu_4 + \nu_5$ band of ¹²C₂H₂ diluted in N₂ from low to room temperatures, Journal of Quantitative Spectroscopy and Radiative Transfer, 111 (2010) 973-989.
- [33] H. Valipour, D. Zimmermann, Investigation of J dependence of line shift, line broadening, and line narrowing coefficients in the $\nu_1 + 3\nu_1 + 3\nu_3$ absorption band of acetylene, The Journal of Chemical Physics, 114 (2001) 3535.
- [34] P.R. Berman, Speed-dependent collisional width and shift parameters in spectral profiles, Journal of Quantitative Spectroscopy and Radiative Transfer, 12 (1972) 1331-1342.
- [35] H.M. Pickett, Effects of velocity averaging on the shapes of absorption lines, The Journal of Chemical Physics, 73 (1980) 6090-6094.
- [36] C. Povey, A. Predoi-Cross, D.R. Hurtmans, Line shape study of acetylene transitions in the $\nu_1 + \nu_2 + \nu_4 + \nu_5$ band over a range of temperatures, J. Mol. Spectrosc., 268 (2011) 177-188.
- [37] B. Lance, G. Blanquet, J. Walrand, J.-P. Bouanich, On the Speed-Dependent Hard Collision Lineshape Models: Application to C₂H₂ Perturbed by Xe, J. Mol. Spectrosc., 185 (1997) 262-271.
- [38] R.H. Dicke, The Effect of Collisions upon the Doppler Width of Spectral Lines, Physical Review, 89 (1953) 472-473.
- [39] J.P. Wittke, R.H. Dicke, Redetermination of the Hyperfine Splitting in the Ground State of Atomic Hydrogen, Physical Review, 96 (1954) 530-531.
- [40] J.P. Bouanich, D. Lambot, G. Blanquet, J. Walrand, N₂- and O₂-broadening coefficients of C₂H₂ IR lines, J. Mol. Spectrosc., 140 (1990) 195-213.

- [41] A. Babay, M. Ibrahimi, V. Lemaire, B. Lemoine, F. Rohart, J.P. Bouanich, Line frequency shifting in the ν_5 band of C_2H_2 , *Journal of Quantitative Spectroscopy and Radiative Transfer*, 59 (1998) 195-202.
- [42] J.-P. Bouanich, G. Blanquet, J.-C. Populaire, J. Walrand, Nitrogen Broadening of Acetylene Lines in the ν_5 Band at Low Temperature, *J. Mol. Spectrosc.*, 190 (1998) 7-14.
- [43] J.-P. Bouanich, G. Blanquet, J. Walrand, Line-Mixing Effects in He- and N_2 -Broadened $\Sigma \leftarrow \Pi$ Infrared Q Branches of C_2H_2 , *J. Mol. Spectrosc.*, 203 (2000) 41-48.
- [44] A. Predoi-Cross, K. Hambrook, R. Keller, C. Povey, I. Schofield, D. Hurtmans, H. Over, G.C. Mellau, Spectroscopic lineshape study of the self-perturbed oxygen A-band, *J. Mol. Spectrosc.*, 248 (2008) 85-110.
- [45] M.C. Pitts, L.W. Thomason, Satellite remote sensing of temperature and pressure by the Stratospheric Aerosol and Gas Experiment III, *Satellite Remote Sensing of Clouds and the Atmosphere IV*, 3867 (1999).
- [46] C.R. Nowlan, C.T. McElroy, J.R. Drummond, Measurements of the O_2 A- and B-bands for determining temperature and pressure profiles from ACE-MAESTRO: Forward model and retrieval algorithm, *Journal of Quantitative Spectroscopy and Radiative Transfer*, 108 (2007) 371-388.
- [47] D.A. Long, D.K. Havey, M. Okumura, C.E. Miller, J.T. Hodges, O_2 A-band line parameters to support atmospheric remote sensing, *Journal of Quantitative Spectroscopy and Radiative Transfer*, 111 (2010) 2021-2036.
- [48] D.M. O'Brien, R.M. Mitchell, Error estimates for retrieval of cloud-top pressure using absorption in the A band of oxygen, *Journal of Applied Meteorology and Climatology*, 31 (1992).
- [49] D.M. O'Brien, R.M. Mitchell, S.A. English, G.D. Costa, Airborne measurements of air mass from O_2 A-band absorption spectra, *Journal of Atmospheric and Oceanic Technology*, 15 (1998).
- [50] D.M. O'Brien, S.A. English, G.D. Costa, High-Precision, High-Resolution Measurements of Absorption in the Oxygen A-Band, *Journal of Atmospheric and Oceanic Technology*, 14 (1997).
- [51] L.S. Rothman, I.E. Gordon, Y. Babikov, A. Barbe, D. Chris Benner, P.F. Bernath, M. Birk, L. Bizzocchi, V. Boudon, L.R. Brown, A. Campargue, K. Chance, E.A. Cohen, L.H. Coudert, V.M. Devi, B.J. Drouin, A. Fayt, J.M. Flaud, R.R. Gamache, J.J. Harrison, J.M. Hartmann, C. Hill, J.T. Hodges, D. Jacquemart, A. Jolly, J. Lamouroux, R.J. Le Roy, G. Li, D.A. Long, O.M. Lyulin, C.J. Mackie, S.T. Massie, S. Mikhailenko, H.S.P. Müller, O.V. Naumenko, A.V. Nikitin, J. Orphal, V. Perevalov, A. Perrin, E.R. Polovtseva, C. Richard, M.A.H. Smith, E. Starikova, K. Sung, S. Tashkun, J. Tennyson, G.C. Toon, V.G.

Tyuterev, G. Wagner, The HITRAN2012 molecular spectroscopic database, *Journal of Quantitative Spectroscopy and Radiative Transfer*, 130 (2013) 4-50.

[52] N. Jacquinet-Husson, R. Armante, N.A. Scott, A. Chédin, L. Crépeau, C. Boutammine, A. Bouhdaoui, C. Crevoisier, V. Capelle, C. Boone, N. Poulet-Crovisier, A. Barbe, D. Chris Benner, V. Boudon, L.R. Brown, J. Buldyreva, A. Campargue, L.H. Coudert, V.M. Devi, M.J. Down, B.J. Drouin, A. Fayt, C. Fittschen, J.M. Flaud, R.R. Gamache, J.J. Harrison, C. Hill, Ø. Hodnebrog, S.M. Hu, D. Jacquemart, A. Jolly, E. Jiménez, N.N. Lavrentieva, A.W. Liu, L. Lodi, O.M. Lyulin, S.T. Massie, S. Mikhailenko, H.S.P. Müller, O.V. Naumenko, A. Nikitin, C.J. Nielsen, J. Orphal, V.I. Perevalov, A. Perrin, E. Polovtseva, A. Predoi-Cross, M. Rotger, A.A. Ruth, S.S. Yu, K. Sung, S.A. Tashkun, J. Tennyson, V.G. Tyuterev, J. Vander Auwera, B.A. Voronin, A. Makie, The 2015 edition of the GEISA spectroscopic database, *J. Mol. Spectrosc.*, 327 (2016) 31-72.

[53] L.R. Brown, C. Plymate, Experimental Line Parameters of the Oxygen A Band at 760 nm, *J. Mol. Spectrosc.*, 199 (2000) 166-179.

[54] G.H. Dieke, H.D. Babcock, The structure of the atmospheric absorption bands of oxygen, *Proceeding of the National Academy of Science*, 13 (1927) 670.

[55] K.J. Ritter, T.D. Wilkerson, High-resolution spectroscopy of the oxygen A band, *J. Mol. Spectrosc.*, 121 (1987) 1-19.

[56] H. Kanamori, M. Momona, K. Sakurai, Diode laser spectroscopy of the atmospheric oxygen band $b^1\Sigma_g^+ - X^3\Sigma_g^-$, *Canadian Journal of Physics*, 68 (1989) 313.

[57] L.C. O'Brien, H. Cao, J.J. O'Brien, Molecular Constants for the $v=0$, $b^1\Sigma_g^+$ Excited State of O_2 : Improved Values Derived from Measurements of the Oxygen A-Band Using Intracavity Laser Spectroscopy, *J. Mol. Spectrosc.*, 207 (2001) 99-103.

[58] A.J. Phillips, P.A. Hamilton, Pressure-Shift of the (0,0) and (1,0) Bands of the Oxygen Transition from Fourier Transform Spectroscopy, *J. Mol. Spectrosc.*, 174 (1995) 587-594.

[59] A.J. Phillips, F. Peters, P.A. Hamilton, Precision Emission and Absorption Spectroscopy of the Oxygen Atmospheric Bands ($b^1\Sigma_g^+ - X^3\Sigma_g^-$) from Fourier Transform Spectroscopy, *J. Mol. Spectrosc.*, 184 (1997) 162-166.

[60] R. Schermaul, R.C.M. Learner, Precise Line Parameters and Transition Probability of the Atmospheric A Band of Molecular Oxygen $^{16}O_2$, *Journal of Quantitative Spectroscopy and Radiative Transfer*, 61 (1999) 781-794.

[61] S. Yang, M.R. Canagaratna, S.K. Witonsky, S.L. Coy, J.I. Steinfeld, R.W. Field, A.A. Kachanov, Intensity Measurements and Collision-Broadening Coefficients for the Oxygen A Band Measured by Intracavity Laser Absorption Spectroscopy, *J. Mol. Spectrosc.*, 201 (2000) 188-197.

- [62] S.-L. Cheah, Y.-P. Lee, J.F. Ogilvie, Wavenumbers, strengths, widths and shifts with pressure of lines in four bands of gaseous $^{16}\text{O}_2$ in the systems $a^1\Delta_g^+-X^3\Sigma_g^-$ and $b^1\Sigma_g^+-X^3\Sigma_g^-$, *Journal of Quantitative Spectroscopy and Radiative Transfer*, 64 (2000) 467-482.
- [63] C. Hill, D.A. Newnham, J.M. Brown, Pressure-shift measurements of the oxygen A-band by Fourier-transform spectroscopy, *J. Mol. Spectrosc.*, 219 (2003) 65-69.
- [64] R.S. Pope, P.J. Wolf, G.P. Perram, Collision broadening of rotational transitions in the O_2 A-band by molecular perturbers, *Journal of Quantitative Spectroscopy and Radiative Transfer*, 64 (2000) 363-377.
- [65] R.S. Pope, P.J. Wolf, G.P. Perram, A study of collision broadening in the O_2 A-band with the noble gases using fourier transform spectroscopy, *J. Mol. Spectrosc.*, 223 (2004) 205-213.
- [66] B. Ray, P.N. Ghosh, Collisional narrowing and pressure broadening of the oxygen A-band transitions, *Spectrochimica Acta Part A: Molecular and Biomolecular Spectroscopy*, 53 (1997) 537-543.
- [67] C.B. Tran H., J.-M. Hartmann, C. Boulet, D. Robert, Line mixing and collision-induced absorption by oxygen in the A band: Laboratory measurements, model, and tools for atmospheric spectra computations, *Journal of Geophysical Research*, 111 (2006) 1.
- [68] M. Vangvichith, H. Tran, J.M. Hartmann, Line-mixing and collision induced absorption for O_2 - CO_2 mixtures in the oxygen A-band region, *Journal of Quantitative Spectroscopy and Radiative Transfer*, 110 (2009) 2212-2216.
- [69] H.C. Fally S, Vandaele AC, Carleer M, Daumont L, Jenouvrier A. , Reinvestigation of the $^{16}\text{O}_2$ atmospheric A-band by high-resolution Fourier Transform Spectroscopy, The Ninth Biennial HITRAN Conference, 2006.
- [70] A. Predoi-Cross, C. Holladay, H. Heung, J.-P. Bouanich, G.C. Mellau, R. Keller, D.R. Hurtmans, Nitrogen-broadened lineshapes in the oxygen A-band: Experimental results and theoretical calculations, *J. Mol. Spectrosc.*, 251 (2008) 159-175.
- [71] D.J. Robichaud, J.T. Hodges, L.R. Brown, D. Lisak, P. Masłowski, L.Y. Yeung, M. Okumura, C.E. Miller, Experimental intensity and lineshape parameters of the oxygen A-band using frequency-stabilized cavity ring-down spectroscopy, *J. Mol. Spectrosc.*, 248 (2008) 1-13.
- [72] D.J. Robichaud, J.T. Hodges, P. Masłowski, L.Y. Yeung, M. Okumura, C.E. Miller, L.R. Brown, High-accuracy transition frequencies for the O_2 A-band, *J. Mol. Spectrosc.*, 251 (2008) 27-37.

- [73] C.E. Miller, D. Wunch, Fourier transform spectrometer remote sensing of O₂ A-band electric quadrupole transitions, *Journal of Quantitative Spectroscopy and Radiative Transfer*, 113 (2012) 1043-1050.
- [74] B.J. Drouin, D.C. Benner, L.R. Brown, M.J. Cich, T.J. Crawford, V.M. Devi, A. Guillaume, J.T. Hodges, E.J. Mlawer, D.J. Robichaud, F. Oyafuso, V.H. Payne, K. Sung, E.H. Wishnow, S. Yu, Multispectrum analysis of the oxygen A-band, *Journal of Quantitative Spectroscopy and Radiative Transfer*, 186 (2017) 118-138.
- [75] S. Urban, S. Klee, K.M.T. Yamada, Ground State Ro-inversional Transitions of ¹⁵NH₃ in the Far-Infrared Region, *J. Mol. Spectrosc.*, 168 (1994) 384-389.
- [76] A. Burrows, Scientific Return of Coronagraphic Exoplanet Imaging and Spectroscopy Using WFIRST, *Earth and Planetary Astrophysics*, DOI (2014).
- [77] S.N.Y. Owens A., W. Thiel and V. Špirko, Accurate prediction of the ammonia probes of a variable proton-to-electron mass ratio, *Monthly Notices of the Royal Astronomical Society*, 450 (2015) 3191-3200.
- [78] Y.S. Owens A, Thiel W, Spirko V., Enhanced sensitivity to a possible variation of the proton-to-electron mass ratio in ammonia, *Physical Review A*, 93 (2016).
- [79] L. Fusina, G. Di Lonardo, E. Canè, A. Predoi-Cross, H. Rozario, M. Herman, The high resolution spectrum of ¹⁵NH₃ in the far-infrared: Rotation-inversion transitions in the ground, v₂=1, 2 and v₄=1 states, *Journal of Quantitative Spectroscopy and Radiative Transfer*, 203 (2017) 417-424.
- [80] S.J. Adriaenssens S, Wuyts K, van Wittenberghe S, Wuytack T, Verheyen K., Pascal B., Roeland S., Canopy uptake of ¹⁵NH₃ by four temperate tree species and the interaction with leaf properties, *Water Air Soil Pollut*, 223 (2012) 5643.
- [81] J. David Felix, E.M. Elliott, T. Gish, R. Maghirang, L. Cambal, J. Clougherty, Examining the transport of ammonia emissions across landscapes using nitrogen isotope ratios, *Atmospheric Environment*, 95 (2014) 563-570.
- [82] C.M. Marty B, Wiens RC, Jurewicz AJC, Burnett DS., A N-15-poor isotopic composition for the solar system as shown by genesis solar wind samples., *Science*, 332 (2011) 1533.
- [83] H.P. Harries D, Langenhorst F., Reactive ammonia in the solar protoplanetary disk and the origin of Earth's nitrogen, *Nature Geoscience*, 8 (2015) 97.
- [84] S.E. McLean IS, Aliado T, Brims G, Kress E, Magnone K, et al., Ground-based and airborne instrumentation for Astronomy, *Proceedings of SPIE*, 6269:B2695 (2006).
- [85] E.E. Becklin, A.G.G.M. Tielens, R.D. Gehrz, H.H.S. Callis, Stratospheric Observatory For Infrared Astronomy (SOFIA), *Proceeding of SPIE*, 2007, pp. 6678:6678.

- [86] A. Wootten, Large ground-based telescopes, in: p.a. 2. (Ed.) Proceeding of SPIE 2003, pp. 110-118.
- [87] H.W. Posselt W, Kulinvak E, Kling G, Kutscheid T, Le Fevre O, et al., NIRSpec - near infrared spectrograph for the JWST, in: M.J. editor. (Ed.) Optical, Infrared, and Millimeter Space Telescopes, Pts1-3, SPIE, Orlando, 2004, pp. 688-697.
- [88] M.J. Gardner JP, Clampin M, Doyon R, Greenhouse MA, Hammel HB, et al., The James Webb Space Telescope, Space Science Reviews 123 (2006) 485-606.
- [89] M.J. Down, C. Hill, S.N. Yurchenko, J. Tennyson, L.R. Brown, I. Kleiner, Re-analysis of ammonia spectra: Updating the HITRAN 14NH₃ database, Journal of Quantitative Spectroscopy and Radiative Transfer, 130 (2013) 260-272.
- [90] M. Carlotti, A. Trombetti, B. Velino, J. Vrbancich, The rotation-inversion spectrum of ¹⁵NH₃, J. Mol. Spectrosc., 83 (1980) 401-407.
- [91] P. Helminger, F.C. De Lucia, W. Gordy, Rotational spectra of NH₃ and ND₃ in the 0.5-mm wavelength region, J. Mol. Spectrosc., 39 (1971) 94-97.
- [92] H. Sasada, Microwave inversion spectrum of ¹⁵NH₃, J. Mol. Spectrosc., 83 (1980) 15-20.
- [93] Š. Urban, D. Papoušek, S.P. Belov, A.F. Krupnov, M.Y. Tret'yakov, K. Yamada, G. Winnewisser, A simultaneous analysis of the microwave, submillimeterwave, and infrared transitions between the ground and ν_2 inversion-rotation levels of ¹⁵NH₃, J. Mol. Spectrosc., 101 (1983) 16-29.
- [94] H. Sasada, Y. Hasegawa, T. Amano, T. Shimizu, High-resolution infrared and microwave spectroscopy of the ν_4 and $2\nu_2$ bands of ¹⁴NH₃ and ¹⁵NH₃, J. Mol. Spectrosc., 96 (1982) 106-130.
- [95] A. Predoi-Cross, H. Rozario, G. Di Lonardo, L. Fusina, F. Tamassia, Far-Infrared Spectra and Spectroscopic Parameters of ¹⁵NH₂D in the Ground State, J. Mol. Spectrosc., 301 (2014) 13-14.
- [96] A. Al Mashwood, A. Predoi-Cross, V.M. Devi, H. Rozario, B. Billinghurst, Measurement and computations of line shape parameters for the 12201 ← 03301, 11101 ← 10002 and 12201 ← 11102 self-broadened CO₂ Q-branches, J. Mol. Spectrosc., 348 (2018) 2-12.
- [97] A. Predoi-Cross, E. Johnson, D. Hemsing, H. Rozario, G.C. Mellau, Climbing up the vibrational ladder of HC¹⁵N: High-temperature near-infrared emission measurements, J. Mol. Spectrosc., 293-294 (2013) 27-32.

- [98] R. Hashemi, H. Rozario, A. Ibrahim, A. Predoi-Cross, Line shape study of the carbon dioxide laser band I, *Canadian Journal of Physics*, 91 (2013) 924-936.
- [99] E. Mollmann, A. G. Maki, M. Winnewisser, B. P. Winnewisser, W. Quapp, High-temperature infrared emission spectra of (DCN)-C-12-N-14 and (DCN)-C-13-N-14, *J. Mol. Spectrosc.*, 212 (2002) 22-31.
- [100] K. Esteki, *Infrared Spectroscopy of Acetylene, Carbon Monoxide, and Deuterated Hydrogen Cyanide for Planetary Atmospheric Applications* University of Lethbridge, Lethbridge, 2016.
- [101] P.F. Bernath, *Spectra of Atoms and Molecules*, Oxford University Press, 400, New York, 1995.
- [102] J. Buldyreva, N. Lavrentieva, V. Starikov, *Collisional Line Broadening and Shifting of Atmospheric Gases*, Imperial College Press, London, 2011.
- [103] N.B. Colthup, L.H. Daly, S.E. Wiberley, *Introduction to Infrared and Raman Spectroscopy*, Academic Press Inc, Boston, 1990.
- [104] P. Duggan, P.M. Sinclair, R. Berman, A.D. May, J.R. Drummond, Testing Lineshape Models: Measurements for 1-0 CO Broadened by He and Ar *J. Mol. Spectrosc.*, 186 (1997) 90-98.
- [105] A.D. May, Molecular Dynamics and a Simplified Master Equation for Spectral Line Shapes, *Physical Review A*, 59 (1999) 3495-3505.
- [106] Beer, Determination of the absorption of red light in colored liquids, *Annalen der Physik und Chemie*, 86 (1852) 78–88.
- [107] J.H. Lambert, *Photometria sive de mensura et gradibus luminis, colorum et umbrae*, Germany: Eberhardt Klett, DOI (1760) 391.
- [108] P. Bouguer, *Essai d'optique sur la gradation de la lumière*, Paris, France: Claude Jombert, DOI (1729) 16–22.
- [109] M. Šimečková, D. Jacquemart, L.S. Rothman, R.R. Gamache, A. Goldman, Einstein A-coefficients and statistical weights for molecular absorption transitions in the HITRAN database, *Journal of Quantitative Spectroscopy and Radiative Transfer*, 98 (2006) 130-155.
- [110] W. Demtröder, *Laser Spectroscopy : Basic Concepts and Instrumentation*, Springer-Verlag, Berlin, 2003.
- [111] W. Demtröder, *Laser Spectroscopy 1 : Basic Principles*. 4th edition, Springer-Verlag, Berlin, 2008.

- [112] J. Humlíček, Optimized computation of the voigt and complex probability functions, *Journal of Quantitative Spectroscopy and Radiative Transfer*, 27 (1982) 437-444.
- [113] M. Kuntz, A new implementation of the Humliceck algorithm for the calculation of the Voigt profile function, *Journal of Quantitative Spectroscopy and Radiative Transfer*, 57 (1997) 819-824.
- [114] J. M. Hartmann, C. Boulet, D. Robert, *Collisional Effects on Molecular Spectra*, 1st edition., Elsevier, UK, 2008.
- [115] P. Joubert, X. Bruet, J. Bonamy, D. Robert, F. Chaussard, X. Michaut, R. Saint-Loup, H. Berger, H₂ vibrational spectral signatures in binary and ternary mixtures: theoretical model, simulation and application to CARS thermometry in high pressure flames, *Comptes Rendus de l'Académie des Sciences - Series IV - Physics*, 2 (2001) 989-1000.
- [116] F. Rohart, M. H., N.H. W., Speed dependence of rotational relaxation induced by foreign gas collisions: Studies on CH₃F by millimeter wave coherent transients, *Journal of Chemical Physics*, 101 (1994) 6475-6486.
- [117] J.P. Wittke, R.H. Dicke, Redetermination of the Hyperfine Splitting in the Ground State of Atomic Hydrogen, *Physical Review*, 103 (1956) 620-631.
- [118] S. Chandrasekhar, *Stochastic Problems in Physics and Astronomy*, *Reviews of Modern Physics*, 15 (1943) 1-89.
- [119] R. Ciuryło, J. Szudy, Speed-dependent pressure broadening and shift in the soft collision approximation, *Journal of Quantitative Spectroscopy and Radiative Transfer*, 57 (1997) 411-423.
- [120] P.W. Anderson, A Method of Synthesis of the Statistical and Impact Theories of Pressure Broadening, *Physical Review*, 86 (1952) 809-809.
- [121] P.W. Anderson, T.J. D., Conference on Broadening of Spectral Lines, University of Pittsburgh, unpublished Bell Teleph Syst Tech Publ No 3117, DOI (1955).
- [122] M.G. Littman, H.J. Metcalf, Spectrally narrow pulsed dye laser without beam expander, *Appl. Opt.*, 17 (1978) 2224-2227.
- [123] T. Day, F. Luecke, M. Brownell, Continuously tunable diode lasers, *Lasers and Optonics*, DOI (1993) 15-17.
- [124] T. Day, M.F. Brownell, I.F. Wu, Widely tunable external cavity diode lasers, 1995, pp. 35-41.
- [125] H.I. Rozario, *Spectroscopic Study of Acetylene and Hydrogen Cyanide* Department of Physics and Astronomy, University of Lethbridge, 2012.

- [126] D. Hurtmans, G. Dufour, W. Bell, A. Henry, A. Valentin, C. Camy-Peyret, Line Intensity of R(0) and R(3) of the $^{12}\text{CH}_4$ $2\nu_3$ Band from Diode Laser Spectroscopy, *J. Mol. Spectrosc.*, 215 (2002) 128-133.
- [127] B.C. Smith, *Fundamentals of Fourier transform infrared spectroscopy*, CRC press, 2011.
- [128] P.R. Griffiths, De Haseth J.A., *Fourier transform infrared spectrometry* (Vol. 171). John Wiley & Sons., United States of America., 2007.
- [129] https://www.cif.iastate.edu/sites/default/files/uploads/Other_Inst/TGA/OPUS_Introduction.pdf.
- [130] K. Levenberg, A Method for the Solution of Certain Problems in Least-squares,, *The Quarterly of Applied Mathematics*., 2 (1944) 164-168.
- [131] D. W. Marquardt, An Algorithm for Least-Squares Estimation of Nonlinear Parameters,, *Journal of the Society for Industrial and Applied Mathematics*, , 11 (1963) 431-441.
- [132] L.R. Brown, D. Chris Benner, V. Malathy Devi, M.A.H. Smith, R.A. Toth, Line mixing in self- and foreign-broadened water vapor at $6\mu\text{m}$, *Journal of Molecular Structure*, 742 (2005) 111-122.
- [133] D.C. Benner, C.P. Rinsland, V.M. Devi, M.A.H. Smith, D. Atkins, A multispectrum nonlinear least squares fitting technique, *Journal of Quantitative Spectroscopy and Radiative Transfer*, 53 (1995) 705-721.
- [134] <http://hitran.iao.ru/bands/simlaunch>.
- [135] L.S. Rothman, I.E. Gordon, A. Barbe, D.C. Benner, P.F. Bernath, M. Birk, V. Boudon, L.R. Brown, A. Campargue, J.P. Champion, K. Chance, L.H. Coudert, V. Dana, V.M. Devi, S. Fally, J.M. Flaud, R.R. Gamache, A. Goldman, D. Jacquemart, I. Kleiner, N. Lacome, W.J. Lafferty, J.Y. Mandin, S.T. Massie, S.N. Mikhailenko, C.E. Miller, N. Moazzen-Ahmadi, O.V. Naumenko, A.V. Nikitin, J. Orphal, V.I. Perevalov, A. Perrin, A. Predoi-Cross, C.P. Rinsland, M. Rotger, M. Šimečková, M.A.H. Smith, K. Sung, S.A. Tashkun, J. Tennyson, R.A. Toth, A.C. Vandaele, J. Vander Auwera, The HITRAN 2008 molecular spectroscopic database, *Journal of Quantitative Spectroscopy and Radiative Transfer*, 110 (2009) 533-572.
- [136] J. Buldyreva, Nguyen, On the role of trajectory modelling in the C_2H_2 infrared line-broadening computation., *Molecular Physics*, 102 (2004) 1523.
- [137] C. Povey, M. Guillorel-Obregon, A. Predoi-Cross, S.V. Ivanov, O.G. Buzykin, F. Thibault, Low pressure line shape study of nitrogen-perturbed acetylene transitions in the $\nu_1 + \nu_3$ band over a range of temperatures, *Canadian Journal of Physics*, 91 (2013) 896-905.

- [138] C. Povey, A. Predoi-Cross, D.R. Hurtmans, Low-pressure line shape study of acetylene transitions in the $\nu_1 + \nu_2 + \nu_4 + \nu_5$ band over a range of temperatures, *Molecular Physics* 110 (2012) 2633-2644.
- [139] P. Wcisło, R. Ciuryło, Influence of the interaction potential shape on the Dicke narrowed spectral line profiles affected by speed-dependent collisional broadening and shifting, *Journal of Quantitative Spectroscopy and Radiative Transfer*, 120 (2013) 36-43.
- [140] D.C. Benner, V.M. Devi, K. Sung, L.R. Brown, C.E. Miller, V.H. Payne, B.J. Drouin, S. Yu, T.J. Crawford, A.W. Mantz, M.A.H. Smith, R.R. Gamache, Line parameters including temperature dependences of air- and self-broadened line shapes of $^{12}\text{C}^{16}\text{O}_2$: 2.06- μm region, *J. Mol. Spectrosc.*, 326 (2016) 21-47.
- [141] I.E. Gordon, L.S. Rothman, C. Hill, R.V. Kochanov, Y. Tan, P.F. Bernath, M. Birk, V. Boudon, A. Campargue, K.V. Chance, B.J. Drouin, J.M. Flaud, R.R. Gamache, J.T. Hodges, D. Jacquemart, V.I. Perevalov, A. Perrin, K.P. Shine, M.A.H. Smith, J. Tennyson, G.C. Toon, H. Tran, V.G. Tyuterev, A. Barbe, A.G. Császár, V.M. Devi, T. Furtenbacher, J.J. Harrison, J.M. Hartmann, A. Jolly, T.J. Johnson, T. Karman, I. Kleiner, A.A. Kyuberis, J. Loos, O.M. Lyulin, S.T. Massie, S.N. Mikhailenko, N. Moazzen-Ahmadi, H.S.P. Müller, O.V. Naumenko, A.V. Nikitin, O.L. Polyansky, M. Rey, M. Rotger, S.W. Sharpe, K. Sung, E. Starikova, S.A. Tashkun, J.V. Auwera, G. Wagner, J. Wilzewski, P. Wcisło, S. Yu, E.J. Zak, The HITRAN2016 molecular spectroscopic database, *Journal of Quantitative Spectroscopy and Radiative Transfer*, 203 (2017) 3-69.
- [142] J.W. Brault, L.R. Brown, C. Chackerian, R. Freedman, A. Predoi-Cross, A.S. Pine, Self-broadened $^{12}\text{C}^{16}\text{O}$ line shapes in the $\nu=2 \leftarrow 0$ band, *J. Mol. Spectrosc.*, 222 (2003) 220-239.
- [143] F. Cuadros, I. Cachadina, W. Ahumada, Determination of Lennard-Jones Interaction Parameters Using a New Procedure, *Molecular Engineering*, 6 (1996).
- [144] T.R. Forester, W. Smith, DLPOLY ,CCP5 Program Library, U.K., 2001.
- [145] S. Nose, A unified formulation of the constant temperature molecular dynamics methods, *Journal of Chemical Physics*, 81 (1984) 511.
- [146] M.P. Allen, W. Smith, *Computer Simulation of Liquids* Oxford, 1987.
- [147] S.N. Yurchenko, A theoretical room-temperature line list for $^{15}\text{NH}_3$, *Journal of Quantitative Spectroscopy and Radiative Transfer*, 152 (2015) 28-36.
- [148] L. Clarisse, C. Clerbaux, F. Dentener, D. Hurtmans, P.-F. Coheur, Global ammonia distribution derived from infrared satellite observations, *Nature Geoscience*, 2 (2009) 479.

- [149] A.B. Burgess, A. Dudhia, R.G. Grainger, D. Stevenson, Progress in tropospheric ammonia retrieval from the MIPAS satellite instrument, *Advances in Space Research*, 37 (2006) 2218-2221.
- [150] J.W.C. Johns, High-resolution far-infrared ($20\text{--}350\text{ cm}^{-1}$) spectra of several isotopic species of H_2O , *J. Opt. Soc. Am. B*, 2 (1985) 1340-1354.
- [151] F. Matsushima, H. Odashima, T. Iwasaki, S. Tsunekawa, K. Takagi, Frequency measurement of pure rotational transitions of H_2O from 0.5 to 5 THz, *Journal of Molecular Structure*, 352 (1995) 371-378.
- [152] R. D'Cunha, Š. Urban, K. Narahari Rao, L. Henry, A. Valentin, The ν_2 band of $^{15}\text{NH}_3$, *J. Mol. Spectrosc.*, 111 (1985) 352-360.
- [153] J.C.P. Shanshan Yu¹, Brian J. Drouin, Keeyoon Sung, Olivier Pirali, Submillimeter-wave and far-infrared spectroscopy of high-J transitions of the ground and $\nu_2=1$ states of ammonia, *The Journal of Chemical Physics*, 133 (2010) 174317–174330.
- [154] K. Sarka, S. HW, Effective Hamiltonian for rotation-inversion states of ammonia-like molecules, *J. Mol. Spectrosc.*, 179 (1996) 195-204.

Appendices

A. Line-shape Tests on R(16) Line of $C_2H_2-N_2$

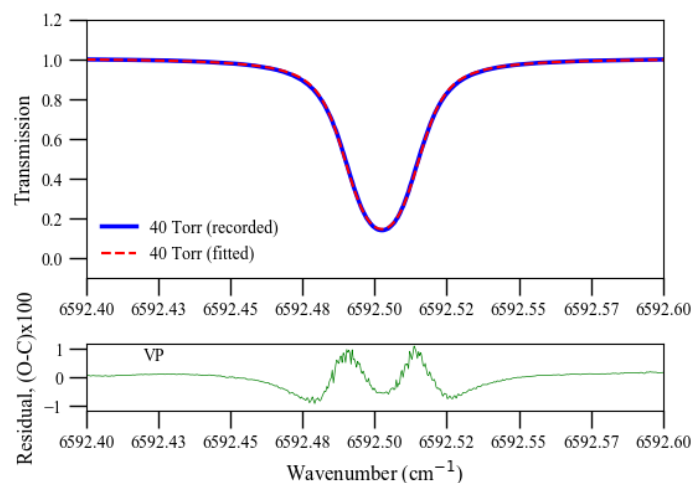


Figure A.1: The top panel shows a spectrum for the R(16) line obtained at a pressure of 40 Torr in blue and the best fit obtained using the Voigt profile (VP) in red. The bottom panel shows the residual spectrum (observed – calculated) from the fit multiplied by 100. The “w” shape indicates that the spectrum was recorded in the Dicke narrowing regime.

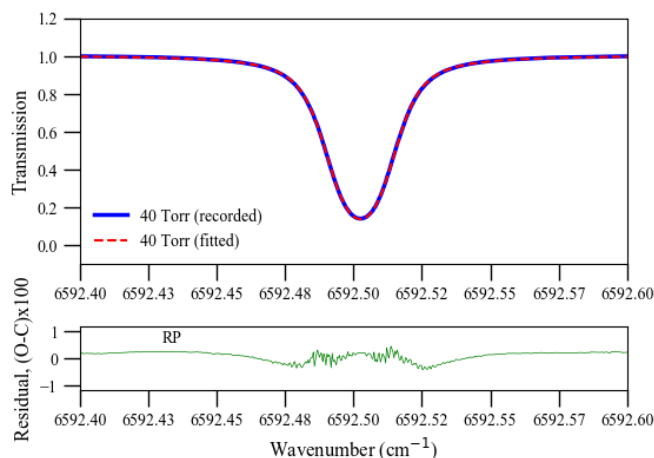


Figure A.2: The top panel shows a spectrum for the R(16) line obtained at a pressure of 40 Torr in blue and the best fit obtained using the Rautian profile (RP) in red. The bottom panel shows the residual spectrum (observed – calculated) from the fit multiplied by 100.

The “w” shape is reduced in the residual spectrum when fitted with Rautian profile, which minimizes the residuals.

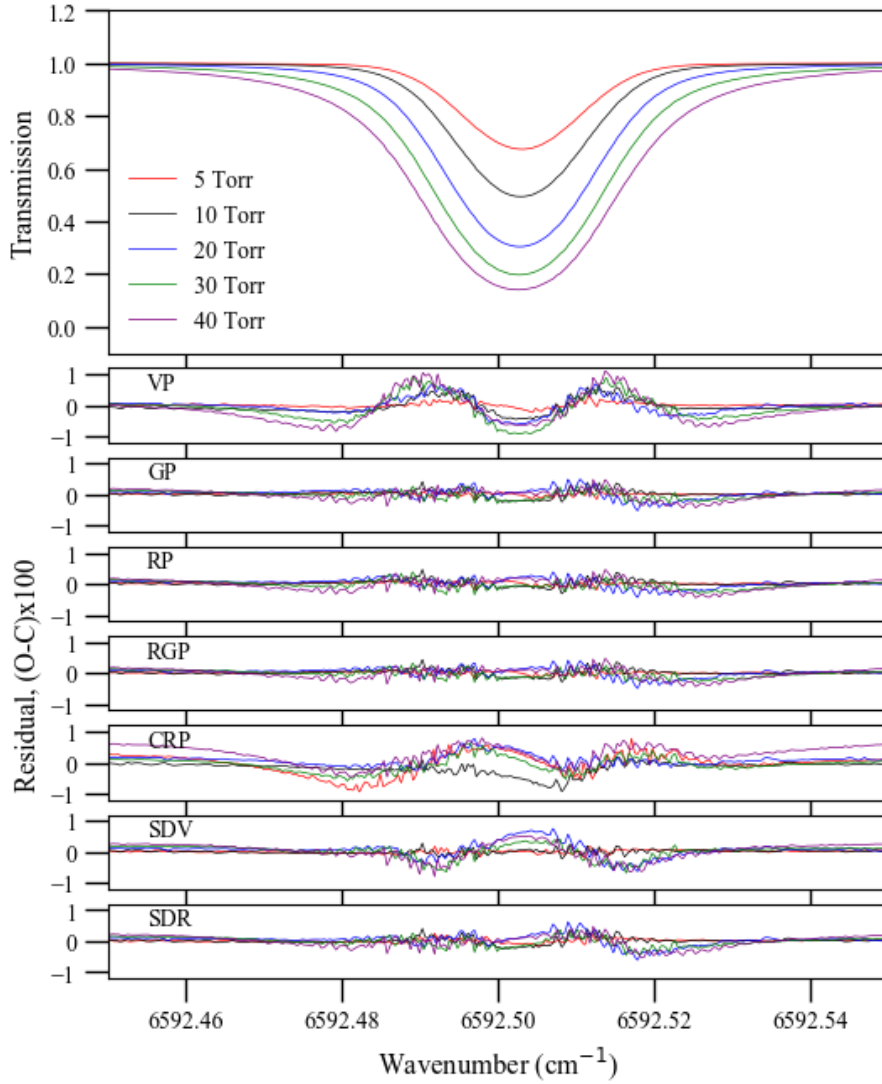


Figure A.3: Room-temperature absorption spectra of line R(16) of $\text{C}_2\text{H}_2\text{-N}_2$ at pressures between 5 Torr and 40 Torr are shown as an example. Lower panels show the residuals (observed – calculated) $\times 100$, resulting from nonlinear least square multi-spectrum fitting of the experimental data with the Voigt (VP), Rautian (RP), Galatry (GP), correlated Rautian (CRP), Rautian-Galatry (RGP), Speed-dependent Voigt (SDV), and Speed-dependent Rautian (SDR) profiles (modification of Figure 1 in [20]).

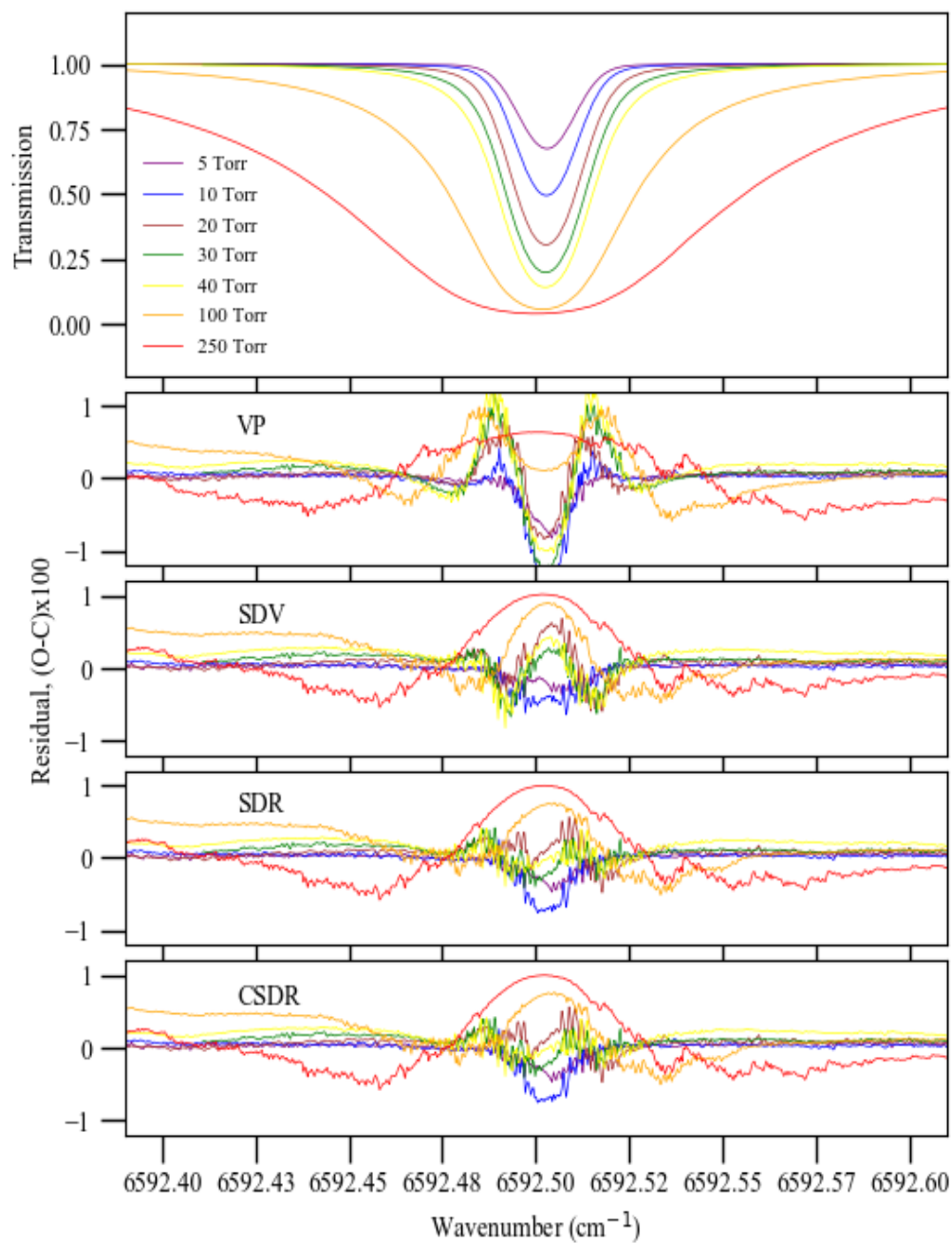


Figure A.4: Room-temperature absorption spectra of line R(16) of the $C_2H_2-N_2$ at pressures between 5 Torr and 250 Torr are shown as an example. Lower panels show the residuals (observed – calculated) $\times 100$, resulting from nonlinear least square multi-spectrum fitting of the experimental data with the Voigt (VP), Speed-dependent Voigt (SDV), Speed-dependent Rautian (SDR), and Correlated Speed-dependent Rautian Profiles (CSDR) (self-generated modified version of Figure 2 in [20]).

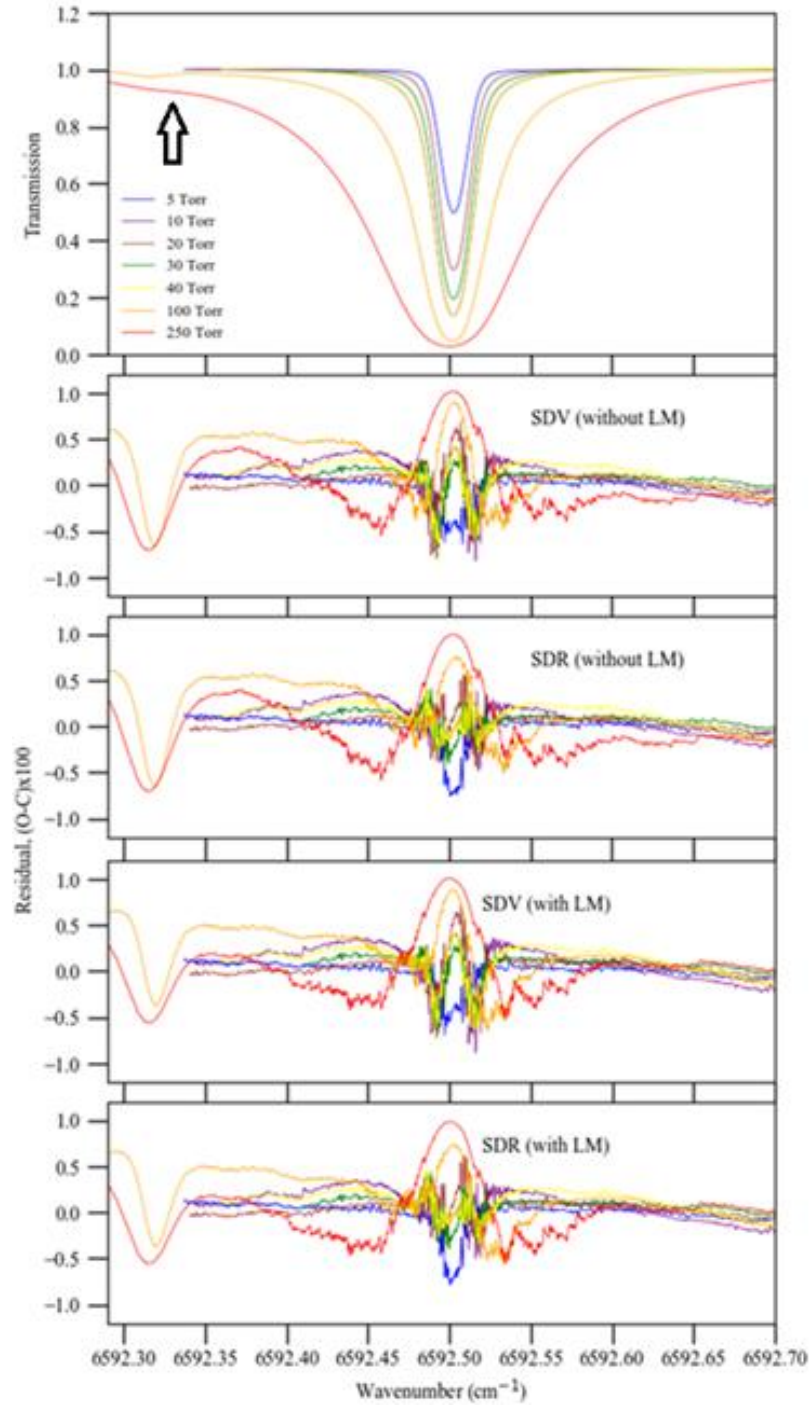


Figure A.5: The line-mixing effect (shown with an arrow) for the R(16) line at the pressure range of 5 – 250 Torr using SDV and SDR profiles. The neighbouring line around 6592.32 cm^{-1} does not exist for the 5 – 40 Torr spectra. The first two residual panels are from fits without taking the line-mixing effect into account, while the last two residual panels are from fits considering the line-mixing effect (self-generated modified version of Figure 8 in [20]).

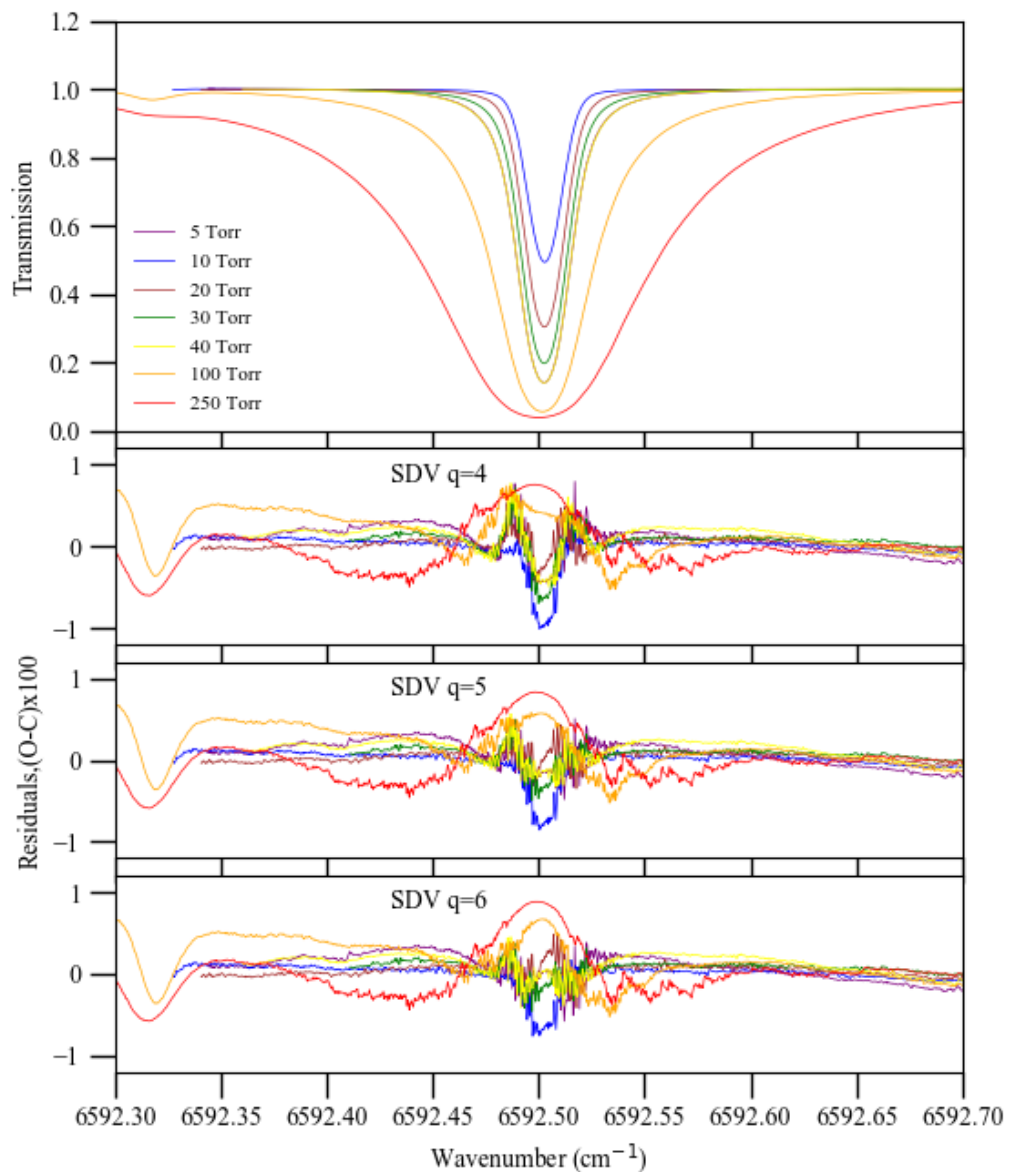


Figure A.6: Room-temperature absorption spectra of line R(16) of the $\text{C}_2\text{H}_2\text{-N}_2$ at pressures between 5 Torr and 250 Torr. Lower panels show the residuals (observed – calculated) $\times 100$, resulting from nonlinear least square multi-spectrum fitting of the experimental data with the speed-dependent Voigt (SDV) Profile to compare the interaction potential power values (self-generated modified version of Figure 3 in [20]).

B. Line-shape Parameters of O₂

Table B.1: Spectroscopic line parameters obtained using the Voigt model. For the P- and R- branches, the m index is $-J''$ and $J'' + 1$, respectively. The uncertainties are given in the parenthesis as one standard deviation (1σ). The uncertainties refer to the last significant digits.

Line label	M	Line Positions cm^{-1}	Line intensities $\text{cm}^{-1}/(\text{molecule. cm}^{-2}) (10^{-24})$	Self Broadening $\text{cm}^{-1}\text{atm}^{-1}$	Self shift $\text{cm}^{-1} \text{atm}^{-1}$	Line-mixing atm^{-1}
P19P19	-19	13050.480996(7)	2.1933(1)	0.04235(4)	-0.00165(4)	0.0016(1)
P19Q18	-19	13052.323165(8)	2.0853(1)	0.04268(4)	-0.00169(5)	0.0008(1)
P17P17	-17	13059.466678(6)	3.3277(1)	0.04391(3)	-0.00152(3)	0.0013(1)
P17Q16	-17	13061.327476(6)	3.1207(1)	0.04402(3)	-0.00148(4)	0.0009(1)
P15P15	-15	13068.081952(5)	4.6823(2)	0.04530(3)	-0.00137(3)	0.0010(1)
P15Q14	-15	13069.962083(5)	4.3311(2)	0.04515(3)	-0.00154(3)	0.0001(1)
P13P13	-13	13076.327293(4)	6.1262(2)	0.04633(3)	-0.00128(3)	0.0014(1)
P13Q12	-13	13078.227878(4)	5.6042(2)	0.04649(3)	-0.00154(3)	0.0005(1)
P11P11	-11	13084.203371(4)	7.4788(2)	0.04798(3)	-0.00108(3)	0.0010(1)
P11Q10	-11	13086.125390(4)	6.6794(2)	0.04772(3)	-0.00149(3)	-0.0003(1)
P9P9	-9	13091.710365(4)	8.3234(3)	0.04896(3)	-0.00113(3)	0.0007(1)
P9Q8	-9	13093.656006(4)	7.2962(2)	0.04895(3)	-0.00119(3)	0.0004(1)
P7P7	-7	13098.848186(4)	8.4578(3)	0.05029(3)	-0.00106(3)	0.0000(1)
P7Q6	-7	13100.821934(4)	7.1238(2)	0.05022(3)	-0.00127(3)	-0.0005(1)
P5P5	-5	13105.616884(4)	7.5775(2)	0.05202(3)	-0.00083(3)	-0.0007(1)
P5Q4	-5	13107.628616(5)	5.9733(2)	0.05244(3)	-0.00096(3)	-0.0012(1)
P3P3	-3	13112.015647(5)	5.7051(2)	0.05446(3)	0.00029(3)	-0.0013(1)
P3Q2	-3	13114.099972(6)	3.9116(2)	0.05637(4)	0.00055(4)	-0.0040(1)
P1P1	-1	13118.044346(8)	3.0524(1)	0.05811(4)	0.00201(5)	-0.0052(1)
R1R1	2	13126.391866(13)	1.5396(1)	0.05945(7)	0.00189(8)	0.0099(2)
R1Q2	2	13128.269325(7)	3.5656(2)	0.05591(4)	0.00005(4)	0.0051(1)
R3R3	4	13131.491465(6)	4.2922(2)	0.05359(3)	0.00100(4)	0.0050(1)
R3Q4	4	13133.441142(4)	6.2213(2)	0.05286(3)	0.00025(3)	0.0029(1)
R5R5	6	13136.217055(4)	6.3051(2)	0.05074(3)	0.00028(3)	0.0023(1)
R5Q6	6	13138.204858(4)	8.0033(3)	0.05024(3)	-0.00029(3)	0.0013(1)
R7R7	8	13140.567196(4)	7.3260(2)	0.04882(3)	-0.00005(3)	0.0010(1)

R7Q8	8	13142.583291(4)	8.7690(3)	0.04864(3)	-0.00043(3)	0.0006(1)
R9R9	10	13144.540692(4)	7.4279(2)	0.04751(3)	-0.00055(3)	-0.0002(1)
R9Q10	10	13146.580388(4)	8.5986(3)	0.04751(3)	-0.00051(3)	-0.0001(1)
R11R11	12	13148.135013(4)	6.7605(2)	0.04639(3)	-0.00066(3)	-0.0007(1)
R11Q12	12	13150.196621(4)	7.6463(3)	0.04617(3)	-0.0008(3)	-0.0007(1)
R13R13	14	13151.348530(4)	5.6459(2)	0.04528(3)	-0.00094(3)	-0.0013(1)
R13Q14	14	13153.430344(4)	6.2815(2)	0.04517(3)	-0.00083(3)	-0.0004(1)
R15R15	16	13154.178733(5)	4.3574(2)	0.04416(3)	-0.00127(3)	-0.0018(1)
R15Q16	16	13156.280026(5)	4.7846(3)	0.04388(3)	-0.00034(4)	-0.0012(1)
R17R17	18	13156.623426(6)	3.1300(2)	0.04316(4)	-0.00132(5)	-0.0033(2)
R17Q18	18	13158.744538(8)	3.4123(7)	0.04354(7)	-0.00216(9)	-0.0036(8)
R19R19	20	13158.679052(12)	2.1082(7)	0.04191(11)	0.00040(14)	0.0003(12)

Table B.2: Spectroscopic line parameters obtained using the Rautian model. The narrowing parameters are fixed to the values from the paper of Long et al. (2010). For the P- and R- branches, the m index is $-J''$ and $J'' + 1$, respectively. The uncertainties are given in the parenthesis as one standard deviation (1σ). The uncertainties refer to the last significant digits. You ha to fit also the narrowing to get smaller broadening than VP

Line				Self		Line-
label	M	Line Positions	Line intensities	Broadening	Self shift	mixing
		cm^{-1}	$\text{cm}^{-1}/(\text{molecule}$			
			$\cdot\text{cm}^{-2}) (10^{-24})$	$\text{cm}^{-1}\text{atm}^{-1}$	$\text{cm}^{-1} \text{atm}^{-1}$	atm^{-1}
P19P19	-19	13050.480997(7)	2.1945(1)	0.04248(4)	-0.00165(4)	0.0016(1)
P19Q18	-19	13052.323161(8)	2.0872(1)	0.0428(4)	-0.00169(5)	0.0009(2)
P17P17	-17	13059.466677(6)	3.3296(1)	0.04401(3)	-0.00152(3)	0.0012(1)
P17Q16	-17	13061.327474(6)	3.1227(1)	0.04411(3)	-0.00148(4)	0.0009(1)
P15P15	-15	13068.081948(5)	4.6831(2)	0.04538(3)	-0.00137(3)	0.0010(1)
P15Q14	-15	13069.961952(5)	4.3339(2)	0.04524(3)	-0.00154(3)	0.0001(1)
P13P13	-13	13076.327291(4)	6.1297(2)	0.04640(3)	-0.00128(3)	0.0014(1)
P13Q12	-13	13078.227876(4)	5.6029(2)	0.04657(3)	-0.00154(3)	0.0005(1)
P11P11	-11	13084.203369(4)	7.4816(2)	0.04805(3)	-0.00108(3)	0.0010(1)
P11Q10	-11	13086.125363(4)	6.6829(2)	0.04779(3)	-0.00149(3)	-0.0003(1)
P9P9	-9	13091.710361(4)	8.3352(3)	0.04901(3)	-0.00113(3)	0.0007(1)
P9Q8	-9	13093.656015(4)	7.2993(2)	0.04901(3)	-0.00119(3)	0.0004(1)
P7P7	-7	13098.848186(4)	8.4603(3)	0.05033(3)	-0.00106(3)	0.0000(1)
P7Q6	-7	13100.821935(4)	7.1262(2)	0.05027(3)	-0.00127(3)	-0.0005(1)
P5P5	-5	13105.616886(4)	7.5791(2)	0.05206(3)	-0.00083(3)	-0.0007(1)

P5Q4	-5	13107.628526(5)	5.9749(2)	0.05249(3)	-0.00096(3)	-0.0012(1)
P3P3	-3	13112.015647(5)	5.7052(2)	0.05451(3)	0.00030(3)	-0.0013(1)
P3Q2	-3	13114.099969(6)	3.9134(2)	0.05642(4)	0.00055(4)	-0.0040(1)
P1P1	-1	13118.044343(8)	3.0541(2)	0.05816(4)	0.00202(5)	-0.0051(1)
R1R1	2	13126.391875(13)	1.5412(1)	0.05956(7)	0.00189(8)	0.0099(2)
R1Q2	2	13128.269327(7)	3.5686(2)	0.05598(4)	0.00005(4)	0.0051(1)
R3R3	4	13131.491468(6)	4.2942(2)	0.05367(3)	0.0010(4)	0.0050(1)
R3Q4	4	13133.441142(4)	6.2235(2)	0.05293(3)	0.00025(3)	0.0029(1)
R5R5	6	13136.217056(4)	6.3082(2)	0.05082(3)	0.00028(3)	0.0023(1)
R5Q6	6	13138.204857(4)	8.0081(3)	0.05031(3)	-0.00029(3)	0.0013(1)
R7R7	8	13140.567197(4)	7.3314(2)	0.04890(3)	-0.00005(3)	0.0010(1)
R7Q8	8	13142.583291(4)	8.7748(3)	0.04872(3)	-0.00043(3)	0.0006(1)
R9R9	10	13144.540691(4)	7.4340(2)	0.04760(3)	-0.00055(3)	-0.0002(1)
R9Q10	10	13146.580390(4)	8.6050(3)	0.04758(3)	-0.00051(3)	-0.0001(1)
R11R11	12	13148.135012(4)	6.7655(2)	0.04648(3)	-0.00066(3)	-0.0006(1)
R11Q12	12	13150.196623(4)	7.6512(3)	0.04625(3)	-0.00081(3)	-0.0007(1)
R13R13	14	13151.348522(4)	5.6020(2)	0.04538(3)	-0.00093(3)	-0.0012(1)
R13Q14	14	13153.430354(4)	6.2862(2)	0.04526(3)	-0.00084(3)	-0.0005(1)
R15R15	16	13154.178726(5)	4.3622(2)	0.04428(3)	-0.00125(3)	-0.0017(1)
R15Q16	16	13156.280016(5)	4.7903(3)	0.04402(3)	-0.00032(4)	-0.0011(1)
R17R17	18	13156.623431(6)	3.1315(2)	0.04333(4)	-0.00133(5)	-0.0033(2)
R17Q18	18	13158.744565(8)	3.4159(7)	0.04369(7)	-0.00216(9)	-0.0045(8)
R19R19	20	13158.679094(12)	2.1066(7)	0.04201(11)	0.00039(14)	0.0017(13)

Table B.3: Spectroscopic line parameters obtained using the Speed Dependent Voigt model. For the P- and R- branches, the m index is $-J''$ and $J'' + 1$, respectively. The uncertainties are given in the parenthesis as one standard deviation (1σ). The uncertainties refer to the last significant digits.

Line label	M	Line Positions	Line intensities $\text{cm}^{-1}/(\text{molecule.})$	Self		Line-mixing	Speed Dependence
				Broadening	Self shift		
		cm^{-1}	$\text{cm}^{-2} (10^{-24})$	$\text{cm}^{-1}\text{atm}^{-1}$	$\text{cm}^{-1} \text{atm}^{-1}$	atm^{-1}	
P19P19	-19	13050.481061(7)	2.1883(2)	0.04200(7)	-0.00168(4)	0.00122(2)	0.010(9)
P19Q18	-19	13052.323219(8)	2.0839(1)	0.04258(7)	-0.00172(5)	0.00112(2)	0.010(9)
P17P17	-17	13059.466732(6)	3.3251(2)	0.04375(5)	-0.00155(3)	0.00123(2)	0.010(7)
P17Q16	-17	13061.327542(6)	3.1200(2)	0.04395(5)	-0.00152(4)	0.00114(2)	0.010(7)
P15P15	-15	13068.082026(5)	4.6868(2)	0.04549(5)	-0.00141(3)	0.00113(2)	0.058(4)
P15Q14	-15	13069.962146(5)	4.3290(2)	0.04508(4)	-0.00157(3)	0.00108(2)	0.011(6)
P13P13	-13	13076.327362(4)	6.1216(2)	0.04618(4)	-0.00131(3)	0.00112(1)	0.010(5)
P13Q12	-13	13078.227943(4)	5.6005(2)	0.04636(4)	-0.00158(3)	0.00095(2)	0.010(5)
P11P11	-11	13084.203461(4)	7.4909(3)	0.04826(4)	-0.00113(3)	0.00097(1)	0.080(3)
P11Q10	-11	13086.125460(4)	6.6760(2)	0.04765(4)	-0.00152(3)	0.00072(1)	0.011(5)
P9P9	-9	13091.710442(4)	8.3207(3)	0.04890(3)	-0.00117(3)	0.00065(1)	0.010(5)
P9Q8	-9	13093.656077(4)	7.2968(3)	0.04895(4)	-0.00123(3)	0.00053(1)	0.016(5)
P7P7	-7	13098.848269(4)	8.4617(3)	0.05035(4)	-0.00111(3)	0.00017(1)	0.035(4)
P7Q6	-7	13100.822006(4)	7.1261(2)	0.05026(4)	-0.00131(3)	-0.00009(1)	0.027(5)
P5P5	-5	13105.616963(4)	7.5772(3)	0.05199(4)	-0.00087(3)	-0.00069(1)	0.011(5)
P5Q4	-5	13107.628695(5)	5.9809(2)	0.05266(5)	-0.0010(3)	-0.00112(2)	0.055(4)
P3P3	-3	13112.015734(5)	5.7064(2)	0.05450(5)	0.00024(3)	-0.00209(2)	0.031(5)
P3Q2	-3	13114.100054(6)	3.9295(2)	0.05744(8)	0.00051(4)	-0.00435(2)	0.123(4)
P1P1	-1	13118.044415(7)	3.0569(2)	0.05833(9)	0.00198(5)	-0.00542(2)	0.045(6)
R1R1	2	13126.391937(13)	1.5446(2)	0.06005(17)	0.00186(8)	0.00864(3)	0.077(9)
R1Q2	2	13128.269392(7)	3.5644(2)	0.05581(7)	0.00002(4)	0.00700(2)	0.011(7)
R3R3	4	13131.491541(6)	4.2935(2)	0.05370(6)	0.00096(4)	0.00443(2)	0.043(5)
R3Q4	4	13133.441233(4)	6.2255(2)	0.05304(5)	0.00020(3)	0.00371(2)	0.059(4)
R5R5	6	13136.217131(4)	6.3082(2)	0.05087(5)	0.00024(3)	0.00216(2)	0.052(4)
R5Q6	6	13138.204937(4)	7.9941(3)	0.05007(4)	-0.00033(3)	0.00188(1)	0.010(5)
R7R7	8	13140.567279(4)	7.3214(3)	0.04874(4)	-0.00009(3)	0.00091(2)	0.012(5)
R7Q8	8	13142.583368(4)	8.7631(3)	0.04856(3)	-0.00047(3)	0.00081(1)	0.01(05)
R9R9	10	13144.540767(4)	7.4181(3)	0.04733(4)	-0.0006(3)	-0.00006(2)	0.010(5)
R9Q10	10	13146.580466(4)	8.5863(3)	0.04732(3)	-0.00055(3)	-0.00007(2)	0.010(5)
R11R11	12	13148.135089(4)	6.7516(3)	0.04621(4)	-0.00070(3)	-0.00073(2)	0.010(5)

R11Q12	12	13150.196697(4)	7.6338(3)	0.04596(4)	-0.00084(3)	-0.00063(2)	0.010(5)
R13R13	14	13151.348605(4)	5.6386(2)	0.04510(4)	-0.00099(3)	-0.00142(2)	0.010(6)
R13Q14	14	13153.430421(4)	6.2665(3)	0.04483(4)	-0.00087(3)	-0.00122(2)	0.010(6)
R15R15	16	13154.178824(5)	4.3528(2)	0.04398(5)	-0.00133(3)	-0.00186(2)	0.010(6)
R15Q16	16	13156.280111(5)	4.7685(3)	0.04344(5)	-0.00040(4)	-0.00194(3)	0.010(7)
R17R17	18	13156.623478(6)	3.1292(3)	0.04299(7)	-0.00137(5)	-0.00251(3)	0.010(8)
R17Q18	18	13158.744904(8)	3.4003(7)	0.04403(13)	-0.00227(10)	-0.00282(3)	0.049(9)
R19R19	20	13158.679399(13)	2.1083(7)	0.0405(17)	0.00062(15)	-0.00249(4)	0.01(15)

Table B.4: Spectroscopic line parameters obtained using the Speed Dependent Rautian model. The narrowing parameters are fixed to the values from the paper of Long et al. (2010). For the P- and R- branches, the m index is $-J''$ and $J'' + 1$, respectively. The uncertainties are given in the parenthesis as one standard deviation (1σ). The uncertainties refer to the last significant digits.

Line label	M	Line Positions cm ⁻¹	Line intensities cm ⁻¹ /(molecule. cm ⁻²) (10 ⁻²⁴)	Self	Self shift cm ⁻¹ atm ⁻¹	Line-mixing atm ⁻¹	Speed Dependence
				Broadening cm ⁻¹ atm ⁻¹			
P19P19	-19	13050.481064(7)	2.1840(2)	0.04167(6)	-0.00168(4)	0.00127(2)	0.0003(8)
P19Q18	-19	13052.323229(8)	2.0799(1)	0.04222(7)	-0.00173(5)	0.00107(3)	0.0003(8)
P17P17	-17	13059.466742(6)	3.3209(2)	0.04348(5)	-0.00155(3)	0.00119(2)	0.0003(7)
P17Q16	-17	13061.327552(6)	3.1153(2)	0.04364(5)	-0.00152(4)	0.00114(2)	0.0003(7)
P15P15	-15	13068.082029(5)	4.6783(2)	0.04514(4)	-0.00141(3)	0.00119(2)	0.0018(6)
P15Q14	-15	13069.962155(5)	4.323(2)	0.04481(4)	-0.00158(3)	0.00094(2)	0.0003(6)
P13P13	-13	13076.327362(4)	6.1138(2)	0.04596(4)	-0.00131(3)	0.00114(2)	0.0003(6)
P13Q12	-13	13078.227949(4)	5.5929(2)	0.04612(4)	-0.00158(3)	0.00095(2)	0.0003(6)
P11P11	-11	13084.203465(4)	7.4814(3)	0.04806(4)	-0.00113(3)	0.00096(1)	0.0313(4)
P11Q10	-11	13086.125467(4)	6.6672(2)	0.04742(4)	-0.00153(3)	0.00073(1)	0.0003(6)
P9P9	-9	13091.710443(4)	8.3122(3)	0.04874(3)	-0.00117(3)	0.00069(1)	0.0003(5)
P9Q8	-9	13093.656080(4)	7.2886(3)	0.04875(4)	-0.00123(3)	0.00050(1)	0.0005(5)
P7P7	-7	13098.848268(4)	8.4528(3)	0.05018(4)	-0.00111(3)	0.00018(1)	0.0011(5)
P7Q6	-7	13100.822011(4)	7.1184(2)	0.05005(4)	-0.00131(3)	-0.00008(1)	0.0008(5)
P5P5	-5	13105.616964(4)	7.5716(3)	0.05184(4)	-0.00087(3)	-0.00068(1)	0.0003(5)
P5Q4	-5	13107.628701(5)	5.9752(2)	0.05244(5)	-0.00101(3)	-0.00115(2)	0.0024(5)
P3P3	-3	13112.015736(5)	5.7005(2)	0.05428(5)	0.00024(3)	-0.00208(2)	0.0098(5)
P3Q2	-3	13114.100074(6)	3.9294(2)	0.05748(8)	0.00049(4)	-0.00438(2)	0.1286(2)
P1P1	-1	13118.044415(8)	3.0518(2)	0.05801(8)	0.00198(5)	-0.00544(2)	0.0017(6)

R1R1	2	13126.391935(13)	1.5397(2)	0.05957(18)	0.00187(8)	0.00871(3)	0.0283(7)
R1Q2	2	13128.269396(7)	3.5582(2)	0.05553(6)	0.00001(4)	0.00706(2)	0.0004(6)
R3R3	4	13131.491537(6)	4.2849(2)	0.05334(6)	0.00096(4)	0.00434(2)	0.0014(6)
R3Q4	4	13133.441239(5)	6.2144(2)	0.05272(5)	0.00019(3)	0.00370(2)	0.0022(5)
R5R5	6	13136.217132(4)	6.2955(2)	0.05053(4)	0.00024(3)	0.0022(2)	0.0016(5)
R5Q6	6	13138.204940(4)	7.9826(3)	0.04985(4)	-0.00033(3)	0.00183(2)	0.0003(5)
R7R7	8	13140.567280(4)	7.3079(3)	0.04846(4)	-0.00001(3)	0.00091(2)	0.0004(6)
R7Q8	8	13142.583373(4)	8.7490(3)	0.04834(3)	-0.00047(3)	0.00078(2)	0.0003(5)
R9R9	10	13144.540771(4)	7.4047(3)	0.04707(4)	-0.00060(3)	-0.00008(2)	0.0003(6)
R9Q10	10	13146.580465(4)	8.5722(3)	0.04710(3)	-0.00054(3)	0.00000(2)	0.0003(6)
R11R11	12	13148.135098(4)	6.7378(3)	0.04592(4)	-0.00071(3)	-0.00077(2)	0.0003(6)
R11Q12	12	13150.196694(4)	7.6206(3)	0.04571(4)	-0.00083(3)	-0.00070(2)	0.0003(6)
R13R13	14	13151.348617(4)	5.6263(2)	0.04479(4)	-0.00100(3)	-0.00137(2)	0.0003(6)
R13Q14	14	13153.430418(4)	6.2558(3)	0.04457(4)	-0.00086(3)	-0.00122(2)	0.0003(6)
R15R15	16	13154.178838(5)	4.3424(2)	0.04362(5)	-0.00135(3)	-0.00182(2)	0.0003(6)
R15Q16	16	13156.280126(5)	4.7590(3)	0.04311(5)	-0.00042(4)	-0.00197(3)	0.0003(7)
R17R17	18	13156.623472(6)	3.1213(3)	0.04256(7)	-0.00136(5)	-0.00246(3)	0.0003(8)
R17Q18	18	13158.745039(8)	3.3830(7)	0.0435(12)	-0.00247(9)	-0.00290(4)	0.0016(9)
R19R19	20	13158.679298(13)	2.1125(7)	0.04047(16)	0.00089(14)	-0.00238(5)	0.0003(12)

C. Calculation of Molecular Constants of $^{15}\text{NH}_3$

The following calculation are taken from the 15-ammonia study [79]. Energy levels (eigenvalues) of a molecular system are generated from a Hamiltonian matrix (discussed in the rotational, ro-vibrational sections of Chapter 2). This Hamiltonian contains a unique set of rotational and vibrational quantum numbers for a given molecular system. The general approximation of the vibration-rotation Hamiltonian for a rigid symmetric-top (non-degenerate vibrational level) C_{3v} rotor is given below as follows [8]:

$$E_v^{vib-rot} = B_v[J(J+1)] + (A_v - B_v)k^2 - D_{vJ}[J(J+1)]^2 - D_{vJK}[J(J+1)]k^2 - D_{vK}k^4, \quad (\text{C.1})$$

where $E_v^{vib-rot}$ is the energy term value, A_v and B_v are the rotational constants for symmetric-top molecules, the D_v terms represent the centrifugal distortion constants, and k represents the inversion term (for GS, $k = \pm K$ and the vibrational mode $v = 0$). Therefore, the transition wavenumber can be determined as follows:

$$\tilde{\nu}^{vib-rot}(v', J', k' \leftarrow v'', J'', k'') = E_v^{vib-rot}(v', J', k') - E_0^{vib-rot}(v'', J'', k''), \quad (\text{C.2})$$

where $E_0^{vib-rot}$ is the energy term value of the lower state and $E_v^{vib-rot}$ of the upper state. Assuming a transition $v = 1 \leftarrow 0$, where the vibration with symmetry provides a parallel band for the above formula. This type of transition (transition term value $\tilde{\nu}^{vib-rot}$) follows the $\Delta K = 0$ and $\Delta J = 0, \pm 1$ selection rule.

The rotation-inversion Hamiltonian for 14-ammonia and for 15-ammonia has been described by Sarka et al. [154] and by Luciano et al. [79], respectively. The rotation-inversion Hamiltonian for the 15-ammonia GS transitions contains the $\Delta K = \pm 3$ term with

a α coefficient and $\Delta K = \pm 6$ term with a η_3 coefficient. The eigenvalues derived from the appropriate energy matrix of GS are the energy-term values of the rotation-inversion transitions. The diagonal elements of this energy matrix include the rotational constant and the centrifugal distortion constants. In this chapter, molecular constants of the GS transition were determined using the following expression [79]

$$\begin{aligned}
\frac{{}^{(i)}E_{v(J,K)}}{hc} = & {}^{(i)}E_v^0 + {}^{(i)}B_v[J(J+1) - k^2] + {}^{(i)}C_vk^2 - {}^{(i)}D_{vJ}[J(J+1)]^2 - \\
& {}^{(i)}D_{vJK}[J(J+1)]k^2 - {}^{(i)}D_{vK}k^4 + {}^{(i)}H_{vJ}[J(J+1)]^3 + {}^{(i)}H_{vJK}[J(J+1)]^2k^2 + \\
& {}^{(i)}H_{vKK}[J(J+1)]k^4 + {}^{(i)}H_{vK}k^6 + {}^{(i)}L_{vJ}[J(J+1)]^4 + {}^{(i)}L_{vJK}[J(J+1)]^3k^2 + \\
& {}^{(i)}L_{vKK}[J(J+1)]^2k^4 + {}^{(i)}L_{vKKK}[J(J+1)]k^6 + {}^{(i)}L_{vK}k^8 + {}^{(i)}M_{vJ}[J(J+1)]^5 + \\
& {}^{(i)}M_{vJK}[J(J+1)]^4k^2 + {}^{(i)}M_{vJJK}[J(J+1)]^3k^4 + {}^{(i)}M_{vJKK}[J(J+1)]^2k^6 + \\
& {}^{(i)}M_{vKKK}[J(J+1)]k^8 + {}^{(i)}M_{vK}k^{10} + {}^{(i)}N_{vJ}[J(J+1)]^6 + {}^{(i)}N_{vJK}[J(J+1)]^5k^2 + \\
& {}^{(i)}N_{vJJK}[J(J+1)]^4k^4 + {}^{(i)}N_{vJJKK}[J(J+1)]^3k^6 + {}^{(i)}N_{vJKKK}[J(J+1)]^2k^8 + \\
& {}^{(i)}N_{vKKKK}[J(J+1)]k^{10} + {}^{(i)}N_{vK}k^{12}, \tag{C.3}
\end{aligned}$$

where the superscript (i) , corresponding to the upper (a) and lower (s) components of the inversion doublet energy states. E is the energy term, B and C are the rotational constants and D , H , L , M , and N are the K dependent centrifugal distortion constants. The rotational distortion constants were calculated up to the 12th power from the diagonal elements (K dependent constants up to N_k). The off-diagonal elements of the matrix are given by the following expression:

$$\begin{aligned} \left\langle \nu_s, J, k \left| \frac{(H_{04} + H_{06} + H_{08})}{hc} \right| \nu_s, J, k \pm 3 \right\rangle_s^a = & \left\{ \left[\alpha + \alpha_J J(J+1) + \alpha_{JJ} J^2(J+1)^2 (2k \pm 3) + \right. \right. \\ & \left. \left[\alpha_K + \alpha_{JK} J(J+1) \right] [k^3 + (k \pm 3)^3] + \alpha_{KK} [k^5 + (k \pm 3)^5] F_{\pm 3}(J, K) \right\} \end{aligned} \quad (C.4)$$

and

$$\begin{aligned} \left\langle \nu_s, J, k \left| \frac{(H_{06} + H_{08})}{hc} \right| \nu_s, J, k \pm 6 \right\rangle_s^a = & \left\{ {}^{(i)}\eta_3 + {}^{(i)}\eta_{3J} J(J+1) + \right. \\ & \left. {}^{(i)}\eta_{3K} [k^2 + (k \pm 6)^2] \right\} F_{\pm 6}(J, K), \end{aligned} \quad (C.5)$$

where the $F_{\pm 3}$ and $F_{\pm 6}$ terms can be generally expressed using the n^{th} term as follows:

$$\begin{aligned} F_{\pm n}(J, K) = & [J(J+1) - k(k \pm 1)]^{1/2} [J(J+1) - (k \pm 1)(k \pm 2)]^{1/2} \dots \{J(J+1) - \\ & [k \pm (n-1)](k \pm n)\}^{1/2}, \end{aligned} \quad (C.6)$$

where ${}^{(i)}\eta_3$ is the interaction parameter.

The above-described calculations were performed by the spectroscopic research group (Fusina, Di Lonardo, Cane) at the Dipartimento di Chimica Industriale "Toso Montanari", University of Bologna, Italy [79] during the collaboration with this research group. They calculated the spectroscopic parameters (molecular constants) using a least-squares analysis procedure by fitting the newly assigned absorption transitions. Pure inversion transition frequencies (microwave region) from the literature, GS rotation-inversion transition frequencies (new assignments in the infrared region) from the present study, and GS combination differences (GSCD) were fitted to obtain molecular distortion constants (GS parameters) up to the 12th power (Equation C.3 – C.6). Previous studies reported transitions only up to $J = 13$ [90] and distortion constants up to the 6th power [93].